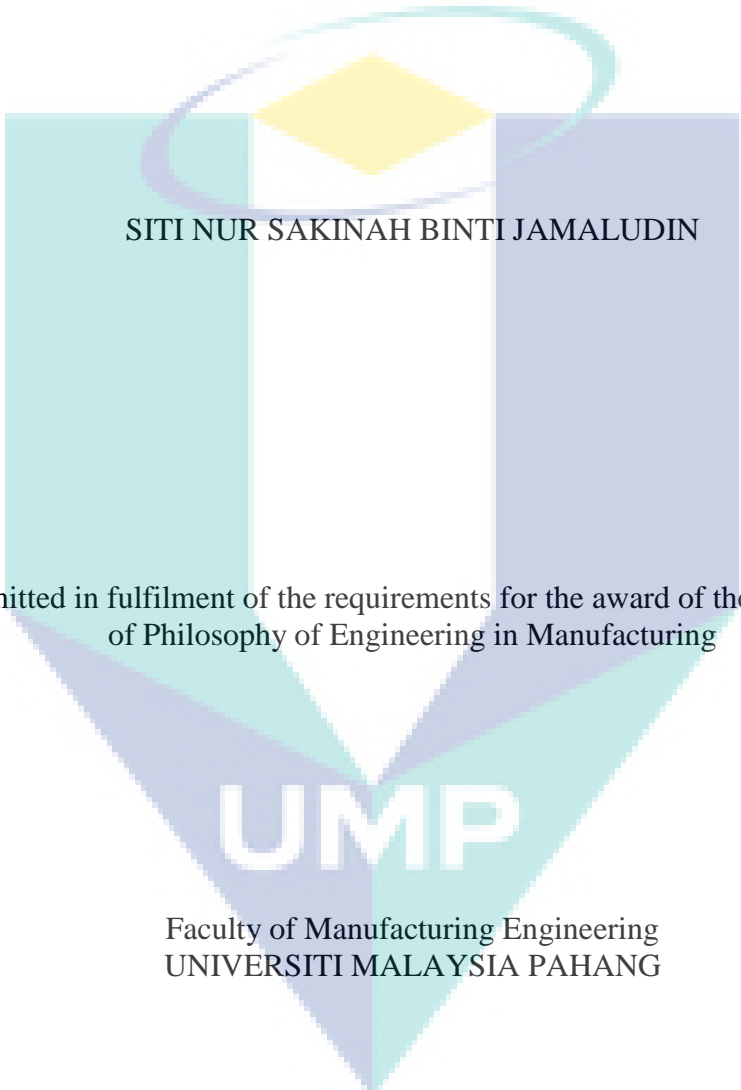


A PARAMETRIC STUDY ON DESIGN AND CHARACTERISTICS OF STEPWISE-
BUILT FUNCTIONALLY GRADED HYDROXYAPATITE/TITANIUM



SITI NUR SAKINAH BINTI JAMALUDIN

Thesis submitted in fulfilment of the requirements for the award of the degree of Doctor
of Philosophy of Engineering in Manufacturing

UMP

Faculty of Manufacturing Engineering
UNIVERSITI MALAYSIA PAHANG

MARCH 2015

UNIVERSITI MALAYSIA PAHANG

DECLARATION OF THESIS AND COPYRIGHT

Author's full name : SITL NUR SAKINAH BINTI JAMALUDIN

Date of birth: 25 JULY 1985

Title : A PARAMETRIC STUDY ON DESIGN AND CHARACTERISTICS OF
STEPWISE-BUILT FUNCTIONALLY GRADED HYDROXYAPATITE/TITANIUM

Academic Session : SEMESTER 2 2013/2014

I declare that this thesis is classified as:

CONFIDENTIAL

(Contains confidential information under the Official Secret Act 1972)*

RESTRICTED

(Contains restricted information as specified by the organization where research was done)*

OPEN ACCESS

I agree that my thesis to be published as online open access (Full text)

I acknowledge that University Malaysia Pahang reserves the right as follows::

1. The Thesis is the Property of University Malaysia Pahang
2. The Library of University Malaysia Pahang has the right to make copies for the purpose of research only.
3. The Library has the right to make copies of the thesis for academic exchange.

Certified By:



(Student's Signature)

850725-07-5706

New IC / Passport Number

Date: 31/03/2015



(Signature of Supervisor)

PROF.IR.DR. SHAHNOR BASRI

Name of Supervisor

Date: 27/03/2015

SUPERVISOR'S DECLARATION

We hereby declare that we have checked this thesis and in our opinion this thesis is adequate in terms of scope and quality for the award of the degree of Doctor of Philosophy of Engineering in Manufacturing.

Signature:

Name of Supervisor:

Position:

Date:



PROF. IR. DR. SHAH NOR BIN BASRI, F.A.S.C.
PROFESOR
FAKULTI KEJURUTERAAN PEMBUATAN
UNIVERSITI MALAYSIA PAHANG
26800 PEKAN
PAHANG DARUL MAKMUR
TEL: 09-424 5940 FAKS: 09-424 5886

Signature:

Name of Co-supervisor:

Position:

Date:



Dr. Faizal Mustapha
Associate Professor
Department of Aerospace Engineering
Faculty of Engineering
Universiti Putra Malaysia



UMP

STUDENT'S DECLARATION

I hereby declare that the work in this thesis is my own except for quotations and summaries which have been duly acknowledged. The thesis has not been accepted for any degree and is not concurrently submitted for award of other degree.

Signature :



Name :

SITI NUR SAKINAH BINTI JAMALUDIN

ID Number :

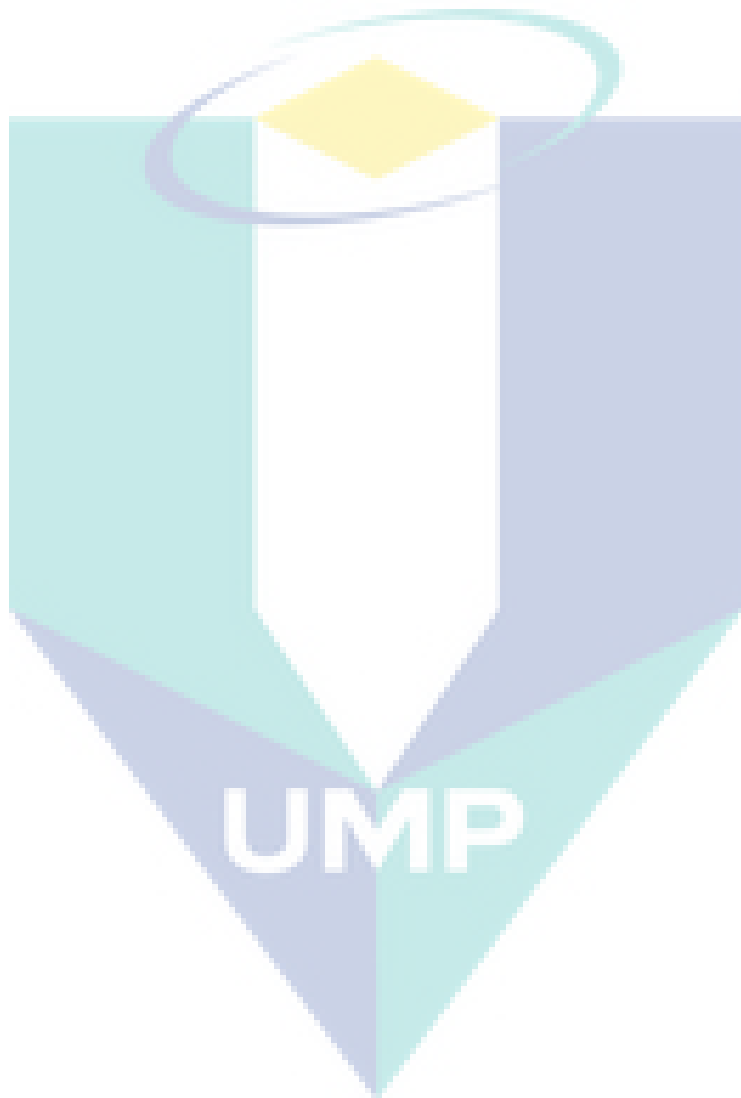
PMA12001

Date :

31/03/2015



UMP



*This thesis is dedicated to my soulmate, parents, parents-in-law, kids and
siblings
for their sincere pray, love, endless support
and encouragement*

ACKNOWLEDGEMENTS

I would like to express my deepest gratitude to the numerous people who have walked with me along the journey of this thesis. First and foremost, I would like to express my deep gratefulness to my supervisor *Prof. Ir. Dr. Shahnor Basri* for his kind assistance, support, critical advice, encouragement, suggestions and direction throughout my research and preparation of this thesis. Many ideas originated in our frequent discussions and his constant support and patience over the years have been of invaluable help.

I also wish to extend my sincere gratitude and appreciation to my co-supervisors, *Assoc. Prof. Dr. Faizal Mustapha* and *Assoc. Prof. Dewan Muhammad Nuruzzaman* for their guidance, encouragement and supervision throughout the course of the study until the completion of this thesis. I truly admire them for their openness and sincerity and appreciate the time they devoted in advising me and showing me the proper directions to continue this research.

Many thanks also goes to *Assoc. Prof. Dr. Tuan Muhammad Yusoff Tuan Ya* for his guidance and ideas on the computational analysis. I also want to acknowledge *Assoc. Prof. Dr. Zawati Harun*, *Dr. Mazni Ismail* and *Dr. Mazli Mustapha* for their help and contributions regarding the experimental study.

I also would like to express my gratitude towards the academic and technical staffs in Faculty of Manufacturing Engineering (UMP), Metallurgical Laboratory (UTHM), Solar Energy Research Laboratory (SERI, UKM) and Sirim Advanced Materials Research Center (AMREC) for their co-operations, knowledge sharing, helpful advice and fruitful discussions that made an invaluable contribution to this dissertation. My sincere thanks also go to all my fellow friends, labmates and members who always keep my spirit on to finish my research.

My heart-full gratitude and love to my husband, *Mr. Muhd Zahiruddin Shukor* whose unconditional support and love has made this dream comes true to me. I also acknowledge my sincere indebtedness and appreciations to my parents, *Mr. Jamaludin Man* and *Mrs. Siti A'shah Jamaludin* for their pray, dream and sacrifice throughout my life. The same goes to my parents-in-law, *Mr. Shukor Nordin* and *Mrs. Zaiton Ibrahim* who consistently encourage me to carry on my higher studies while my kids are growing up. I am also grateful to my siblings and kids for their encouragement, help, patience and understanding that were inevitable to make this work possible. I cannot find the appropriate words that could properly describe my appreciation for their devotion, support and faith in my ability to attain my goals. May Allah bless us all the time.

ABSTRACT

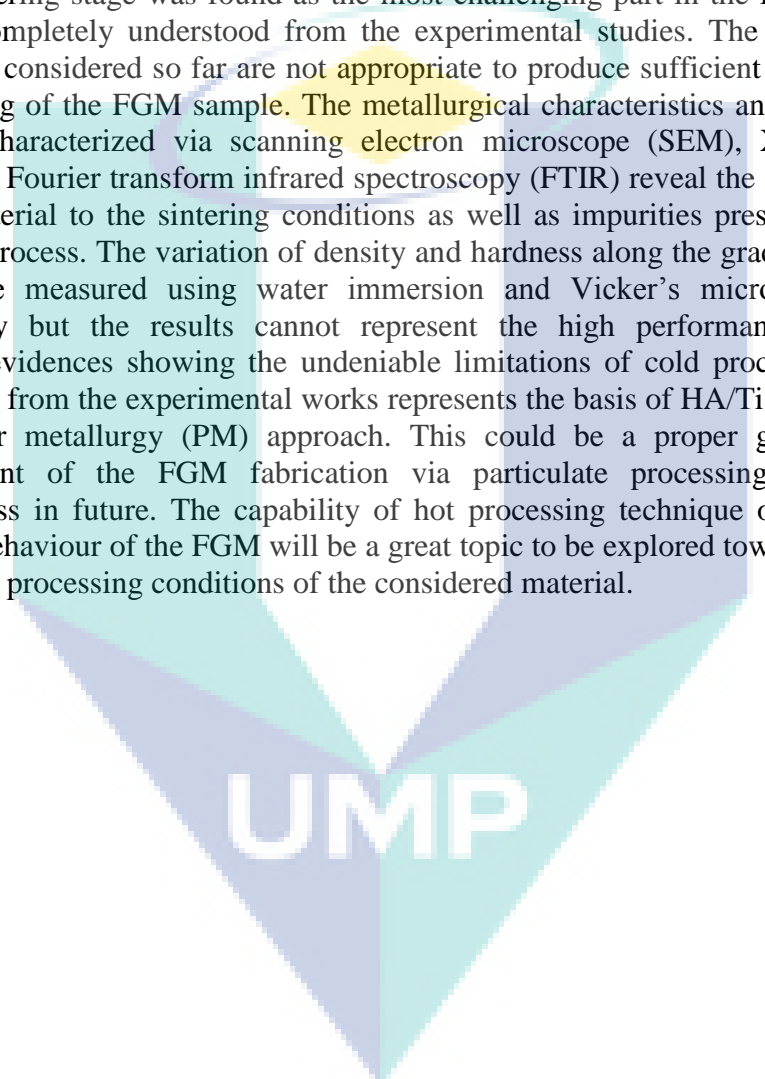
Demand exists to enhance the performance and capability of engineering materials for various advanced engineering applications such as bioengineering, biomedical, aerospace and electronic devices. In order to fulfil the demand, concept of property gradation in functionally graded materials (FGMs) has been introduced and it allows the elimination of many limitations found in conventional materials. As the material selection is the key element of developing an FGM, the composition of hydroxyapatite (HA) as the ceramic phase and titanium (Ti) as the metallic phase in HA/Ti FGM is seen as an excellent combination of high biocompatibility and high thermal resistance with high mechanical properties in a structural domain. However as far as the author is aware, a comprehensive data on various characteristics of the FGM as well as its optimal processing condition is yet been reported thus it becomes the main direction of this study.

This thesis reports the development and the results of a combined theoretical and experimental investigation of HA/Ti as FGM under various geometrical design parameters that affect the property gradient and loading conditions. The theoretical model has been developed based on finite element method (FEM) to solve for the stress and the coupled thermal stress equations. Several numerical studies for HA/Ti FGM plate were then carried out using analysis system (ANSYS) software and rule of mixture (ROM) formulations to verify the basis of the present model. It includes the investigation of the parametric effects on the performance of the FGM towards optimizing the geometrical design of a pre-designed cylindrical HA/Ti FGM plate using a 2-D axisymmetric FE Model. The cylindrical shape is selected to minimize sintering issue due to the sharp edge effects. Subsequently, a 3-D FE model is further developed for the parametric study on various responses fields such as displacement and stress components included in the FGM plate under various loading conditions. These models are verified by quantitative agreement achieved between present results and those published in literature. Concurrently, an experimental program was conducted using HA and Ti powders which were prepared via powder metallurgy technique for the measurement of the actual mechanical properties of the FGM. From these parametric studies, it is expected that a lot of numerical and empirical data on the characteristics corresponding to various loading conditions as well as criteria for designing and preparing the optimum HA/Ti FGM can be provided.

In the numerical studies, the optimization analysis is used to quantify the effects of grading parameter, number of layer and thickness on residual stresses distribution of the FGM. The effects of these geometrical parameters are further considered in the parametric study on various behaviours of the FGM under isothermal, thermal and thermo-mechanical loading conditions. The aim of these studies is to reveal that the property gradation profile does influence the material's performance under various conditions. The results from the optimization analysis concluded the optimum FGM design which can be developed by linearly graded the material composition and providing minimum six number of layer with each having a particular thickness that can preserve the material gradation effectiveness. These criteria were acquired by the minimum residual stresses distribution and higher residual stresses relaxation profiles. The findings from the parametric study revealed that the loading field distribution was

another factor that reflects the thermo-elastic properties of the HA/Ti FGM plate and the stress intensity distributions were found as a good indicator to the spot of failures initiation on the FGM structure. The HA/Ti FGM plate is found to be able to withstand the thermal stresses while preserving the high toughness properties and thus shows its ability to operate at high temperature.

Due to the limited available facilities, the fabrication of the HA/TiFGM via cold compaction and pressure-less sintering techniques does not guarantee good findings. The densification and grain boundary energy minimization of the powdered compacts during sintering stage was found as the most challenging part in the fabrication which still not completely understood from the experimental studies. The varied operating parameters considered so far are not appropriate to produce sufficient driving force for the sintering of the FGM sample. The metallurgical characteristics and microstructural topology characterized via scanning electron microscope (SEM), X-ray diffraction (XRD) and Fourier transform infrared spectroscopy (FTIR) reveal the sensitivity of HA and Ti material to the sintering conditions as well as impurities presence during heat treatment process. The variation of density and hardness along the gradient plane of the FGM were measured using water immersion and Vicker's micro-hardness tester respectively but the results cannot represent the high performance criteria. The empirical evidences showing the undeniable limitations of cold processing technique highlighted from the experimental works represents the basis of HA/Ti FGM processing via powder metallurgy (PM) approach. This could be a proper guideline for the improvement of the FGM fabrication via particulate processing which is cost effectiveness in future. The capability of hot processing technique on enhancing the sintering behaviour of the FGM will be a great topic to be explored towards determining the optimal processing conditions of the considered material.

The logo for UMP (Universiti Malaysia Perlis) is a large, stylized letter 'V' shape. The left side of the 'V' is light blue, the right side is light green, and the bottom point is a darker blue. The letters 'UMP' are written in white, bold, sans-serif font across the center of the 'V'.

ABSTRAK

Terdapat permintaan untuk meningkatkan prestasi dan keupayaan bahan kejuruteraan untuk pelbagai aplikasi kejuruteraan termaju seperti biokejuruteraan, bioperubatan, aeroangkasa dan peranti elektronik. Bagi memenuhi permintaan tersebut, konsep penggredan sifat dalam bahan berfungsi mengikut gred (FGMs) telah diperkenalkan dan ia membolehkan penghapusan banyak keterbatasan yang terdapat dalam bahan konvensional. Oleh kerana pemilihan bahan adalah unsur utama yang perlu dipertimbangkan dalam membangunkan FGM, komposisi hydroxyapatite (HA) sebagai fasa seramik dan titanium (Ti) sebagai fasa logam dalam FGM HA/Ti dilihat sebagai kombinasi terbaik antara sifat keserasian-bio yang tinggi dan keupayaan ketahanan terma yang tinggi dengan sifat-sifat mekanik yang tinggi dalam satu struktur bahan. Walaubagaimanapun, mengikut pengetahuan pengarang, data menyeluruh terhadap pelbagai sifat FGM termasuk keadaan optimal pemprosesan bahan masih terbatas, oleh itu ia menjadi fokus utama kajian ini.

Tesis ini melaporkan perkembangan dan hasil penyelidikan secara teori dan eksperimen ke atas bahan FGM HA/Ti yang terdiri daripada pelbagai parameter geometri reka bentuk yang memberi kesan terhadap kecerunan sifat bahan dan pelbagai kondisi bebanan. Model teori telah dihasilkan berdasarkan kaedah unsur terhingga (FEM) untuk mengesan profil tegasan dan profil tegasan termo-mekanikal. Beberapa kajian berangka bagi plat FGM HA/Ti kemudian dilakukan dengan menggunakan perisian sistem analisa (ANSYS) dan persamaan peraturan campuran (ROM) untuk menentusahkan asas model ini. Ini termasuk kajian terhadap kesan parametrik pada perilaku FGM ke arah pengoptimuman pra-rekabentuk geometri plat silinder FGM HA/Ti menggunakan model unsur terhingga sepaksi simetri 2-D. Bentuk silinder dipilih untuk mengurangkan masalah pensinteran disebabkan oleh kesan ketajaman tepian. Selepas itu, model 3-D dibangunkan untuk kajian parametrik pada berbagai aspek seperti komponen-komponen anjakan dan tegasan di dalam plat FGM di bawah pelbagai keadaan bebanan. Model-model ini ditentusahkan melalui persetujuan secara kuantitatif yang dicapai antara hasil kajian ini dengan hasil kajian yang telah diterbitkan. Pada masa yang sama, satu program eksperimen telah dijalankan ke atas serbuk HA dan Ti yang disediakan menggunakan kaedah metalurgi serbuk untuk mengukur sifat-sifat mekanik yang sebenar FGM tersebut. Daripada kajian parametrik ini, pelbagai data berangka dan empirikal yang menunjukkan ciri-ciri serta kriteria reka bentuk optimum dan pemprosesan FGM tersebut dijangka dapat disediakan.

Dalam kajian berangka, analisis pengoptimuman adalah bertujuan untuk mengukur kesan parameter penggredan, bilangan lapisan dan ketebalan ke atas taburan tegasan sisa FGM. Kesan parameter geometri ini kemudiannya dipertimbangkan dalam kajian parametrik ke atas pelbagai sifat isothermal, sifat di bawah pengaruh perubahan terma dan juga pengaruh gabungan bebanan termo-mekanikal FGM. Tujuan kajian ini adalah untuk mendedahkan bahawa profil penggredan sifat bahan menjejaskan prestasi bahan di bawah kesan dari pelbagai keadaan. Hasil kajian berangka menunjukkan bahawa reka bentuk optimum FGM boleh dihasilkan dengan menyusun secara linear komposisi bahan, menyediakan sekurang-kurangnya enam lapisan dengan masing-masing mempunyai ketebalan tertentu yang dapat mengekalkan keberkesanan fungsi penggredan bahan. Kriteria ini diperolehi melalui taburan tegasan sisa minima dan

profil santonan tegasan sisa tinggi. Penemuan kajian parametrik mendedahkan bahawa taburan medan bebanan merupakan faktor lain yang memberi kesan kepada sifat termoelastik plat FGM HA/Ti dan taburan keamatan tegasan ditemui sebagai petunjuk yang baik kepada tanda-tanda permulaan kegagalan struktur FGM. Plat FGM HA/Ti didapati mampu menahan tegasan terma di samping mengekalkan ciri-ciri kekuatan yang tinggi dan dengan itu menunjukkan kemampuan untuk beroperasi pada suhu yang tinggi.

Disebabkan kemudahan penyelidikan yang terhad, penyediaan sampel FGM yang melibatkan pemadatan sejuk dan teknik pensinteran tanpa tekanan tidak menjamin hasil kajian yang baik. Penumpatan dan pengurangan tenaga sempadan bijian serbuk padat semasa peringkat pensinteran masih tidak dapat difahami sepenuhnya daripada kajian eksperimen dan dilihat sebagai proses yang paling mencabar dalam proses fabrikasi. Pelbagai parameter operasi yang dipertimbangkan setakat ini tidak sesuai untuk menghasilkan proses pensinteran sampel FGM yang terbaik. Ciri-ciri logam yang diperhatikan melalui imbasan mikroskop elektron (SEM), pembelauan x-ray (XRD), analisa spektroskopi inframerah Fourier (FTIR) dan juga sifat-sifat asas mekanik yang diukur dengan menggunakan kaedah sesaran air dan alat pengukur kekerasan mikro Vicker mendedahkan sensitiviti bahan HA dan Ti terhadap keadaan pensinteran serta kehadiran benda asing semasa proses rawatan terma. Bukti kajian tersebut membuktikan bahawa keterbatasan teknik pemprosesan sejuk tidak dapat dinafikan namun hasil eksperimen dipercayai dapat dijadikan asas untuk pemprosesan FGM HA/Ti melalui pendekatan pemprosesan serbuk (PM). Ini boleh menjadi satu garis panduan yang betul untuk penambahbaikan pemprosesan sampel FGM menggunakan kaedah pemprosesan serbuk. Kebolehmampuan kaedah pemprosesan panas untuk meningkatkan sifat-sifat pensinteran FGM merupakan tajuk penyelidikan yang harus diketengahkan bagi menghasilkan proses yang optimum bagi bahan yang dipertimbangkan.

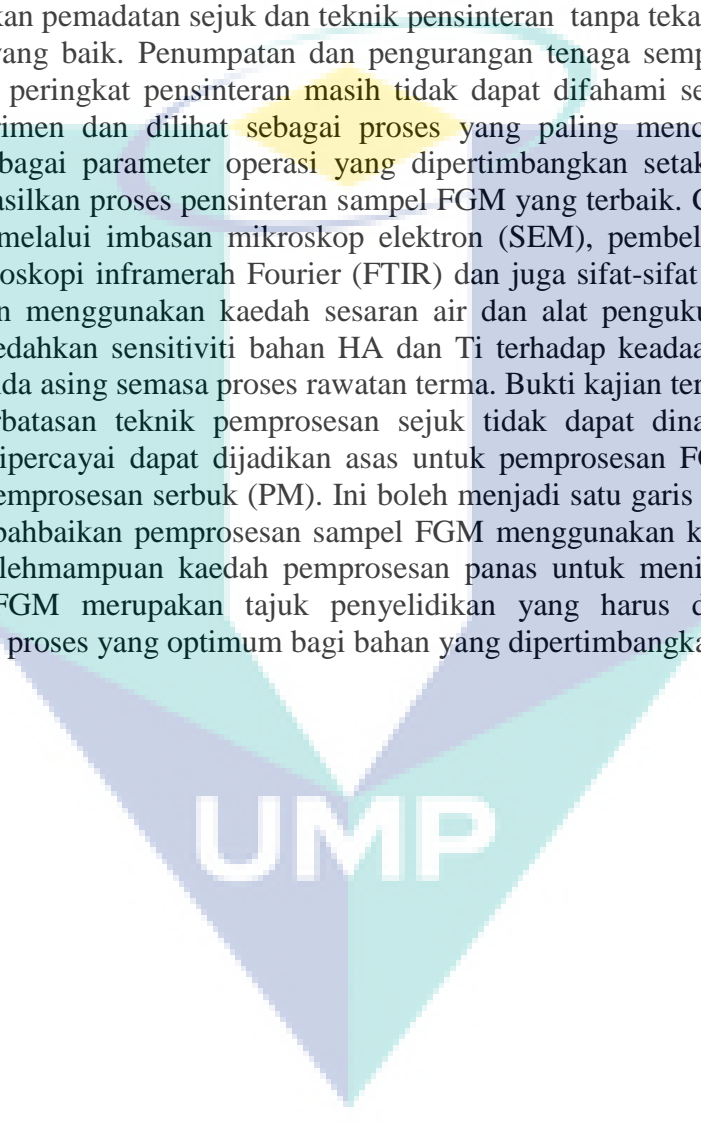
The logo of Universiti Malaysia Perlis (UMP) is a large, stylized letter 'V' shape. The left side of the 'V' is light blue, the right side is light green, and the bottom point is a darker blue. The letters 'UMP' are written in white, bold, sans-serif font across the center of the 'V'.

TABLE OF CONTENTS

	Page
SUPERVISOR'S DECLARATION	ii
STUDENT'S DECLARATION	iii
ACKNOWLEDGEMENTS	v
ABSTRACT	vi
ABSTRAK	viii
TABLE OF CONTENTS	x
LIST OF TABLES	xiv
LIST OF FIGURES	xvi
LIST OF ABBREVIATIONS	xxii
LIST OF SYMBOLS	xxiii
CHAPTER 1 INTRODUCTION	
1.1 General Background	1
1.2 Problem Statement	4
1.3 Motivation and Objectives of the Research	5
1.4 Scope of Studies	6
1.5 Thesis Layout	6
CHAPTER 2 LITERATURE REVIEW	
2.1 Introduction	8
2.2 Fabrication Techniques for FGMs	8
2.2.1 The Powder Metallurgy Technique	9
2.2.2 The Infiltration Method	17
2.2.3 The Graded Casting Process	19
2.2.4 Thermal Spraying	23
2.2.5 Laser Cladding	24
2.2.6 Vapor Deposition Method	27
2.3 Theoretical Works of FGM	29
2.3.1 FGM Model Development	29
2.3.2 FGM Responses Analysis	31

2.3.3	Numerical Investigation on FGM	33
2.4	Experimental Works of FGM	34
2.4.1	Metallurgical Analysis	34
2.4.2	FGM Properties Measurement	37
2.5	Closure	39
CHAPTER 3 THEORETICAL STUDIES		
3.1	Introduction	41
3.2	Material Gradient	42
3.2.1	Prediction of Effective Thermo-mechanical Properties	43
3.2.2	Basic FGM's Properties	45
3.3	Theoretical Formulations	47
3.3.1	Stress-strain Relationships	48
3.3.2	Thermal field of FGM	51
3.4	Closure	51
CHAPTER 4 NUMERICAL INVESTIGATION		
4.1	Introduction	52
4.2	Finite Element Formulations	52
4.2.1	Structural Analysis	54
4.2.2	Thermal Analysis	57
4.2.3	Thermal-Structural Analysis	58
4.3	2-D Analysis for the Optimization of FGM Design	59
4.4	3-D Analysis of FGM Plate Responses	62
4.4.1	Isothermal Loading	62
4.4.2	Thermal Loading	65
4.4.3	Thermo-mechanical Loading	67
4.5	Model Verification	69
4.6	Closure	74

CHAPTER 5 NUMERICAL RESULTS AND DISCUSSION

5.1	Introduction	75
5.2	Material Properties	75
5.3	2-D Analysis: Optimization of Design Parameters	80
	5.3.1 Evaluation of the Grading Index	80
	5.3.2 Evaluation of the Number of Layers	82
	5.3.3 Evaluation of the FGM's Thickness	83
5.4	3-D Analysis: Responses of FGMs under Various Loadings	85
	5.4.1 Isothermal Loading	85
	5.4.2 Thermal Loading	98
	5.4.3 Thermo-mechanical Loading	112
5.5	Closure	131

CHAPTER 6 EXPERIMENTAL PROGRAM, RESULTS AND DISCUSSION

6.1	Introduction	132
6.2	The Experimental Process	132
6.3	Experimental Results and Discussion	143
	6.3.1 Qualitative Results	143
	6.3.2 Basic Mechanical Properties	151
	6.3.3 Metallurgical Characteristics	156
6.4	Closure	174

CHAPTER 7 CONCLUSIONS AND RECOMMENDATIONS FOR FUTURE WORK

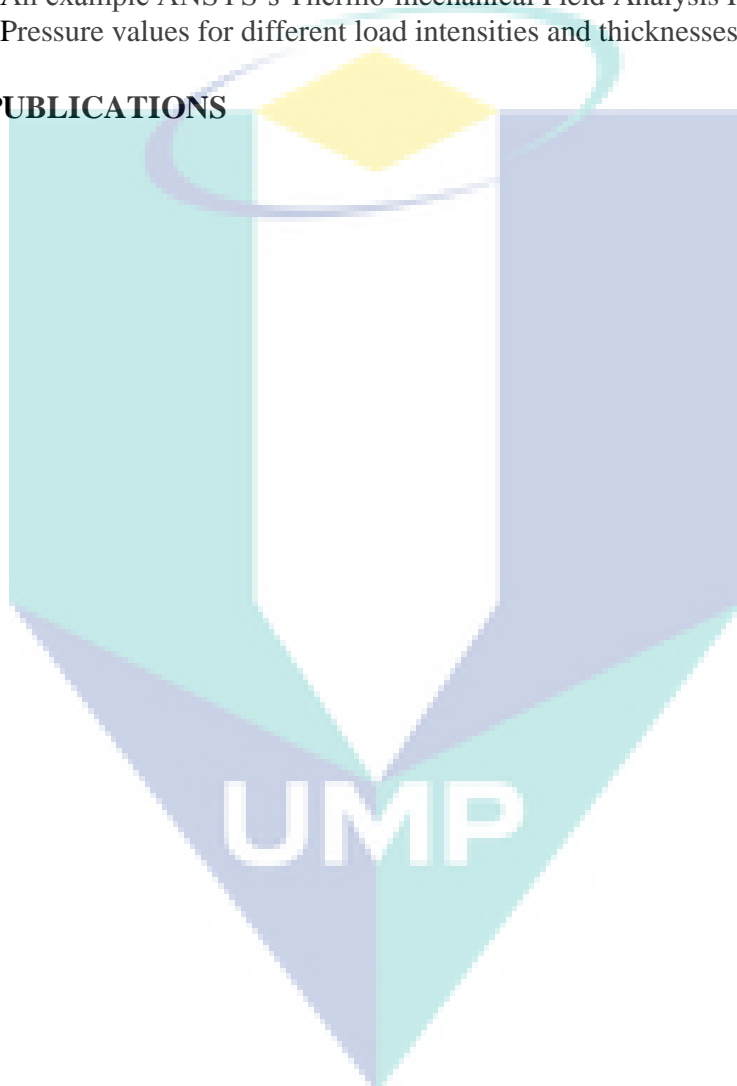
7.1	Conclusions	175
7.2	Recommendations for Future Work	178

REFERENCES	180
-------------------	-----

APPENDICES

A-1	An example of ANSYS's Output File for Optimization 2-D Analysis	193
-----	---	-----

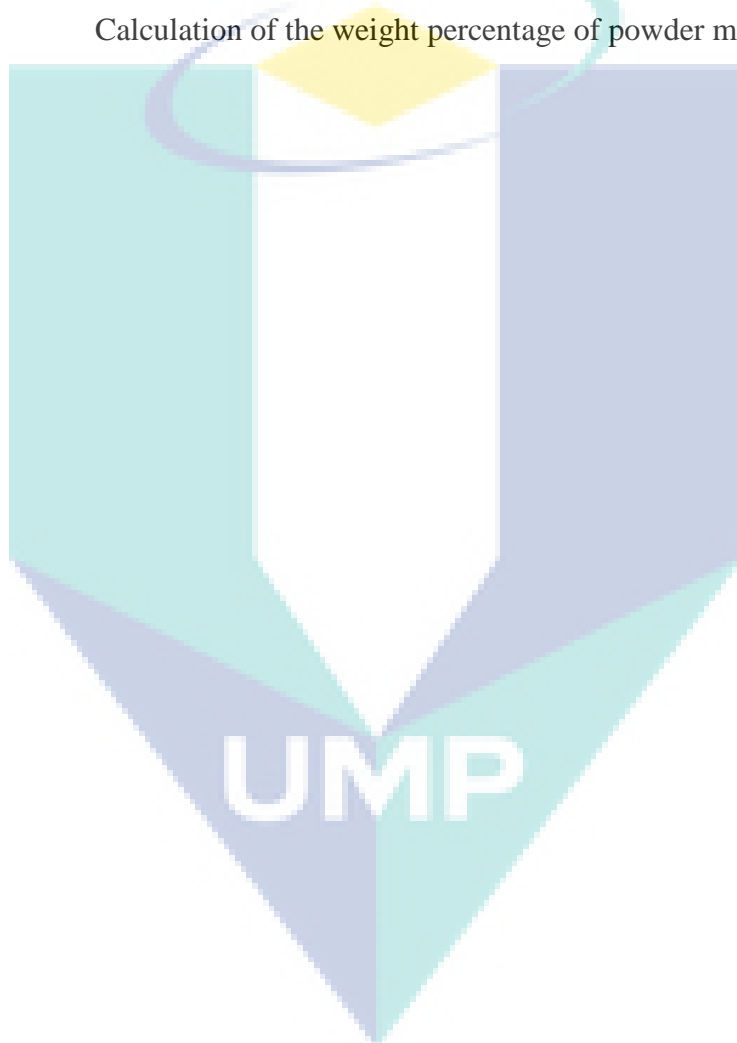
A-2	An example of ANSYS's Output File for Mechanical Field 3-D Analysis	196
A-3	An example of ANSYS's Output File for Thermal Field 3-D Analysis	199
A-4	An example of ANSYS's Output File for Thermo-mechanical Field 3-D Analysis	203
B-1	An example ANSYS's Optimization Analysis Results	207
B-2	An example ANSYS's Mechanical Field Analysis Results	215
B-3	An example ANSYS's Thermal Field Analysis Results	219
B-4	An example ANSYS's Thermo-mechanical Field Analysis Results	223
C	Pressure values for different load intensities and thicknesses	227
LIST OF PUBLICATIONS		228
VITA		229



LIST OF TABLES

Table No.	Title	Page
4.1	Convergence study of a simply supported Ni/ZrO ₂ FGM plate subjected to thermal loadings with respect to different mesh divisions	72
4.2	Convergence study of simply supported Ni/ZrO ₂ FGM plates subjected to thermal loadings with respect to different number of layers	72
4.3	Dimensionless central deflection of Al/ZrO ₂ FGM plates subjected to mechanical loadings	73
4.4	Dimensionless deflection at the central point of Al/ZrO ₂ FGM plates subjected to thermo-mechanical loadings	74
5.1	Properties of materials	76
5.2	Properties of two different HAs	76
5.3	Maximum thermal residual stress and the maximum thermal stresses differences of the HA/Ti FGM plates with different number of layer	83
5.4	Maximum thermal residual stresses and jumps in HA/Ti FGM plates with different thicknesses of the FGM phase	85
5.5	Dimensionless central deflection of FGM plates subjected to various load intensities	91
5.6	Variation of deflection along the mid-plane of HA/Ti FGM plates under isothermal conditions for three different numbers of layers	94
5.7	Normal stress along the thickness of HA/Ti FGM plates for three different number of layers subjected to mechanical loading	95
5.8	Deflection of HA/Ti FG plates with various grading indices subjected to thermo-mechanical loading corresponding to various load intensities	117
5.9	Central deflections at the mid-plane of FGM plates with three different number of layers subjected to thermo-mechanical loading	120

5.10	Normal stress values along the thickness of FGM plates with three different number of layers subjected to thermo-mechanical loading	121
5.11	Central deflections of the HA/Ti FGM plates subjected to thermo-mechanical loading with a heat source corresponding to various load intensities	129
6.1	The physical and chemical properties of the base materials (manufacturer's specifications)	133
6.2	Calculation of the weight percentage of powder mixtures	134



LIST OF FIGURES

Figure No.	Title	Page
1.1	Concept and properties variation in FGMs	2
1.2	Structure of research	7
2.1	Vicker's hardness against HA percentage of HA/Ti FGM	11
2.2	XRD spectra of HA-20 vol.% Ti composites sintered at different temperatures for 60 min. (a) 1000°C; (b) 1100°C	16
2.3	Scanning electron images of the Al ₂ O ₃ /Ti/TiN functional materials produced by nitriding Al ₂ O ₃ /Ti composites in ammonia salts at 570°C for 24hrs	35
3.1	The geometry configuration of a metal-ceramic FGM plate	42
3.2	Schematic diagram of Vicker's micro-hardness testing	46
3.3	Schematic illustration of the contact area of the indenter and material	47
4.1	Element types	53
4.2	Transformation of the cylindrical FGM plate into a 2-D axisymmetric model	60
4.3	Flowchart of the 2-D FE optimization analysis	61
4.4	Schematic diagram of the FGM plate subjected to mechanical loading analysis	63
4.5	Flowchart of 3-D FE analysis of the FGM subjected to mechanical loading	64
4.6	Schematic diagram of the FGM plate subjected to thermal loading analysis	65
4.7	Flowchart of 3-D FE analysis of the FGM subjected to thermal loading	66
4.8	A simply supported FGM under thermo-mechanical loading	67
4.9	Flowchart of 3-D FE analysis of the FGM subjected to thermo-mechanical loading	68

4.10	Verification of the 2-D modelling method	70
4.11	Temperature field distribution along the thickness of FGM and pure plates	71
5.1	Young's modulus distribution along the thickness of the HA/Ti FGM plate with different HAs	77
5.2	Responses of HA/Ti FGM plates with different Young's modulus of HA under mechanical loading ($\bar{P}=1$, $n=1$, $L=6$, $h=0.0072m$)	78
5.3	Effect of various Young's modulus of the base materials ratios on the stress intensity factor of a HA/Ti FGM plate under thermo-mechanical loading	79
5.4	Compositional distribution profiles of the HA/Ti FGM plates with a variation of the grading parameter	81
5.5	Residual thermal stress distribution along the thickness of the HA/Ti FGMs with various grading indices ($L=11$, thicknesses of pure Ti, FGM and pure HA layers: 1.5mm, 4mm, 1.5mm, respectively)	81
5.6	Residual thermal stress distribution along the thickness of HA/Ti FGM plates with various number of layers ($n=1$, thickness of pure layers, FGM layer: 1.5mm, 0.007m)	82
5.7	Residual thermal stress distribution of the HA/Ti FGM plates with various graded layers' thicknesses ($L=11$, $n=1$, the thickness of pure Ti and HA layers: 1.5mm)	84
5.8	Deflection distribution of the HA/Ti FGM plates under isothermal conditions ($\bar{P}=1$, $n=1$, $L=6$, $h=0.0072m$)	87
5.9	Normal stress distribution of the HA/Ti FGM plates under isothermal conditions ($\bar{P}=1$, $n=1$, $L=6$, $h=0.0072m$)	88
5.10	Transverse shear stress distribution of the HA/Ti FGM plates under isothermal conditions ($\bar{P}=1$, $n=1$, $L=6$, $h=0.0072m$)	89
5.11	Stress intensity distribution of the HA/Ti FGM plates under isothermal conditions ($\bar{P}=1$, $n=1$, $L=6$, $h=0.0072m$)	90
5.12	Variations of various responses of the HA/Ti FGM plates under isothermal conditions, for various grading indices ($\bar{P}=1$, $L=6$, $h=0.0072m$)	93

5.13	Variations of various responses of the HA/Ti FGM plates under isothermal conditions, for various numbers of layers ($\bar{P}=1$, $n=1$, $h=0.0072\text{m}$)	96
5.14	Variations of various responses of the HA/Ti FGM plates under isothermal conditions, for various thicknesses ($\bar{P}=1$, $n=1$, $L=6$)	97
5.15	Deflection distribution of the HA/Ti FGM plates under thermal excitation ($\bar{P}=1$, $n=1$, $L=6$, $h=0.0072\text{m}$)	99
5.16	Normal stress distribution of the HA/Ti FGM plates under thermal excitation ($\bar{P}=1$, $n=1$, $L=6$, $h=0.0072\text{m}$)	100
5.17	Transverse shear stress distribution of the HA/Ti FGM under thermal excitation ($\bar{P}=1$, $n=1$, $L=6$, $h=0.0072\text{m}$)	101
5.18	Stress intensity distribution of the HA/Ti FGM plates under thermal excitation ($\bar{P}=1$, $n=1$, $L=6$, $h=0.0072\text{m}$)	102
5.19	Temperature distribution along the thickness of the HA/Ti FGM subjected to thermal loading ($\bar{P}=1$, $L=6$, $h=0.0072\text{m}$)	103
5.20	Responses of the FGM plates with different grading indices subjected to thermal loading ($\bar{P}=1$, $L=6$, $h=0.0072\text{m}$)	105
5.21	Responses of the HA/Ti FGM plates with different number of layers under thermal loading ($\bar{P}=1$, $n=1$, $h=0.0072\text{m}$)	107
5.22	Responses of the FGM plates with different thicknesses of the FGM phase subjected to thermal loading ($\bar{P}=1$, $n=1$, $L=6$)	109
5.23	Responses of the FGM plates subjected to thermal loading with and without a heat source ($\bar{P}=1$, $n=1$, $L=6$, $h=0.0072\text{m}$)	111
5.24	Deflection of the HA/Ti FGM plates under thermo-mechanical loading ($\bar{P}=1$, $n=1$, $L=6$, $h=0.0072\text{m}$)	113
5.25	Normal stress distribution of the HA/Ti FGM plates under thermo-mechanical loading ($\bar{P}=1$, $n=1$, $L=6$, $h=0.0072\text{m}$)	114
5.26	Transverse shear stress distribution of the HA/Ti FGM plates under thermo-mechanical loading ($\bar{P}=1$, $n=1$, $L=6$, $h=0.0072\text{m}$)	115
5.27	Stress intensity distribution of the HA/Ti FGM plates under thermo-mechanical loading ($\bar{P}=1$, $n=1$, $L=6$, $h=0.0072\text{m}$)	116

5.28	Variations of various responses of the HA/Ti FGM plates under thermo-mechanical loading, for various grading indices ($\bar{P}=1$, $L=6$, $h=0.0072\text{m}$)	119
5.29	Transverse shear stress along the thickness of the HA/Ti FGM plates with a different number of layers under thermo-mechanical loading ($\bar{P}=1$, $n=1$, $h=0.0072\text{m}$)	122
5.30	Responses of the FGM plates with different thicknesses subjected to thermo-mechanical loading ($\bar{P}=1$, $n=1$, $L=6$)	123
5.31	Deflection of the HA/Ti FGM plates under thermo-mechanical loading with a heat source ($\bar{P}=1$, $n=1$, $L=6$, $h=0.0072\text{m}$)	125
5.32	Normal stress distribution of the HA/Ti FGM plate under thermo-mechanical loading with a heat source ($\bar{P}=1$, $n=1$, $L=6$, $h=0.0072\text{m}$)	126
5.33	Transverse shear stress distribution of the HA/Ti FGM plate under thermo-mechanical loading with a heat source ($\bar{P}=1$, $n=1$, $L=6$, $h=0.0072\text{m}$)	127
5.34	Stress intensity distribution of the HA/Ti FGM plate under thermo-mechanical loading with a heat source ($\bar{P}=1$, $n=1$, $L=6$, $h=0.0072\text{m}$)	128
5.35	Responses of FGM plates under thermo-mechanical loading with and without a heat source ($\bar{P}=1$, $n=1$, $L=6$, $h=0.0072\text{m}$)	130
6.1	The powder metallurgy route	133
6.2	Planetary ball mill machine – Faculty of Industrial Science and Technology (FIST) Laboratory, Universiti Malaysia Pahang (UMP)	135
6.3	Customized dies for the compaction process	136
6.4	Cross-sectioned view of the stepwise HA/Ti FGM configuration	137
6.5	Hydraulic pressing machine	138
6.6	The HA/Ti green compact	138
6.7	Vacuum oven used for drying the green compacts	139
6.8	Furnaces used for the sintering process	141

6.9	Sintering curves applied during sintering using different furnaces	142
6.10	Samples sintered under different sintering atmospheres (L=6, T _s =1000°C, h=±7mm)	145
6.11	Effects of flowing gas duration during sintering on FGM samples (L=6, T _s =1000 °C, h=±7mm)	147
6.12	Effects of the drying process on FGM samples (L=6, T _s =1000°C, h=±7mm)	148
6.13	The effects of the sample's direction on FGM samples (L=6, T _s =1000°C, h=±7mm)	150
6.14	Measured and ROM-formulated densities of HA/Ti composites sintered at 1100°C under an O ₂ atmosphere for various constituents' compositional percentages	151
6.15	Measured and ROM-formulated densities of HA/Ti composites sintered at 1200°C under an O ₂ atmosphere for various constituents' compositional percentages	152
6.16	Vicker's micro-hardness distribution through the thickness of the green FGM sample compacted under 10ton of pressure (L=6, h=±7mm)	153
6.17	Vicker's micro-hardness distribution through the thickness of FGM samples for different compaction loads (L=6, T _s =1100°C (Ar), h=±7mm)	154
6.18	FGM samples sintered at 1100°C under an Ar atmosphere for different compaction loads (L=6, h=±7mm)	154
6.19	FGM sample with higher number of layers (L=8, T _s =1100°C (Ar), p=10ton, Ø=15mm, h=±7mm)	155
6.20	Vicker's micro-hardness distribution through the thickness of an FGM sample containing higher number of layers (L=8, T _s =1100°C (Ar), p=10ton, Ø=15mm, h=±7mm)	155
6.21	SEM images of FGM green samples for various compaction loads (L=6, h=±7mm)	158
6.22	SEM images of FGM samples sintered under a N ₂ atmosphere for various compaction loads (L=6, T _s =1000°C, h=±7mm)	159

6.23	SEM images of FGM samples sintered under a N_2+H_2 atmosphere for various compaction loads ($L=6$, $T_s=1000^\circ C$, $h=\pm 7mm$)	160
6.24	SEM images of FGM samples sintered under an Ar atmosphere for various compaction loads ($L=6$, $T_s=1000^\circ C$, $h=\pm 7mm$)	161
6.25	SEM images of green ($L=6$, $h=\pm 7mm$) and sintered FGM samples ($L=6$, $T_s=1000^\circ C$, $h=\pm 7mm$)	162
6.26	SEM images of non-dried and dried FGM samples before sintering ($L=6$, $T_s=1000^\circ C$, $h=\pm 7mm$)	163
6.27	FTIR spectra at the white region on the Ti surface of the HA/Ti FGM sintered under an Ar atmosphere ($L=6$, $T_s=1000^\circ C$, $h=\pm 7mm$)	164
6.28	FTIR spectra at the shining region on the Ti surface of the HA/Ti FGM sintered under a N_2 atmosphere ($L=6$, $T_s=1000^\circ C$, $h=\pm 7mm$)	165
6.29	FTIR spectra at the greenish region on the Ti surface of the HA/Ti FGM sintered under an O_2 atmosphere ($L=6$, $T_s=1000^\circ C$, $h=\pm 7mm$)	166
6.30	FTIR spectra at the black region on the Ti surface of the HA/Ti FGM sintered under Ar atmosphere ($L=6$, $T_s=1000^\circ C$, $h=\pm 7mm$)	166
6.31	XRD pattern of the base materials	168
6.32	The XRD pattern of the FGM sintered under different N_2+H_2 flowing time ($L=6$, $T_s=1000^\circ C$, $h=\pm 7mm$)	170
6.33	The XRD pattern of dried and non-dried FGMs sintered under N_2+H_2 atmosphere during the holding time and N_2 during the cooling time ($L=6$, $T_s=1000^\circ C$, $h=\pm 7mm$)	171
6.34	The XRD pattern of dried and non-dried FGMs sintered under N_2+H_2 atmosphere during holding time only ($L=6$, $T_s=1000^\circ C$, $h=\pm 7mm$)	173

LIST OF ABBREVIATIONS

2-D	Two-dimensional
3-D	Three-dimensional
BFS	Biaxial Flexural Strength
CAD	Computer Aided Design
CIP	Cold Isostatic Pressing
CNTR-FG	Carbon Nanotube Reinforced
CTE	Coefficient of Thermal Expansion
CVD	Chemical Vapor Deposition
DLC	Diamond Like Coating
DOF	Degree of Freedom
DTA	Differential Thermal Analysis
EDS	X-ray Spectrometry
EP	Tape laminating process of epoxy
EPD	Electrophoretic Deposition
EPMA	Electron Probe Microscope Analysis
FEA	Finite Element Analysis
FEM	Finite Element Method
FGM	Functionally Graded Material
FTIR	Fourier Transform Infrared Spectroscopy
MWCNT	Multi Walled Carbon Nanotube
PFA	Pore-Forming Agent
PM	Powder Metallurgy
PVD	Physical Vapor Deposition
ROM	Rule Of Mixture
SEM	Scanning Electron Microscope
SLS	Selective Laser Sintering
SPS	Spark Plasma Sintering
TBC	Thermal Barrier Coating
TEM	Transmission Electron Microscope
XRD	X-ray Diffraction
XSAM	X-ray Scanning Analytical Microscope
mol.	molecule
vol.	volume
wt.	weight

LIST OF SYMBOLS

A_u	area of the uniform resistance
A_p	area on which the pressure is given
B	Bulk modulus
C, K	Celcius, Kelvin (unit of temperature)
C_v	specific heat at constant strain or volume
E	Young's modulus
E_x, E_y, E_z	Young's modulus in x, y and z-directions, respectively
HB	Brinell Hardness
HV	Vicker's Hardness
K, \bar{K}	dimensional, non-dimensional stress intensity factor
L	number of layers
N	shape function
$P, \{P\}$	Pressure, vector of applied pressure
\bar{P}, p	Non-dimesional, dimensional load intensity
$Pa, MPa, ton, torr$	Pascal, Megapascal, ton, torr (unit of pressure)
S	density entropy
T	temperature
T_0	absolute reference temperature
T_g	glass-transition temperature
T_s	sintering temperature
V	external work
W	Watt (unit of power)
Z, \bar{z}	dimensional, non-dimensional coordinate along z-direction
d	diameter
g	gram, unit of mass
h	thickness
hr, hrs, min, s, Ks	hour, hours, minute, second, kilosecond (unit of time)
k	thermal conductivity
k_{xx}, k_{yy}, k_{zz}	conductivity of the element at x, y and z-directions, respectively
kN	kiloNewton (unit of force)
$m, cm, mm, \mu m$	meter, centimeter, millimeter, micrometer (unit of length)
m_l	mass of immersed liquid
n	grading index
pH	Power of H_2 (unit of acidity)
$q, \{q\}$	heat flux, heat flux vector
\ddot{q}	heat generation rate per unit volume
t	thickness of FGM phase
u	translation at x-direction
v	translation at y-direction
w	translation at z-direction
x, \bar{x}	dimensional, non-dimensional coordinate along x-direction
$\alpha, \{\alpha\}$	CTE, CTE vector
$\alpha_x, \alpha_y, \alpha_z$	CTE in the x, y and z-directions, respectively
$\{\beta\}$	thermo-elastic coefficient vector
$\{\varepsilon\}$	strain vector

$\{\sigma\}$	stress vector
$\{w\}$	vector of displacement of general point
$\{w_{-}\}$	vector of motion transverse to the surface
$[B]$	strain-displacement matrix
$[B_T]$	thermal strain-displacement matrix
$[D]$	elastic stiffness matrix
$[D_T]$	conductivity matrix
$[G]$	thermal gradient vector
$[N]$	shape function matrix
$[N_{-}]$	matrix of the shape function for transverse motion at the surface
$\varepsilon_x, \varepsilon_y, \varepsilon_z$	direct strain in x, y and z-planes, respectively
$\varepsilon_{xy}, \varepsilon_{yz}, \varepsilon_{xz}$	shear strain in x-y, y-z and x-z planes, respectively
$\sigma_x, \sigma_y, \sigma_z$	direct stress in x, y and z-planes, respectively
$\overline{\sigma_{xx}}, \overline{\sigma_{xx}}$	dimensional, non-dimensional axial stress
$\sigma_{xy}, \sigma_{yz}, \sigma_{xz}$	shear stress in x-y, y-z and x-z planes, respectively
$\overline{\tau_{xz}}, \overline{\tau_{xz}}$	dimensional, non-dimensional transverse shear stress
ν	Poisson's ratio
ν_{xy}, ν_{xz}	major Poisson's ratio
ν_{yz}	minor Poisson's ratio
v	volume fraction
Λ	volume of element
δ	unknown operator
θ	theta, unit of angle
μ	shear modulus
$\omega, \overline{\omega}$	dimensional, non-dimensional deflection
ρ	density
\dot{U}	strain energy or internal work

Subscript

1	represents material 1
2	represents material 2
b	represents bottom material
c	represents ceramic
l	represents lower material
m	represents metal
t	represents top material
u	represents upper material

CHAPTER 1

INTRODUCTION

1.1 GENERAL BACKGROUND

Developing applications in bioengineering, biomedical engineering, aerospace and electronics demands properties that are unobtainable in any single material. These properties should include resistance against high mechanical and thermal stresses. Combining ceramic and metallic materials may have the potential to overcome the aforementioned situation. In situations where the operating temperature is extremely high, structural ceramic materials are used because of their refractory qualities, their resistance to corrosion and their resistance to wear in situations where metallic materials cannot survive. However, ceramic materials cannot withstand the mechanical stresses that metals easily overcome. Metals offer properties such as fracture toughness, resistance to wear and resistance to corrosion, but they should be shielded from excessive or extreme heat under operating conditions.

Composite materials were developed to provide the desirable characteristics of both ceramic and metallic materials in order to meet such requirements. A special material designed with a soft transition from a metallic core to a ceramic surface would avoid thermal and thermo-mechanical stresses, because of the internal stresses caused by the elastic and thermal differences at the interface between two different materials. Recent advances in processing technology have led to a new class of materials with the aforementioned characteristics, called Functionally Graded Materials (FGMs). FGMs overcome problems arising in composites due to their sharp-grading structures, bringing together the properties of ceramics and metals more effectively.

In FGMs, the chemical composition and microstructure of two or more constituents are varied gradually and alternately across its opposing surfaces as shown in Figure 1.1. This arrangement provides an alternate smooth variation of each constituent's properties, which is advantageous for thermal stress relaxation. The FGM's property gradient can be predicted based on various theoretical formulations published in the literature. The simplest way is to use a linear rule of mixture where the properties at the interfaces are defined by considering the volume fraction at the local region and the properties of the base materials.

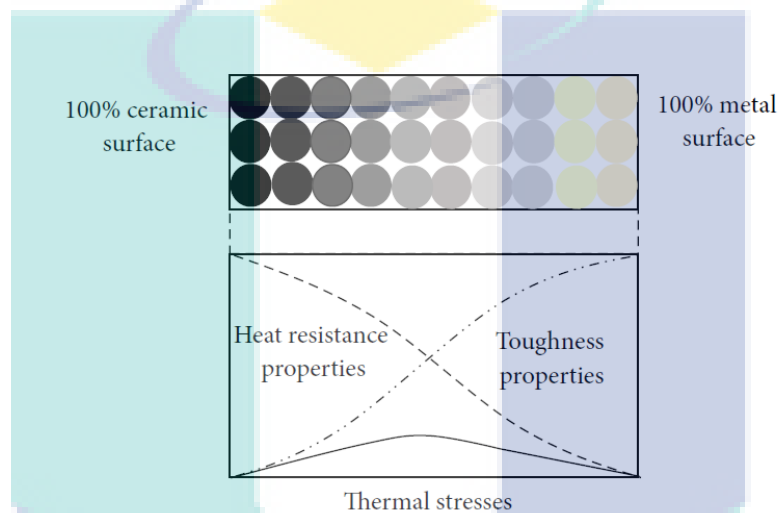


Figure 1.1: Concept and properties variation in FGMs

Source: Nomura *et al.*, 1999

Due to the position-dependent distribution of properties in FGMs, the temperature, displacement and stress distributions will not be similar to those found in homogeneous or single materials when considering different loading conditions. Since property gradation has a dominant effect on the heterogeneous mechanical, thermal and thermo-mechanical characteristics of FGM, extra consideration need to be taken on the parameters that affect this matter, especially while designing the FGM system. When considering the geometrical aspects, the grading index, the number of layers and the thickness of layers are among the parameters that control the property gradient. Therefore, an investigation of the correlation between these parameters and their residual stresses response (which are generated mainly because of the temperature change while the material is sintering) is important to find the performance of the FGM.

The residual stresses relaxation (acquired by the minimum stresses' values and jumps) will represent the optimum criteria of the FGM.

The performance of FGMs can be determined experimentally by characterizing two of their most important elements. The first element, the metallurgical criteria, is very important to obtain quantitatively because it determines the physical characteristics of the FGM such as orientation, configuration, phase distribution as well as the geometry or size of its microstructures. It also includes the micro-scale chemical composition characterization, which ensures the level of purity of the sample and reflects the detection of impurities, chemical reactions and the existence of contamination. The second aim of the characterization process is to determine the properties' distribution along the graded axis, as well as the overall effective properties of the FGM. For the characterization process, the conventional methods used to measure the properties of homogeneous materials are applicable for measuring the properties' distribution at a local thickness coordinate of the FGM. However for the FGM's overall effective properties, because the continuous variation of the properties leads to difficulties in the measurement, some modifications of the conventional technique are implemented.

Due to a change in thermo-elastic properties at a local region of an FGM, the manufacturing of this material is more challenging than that of single materials. The processing of FGMs is comprised of two main steps. In the initial step, laminated layers with various composition and microstructure configurations are created. In the next step, the consolidation process, the laminated-built layers are transformed into a bulk or solid structure. This step is generally implemented by conducting heat treatment on the sample to reduce the surface energy between the constituents' particles. During the process, the discontinuity of the material properties through the interfaces of the FGM layers can lead to the generation of additional residual stresses. A lot of factors reflect the unstable stress distribution such as drastic thermal expansion, abrupt material deformation, inaccurate compositional distribution as well as other parametric effects that should be considered to avoid failure.

Various metal and ceramic pairs have been considered in the development of FGMs for several advanced engineering applications. Among the various pairs, HA and Ti materials were among the well-known combinations, but so far their applications are limited to biomedical engineering and human implants. Looking at the advantages of HA and Ti materials from a different perspective, this thesis highlights the potential of HA/Ti FGMs in high thermal barrier applications. The FGM's mechanical properties, such as its high strength-to-weight ratio, high resistance to corrosion and the lower density of Ti material, have been thoroughly analyzed as it is widely utilized in industrial aerospace applications. However the low thermal conductivity of HA has not often been considered for applications that require good heat resistance.

This study intends to highlight the significance of the extremely low thermal conductivity of HA in enhancing the performance of the advanced material. A parametric investigation of various fundamental characteristics of the HA/Ti FGM has been conducted. The study's analyses were undertaken to determine the optimum design parameters of the HA/Ti FGM. It has also evaluated the mechanical, thermal and thermo-mechanical responses of the structure under various parametric effects has also been evaluated using an FEM formulated by ANSYS Multiphysics software. In addition, the evaluation of the structural performance of the HA/Ti FGM is carried out using cold compaction and pressure-less sintering methods after considering the existing facility. During the experimental work, the optimum design parameters were identified using numerical calculations and by considering various operating parameters. The performance of the FGM was determined by evaluating its metallurgical characteristics and the property distribution profiles of the structure.

1.2 PROBLEM STATEMENT

As discussed in the chapter on literature review, the key issues related to FGM particularly to HA/Ti FGM are application of FGM (Watari *et al.*, 2004; Chu *et al.*, 2006; Nomura *et al.*, 2010), fabrication technique (Watari *et al.*, 1997; Chu *et al.*, 2003; Shahrjerdi *et al.*, 2011), experimental evaluation (Tsipas *et al.*, 2003; Ye *et al.*, 2009; Batin *et al.*, 2011) and parametric design data (Chu *et al.*, 2003; Zhang *et al.*, 2008; Alshorbagy *et al.*, 2013). One of the key issues on principal concern is the availability

of a comprehensive design data of HA/Ti FGM. This involves the study of constitutive relation of the FG materials and analysis of solid made FGM under various loading conditions, thermal stress effects and other optimum design parameters such as grading index, number of layer and thickness.

For applications requiring multifunctional performance, such as heat and corrosion resistance, HA/Ti FGM is an ideal combination which exhibits good service performance under some severe environmental conditions including high temperature, high mechanical load and high coupled loadings. To date, very limited data is available on the various characteristics of HA/Ti FGM. Detailed investigation of the characteristics of HA/Ti FGM under mechanical, thermal and thermo-mechanical loadings have not been reported yet. There is a great demand for modelling the complex behaviour of HA/Ti FGM, especially under the conditions of various loadings conditions. Modelling may allow the prediction of suitable processing parameters for HA/Ti FGM, helping to reduce the experimental efforts in order to produce the graded material. Particular emphasis should be given to modelling the HA/Ti FGM and the research to be implemented should provide information on various mechanical, thermal and thermo-mechanical characteristics of HA/Ti FGM under a range of operating conditions for example under isothermal, thermal and themomechanical loadings.

1.3 MOTIVATION AND OBJECTIVES OF THE RESEARCH

Detail parametric studies of the responses under steady state static analysis are essential. The development of the HA/Ti FGM requires advanced numerical methods to accurately analyze the structures and hence, the motivation for carrying out the present research study. Therefore, the main objective of this research is to investigate the behaviour of HA/Ti FGM by numerical and experimental methods. The specific objectives are given as follows:

- To study numerically the influence of design parameters that affect the property gradient on the performances of HA/Ti FGM
- To analyze various characteristics of HA/Ti FGM models under various loading conditions and parametric effects using FEA

- To evaluate experimentally the performance of a HA/Ti FGM sample fabricated via cold particulate processing

1.4 SCOPE OF STUDIES

This study is divided into theoretical and experimental sections. The scopes included in the theoretical sections are:

- Optimization of the grading index number, the number of layers and the thickness of the pre-designed HA/Ti FGM plate using a 2-D FE model
- The parametric study of the mechanical, thermal and thermo-mechanical characteristics of the HA/Ti FGM plate using a 3-D FE model

The scopes of the experimental works are:

- HA/Ti FGM preparation using the cold processing of powder metallurgy technique
- Physical microstructural characterization of the FGM sample using SEM
- Detection of the chemical reactions and phase transformation in the FGM using FTIR
- Phase contamination characterization of the FGM using an XRD test
- The measurement of the FGM density using the water immersion test
- The measurement of the FGM hardness using a Vicker's micro-hardness tester

1.5 THESIS LAYOUT

The proposed thesis starts with the background and objective of the research work in Chapter One. Chapter Two presents a significant review of the related literature. The theoretical formulation for the development of a metal-ceramic FGM model is presented in Chapter Three. Chapter Four discusses the finite element solutions, modelling methods and models' verification. Chapter Five includes the results and a discussion of the numerical works implemented for the design parameters' optimization and the computation of various characteristics of the HA/Ti FGM plate.

The experimental program, results and discussions are explained in Chapter Six. Finally a conclusion and recommendations are given in Chapter Seven. The structure of the thesis is given in Figure 1.2.

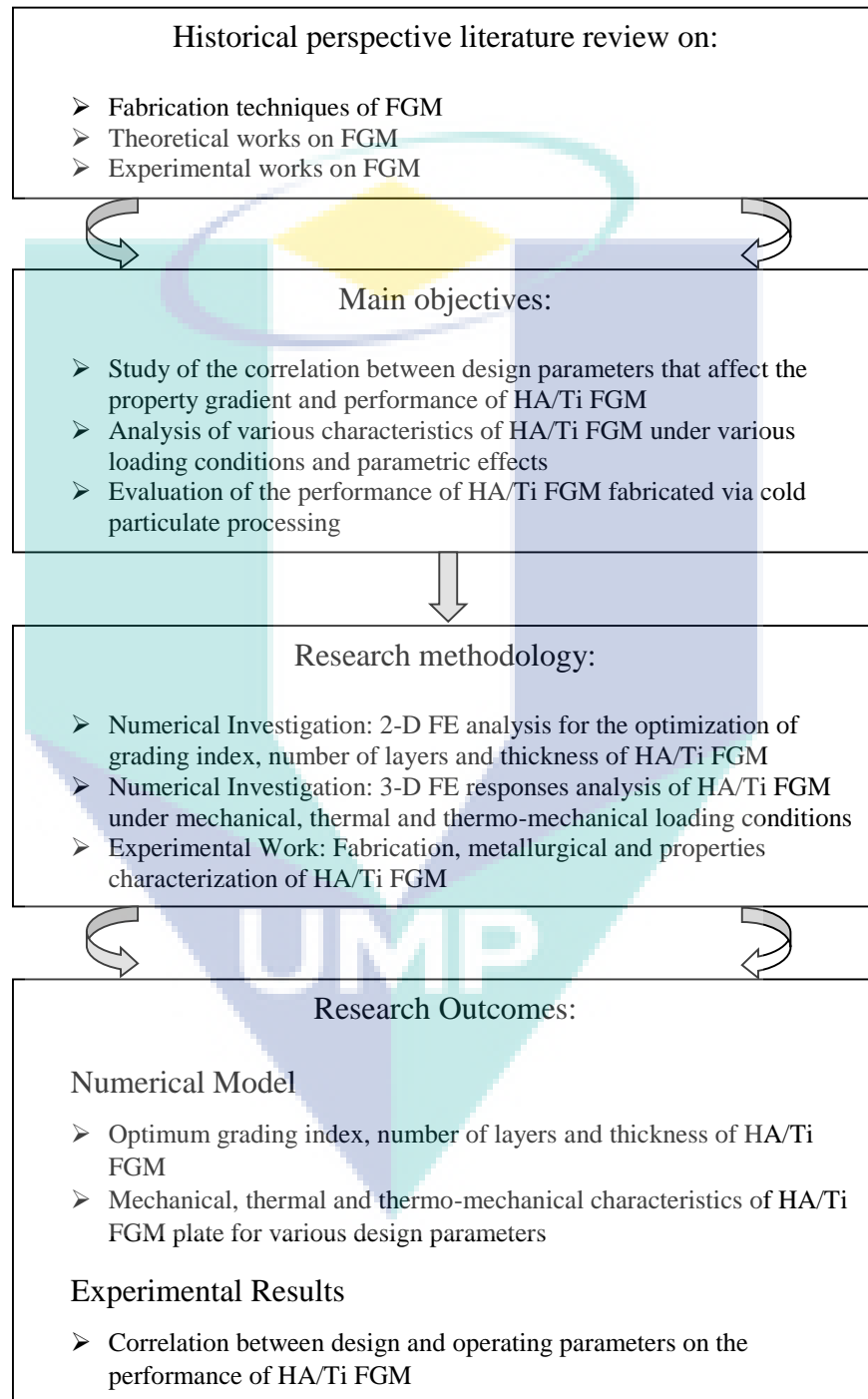


Figure 1.2: Structure of research

CHAPTER 2

LITERATURE REVIEW

2.1 INTRODUCTION

This chapter provides a review of literature that is directly relevant to this study. In order to provide a balanced and comprehensive perspective for the review, various theoretical and experimental studies that have been implemented to explore the characteristics and processing of FGMs are included. The framework and conceptual ideas for the present study are therefore expected to be generated from the relevant information obtained.

2.2 FABRICATION TECHNIQUES FOR FGMS

There are several different physical and chemical methods for fabricating FGMs depending on the type of constituents, the designated application and the available facilities (Schwartz, 2002). However the most applicable and reliable method is difficult to determine because each method may have disadvantages as well as several advantages. In order to successfully fabricate FGMs, previous researchers have applied the optimal combination of several methods depending on the properties of the component materials (Li *et al.*, 2003; Watanabe *et al.*, 2013; Preiss *et al.*, 2010). The fabrication of FGMs usually begins with the gradation process, in which the spatially inhomogeneous structure is built. In the next step, called the consolidation process, the spatial structure is transformed into bulk material through heat treatment. Several comprehensive studies on the various and most up-to-date fabrication techniques for FGMs are available in the literature (Kiebeck *et al.*, 2003; Jamaludin *et al.*, 2013; Mahamood *et al.*, 2012).

2.2.1 The Powder Metallurgy Technique

The Powder Metallurgy (PM) technique is an emerging technology for the fabrication of FGMs and is increasingly used to create gradients on materials. This method is appropriate for FGM particulates processing. The micro-structural control and the inherent versatility of solids are the advantages of using PM for FGM fabrication. The process consists of four basic steps namely: powder production, powder processing (weighing and mixing of powder according to the desired percentage composition), forming operations (the stacking and ramming of premixed powders) and finally sintering or pressure-assisted hot consolidation. The gradation that has been performed in the powder compact needs to be preserved during sintering or the consolidation process. Some light metallic powders such as magnesium (Mg) and aluminum (Al) will tend to react with the oxygen (O₂) and disperse into the atmosphere during oxidation. This should be avoided in order to get the proper resulting materials. In the hot pressing process, sintering is performed simultaneously with compaction. However in the cold pressing process, sintering is performed only after the powders were compacted. Each of these processes can be implemented using various kinds of sintering equipment. The effectiveness of the three different sintering methods (electric furnace heating, high frequency induction heating and spark plasma sintering (SPS)) were investigated by Watari *et al.* (2003).

Many researchers have used the cold sintering technique for preparing FGM samples composed of various constituents. Li *et al.* (2003) have successfully fabricated a beam-shaped porous lead zirconate titanate-alumina (PZT-Al₂O₃) FGM actuator which exhibited the theoretically matched electric-mechanical response. It had a crack-free structure that was built using the pyrolyzable pore-forming agent (PFA) porosity gradient and the cold sintering method. The powder mixture of PZT, Al₂O₃ and stearic acid as the PFA was initially stacked in a die at 100MPa and then restacked using cold isostatic pressing (CIP), before being heat-treated at 1473K for 1hr under a normal sintering atmosphere. Michael and Hugh (2006) added a binding agent called Q-PAC 40 in a nickel/alumina (Ni/Al₂O₃) FGM compacted at a lower pressure of 86MPa prior to pressure-less sintering at 1350°C.

In another work, Sun *et al.* (2008) investigated the optimum processing parameters for the fabrication of an alumina/zirconia ($\text{Al}_2\text{O}_3/\text{ZrO}_2$) FGM by changing the compacting parameter (ranged from 60 to 210MPa), the cooling rate and the heating rate over several ramp and soak-sintering cycles. Nowadays, most researchers intend to use micro-scale particles in the fabrication of FGMs instead of nanoparticles due to the need for more precision during processing. Only a small number of limited studies were reported using the nano-sized composition particles. For example, an FGM produced from cobalt (Co) and Al_2O_3 nano-sized powders was successfully fabricated using a high pressure torsion procedure (Menéndez *et al.*, 2008). This procedure was classified under the PM method and used cold pressing as the consolidation or sintering process performed after compaction.

Li *et al.* (2003) fabricated a yttria-stabilized zirconia/nickel chromium (YSZ/NiCr) FGM using the hot sintering process by initially applying lower pressure to each interface before consolidating the FGM at 1200°C for 1hr under a vacuumed (5×10^{-5} torr) atmosphere and 10MPa of pressure simultaneously. A similar technique was used by Wu *et al.* (2005) to prepare a silicon carbide/carbon (SiC/C) FGM which is a highly effective thermal conductor at the interface of a 1mm SiC layer, compared to that prepared using different methods. In a different work Lee *et al.* (2008) initially cold-pressed 15 stepwise-built layers of various silicon nitride (Si_3N_4) and Al_2O_3 compositions to obtain a cylindrical $\text{Si}_3\text{N}_4/\text{Al}_2\text{O}_3$ FGM green compact. The green compact was then hot pressed under a flowing reducing gas of N_2 at 1700°C for 2hrs and 45MPa of pressure before it was furnace-cooled to room temperature at $2^\circ\text{C}/\text{min}$. Henriques *et al.* (2011) have fabricated the Keramit750/Ceramco3 FGM by following a very similar technique to that applied by Lee *et al.* (2008). This team have proposed the use of a stainless steel die to compact the pure metal green compact and a graphite die for the pure ceramic and composite layer compacts. The consolidation of the green compacts is performed by pressing all layers together at a constant pressure of 20MPa, while applying a temperature of 970°C with a heating rate of approximately $60^\circ\text{C}/\text{min}$ in a vacuum (5×10^{-5} torr) atmosphere. At the end of the processing, the sample inside the die was left to cool down naturally in the furnace. The performance (in terms of the shear bond strength of the fabricated FGM samples) was found to be greater than those prepared using conventional porcelain fused to metal (PFM) techniques.

Since the early introduction of FGM technology in the 1990s, Watari *et al.* (1997) implemented several experimental studies on HA/Ti FGM. In this study a high performance cylindrical HA/Ti FGM plate was fabricated using a different compaction technique called CIP at a pressure of 400MPa and using the SPS method. Using the CIP technique, the pressure was applied to the sample surface from all directions simultaneously while the SPS technique is implemented by using pulsed electric current as the heat source for the sintering process. However these two techniques involved the operation of expensive facilities. Marcelo *et al.* (2006) have compacted the CIPed HA/Ti FGM green cylinders using uniaxial pressing between 390MPa to 1180MPa to obtain higher density samples. The HA/Ti FGM samples were then sintered in a vacuum (1×10^{-3} Pa) at 1150°C for 2hrs with heating and cooling rates of 10 and 20°C/min respectively. A rectangular HA/Ti FGM was fabricated via hot pressing by Chu *et al.* (2006) for in-vivo study, followed by hot pressing at 1100°C and a pressure of 20MPa in an N₂ atmosphere for 30mins with heating and cooling rates of 10°C/min and 6°C/min respectively. A cylindrical HA/Ti FGM sample was fabricated, consisting of five stepwise layers with a gradual composition variation. The total thickness was 6mm and it had a diameter of 20mm, produced by cold compaction (10 ton) and a pressure-less sintering process (1200°C) (Shahrjerdi *et al.*, 2011). The result of a Vicker's micro-hardness test conducted on the FGM sample showed that the hardness at the FGM cross-sectional area lay between 300-450HV (refer to Figure 2.1). Thus it revealed the high brittleness of the sample.

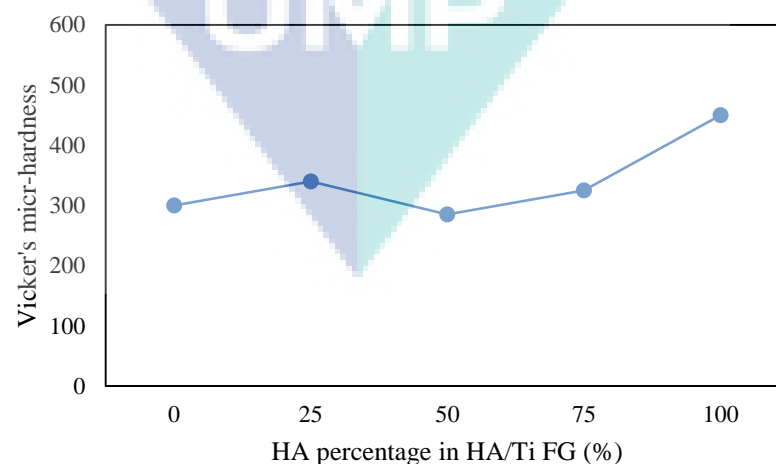


Figure 2.1: Vicker's hardness against HA percentage of HA/Ti FGM

Source: Shahrjerdi *et al.*, 2011

The manufacturing process of an FGM is divided into two stages which are known as the gradation and the consolidation processes. Some parameters applied during gradation (mainly in terms of the ways the powder characterization were determined) could affect the mechanical properties of the FGMs. Thus, the methods of powder processing should be taken into account to make sure the best technique is applied. Besides that, the consolidation process (which refers to the drying and sintering or solidification activity after the gradation) may also requires a lot of consideration. The processes included in this stage need to be adapted to the processed FGMs and every single parameter or condition should be chosen in such a way that the gradient can be preserved. The following sections clearly elaborate on the influence of the powder characteristics and the processing parameters on the structural and catalytic properties of FGMs.

The Influence of Powder Characteristics

Particle size, which is generally measured in term of the diameter of individual particles, refers to the size of the initial powder before processing. An investigation of the effect of particle size has been made by comparing the thermal profiles of copper (Cu) powder compacts of varying particle size, sintered in a multimode microwave furnace. The study found that as particle size increased the heating rate decreased. However, the size increment stopped after a certain time at a particular power setting (Mondal *et al.*, 2009). In addition, Velhinho *et al.* (2005) evaluated particle clustering in terms of number and volume. It was found that the mean particle size increases as a function of the number of particles within a cluster. Therefore, the probability of larger particles coming into contact with each other becomes higher. A lower mean particle size is related to more clustering. This is proved when the dispersion of smaller SiC particles used in the experimental study is harder to achieve when compared to particles of a larger size.

The volume fraction of a mixture is defined as the volume of a constituent divided by the volume of all the constituents of the mixture prior to mixing. Chen *et al.* (2012) compared the experimentally measured porosity of a silicon carbide/molybdenum disilicide (SiC/MoSi₂) composite with that estimated using two

different theoretical models. The study revealed that the content of the reinforced particles influenced the porosity profile. In a different study, Shi *et al.* (2002) investigated the effect of the addition of magnesia particles on the mechanical and bioactive properties of a magnesium/titanium (Mg/Ti) composite. The study revealed that the tensile strength decreased with the increased volume fraction of the smaller Mg ($-25\mu\text{m}$) particles. In addition, Chu *et al.* (2003) gradually diversified the volume fraction along the thickness direction of a HA/Ti asymmetric FGM in the range of 0 to 1 to determine the optimum design of the structure. From the study, an optimum rectangular HA/Ti FGM plate was obtained and it has six layers.

The relationship between the concentration of lubricant, the compacting pressure and the densification level was obtained from an investigation performed on ATOMET 1001HP and ATOMET 4401 (Chagnon, 2010). The results showed that at a compacting pressure of below 620MPa, powder compressibility is a key parameter for achieving a high density, while above 690MPa low density additives (lubricant and graphite) may have the largest impact.

Lee *et al.* (2008) used FEM modelling to find the optimal number of layers to insert between the pure layers of a crack-free $\text{Si}_3\text{N}_4/\text{Al}_2\text{O}_3$ FGM. This optimization is based on an evaluation of the distribution of residual thermal stresses induced during the cooling stage of the sintering process. The cracks predicted by the FEM were verified with experimental findings and as a result of the study the number of layers in the FGM was reduced from 20 to 15. However Shahrjerdi *et al.* (2011) have stated that stepwise-based FGMs should have at least five layers in order to obtain the graded properties effectiveness. This research team has demonstrated the steps for the processing of HA/Ti FGM via pressureless sintering technique at 1200°C as the optimum sintering temperature.

In order to achieve a good homogeneity of the constituent mixtures in FGMs, the elemental powders need to be mixed in such way that the particles can disperse uniformly. High energy ball milling is one of the methods used to achieve the successful production of the FGMs because the homogeneous mixture of the elemental powders can be processed to a very fine scale prior to consolidation (Chagnon *et al.*, 2010).

However an investigation of the effect of the ball milling process on the microstructure of the HA/Ti FGM made by Tsipas *et al.* (2003) was disappointing because a homogeneous distribution of HA particles was not observed among the titanium particles. In addition, there were also continuous surface layers of HA formed on the titanium particles, leading to very poor behaviour during sintering. A longer period of ball milling led to surface layer disruption as well as the amorphization of the HA. Hot extrusion was suggested as an alternative method to consolidate the HA/Ti FGM instead of using hot pressing. This is because some signs of breakup on the HA surface layers were observed (due to the plastic deformation of titanium particles), which led to the formation of regions with a lamellar structure on the HA/Ti FGM prepared via the hot pressing process.

The Influence of Processing Parameters

The application of continuous force from the die to the surface of the powder mixtures that contact the die wall is one of the important parameters that can influence the processing of an FGM. When the powder mixtures are sintered under an applied pressure, higher densification can be achieved with a constant temperature. The relative contribution of pressure on an FGM containing smaller particles is less significant when compared to those found on FGMs consisting of larger particles (Munir and Anselmi-Tamburini, 2006). The optimal pressure for the good performance of a HA/Ti FGM fabricated by methods such as CIP could be reach at 700-1000MPa (Watari *et al.*, 2004). Dobrzanski *et al.* (2011) proposed an experimental method to determine the minimum pressure for the compaction of a tungsten carbide-cobalt (WC-Co) FGM. The method was implemented by pressing the powders in a closed moulding on a uniaxial hydraulic press under a pressure that varied within the range 300 to 450MPa. Sufficient pressure for the fabrication was determined by measuring the densification of the powder mixture and observing the metallographic compacts.

The influence of sintering temperature on the microstructure of a HA/Ti FGM was investigated for a temperature range of 400-1100°C. It was indicated that the temperature at which the length of the isostatically pressed Ti-20% HA specimen began to decrease was when the sintering temperature reached 800°C. However the shrinkage

was found to decrease to only 0.4% for the Ti-40%HA specimen when the sintering temperature was in the range of 800°C to 1100°C (Tsipas *et al.*, 2003). Chen *et al.* (2012) found that the temperature in which the powders began to react could be different for different composites. Their investigation of a SiC/MoSi₂ composite microstructure at a temperature range of 800°C to 1550°C showed that SiC particles dispersed uniformly in the MoSi₂ matrix only after being treated at 1300°C for 60mins and sintered at 1550°C for 120mins. At the lower temperature of 800°C no reaction was observed in the microstructure of the composites. Pattanayak *et al.* (2011) investigated the effect of the sintering temperature on the physical and mechanical properties of HA/Ti FGM. The study found that the sintered density and the biaxial flexural strength (BFS) of the HA/Ti FGM was directly proportional to the sintering temperature and independent of Ti content. The samples sintered at 1100°C have a high BFS which is in the range of 35-40MPa. The conclusion made by Pattanayak *et al.* (2011) was subsequently supported by Hilal *et al.* (2012) who found the density, shrinkage and BFS of their pure Hydroxyapatite/yttria partially stabilized zirconia (HAp/Y-PSZ) FGM increased with increased sintering temperature, time and the addition of Y-PSZ.

A study of the structural stability of the HA phase of the HA/Ti composite by means of spectrometry and X-ray diffractometry as a preliminary investigation for the phase contamination for the HA/Ti FGM was conducted by Chu *et al.* (2002). The findings show that at a high temperature, the existence of a Ti metal phase could lead to the dehydration and decomposition of the HA ceramic phase into a more stable calcium phosphate phase, such as α -Ca₃(PO₄)₂ (α -TCP) and Ca₄O(PO₄)₂ (refer to Figure 2.2). The decomposition reaction of the HA phase, with the generation of new phases, and the difference of sintering shrinkages between HA and Ti particles can block the sintering densification and affect the mechanical properties of the FGM. An experiment performed on the HA-20vol.%Ti sample fabricated using the hot pressing method drew the conclusion that applying stress via hot pressing decreased the temperature and the duration required to densify the composite. This avoids or minimises the decomposition reaction of HA in the composite during sintering.

The influence of the rate of heating on both hot and cold sintering has been comprehensively studied. In pressure-less or cold sintering, higher heating rates lead to

greater densification by bypassing the non-densifying mechanism of surface diffusion and instead creating an additional driving force through large thermal gradients (Liu and German, 1999). Conflicting effects have been reported when the heating rate is between 50 and 700°C/min, producing no change in the final density of SPSed Al₂O₃/MoSi₂ FGM (Stanciu *et al.*, 2001). The experiment also revealed that the necessary sintering rate should be determined by considering the grain size of Al₂O₃. However Shen *et al.* (2002) reported a different observation, showing the less significant effect of the heating rate on the density of Al₂O₃ until 350°C/min. This study also found there was a negative effect on the final density with higher heating rates: the density decreased at the same time as the heating rate increased up to 600°C/min. In addition, grain size had an influence, especially at lower heating rates. The grain size decrement was significant as the heating rate increased from 50 to 200°C/min.

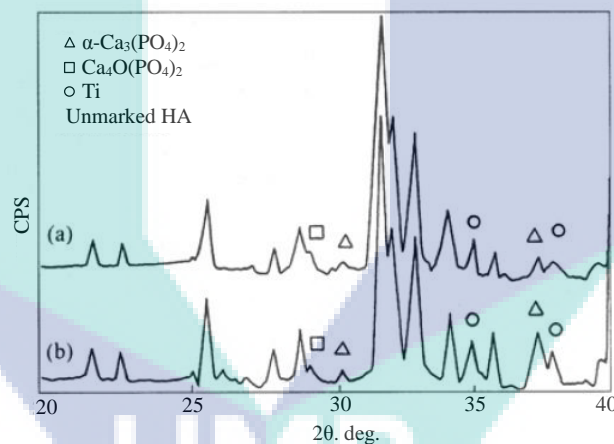


Figure 2.2: XRD spectra of HA-20 vol.% Ti composites sintered at different temperatures for 60 min. (a) 1000°C; (b) 1100°C

Source: Chu *et al.*, 2002

Further investigation of the same materials found that the final density of Al₂O₃ was not affected by a heating rate in the range of 50-300°C/min but was influenced by grain size when the grain size decreased at the same time as an increased heating rate (Zhou *et al.*, 2003). Similar results were reported from the work on the densification of nano-metric fully-stabilized cubic ZrO₂ (Munir and Anselmi-Tamburini *et al.*, 2006). The effect of heating rates on the partially-stabilized (3mol.% ultra) ZrO₂ has been performed with two different particle sizes but it showed some contradictory results.

The final density of the micro-sized powders showed no dependence on the heating rate but an increasing heating rate resulted in a lower final density. These observations were explained on the basis of large thermal gradients existing with high heating rates which in turn caused sintering of the outside of the sample without fully sintering the inner element (Chen and Mayo, 1996). It should be noted that slow diffusional processes that give some densification are not always suitable for real FGM fabrication as the process is not time-frame compatible with many industrial sintering cycles (German, 2001).

The atmosphere of the sintering process is another important aspect to be taken into account during the consolidation of FGM powders. The type of flowing gas type is determined by the elemental material used to produce the FGMs. In the fabrication of $\text{Al}_2\text{O}_3/\text{Si}_3\text{N}_4$ FGM, Lee *et al.* (2008) sintered the FGM using a hot press in flowing nitrogen (N_2) gas to prevent the decomposition of Si_3N_4 . However many researchers prefer to use a vacuum for the sintering process because the empty space protects the elemental mixtures from chemical degradation (Dobrzanski *et al.*, 2011; Batin *et al.*, 2011; Chen *et al.*, 2012).

2.2.2 The Infiltration Method

Infiltration, or the scientific term called hydrology, is the process by which fluid on the surface of the ground surface precipitates into the soil. This process is governed by either gravity or capillary action forces. The infiltration method was introduced for the preparation of certain FGMs with a complex shape. Fabrication with this method needs little or no bulk shrinkage and has more rapid-reaction kinetics. As the common process for mold shaping is heating the powder to a temperature that is higher than its liquid phase, the requirement to make sure there is no bulk shrinkage is quite challenging.

There is limited research on the implementation of the infiltration process. It is believed that the ticklish process of handling and its high costs are the two main factors that make infiltration challenging. A compositionally graded Al-SiC_p composite was successfully fabricated using a pressure-less infiltration method by Cho *et al.* (2004). It was indicated that the thermal conductivity of the produced FGM increased in a

nonlinear trend while the volume fraction of the ceramic element decreased. An innovative approach that combined the infiltration process with microwave sintering and environmental barrier coating (EBC) was subsequently presented for the fabrication of Si_3N_4 FGM containing α - Si_3N_4 -Yb-silicate green parts and porous β - Si_3N_4 ceramics as the substrates (Willert-Porada *et al.*, 2005).

Another approach based on the concept of infiltration was developed for the fabrication of a micro-ceramic FGM (Hassannin and Jiang, 2010). Using this approach, highly stable suspensions were carried out by controlling the colloidal behaviour of the structures. It was highlighted that the highest possible stable suspension and the demanded porosity of the FGM structure could be obtained by selecting a certain pH and dispersant concentration during the fabrication. This technique proved that the free standing microcomponents in a YSZ/SiC FGM can be fabricated via the infiltration method.

A different composition of porous pTi/HA FGMs was also fabricated using the infiltration method. It was performed in a vacuum of less than 1×10^{-2} Pa and was sintered at 1173K for 7.2ks (Nomura *et al.*, 2010). This study revealed that the porosity of the compacts was controllable in the range of 7 to 39% by hot pressing temperature and the applied load. The Young's Modulus of fabricated FGMs was comparable to the human cortical bone, with a porosity in the range of 24 to 34%. The study concluded that the Young's Modulus of pure titanium (pTi) can be customized by adjusting the content or volume fraction of the HA.

The influence of the particle size of the component materials on a tungsten-copper (W-Cu) FGM has been studied by evaluating two specimens fabricated using different particle sizes (Raharijaona *et al.*, 2010). For liquid phase processing, this study concluded that the phenomenon of phase migration is driven by a differential sinterability in the gradient. Besides that, the effect of glass infiltration was investigated on a calcium oxide-zirconia-silicon dioxide ($\text{CaO-ZrO}_2\text{-SiO}_2$) system in the development of glass-alumina FGMs (Cannillo *et al.*, 2008). In order to obtain the final compositional gradient which is indicated by blue glass, the glass formulation of the system was doped with cobalt by adding a small molar percentage (0.1 mol.%) of cobalt oxide (CoO). The

characterization of the specimens proved that the cobalt-doped glass had interesting mechanical properties including a high elastic modulus, good fracture toughness and acceptable CTE. From the detailed micro-diffraction test made on the FGM cross-section, the study revealed that the heat treatment and the glass porcelain did not lead to any relevant crystallization of the new phases after the process.

In order to investigate the effect of the heating or sintering method, some different methods are considered. These are based on plasma-facing factors including the infiltration welding method, plasma spraying and the process of resistance sintering under ultra-high pressure. Each of these methods were used to fabricate W/Cu FGM (Zhou *et al.*, 2007). This was an extended study of the efficiency of the infiltration-diffusion method which was previously implemented on a tungsten-carbon/brass (W-C/brass) FGM (Li *et al.*, 2005). The analysis of the thermal properties of these specimens indicated that the element fabricated using infiltration-welding has the best thermal shock resistance compared to the others. An analytical analysis of the residual thermal stress of the FGM was performed on three types of mullite-type aluminoborates/magnesium ($\text{Al}_{18}\text{B}_4\text{O}_{33}/\text{Mg}$) FGMs, each with a different layer number and compositional gradient from 0 to 35% (Lee *et al.*, 2009). The stresses were found to decrease in the macro-interface with the increasing number of layers.

2.2.3 The Graded Casting Process

Graded casting is another process used to prepare a complex-shaped FGM. It is a manufacturing process by which a liquid material is poured into a hollow cavity of the desired shape before being solidified. There are three kinds of processes for FGM preparation classified under graded casting: centrifugal casting, slip casting and tape casting. All of these processes are based on a similar principle, which means that whenever a porous body is dipped sequentially into slurries with different powder characteristics, capillary forces will pull the liquid into the pores, moving from the surface layers with a stepped gradient behind (Nan, 1993).

Centrifugal Casting

An investigation of the microstructure and composition gradients of some Al-based FGMs including Al/SiC, Al/Shirasu, Al/Al₃Ti, Al/Al₃Ni and Al/Al₂Cu combinations have been made by evaluating the dispersion of phase particles within FGM structures fabricated using different centrifugal casting processes (Watanabe *et al.*, 2005). The study found that Al/SiC, Al/Shirasu and Al/Al₃Ti FGMs can be fabricated by the centrifugal solid-particle method, while the centrifugal in-situ method is suitable for the fabrication of Al/Al₃Ni and Al/Al₂Cu FGMs. The combination of both processing methods are then required for Al/(Al₃Ti+Al₃Ni) hybrid FGMs. Centrifugal casting is a practical mechanism for FGM fabrication because it can be feasibly scaled up to mass production while maintaining low costs, this method is limited to the fabrication of FGMs with a continuous gradient in their composition.

The phase compositions of FGMs fabricated using this approach are strongly dependant on the conditions of the centrifugal sedimentation process including the duration time, rotation speed, the solid and the dispersive fluid contents (Jaworska *et al.*, 2006). A self-propagating high temperature synthesis reaction is added as one of the steps followed by centrifugal casting in the fabrication of a TiC-reinforced iron base (Fe-TiC) FGM. Observation of the fabricated specimen indicated that the hardness profile trended upwards from from the outer surface to the TiC-rich inner surface. The wear performance of the TiC-rich inner face was found to be better when compared to the particle free outer surface of ferritic steel matrices. The centrifugal mixed-powder method (CMPM) was another method introduced as a solution to the limitations of the centrifugal casting method when fabricating FGMs containing nano-sized particles (Gowtam *et al.*, 2008). The study was extended to propose another method, called the reactive centrifugal mixed-powder method (RCMPM), which was able to produce better surface properties instead of controllable compositional gradients (El-Hadad *et al.*, 2009).

The formation of gradient solidification was another aspect evaluated in the investigation made on FGMs fabricated via centrifugation. In this study, SiC, boron carbide (B₄C), an SiC graphite hybrid, primary silicon, magnesium silicide (Mg₂Si) and

an Al₃Ni reinforced aluminum based FGM were prepared by centrifugal casting. Two major roles that influenced the formation of graded microstructure were found to be the density and size of reinforcements (Rajan and Pai, 2009). High density particles such as SiC and Al₃Ni formed a gradation towards the outer periphery while a lower density particle, such as graphite, primary silicon or Mg₂Si, formed a gradation towards the inner periphery. The B₄C particle, which has a similar density to the Al alloy, was the only particle that was distributed more randomly compared to the other systems. When considering the processing of slurry from raw materials, another step named floc-casting has been proposed. It would be implemented after the centrifugation. During the fabrication, floc-casting at 80°C was applied to the SiO₂-Mo FGM to form an homogeneous slurry green body before being fired at 1750°C for 10mins in Ar. Floc-casting was found to benefit control of the slurry's characteristics and helped to make the slurry centrifugation successful.

Slip Casting

The tetragonal zirconia polycrystals/stainless steel 304 (TZP/SUS304) FGM was developed using a slip casting technique (He *et al.*, 2008). This study concluded that constitutional variation influenced the mechanical properties of the fabricated TZP/SUS304 system. Using the same method of slip casting, Ti foams with high purity and high strength macro-porous elements, which were successfully fabricated with the addition of an emulsion process to stabilize the Ti (Neirinck *et al.*, 2009). During the process, the stability of the emulsion's activity was increased by partially hydrophobizing the titanium particles. This was important as the emulsion properties were the parameters that influenced the porous properties of the resulting materials. As density was another important consideration when evaluating the emulsion's properties, a material that can reduce the sintering temperature and the time needed for high density struts should be selected as the strut's element. For this purpose, titanium hydride was used as the struts in the study. The final product of the titanium foams were found to have compressive strengths ranging from 120 to 150MPa.

The Al₂O₃/W FGM, which has potential when applied as a conducting and sealing component for high-intensity discharge lamps (HiDLs), is another FGM that

was successfully fabricated via the slip casting method (Katayama *et al.*, 2011). The oxidizing properties of Al₂O₃/W FGM specimens made from two types of W powders have been evaluated for the discussion. In this process, the oxidized W was prepared by heat treatment at 200°C for 180mins in air before being mixed together with the Al₂O₃ powders in ultrapure water by ultrasonic stirring. The slurry was then cast into a porous Al₂O₃ shaped mold under controlled pressure. The study found that the larger ζ -potential of the oxide layer coated on the W powder core induced the dispersion of the oxidized W powder.

Tape Casting

In the tape casting process, a powder was blended into an organic solvent with suitable binders and plasticizers to form a slurry with a viscosity that ranged from 500 to 6000mPa.s (Martin and Nguyen, 2005). The slurry was then cast into a film shape to form a tape which ranged in size from several μ m to mm thickness. The individual layer processing was completed by a drying process to remove the residual solvent trapped in the tape. The laminating process took place under elevated temperatures ranging from 50 to 200°C and at a pressure from 3 to 30MPa, which followed for the construction of the other layers. The final processing of the laminate involved heating at an elevated temperature to remove the organic binder and then hot pressing the film to full density. A Mg-Cu FGM system was cast into a series of tapes with continuous composition changes ranging from 100% Mg to 100% Cu to be used as light-gas gun impactors. The fabrication of graded impactors using this technique has generated significant interest because it provides improved control of the pressure profile in gas gun experiments.

The glass-transition temperature (T_g) and modulus of elasticity (E) are two other aspects evaluated through the fabricated tape laminating process of an epoxy (EP)/ polyurethane (PU) FGM system (Liu *et al.*, 2004). These two materials of EP and PU have $E=3.2$ GPa, $T_g=162^\circ\text{C}$ and $E=0.069$ GPa, $T_g=-54^\circ\text{C}$ respectively. The FE simulations made on the FGM structure under a steady-state and non-uniform temperature field show that the temperature and thermal stress distribution decreased along the graded direction. For a deeper exploration of the tape casting process of composites, the calculation of the FGM tape thickness results were characterized by

wide adaptability. The blade gap, casting speed and considerations related to the slurry's rheological properties were also included in the calculations (Liu *et al.*, 2012).

2.2.4 Thermal Spraying

In order to fabricate FGMs using a thermal spraying technique, the coating precursor was either heated electrically or chemically until it melted. The melted materials with different compositions were subsequently layered on a substrate material using a spraying technique to build the FGM coating. The advantage of this technique is that the coating can be built up in thickness, ranging from 20 μ m to mm, over a large area at a high rate of deposition better than those made by electroplating and vapor deposition methods.

Three types of functionally-graded thermal barrier coatings (TBCs) and duplex coatings with the same thermal resistance have been designed in order to investigate the thermal fracture behavior of FGM structures (Kawasaki and Watanabe, 2002). In the study, a (PSZ)/IN100 FGM containing mixed microstructures and a PSZ/Inco718 containing coarse microstructures were fabricated using slurry dipping and hot isostatic sintering (HIP) methods. The study found that the specimens fabricated via the duplex coatings method had a better or improved spallation life under cyclic thermal loads.

The shot-control method is another approach that applied the concept of a gun spray process to fabricate functionally graded TBCs (Kim *et al.*, 2003). This method has been used to prepare NiCrAlY/ZrO₂ FGM coatings. A finely mixed microstructure of metal and ceramic phases with no obvious interfaces was observed at the interfaces of the resulting materials. The process was considered reliable when the individual properties of the composed materials were maintained without any phase transformation in the fabricated FGM.

Another FGM that has been successfully fabricated via the thermal spraying process contains a TiO₂ membrane and a planar/tubular porous metallic material as its constituents. During fabrication it was found that intermediate layers made of the same materials are necessary to prevent the penetration of the powder suspension into the

pores of the support. The ultrasonic wave and grinding methods were found to be beneficial for the minimization of imperfections in the structures (Zhao *et al.*, 2004).

A spark plasma technique during the thermal spraying process was used in another study for the fabrication of an FGM composed of pure Hydroxyapatite (HAp) and titanium nitride (TiN) (Kondo *et al.*, 2004). The FGM was prepared by sintering at a range of 1100 and 1200°C and under a pressure of 150MPa. The resulting material had a Brinell hardness of 60HB and this value was uniformly distributed over the whole composition.

In order to improve the adhesion between the adjacent graded layers of FGM, a proper bond coat was introduced. It is believed that by arranging a smooth change in the thermal expansion coefficient mismatch of the composition, the delamination within the FGM structure could be handled. The investigation made into the HAp/TiO₂ FGM fabricated via plasma spraying techniques found that the crystallinity of HAp and the Vicker's hardness increased with a raised temperature (Ye *et al.*, 2007). However, at a high temperature of more than 750°C, the stress induced by re-crystallization promoted the propagation of cracks and failures on the interface. In another study, the influence of powder characteristics on the mechanical properties of the air plasma-sprayed YSZ/mullite coats deposited on Si substrates was investigated using indentation testing set up with loads of between 10 to 500mN (Cojocaru *et al.*, 2010). The spray coatings were performed at a temperature of 1300°C for 500hrs in a water environment. The study found that the elastic modulus and hardness of the resulting materials were highly dependant on the size distribution of the starting powders. Using the same approach, SPS, the WC/Co FGM was also successfully fabricated (Eriksson *et al.*, 2013).

2.2.5 Laser Cladding

Laser cladding or laser deposition is a technique in which a material is layered on the surface of another material using a laser intersection system controlled by computer aided design (CAD). Although this technique has become the most appropriate technique for coating various shapes and graded materials, limitations still exist when the process involves many processing parameters and high costs.

The most appropriate uses for the selective laser sintering (SLS) technique based on the free-form concept parameters for the fabrication of polyamide 12 and multi-walled carbon nanotubes (MWCNTs) have been investigated (Paggi *et al.*, 2012). The laser energy density was adjusted to improve the properties of the resulted material properties such as density, flexural modulus and stress distribution at 10% elongation. The study found that the overwhelm mixing of the MWCNTs content, when compared to the polyamide content, interferes with the laser sintering process.

The compositional gradient distribution and the bonding strength of FGMs fabricated based on rapid prototyping with laser cladding techniques have been investigated (Ouyang *et al.*, 2002). The final WC-NiSiB alloy FGM products that possess the improved highlighted properties fabricated in this study were found to be applicable for use in high-temperature tribological applications. The study mentioned that the surface roughness and the geometrical properties of the synthesized FGMs can be controlled by adjusting the heat input during the laser cladding process.

The effect of different laser strategies is another aspect that was investigated to improve the laser cladding process in producing FGMs. In order to see the correlation between the laser strategy and the FGM's properties, the dispersion of the laser fusion of the different weight proportions of Cu (0, 25, and 50%) powder in H13 was analyzed. From the analysis, a refill strategy was found to be the best technique as it produced the lowest porosity of H13 with fine dendrite structures (Beal *et al.*, 2006).

Elperin and Rudin (2007) analyzed the theoretical principles used in the photo thermal displacement (thermal mirror) method which was constructed for measuring the physical properties of opaque multilayered and graded coatings with low thermal conductivity. This study proved that the properties of the laser assisted coatings, including thermal diffusivity and the coefficient of linear thermal expansion, can be determined as the 2-D thermal elasticity. The expressions for photo induced displacement, the slope of the coating surface as a function of time and the physical properties of the sample were also analytically solved.

The suitability of using FGMs in applications where they are subjected to thermal fatigue is another aspect that was investigated. During FGM specimen fabrication, two different filler materials from AISI H13 tool steel were used. The content of the silicon was varied to make the gradation of the secondary carbide content. The study found that thermal fatigue resistance decreased with increasing silicon content in the filler materials (Fazarinc *et al.*, 2011).

The pulse-periodic Nd:YAG with wavelength of $1.06\mu\text{m}$ was found to be the most preferable laser source for the development of FGM components (Yakovlev *et al.*, 2005). This technique allows the development of pre-defined compositional gradients, which is done by changing the powder composition to appropriate composition values. The resulting FGM fabricated using this technique shows a minimal transition zone of only $70\mu\text{m}$ between the composed materials. The Nd:YAG laser power type has also been used in FGM fabrication via the selective laser melting (SLM) of super nickel alloy and zirconia. The resulting materials contained an average porosity of 0.34% and a gradual change between layers without any major interface defects (Mumtaz and Hopkinson, 2007).

In addition to solid freeform fabrication (SFF) and laser-based flexible fabrication (LBFF) methods which were developed based on the laser cladding principal, there are two other methods that have been introduced for the fabrication of FGMs. By these methods, a hollow square mold insert with additive layers of H13 steel, Ni/Cr alloy and TiC were successfully fabricated using circular and rectangular beam (RB) profiles determined by ANSYS analysis (Jiang *et al.*, 2005). The fabricated FGM mold insert has excellent integrity, beneficial microstructure, strong interfaces and a high level of hardness. These properties were confirmed through a comparison with H13 steel molds that were tested together in a thermal fatigue environment to evaluate the ability of the structures to resist crack initiation, thermal strain and oxidation.

Laser rapid manufacturing was another method introduced to under laser assisted processing. Using this method, a bi-metallic tube (a cobalt-based alloy Stellite 21) and austenitic stainless steel (316L) were fabricated using a 3.5kW carbon dioxide (CO_2) laser which was integrated with a beam delivery system, a 5-axis computer

numerical control (CNC) work station and a power feeding sub-system. The fabricated specimens exhibited the desired transition in chemical composition and hardness across their wall thickness. In order to achieve the proper dimensional control and the desired heterogeneity of the chemical composition of the specimens, an on-line control system was developed with three digitally-controlled processes known as 3-D laser cladding, 3-D laser-engineered net shaping (LENS) and selective laser sintering (SLS) (Ganesh *et al.*, 2009; Joshi *et al.*, 2012). These three methods were used to obtain coatings of FGM. The first used direct powder injection into the laser beam. The second used CAD solid models with minimal lead times, especially for metal art fabrication and the third constructed 3-D FGM structures through layered manufacturing. The main advantage of all these methods was the short time interval needed to complete processing.

2.2.6 Vapor Deposition Method

Vapour deposition is a process used to make coatings that alter the properties of substrates, for example in terms of their mechanical, electrical and thermal properties or wear etc. This process is classified into two categories: chemical vapour deposition (CVD) and physical vapour deposition (PVD) (Kiebeck *et al.*, 2003). In order to produce the desired deposit using the CVD process, the substrate is exposed to volatile precursors to allow the reaction and decomposition on the substrate surface. In PVD coating the chemical reaction part of CVD is replaced by purely physical processes such as high temperature vacuum evaporation or plasma sputter bombardment. The processing sources distinguish the two different methods during the vapour deposition process.

FGMs consist of carbon-based materials that have the ability to produce an excessive chemical sputtering at 600-1000K and irradiation that enhanced sublimation at a temperature of more than 1200K when exposed to plasma erosion. FGMS such as SiC/C, B₄C/Cu SiC/Cu and B₄C/C have been fabricated by CVD method (Ge *et al.*, 2002). The problem of serious C-contamination of the plasma was solved by chemically depositing the SiC coatings on the substrate's surface. However the performance of the resulting materials was not considered satisfying because crack initiation was observed on the structures. The study found that better thermal stress relaxation on the structure

can solve the crack initiation problem. In order to evaluate the rate of thermal stresses reduction, Kim *et al.* (2003) applied the low pressure chemical vapor deposition (LPCVD) method to fabricate the SiC/C FGM. The thermal stresses were evaluated by determining the deposition conditions of the entire compositional range of the structures using thermodynamic calculation. Kim *et al.* (2005) then proposed an effective SiC-rich compositional profile in the FGM interlayer to relieve the thermal stresses distribution.

Wang *et al.* (2004) have highlighted the importance of using CH_3SiCl_3 or methyltrichlorosilane (MTS) for the fabrication of both an oxidation-resistant SiC coating and a functional SiC film using the CVD process. The decomposition product of MTS was calculated using thermodynamic calculations after obtaining the correct data from authoritative data sources. Observation of the Ni/SiC FGM fabricated via the electro-deposition method indicated that the content of the SiC powder increased gradually in the direction of the deposit growth, while the crystal size decreased to 27.5%.

A different deposition method called 'diamond like carbon' (DLC) is based on another method introduced by vapor deposition. The main limitations of this technique are the tendency of the DLC-coated FGM to peel off due to the high contact stresses and the thickness of deposition. Bulbul and Efeoglu (2010) implemented the DLC technique to fabricate two FGM films where Ti:a:C and Ti-TiC-a:C were deposited on AISI M2 steel using a closed field unbalanced magnetron sputtering (CFUBMS) method. The study found that the incorporation of a TiC buffer layer between the Ti interlayer and the a:C matrix contributed to an improvement in the hardness, wear rate and adhesion properties of the resulting materials.

Another deposition method under PVD technique is called electrophoresis deposition (EPD). In this technique, the charged particles from a stable suspension are deposited on a substrate with opposite charge using direct current (DC) electric field. Gasik *et al.* (2003) have fabricated FGM hardmetal cutting tools (WC-Co-TiC) and $\text{ZrO}_2\text{-Al}_2\text{O}_3$ via EPD and pressure-less sintering to verify the optimum design predicted by FEM in ABAQUS. The study found that the optimal parameters in the FGM determined by the numerical calculation were highly consistent with those characterized

in the experimental work. Sarkar (2004) have highlighted EPD technique as a powerful and versatile forming and consolidation method as it can produce homogeneous and dense green bodies with complicated shapes and allow flexibility in microstructural manipulation.

2.3 THEORETICAL WORKS OF FGM

Previous researchers have implemented various theoretical studies to explore the FGM technology. The theoretical works were taken as the starting point to gain understanding on the design, behaviour as well as the processing of FGMs. The review of theoretical works implemented on FGM described in this section is divided into two parts. The first part shows the prediction on the FGM properties distribution and the subsequent part includes the modelling of various problems reflect to the behaviour and characteristics of the FGMs.

2.3.1 FGM Model Development

In order to develop an FGM model, the material properties such as thermal conductivity, Young's modulus, Poisson's ratio, thermal expansion coefficient and etc. gradient along the transverse plane of the structure need to be accurately estimated. The prediction methods of the entire effective properties within the framework of single continuum mechanics can be divided into three main approaches known as direct, variational and approximation approaches. Based on the direct approach described in Hill (1963), the FGM material properties are estimated by seeking the closed-form analytical solutions to the overall properties of ideal composites.

The variational approach which implements the variational principles of thermo-mechanics for the bounds derivation which directed to the determination of the FGM's effective thermo-physical properties. This method assumes that the properties of each layer inside the FGM is homogeneous and isotropic. Hashin and Shtrikman (1963) have shown the relationship between the effective bulk modulus and shear modulus of the upper and lower bounds of the material.

Besides the direct and variational approaches, another approach which is commonly used for the prediction of the material properties of FGMs is based on a rule of mixture (Lee *et al.*, 2008; Park *et al.*, 2009; Ryu *et al.*, 2009; Alshorbagy *et al.*, 2013). By using this rule, the material properties of FGM are estimated by taking into account the individual properties and compositional percentage of the constituents. The constituent particles are assumed to uniformly dispersed while remain separately without react one another.

Tomota *et al.* (1976) then have introduced modified rule of mixture (MROM) as an effort to take into account the interaction between constituents' particles. The effects of interaction between the particles is included in the formulation in two ways which is first by utilizing the in-situ constituents properties or second by obtaining and including empirical data in the calculation. Fan *et al.* (1994) then introduced generalized rule of mixtures which considers the effects of grain shape and phase distribution. This rule is purely based on theoretical assumption since it is derived from continuum mechanics and no empirical data is considered.

Exponential function is another method that have been widely used for estimating the material properties of FGMs (Bhangale and Ganesan 2006; Sevcik *et al.*, 2009; Shariyat and Mohammadjani 2013). The exponential-based FGM material properties was initially proposed by Delale and Erdogan (1983) and this approach has been chosen among the researchers due to its simplicity in numerical manipulation.

It is also possible to determine the FGM properties based on the concept of power-law. The material properties based on single power-law was initially developed by Bao and Wang (1995). In order to add an FGM of single power-law function to a laminated composite, Chung and Chi (2001) introduced two power-law functions for determining the smoother volume fraction distribution of constituents which contributes to the reduction of stress concentration discontinuity along the transverse plane of the FGM structure. The power-law formulations have been implemented in many researchers and various characteristics of power-law based FGM were established in literature (Kursun *et al.*, 2011; Sevcik *et al.*, 2009; Ramu and Mohanty, 2014).

2.3.2 FGM Responses Analysis

In a microscopic scale, the architecture of the FGMs is contrasted against the surrounding matrix of pure materials. This factor leads to various responses in displacement and stress fields at different loading conditions. The effect of radial and normal loads under thermal excitation on the post-buckling response of a shear deformable FG cylindrical shell has been analyzed using a singular perturbation technique in which a higher shear deformation shell theory was applied (Shen and Noda, 2005). The study concluded that the properties' variation along the thickness direction of the FG shell and the temperature field distribution are the two parameters that affect the post-buckling characteristics and the imperfection sensitivity of the shell.

Matsunaga (2009) developed a two-dimensional model using a higher order deformation theory to analyze the response of FGM plates subjected to thermal and mechanical loads. In the computation, equations that consider the effect of normal and transverse shear stress were derived using the power series expansion of the continuous displacement components method. The study revealed that the effect of the properties' variation along the thickness of the FGM plate is larger on the response of FGM plates subjected to thermal loadings. The effects of thermal and mechanical loads on the response of simply supported rectangular FGM plates have been analyzed using a 3-D thermo-elastic model based on the Fourier series and state-space methods (Alibeigloo, 2010). The material properties of the FGM plates were assumed to vary exponentially along the thickness direction except for the Poisson ratio, which was taken as constant. The research results in Alibeigloo (2010) show that the contribution of the thermal loads on the thermo-elastic response of the FGM plates is bigger than that of mechanical loads.

The effects of thermo-mechanical loading on the buckling response of FGM beams were analyzed by Kiani and Eslami (2013) using a derivation of the Timoshenko beam theory. In this analysis, various types of boundary conditions including clamps, simply supported, and roller combination were taken into account to observe the response field distribution. This study revealed that the critical buckling temperature field is greatly affected by the constituent temperature dependency. A local mesh-less

method based on the Petrov-Galerkin approach with moving Kriging interpolation has been used to solve large deformation problems in the geometrically nonlinear thermo-mechanical analysis of moderately thick FGM plates (Zhu *et al.*, 2014). The study revealed that the thermal conductivity on temperature does affect the stress field analysis on the Al/Al₂O₃ and Ti-6Al-4V/Al₂O₃ FGM plates. Using the similar method also, Zhang *et al.* (2014) have investigated the dependency of the FGM buckling performances on the volume fraction exponent under thermal and mechanical loadings with different combined essential conditions and loading conditions. The effectiveness and accuracy of this method in predicting the buckling performances of the FGMs have been proved from this study.

The element-free kp-Ritz method combined with the first-order shear deformation shell theory and von Karman strains is another approach used for a post-buckling analysis of carbon nanotube reinforced functionally graded (CNTR-FG) cylindrical panels. The influence of volume fraction, length-to-thickness ratio, radius, boundary conditions, and distribution types of CNTs on the post-buckling behavior of the CNTR-FG panels are discussed in this study (Liew *et al.*, 2014). An extended work on the static and dynamic analyses on the CNTR-FG cylindrical panels revealed that the influencing parameters studied in the earlier paper have significant influences on the flexural strength and free vibration responses of the panels (Zhang *et al.*, 2014).

Approaches towards the prediction of fracture or damage characteristics of FGM structures have been reported in literature. The approaches basically are classified based on analytical (Delale and Erdogan, 1988; Bahr *et al.*, 2003; Chan *et al.*, 2008) and numerical (Tilbrook *et al.*, 2006; Sevcik *et al.*, 2009; Park *et al.*, 2009; Tang *et al.*, 2012) solutions. The analytical solution based on weight function was presented by Bahr *et al.* (2003) for the analysis of crack growth behaviors in FGMs with a rising crack growth resistance curve. Various stages of damages including vertical cracking, delamination, blistering and spall were identified in this study. Besides that, a mode-3 crack problem in an FGM model was developed by Chan *et al.* (2008) based on anisotropic strain-gradient elasticity theory. In this modelling, the crack formulations were solved using integral equation method.

2.3.3 Numerical Investigation on FGM

Previously, there are some numerical studies of thermal stress using FEM performed in order to find the optimum design of FGMs structures (Zhang et al., 2006; Lee et al., 2008; Park *et al.*, 2009). Many recent studies on the importance of joining two different materials while simultaneously eliminating or minimizing the sharp interfaces within the structures have been reported for the development of high quality FGMs. In the optimum design of FGMs, FEM has become among the best technique to model and predict the FGMs' thermal stresses. Park *et al.* (2009) has presented a crack-free joint between Al_2O_3 and Ni material which produced by controlling the composition of the inter-layers and optimizing the dispersion process. The work was inspired by the study made by Lee *et al.* (2008) which demonstrated the joining of two ceramic materials which is Si_3N_4 and Al_2O_3 using sialon polytypoid functional gradient joining. In the achievement, 15 layers of Si_3N_4 - Al_2O_3 FGM were obtained as the optimum number of layers for the materials combination. The computation of residual thermal stresses of some ceramic/metallic FGM system using FEM also reported in literature (Sarıkaya and Celik, 2002; Chen and Jie, 2007). In a most recent research, Bouchafa *et al.* (2010) have developed an analytical model which generated from the fabrication of exponential FGM (E-FGM) systems for the prediction of thermal residual stresses.

Tilbrook *et al.* (2006) predicted crack-tip stress fields and crack initiations on graded alumina/epoxy composites layers using FEM and showed good agreement with that observed experimentally. In a different study, Servick *et al.* (2009) have evaluated the stress intensity distribution simulated using 2-D FE model to predict crack propagating through FGM structure. Park *et al.* (2009) have estimated cracks in 10 layers Ni/ Al_2O_3 FGM by evaluating the residual stresses field calculated using a 2-D axisymmetric FE model. The results achieved numerically were highly matched with the experimental values.

In a most recent research, Tang *et al.* (2012) have investigated the failure criteria of HA/Ti FGM under the effect of structural defects using repeated unit cell approach. Using this approach, an FE FGM model was developed and the Ti materials was

defined as the matrix element. The matrix was modeled to be an isotropic hardening elastic plastic solid based on incremental J_2 theory of plasticity. The results achieved from this study revealed that the volume fraction of HA has a significant effect on the load-bearing capability of HA/Ti FGMs.

2.4 EXPERIMENTAL WORKS OF FGM

The experimental investigations for the characterization of FGMs' behaviors have been carried in line with the theoretical studies. The experimental works involve the samples preparation, characterization of metallurgical characteristics as well as the measurement of properties distribution of the materials. In order to determine the critical findings obtained on the FGMs' behaviours, this section includes a review on the experimental achievements implemented on the advanced materials.

2.4.1 Metallurgical Analysis

The microstructure profiles of FGMs can be characterized either by using optical microscope or SEM. The SEM is more preferable due to the higher resolution of the images and greater capability in capturing various elemental microstructure compared to the optical microscope. The metallurgical characters investigation can start from the characterization of the raw materials used for the preparation of FGM. Using SEM characterization, Sun *et al.* (2008) have determined the powder size distribution profile of Al_2O_3 (TMDAR a CR-15) and ZrO_2 (TZ3YS, CERAC-2003) powders. The single-peak and dual-peak micrographs obtained from the characterization of the four powders represent the agglomerate-free Al_2O_3 and agglomerate-rich ZrO_2 respectively. Balbinotti *et al.* (2011) have analysed the mean particle size of HA and Ti powders using SEM. The results showed that both powders have significantly different particle size distribution profile. Slosarczyk *et al.* (2010) have characterized the microstructure of undoped HA and HA with 0.5, 1.0 and 2.0 wt.% Ti surfaces before and after incubation in simulated body fluid (SBF) solution and distilled water by SEM. The analysis found that the Ti content interferes the growth in HA grains.

Pines and Bruck (2006) have observed the topology of a smooth FGM transition layers in Ni/Al₂O₃ FGM fabricated via pressure-less sintering method. The similar topology of HA/TiO₂ FGM was characterized by Fidancevska *et al.* (2007). Lee *et al.* (2008) have used optical micrographs to observe cracks at the cross section of hot pressed Si₃N₄-Al₂O₃ FGM samples. In the study, the number of layers of the crack-free FGM was reduced from 20 to 15 layers. Henriques *et al.* (2011) have presented the SEM and energy dispersive X-ray spectrometry (EDS) results on the inter-diffusion between Keramit and Ceramco3 mixtures. The analysis found that the diffusion rate of oxygen (one of the ceramic elements) was the highest in the metal side compared to other elements. The SEM equipped with an EDS also has been used by Refugio-Garcia *et al.* (2011) to observe the chemical composition in sintered Al₂O₃/Ti/TiN FGM. Three distinctive regions containing complete nitride metal particles, partially nitride particles and non nitride metallic particle were detected from this analysis (refer to Figure 2.3). The physical characteristics of MoSi₂ and SiC particles in SiC/MOSi₂ FGM sintered different temperatures were identified using EDS analysis (Chen *et al.*, 2012). The results indicated that the SiC particle disperse evenly in the MoSi₂ matrix after sintered at 1300 C for 1 h and 1550 C for 2 hrs. Ladkawala and Malik (2013) have observed the thick coating and packed sintered crystals morphology of HA/Ti FGM coating using SEM. The study detected that the low rate cooling after sintering at 950 C can cause crack initiation.

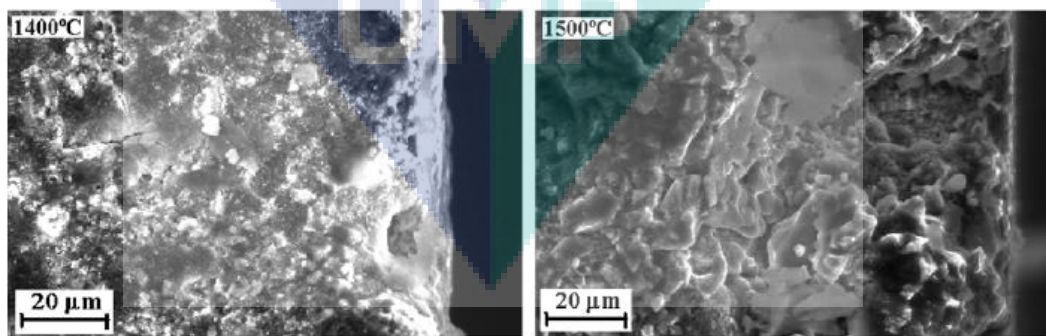


Figure 2.3: Scanning electron images of the Al₂O₃/Ti/TiN functional materials produced by nitriding Al₂O₃/Ti composites in ammonia salts at 570°C for 24hrs

Source: Refugio-Garcia *et al.*, 2011

XRD test is another metallurgical characterization technique that have been widely implemented by previous researchers. The diffracted intensities from some WC and Co lattice planes in the five homogeneous WC-Co samples were determined (Larsson and Oden, 2004; Dobrzanski *et al.*, 2011). The distinctive samples were identified by the Co content grain size profile. Chu *et al.* (2006) have detected the phase constitution of HA/Ti FGM prepared using hot pressing technique. The study confirmed that there is no reaction act during sintering and the base materials phases were dominant in the sintered FGM. Wang *et al.* (2010) have analysed the phase constitution of porous Ti-10Mg composite concentrated with NH_4HCO_3 where the main phases found on the composite were Ti and Mg. This analysis proved that the NH_4HCO_3 addition gives a little effect on the composite structure. Askari *et al.* (2012) have observed the phase constitution in $\text{Al}_2\text{O}_3/\text{SiC}/\text{ZrO}_2$ FGM prepared using HIP and EPD processes. The XRD results showed that the Al_2O_3 -SiC layer contains rhombohedral alumina and cubic silicon carbide phases while the Al_2O_3 -SiC and zirconia layer contain rhombohedral alumina, cubic silicon carbide, and tetragonal zirconia phases. This proved that there was no reaction between Al_2O_3 , SiC and ZrO_2 during the processing. Balbinotti *et al.* (2011) have observed the crystalline structure of sintered HA-Ti composites using the similar analysis. The XRD patterns obtained showed that the nanometric and micrometric HA powders exhibit a similar spectra. The impurities and solid solution content in the composites also have been detected from the results.

The XRD analysis also can be used to measure the residual stress of a material. This analysis however needs measurement of the diffractions line shift and the process will be easier when the lines are sharp. El-Desouky and El-Wazery (2013) have implemented XRD analysis to measure the residual stress of YSZ/Ni FGM. The residual stress found on the YSZ/50%Ni layer was 122 MPa. Dobrzanski *et al.* (2006) have used the inverse pole figures method to examine the texture of two FGM coatings. Using this method, the intensities were analyzed using $\{111\}$, $\{200\}$, $\{220\}$, and $\{311\}$ diffraction lines. The study found that the Zr/ZrN and Cr/CrN coatings exhibit the binary texture $\{100\} + \{111\}$ of the ZrN phase and uniform $\{100\}$ texture of the CrN phase respectively. Hilal *et al.* (2012) have used XRD and differential thermal analysis (DTA) to determine the interaction between zirconia and Hap materials during the sintering of phosphate/Y-PSZ composites. The study concluded that the sintering temperature and

compositional percentage are the two factors that influence the densification behaviour of the composites. Watari *et al.* (2004) have used X-ray scanning analytical microscope (XSAM) to analyse the compositional percentage of Ti/HAP FGM fabricated using sedimentation method. The compositional gradient at the FGM cross-section were determined by the percentage of the elements of the base materials shown by XSAM graphs.

An alternative method namely FTIR can provide detailed information in conjunction to the chemical structures of the analysed FGMs. Generally FTIR is used to confirm the existence of any impurities of chemical band inside the material. Using FTIR, Ye *et al.* (2009) and Silva and Carvalho (2003) have found the dehydroxylation rate of HA with respect to the sintering temperature which cannot be detected by XRD.

Some other metallurgical characterization techniques are including electron probe micro analysis (EPMA), differential thermal analysis (DTA) and transmission electron microscopy (TEM) analysis. EPMA has been used to prove the gradation in FGMs (Watari *et al.*, 2004; Shahrjerdi *et al.*, 2011). DTA has been used to identify the crystalline phase (Hilal *et al.*, 2012) and sintering schedule (Fidancevska *et al.*, 2007) of fired FGM samples. TEM analysis then is required for the metallurgical characterization of FGM composed of nano-metric powders (Balbinotti *et al.*, 2011).

2.4.2 FGM Properties Measurement

Various experimental analyses for the measurement of various mechanical and thermal properties of FGMs have been reported in literature. Generally, density or level of compactness of the material is measured right after the fabrication process completed. In addition, the density measurement also aims to quantify the porosity details in the structures (Bhattacharyya *et al.*, 2008). However for the application of FGM in human implants, aspect of pores is the important characteristic to be considered rather than the overall porosity (Batin *et al.*, 2011). During the manufacturing of FGMs, in addition to reduce the surface energy between the adjacent particles in the FGMs, the reason of implementing the heat treatment process is also to enhance the apparent density of the green compact.

The densification behaviour of the structures is determined by examining the porosity existence inside the bodies. The higher porosity level in a solid leads to the lower density of the structure. For FGMs, the bending strength of the structures is affected by the porosity (El-Wazery *et al.*, 2012). The structures with lower porosity exhibit higher bending strength. In comparison to homogeneous materials, FGMs generally have higher bending strength. However, the other factors leads to the higher strength of the FGMs in terms of well-dispersion and ideal joining between the heterogeneous layers need to be considered. The bulk density of sintered FGM samples often obtained using water immersion test which based on Archimedes principal (Matula and Dobrzanski, 2006; Refugio-Garcia *et al.*, 2011; Wang *et al.*, 2012). The density of distinctive layers inside the FGM can be obtained by measuring the density of the parts discretised based on the viewable different layer characteristics (Watanabe *et al.*, 2007). They observed the increasing density toward the inner region of Al-Al₂Cu FGM ring.

The most used technique for the measurement of FGMs hardness is Vicker's micro-hardness test (Askari *et al.*, 2012; Watanabe *et al.*, 2007; Dobrzanski *et al.*, 2011; Refugio-Garcia *et al.*, 2011; Shahrjerdi *et al.*, 2011). The micro-size indentation used in Vicker's hardness testing is practical and more preferable for the structure whose thickness is usually small like FGM. The other techniques that implement bigger indentation size such as Rockwell hardness (Fu *et al.*, 2012) and Brinell hardness (Watari *et al.*, 2004; Parvin and Rahimian, 2012) testings are still acceptable but not convenient for transverse cross-sectional hardness of sintered FGM. All the researchers reveal that hardness along the thickness of FGM varies with the different chemical composition and the change depends on the hardness of the constituents.

The variation of elastic modulus in FGMs can be measured directly by performing three-point bending test on the various non-graded composites specimens (Kumar and Wang, 2002; Fidancevska *et al.*, 2007; El-Desouky and El-Wazery, 2013). Henriques *et al.* (2011) have used the similar setup to measure the bonding strength of Keramit750/Ceramco3 FGM specimen. The ultimate load which can be held by the FGM due to three-point-bending indentation has been used to calculate the flexural strength of the material (Slosarczyk *et al.*, 2010; Bhattacharyya *et al.*, 2008). Besides

that the fracture toughness of the FGMs have been measured from the stress-strain curve obtained from three-point-bending test performed on specimen indented under certain load on the material surface (El-Desouky and El-Wazery, 2013; Larsson and Oden, 2004; Askari *et al.*, 2012; Watari *et al.*, 2004).

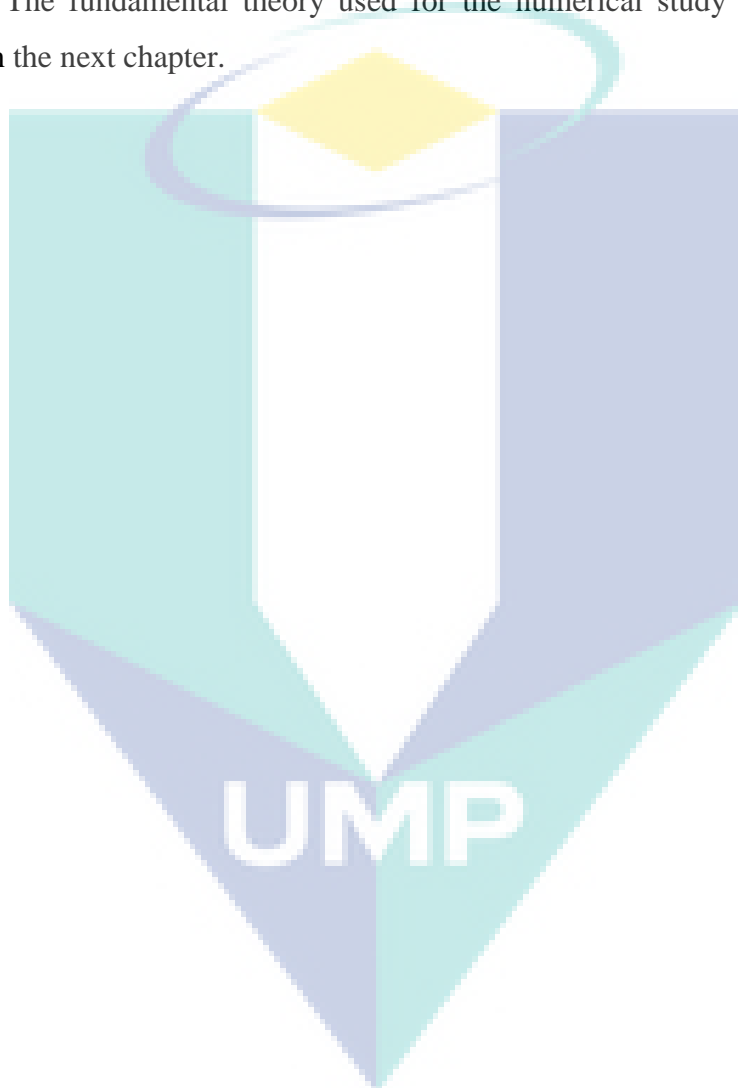
Another testing that often implemented by the previous researchers on FGMs is for the compressive strength measurement based on ASTM E9 standard (Parvin and Rahimian, 2012). Most researchers have used universal testing machine interfaced to a computer-related to the microstructure and phase variation in the composite for the testing (Batin *et al.*, 2011; Balbinotti *et al.*, 2011; Fidancevska *et al.*, 2007). Balbinotti *et al.* (2011) revealed that the compressive strength varies with microstructure and phase distribution in FGM when they found the decreasing compressive strength within increasing compositional percentage of HA in their HA/Ti FGM specimens.

In addition to the common mechanical testing explained previously, Dobrzanski *et al.* (2011) have performed the measurement of abrasive wear and brittleness performance of WC/Co FGM using some customized experimental setup. Besides that, Kumar and Wang (2002) have measured the stiffness of HA/Ti FGM specimen using continuous stiffness measurement (CSM) technique. For thermal behaviour measurement, Bhattacharyya *et al.* (2008) have conducted thermal shock treatment for thermal shock and fatigue performances and Fidancevska *et al.* (2012) have obtained the thermal expansion coefficient of FGM specimen using dilatometer.

2.5 CLOSURE

Review on some of the current achievements on FGMs' processing and behaviours have been presented covering both experimental and computational works. The literature review presents various processes and approaches to explore the development of a reliable and applicable FGM in engineering applications. From the theoretical perspective, the most pertinent works on FGM design and responses analyses were discussed. It is also observed from the literature that a rather scanty experimental work exists which cannot give a clear understanding on the FGM. Although the previous work have concerned various kinds of metal-ceramic

combination including HA and Ti, detail informations and data on the characteristics and processing technique of the HA/Ti FGM are very limited. A further research work is required in order to understand the HA/Ti FGM fabrication and behaviors more clearly. Hence, it is proposed to carry out a through and systematic numerical and experimental study to determine the characteristics of HA/Ti FGM under the effects of various design parameters, processing parameters as well as different loading conditions. The fundamental theory used for the numerical study of HA/Ti FGM is presented in the next chapter.



CHAPTER 3

THEORETICAL STUDIES

3.1 INTRODUCTION

The results of numerous studies in the preceding chapter have revealed that detailed theoretical and experimental research on FGMs is still lacking. Even though new findings are being made known which can help to improve the manufacturing and fabrication process of FGMs, the theory is still incomplete because of the complexity of the physics involved. The conclusive fundamental studies which cover the classical theory of the structural mechanics and the material properties of FGMs are discussed in detail throughout this chapter. The study of the mechanics of FGMs as multifunctional laminated composite materials containing various microstructures and compositions is at the level of enhancement and implementation. It is a rather complex problem that has challenged researchers in this field. Presently, although progress in the development of engineering mechanics of FGMs is noticeable, it does not claim to be exhaustive. As a result, broad investigations and studies on various topics in the mechanics of FGMs needs to be explored and established.

In theory, a significant feature of FGMs is highlighted when the physical behaviours of the structures are different from those of most common engineering materials without a graded profile. The composition and microstructure profiles of FGMs vary gradually along the thickness plane, which leads to the corresponding difference in the properties of the structures. From a theoretical perspective, the mechanics of a structure are mostly affected by elastic properties such as Young's modulus, the shear modulus and Poisson's ratio. Therefore, the stress-strain relations stimulated within various elastic properties are required to obtain the responses of FGMs subjected to certain loading conditions. The theoretical basis of FGMs, which

describes the consecutive relations between the ingredients and the responses under an equilibrium state, are presented in this section.

3.2 MATERIAL GRADIENT

As mentioned earlier, FGMs are microscopically inhomogeneous materials in which the properties vary continuously from one surface to the other. The schematic representation and structure configuration of a developed metal-ceramic FGM with a Cartesian coordinate of (O, x, θ, z) is depicted in Figure 3.1. It is shown that the pure layers with single-phase ingredients take place at the end surfaces of the structure. As the microstructural features and properties of these layers are homogeneous in all directions, the material properties at all coordinates inside the layers refer to the properties of the base materials. Unlike the properties at the end surfaces, the variation in composition and microstructure along the orthogonal plane of the intermediate layers reflects various corresponding properties. Realistic assumptions of the behaviours of the FGM layers need appropriate consecutive relations containing approximated thermo-physical property data. The estimation process is quite complicated since the fabrication process and the utilization of FGMs definitely involve significant temperature changes. To date, the empirical properties data of FGMs is often limited because various measurements are required to define the temperature-dependent properties of multiphase materials.

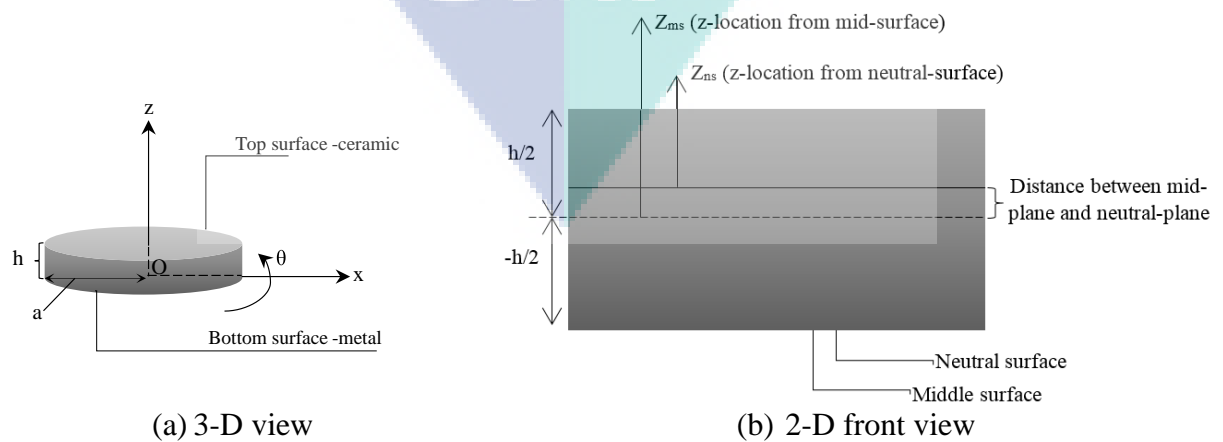


Figure 3.1: The geometry configuration of a metal-ceramic FGM plate

3.2.1 Prediction of Effective Thermo-mechanical Properties

Defining the material-property gradient for the FGM layers starts with an analysis of the volume fractions of the constituents. Volume fraction is the most important parameter that affects the material-property variation in multiphase materials. By taking n as the grading parameter, the volume fractions along the thickness of the FGM are written as:

$$v(z) = \left(\frac{z + \frac{h}{2}}{h} \right)^n \quad (3.1)$$

For metal-ceramic FGM case, the volume fraction of the composed materials leads to either metal or ceramic phase domination in each FG layer. The sum of each constituent mixing ratio will fulfill the following expression:

$$v_m(z) + v_c(z) = 1 \quad (3.2)$$

Since the FG structure contains various two-phase compositions, it is sufficient to analyze the volume fraction of only one of the constituents (Miyamoto *et al.*, 1999). It should be noted that the existence of naturally inherent phases, such as residual porosity can be considered as the third phase in the composition, which has been neglected throughout numerical studies. This is because the theoretical analysis assumes the FGM structure as a solid object without any porosity.

A review of the theoretical approaches to predict the material-property variation in FGMs has been presented in Chapter 2. Since the empirical properties data for the effective materials is limited, the implementation of the formulations which consider the interaction and dispersion of the bulk constituent phases is almost impossible for present study. By neglecting the interaction and dispersion of the constituents' particles effects (and taking v_f as the volume fraction of ceramic constituent) the ROM equation for the material-property (ξ) definition is written as:

$$\xi(z) = (\xi_c(z) - \xi_m(z))v_f + \xi_m(z) \quad (3.3)$$

Unlike the other properties, the Poisson ratio for each distinctive FGM layers was taken as constant by some of the previous researchers (Shen and Noda, 2005; Lee *et al.*, 2008; Alshorbagy *et al.*, 2013). This was due to the effect of the small variation in Poisson's ratio values in comparison to the elastic properties variation. In fact varying or fixing the Poisson ratio through the thickness plane of the FGM structure does not affect the analysis results (Ghanbari and Shafiee, 2013). The constant Poisson's ratio value which represents the overall Poisson's ratio of the FGM structure is calculated using MROM formulation, which written as:

$$v = \frac{3B - 2\mu}{2(3B + \mu)} \quad (3.4)$$

Each of these properties can be defined respectively using the homogenization method (Mori and Tanaka, 1973) expressed as follows:

$$\frac{B - B_c}{B_m - B_c} = \frac{v_m}{1 + \frac{(1 - v_m)(B_m - B_c)}{B_c + \frac{4}{3}\mu_c}} \quad (3.5)$$

$$\frac{\mu - \mu_c}{\mu_m - \mu_c} = \frac{v_m}{1 + \frac{(1 - v_m)(\mu_m - \mu_c)}{\mu_c + f_c}} \quad (3.6)$$

where f_c is given by the following equation:

$$f_c = \frac{\mu_c(9B_c + 8\mu_c)}{6(B_c + 2\mu_c)} \quad (3.7)$$

For the FGMs subjected to thermal effects, thermal conductivity at a certain thickness location based on linear ROM is calculated as:

$$k(z) = k_t + (k_b - k_t) \left(\frac{z + \frac{h}{2}}{h} \right)^n \quad (3.8)$$

In addition to the prediction based on theoretical approaches, the material properties of FGMs also can be measured experimentally. In some cases where complete experimental material-property data cannot be achieved, combining the limited empirical data with the theoretical approaches is possible in order to estimate the material properties (Miyamoto *et al.*, 1999). From a practical perspective, the evaluation of the effective performance of FGMs is complicated in comparison to that of the homogeneous composite materials. The characterization of the spatial variation in the material properties at a local region of the FGM becomes difficult when some modifications are required in the measurement technique. To date most of the methods explored in an attempt to characterize the material properties of FGMs still need to be standardized due to their complexity. The results of experimental testing are required to calculate the properties of the material. The equations used to determine the basic properties of FGMs using experimental methods are shown and discussed in the following sections.

3.2.2 Basic FGM's Properties

Density

The method that has been widely used to check the level of compactness or density of FGMs before and after sintering is based on Archimedes' Principle, which is given by the following equation:

$$F_B = m_l g \quad (3.9)$$

where F_B , m_l and g are the upward force, mass of immersed liquid and gravitational acceleration respectively.

The mass of immersed liquid measured using Equation 3.9 is consequently used to calculate the density of the FGM using the following general formula:

$$\rho = \frac{m_1}{\Lambda_1} \quad (3.10)$$

where Λ_1 represents the volume of the immersed liquid.

Hardness

The hardness at the thickness plane of FGMs is affected by their composition and microstructure profiles at the distinctive layers (Watanabe *et al.*, 2007). The hardness of the green compact and heat-treated FGMs are different since the microstructure morphological conditions change due to the sintering process. The hardness of both green compact and sintered FGMs with uniform and homogeneous morphological profiles are measured using a micro-indentation method known as Vickers micro-hardness. Figure 3.2 depicted the flow of Vicker's micro-hardness and a schematic configuration of the load and indenter displacements is considered in the measurement.

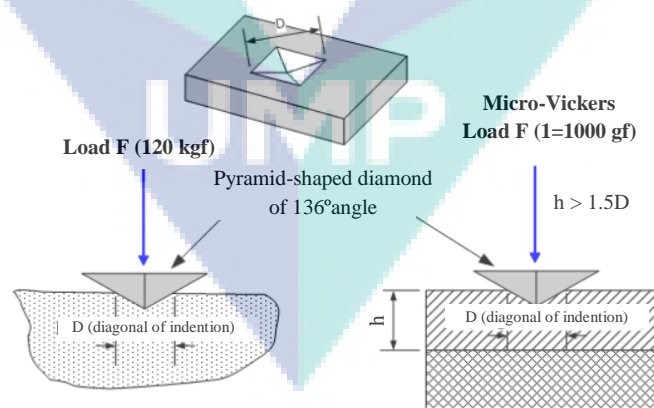


Figure 3.2: Schematic diagram of Vicker's micro-hardness testing

Source: Kopeliovich, 2014

The micro-hardness of the material is determined based on the following formulation:

$$HV = \frac{P_{\max}}{A} \quad (3.11)$$

where P_{\max} and A are the maximum load applied to the material's surface and the area of indentation respectively.

The contact area of the indenter and the material surface is found in a diamond cross-sectional shape as shown in Figure 3.3. In the characterization process, lengths of the middle vertical and horizontal planes of the diamond imprint are measured for the contact area calculation.

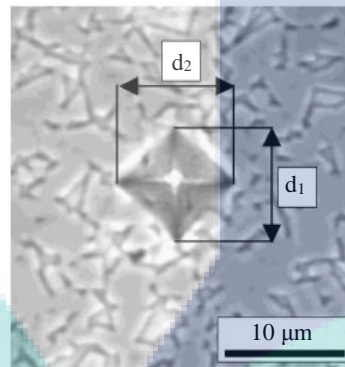


Figure 3.3: Schematic illustration of the contact area of the indenter and material

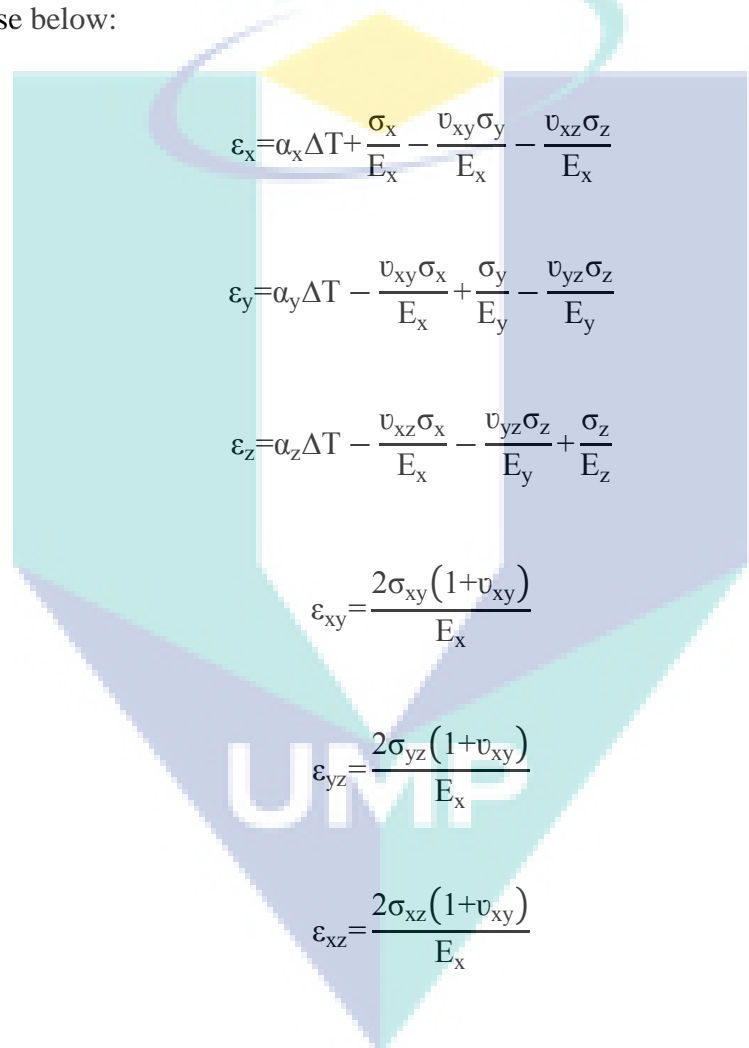
Source: Larsson and Oden, 2004

3.3 THEORETICAL FORMULATIONS

The strength of a material is the most important behaviour that can show its potential for certain applications. This behaviour is highly dependant on its structural responses such as temperature, displacement as well as stresses distribution profiles under an applied loading condition. The evaluation of these responses leads to a clear understanding of the mechanics of the FGM and its capability in a designated application. The fundamental formulations for the determination of various responses of the FGM under static loading will be shown and discussed in this section.

3.3.1 Stress-strain Relationships

When any load is applied to a structure, it tends to form a deformation. For FGMs, the responses at the local coordinate on the structures after deformation are different due to the various compositions and microstructures which correspond to different behaviours along the gradient plane. The material relationships can be described from the definition of strain components at different Cartesian axes (x, y, z) such as those below:



$$\begin{aligned}
 \varepsilon_x &= \alpha_x \Delta T + \frac{\sigma_x}{E_x} - \frac{\nu_{xy} \sigma_y}{E_x} - \frac{\nu_{xz} \sigma_z}{E_x} \\
 \varepsilon_y &= \alpha_y \Delta T - \frac{\nu_{xy} \sigma_x}{E_x} + \frac{\sigma_y}{E_y} - \frac{\nu_{yz} \sigma_z}{E_y} \\
 \varepsilon_z &= \alpha_z \Delta T - \frac{\nu_{xz} \sigma_x}{E_x} - \frac{\nu_{yz} \sigma_z}{E_y} + \frac{\sigma_z}{E_z} \\
 \varepsilon_{xy} &= \frac{2\sigma_{xy}(1+\nu_{xy})}{E_x} \\
 \varepsilon_{yz} &= \frac{2\sigma_{yz}(1+\nu_{xy})}{E_x} \\
 \varepsilon_{xz} &= \frac{2\sigma_{xz}(1+\nu_{xy})}{E_x}
 \end{aligned} \tag{3.12}$$

where ΔT is the change in material temperature and is given by the following equation:

$$\Delta T = T - T_{\text{ref}} \tag{3.13}$$

The corresponding stress components related to the strain components, defined previously, are expressed as:

$$\begin{aligned}
\sigma_x &= \frac{E_x}{\hat{h}} \left(1 - (v_{yz})^2 \frac{E_z}{E_y} \right) (\epsilon_x - \alpha_x \Delta T) + \frac{E_y}{\hat{h}} \left(v_{xy} + v_{xz} v_{yz} \frac{E_z}{E_y} \right) (\epsilon_y - \alpha_y \Delta T) + \\
&\quad \frac{E_z}{\hat{h}} (v_{xz} + v_{yz} v_{xy}) (\epsilon_z - \alpha_z \Delta T) \\
\sigma_y &= \frac{E_y}{\hat{h}} \left(v_{xy} + v_{xz} v_{yz} \frac{E_z}{E_y} \right) (\epsilon_x - \alpha_x \Delta T) + \frac{E_y}{\hat{h}} \left(1 - (v_{xz})^2 \frac{E_z}{E_x} \right) (\epsilon_y - \alpha_y \Delta T) + \\
&\quad \frac{E_z}{\hat{h}} (v_{yz} + v_{xz} v_{xy} \frac{E_y}{E_x}) (\epsilon_z - \alpha_z \Delta T) \\
\sigma_z &= \frac{E_z}{\hat{h}} (v_{xz} + v_{yz} v_{xy}) (\epsilon_x - \alpha_x \Delta T) + \frac{E_z}{\hat{h}} \left(v_{yz} + v_{xz} v_{xy} \frac{E_y}{E_x} \right) (\epsilon_y - \alpha_y \Delta T) + \\
&\quad \frac{E_z}{\hat{h}} \left(1 - (v_{xy})^2 \frac{E_y}{E_x} \right) (\epsilon_z - \alpha_z \Delta T) \\
\sigma_{xy} &= \frac{E_x}{2(1+v_{xy})} \epsilon_{xy} \\
\sigma_{yz} &= \frac{E_x}{2(1+v_{xy})} \epsilon_{yz} \\
\sigma_{xz} &= \frac{E_x}{2(1+v_{xy})} \epsilon_{xz}
\end{aligned} \tag{3.14}$$

where \hat{h} is calculated as:

$$\hat{h} = 1 - (v_{xy})^2 \frac{E_y}{E_x} - (v_{yz})^2 \frac{E_z}{E_y} - (v_{xz})^2 \frac{E_z}{E_x} - 2v_{xy}v_{yz}v_{xz} \frac{E_z}{E_x} \tag{3.15}$$

The strain and stress components are required for the determination of the system equilibrium using the strain energy formulation. The principle of virtual work expresses that a change in the internal strain energy can be obtained by an identical variation in the external work induced by the applied loads, such as:

$$\delta\check{U}=\delta V \quad (3.16)$$

The strain energy in terms of strain and stress components are written as:

$$\delta\check{U}_1 = \int_{\Lambda} \{\delta\varepsilon\} \{\sigma\} d(\Lambda)^T \quad (3.17)$$

where $\{\varepsilon\}$ and $\{\sigma\}$ are the strain and stress vectors respectively whereas Λ is the volume of element. Another strain energy which considers a surface which acts against a uniform resistance is expressed as:

$$\delta\check{U}_2 = \int_{A_-} \{\delta w_-\}^T \{\sigma\} d(A_-) \quad (3.18)$$

where $\{w_-\}$ and A_- are representing the motion transverse to the surface and the area of the uniform resistance respectively.

In the definition of the external work acting on the model, the inertial effects will be considered first as following:

$$\delta V_1 = - \int_{\Lambda} \{\delta w\}^T \frac{\{F^a\}}{\Lambda} d(\Lambda) \quad (3.19)$$

where $\{F^a\}$ is defined as the acceleration (D'Alembert principle) force vector. By taking ρ and t as the density and time respectively, the $\{F^a\}$ is determined based on Newton's second law of motion as:

$$\{F^a\} = \Lambda \rho \frac{\partial^2}{\partial t^2} \{w\} \quad (3.20)$$

where $\{w\}$ is the vector of displacement of general point. The formulation for the work done by the pressure load is given as:

$$\delta V_2 = - \int_{A_p} \{\delta w_{-}\}^T \{P\} d(A_p) \quad (3.21)$$

where $\{P\}$ and A_p represent the applied pressure vector and the area on which the pressure is given respectively. Another equation for the work done by external force is expressed as:

$$\delta V_3 = \{\delta u\}^T \{F_{\epsilon}^{nd}\} \quad (3.22)$$

where $\{F_{\epsilon}^{nd}\}$ is the nodal forces acting on the element.

3.3.2 Thermal field of FGM

Predicting the temperature distribution within a structure is essential in highlighting the thermal-dependent behaviours of many engineering materials. The information about thermal distribution is essential as it is the input required for the simulation of heat flow inside or outside the structure. The heat flux due to conduction activity is defined as:

$$q = -k \frac{dT}{dz} \quad (3.23)$$

The heat conduction through FGMs is strongly dependant on the variation of thermal conductivity through the gradient plane. Detailed explanation of the heat conduction phenomena is described in the next chapter.

3.4 CLOSURE

In this chapter, the fundamental theory of the mechanics of FGMs has been presented and discussed. The next chapter focuses on the finite element formulation and analyses of the optimization of the FG plate design, as well as the simulation of the thermal, displacement and stress responses of the HA/Ti FGM subjected to various loading conditions using ANSYS software.

CHAPTER 4

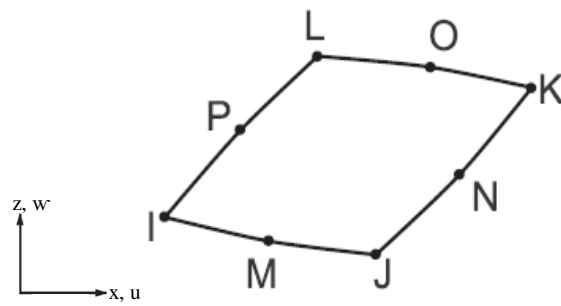
NUMERICAL INVESTIGATION

4.1 INTRODUCTION

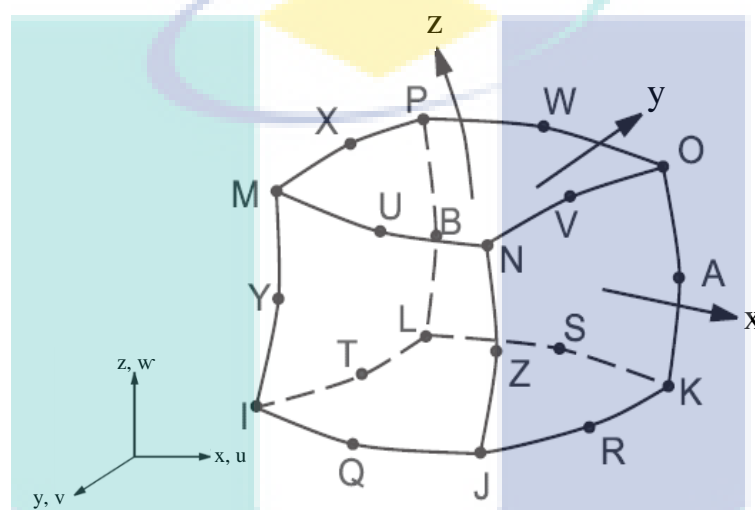
With the growth in computer and software technologies the use of numerical simulation tools for the analysis and optimization of materials and structures has become widespread. For FGMs, modelling is very important from an early stage of the analysis since various problems occur because of the uncertain dependence of elastic properties on the various compositions found along the gradient plane. Currently, the numerical investigation of HA/Ti FGMs plate is performed using the FE method. The numerical work focusses on determining the optimized design parameters of the FGM specimen, followed by an investigation into the behaviour of the plate as a result of various applied loads. In this chapter, the FE formulations used for the simulation will be discussed, followed by a detailed explanation of the 2-D and 3-D models (Khonke, 2013). The 2-D model is used to optimize the FGM design parameters and the 3-D model, is used to analyze the behaviours of the FGM plate under constant functional mechanical, thermal and thermo-mechanical loading. In order to ensure the reliability of the models when simulating the problems found in FGMs, verification is shown and discussed.

4.2 FINITE ELEMENT FORMULATIONS

Numerical analysis using ANSYS provides various types of elements for the analysis of laminated composites structures. Figure 4.1 shows two element types used in the present study. At an initial stage of the analysis, the shape functions of these elements are required to determine the displacement function.



(a) 8-node quadrilateral solid element



(b) 20-node brick solid element

Figure 4.1: Element types

The shape function of the axisymmetric 8-node quadrilateral element is given as:

$$N = \frac{1}{4} (N_I(1-x)(1-y)(-x-y-1) + N_J(1+x)(1-y)(x-y-1) + N_K(1+x)(1+y)(x+y-1) + N_L(1-x)(1+y)(-x+y-1)) + \frac{1}{2} (N_M(1-x^2)(1-y) + N_N(1+x)(1-y^2) + N_O(1-x^2)(1+y) + N_P(1-x)(1-y^2)) \cos \theta \quad (4.1)$$

where N can represent u and T for the translation in the x -directions and temperature, respectively. N which represents w for the translation in the z -direction is written as:

$$N = \frac{1}{4} (N_I(1-x)(1-y)(-x-y-1) + N_J(1+x)(1-y)(x-y-1) + N_K(1+x)(1+y)(x+y-1) + N_L(1-x)(1+y)(-x+y-1))$$

$$\frac{(-x+y-1)+\frac{1}{2}(N_M(1-x^2)(1-y)+N_N(1+x)(1-y^2)+N_O(1-x^2)(1+y)+N_P(1-x)(1-y^2))}{\sin \ell \gamma} \quad (4.2)$$

ℓ refers to the input quantity on MODE command in ANSYS and when $\ell=0$, $\cos \ell \gamma = \sin \ell \gamma = 1$. The shape function of the 20-node brick element is provided as:

$$\begin{aligned} N = & \frac{1}{8}(N_I(1-x)(1-y)(1-z)(-x-y-z-2)+N_J(1+x)(1-y)(1-z)(x-y-z-2)+N_K(1+x)(1+y)(1-z) \\ & (x+y-z-2)+N_L(1-x)(1+y)(1-z)(-x+y-z-2)+N_M(1-x)(1-y)(1+z)(-x-y+z-2)+N_N(1+x) \\ & (1-y)(1+z)(x-y+z-2)+N_O(1+x)(1+y)(1+z)(x+y+z-2)+N_P(1-x)(1+y)(1+z)(-x+y+z-2)) \\ & + \frac{1}{4}(N_Q(1-x^2)(1-y)(1-z)+N_R(1+x)(1-y^2)(1-z)+N_S(1-x^2)(1+y)(1-z)+N_T(1-x)(1-y^2) \\ & (1-z)+N_U(1-x^2)(1-y)(1+z)+N_V(1+x)(1-y^2)(1+z)+N_W(1-x^2)(1+y)(1+z)+N_X(1-x) \\ & (1-y^2)(1+z)+N_Y(1-x)(1-y)(1-z^2)+N_Z(1+x)(1-y)(1-z^2)+N_A(1+x)(1+y)(1-z^2)+N_B(1-x) \\ & (1+y)(1-z^2) \end{aligned} \quad (4.3)$$

where N can represents u, v, w and T. v is the translation in y-direction.

4.2.1 Structural Analysis

Structural analysis shows the computation of the displacement and stresses responses of a body subjected to certain loading conditions. The finite element formulation for this analysis is derived initially by calculating the displacement field. In this situation displacement is interpreted in term of the elongation or strain of the body. By taking the strain components as defined in Equation 3.12 (see Chapter 3), the total strain vectors, $\{\varepsilon\}$ are determined as:

$$\{\varepsilon\} = [\varepsilon_x \quad \varepsilon_y \quad \varepsilon_z \quad \varepsilon_{xy} \quad \varepsilon_{yz} \quad \varepsilon_{xz}]^T = \{\varepsilon^E\} + \{\varepsilon^T\} \quad (4.4)$$

where $\{\varepsilon^E\}$ and $\{\varepsilon^T\}$ refer to the elastic and thermal strain vectors respectively. These variables are determined as:

$$\{\varepsilon^T\} = \Delta T [\alpha_x^{se} \quad \alpha_y^{se} \quad \alpha_z^{se} \quad 0 \quad 0 \quad 0]^T \quad (4.5)$$

$$\{\varepsilon^d\} = [B]\{u\} - \{\varepsilon^T\} \quad (4.6)$$

where α_x^{se} , α_y^{se} and α_z^{se} represent the secant coefficient of the thermal expansion in the directions of x, y and z respectively, while [B] and {u} represent the strain-displacement matrix and the nodal displacement vectors. The strain vector is related to the stress and material matrix by:

$$\{\varepsilon\} = \{\varepsilon^T\} + [D]^{-1}\{\sigma\} \quad (4.7)$$

where $\{\sigma\}$ and $[D]^{-1}$, which represents the stress vector (see Equation 3.14 in Chapter 3 for stress components equations) and the inverse elasticity matrix, are written respectively as:

$$\{\sigma\} = [\sigma_x \quad \sigma_y \quad \sigma_z \quad \sigma_{xy} \quad \sigma_{yz} \quad \sigma_{xz}]^T = [D]\{\varepsilon^d\} \quad (4.8)$$

$$[D]^{-1} = \begin{bmatrix} 1/E_x & -\nu_{xy}/E_x & -\nu_{xz}/E_x & 0 & 0 & 0 \\ -\nu_{yx}/E_y & 1/E_y & -\nu_{yz}/E_y & 0 & 0 & 0 \\ -\nu_{zx}/E_z & -\nu_{zy}/E_z & 1/E_z & 0 & 0 & 0 \\ 0 & 0 & 0 & 2(1+\nu_{xy})/E_x & 0 & 0 \\ 0 & 0 & 0 & 0 & 2(1+\nu_{xy})/E_x & 0 \\ 0 & 0 & 0 & 0 & 0 & 2(1+\nu_{xy})/E_x \end{bmatrix} \quad (4.9)$$

For the analysis of an axisymmetric model, the orthotropic material property, P transformation is calculated from the cylindrical system with a coordinate system (R, θ , Z) related to the x, y, z system by taking $P_R = P_x$, $P_\theta = P_z$ and $P_Z = P_y$.

Continuing the formula derivation with the assumption that the geometry and material are linear, the matrix element is included in the internal strain energy components general equation in Equations 3.16 and 3.17 as followings:

$$\delta\check{U}_1 = \int_{\Lambda} (\{\delta\varepsilon\}^T [D] \{\varepsilon\} - \{\delta\varepsilon\}^T [D] \{\varepsilon^T\}) d(\Lambda) \quad (4.10)$$

$$\delta\check{U}_2 = \{\delta u\}^{Tk} \int_{A_-} [N_-]^T [N_-] d(A_-) \{u\} \quad (4.11)$$

where $[N_-]$ represents the matrix of the shape functions for transverse motions at the surface and k is the foundation stiffness in units of force per length per unit area. By taking $[N]$ as the matrix of the shape functions, the external works components, when related to the material matrix, are expressed as:

$$\delta V_1 = -\{\delta u\}^T \rho \int_{\Lambda} [N]^T [N] d(\Lambda) \frac{\delta^2}{\delta t^2} \{u\} \quad (4.12)$$

$$\delta V_2 = \{\delta u\}^T \int_{A_p} [N] \{P\} d(A_p) \quad (4.13)$$

Finally, the equation for the equilibrium condition representing the virtual work of the system is determined by combining Equations 4.10-4.13 as follows:

$$\{\delta u\}^T \int_{\Lambda} [B]^T [D] [B] d(\Lambda) \{u\} - \{\delta u\}^T \int_{\Lambda} [B]^T [D] \{\varepsilon^T\} d(\Lambda) + \{\delta u\}^{Tk} \int_{A_-} [N_-]^T [N_-] d(A_-) \{u\} - \{\delta u\}^T \rho \int_{\Lambda} [N]^T [N] d(\Lambda) \frac{\delta^2}{\delta t^2} \{u\} + \{\delta u\}^T \int_{A_p} [N] \{P\} d(A_p) + \{\delta u\}^T \{F_{\varepsilon}^{nd}\} \quad (4.14)$$

In a case where combined stresses are considered, the principal stresses, represented as $(\sigma_1, \sigma_2, \sigma_3)$, are computed as:

$$\begin{bmatrix} \sigma_x - \sigma_0 & \frac{1}{2} \sigma_{xy} & \frac{1}{2} \sigma_{xz} \\ \frac{1}{2} \sigma_{xy} & \sigma_y - \sigma_0 & \frac{1}{2} \sigma_{yz} \\ \frac{1}{2} \sigma_{xz} & \frac{1}{2} \sigma_{yz} & \sigma_z - \sigma_0 \end{bmatrix} = 0 \quad (4.15)$$

where σ_O is the principal stress. The von-Mises, or equivalent stress, and the stress intensity are calculated respectively as:

$$\sigma_{VM} = \left(\frac{1}{2} [(\sigma_1 - \sigma_2)^2 + (\sigma_2 - \sigma_3)^2 + (\sigma_3 - \sigma_1)^2] \right)^{\frac{1}{2}} \quad (4.16)$$

$$K = \text{MAX}(|\sigma_1 - \sigma_2|, |\sigma_2 - \sigma_3|, |\sigma_3 - \sigma_1|) \quad (4.17)$$

4.2.2 Thermal Analysis

Thermal analysis is implemented to compute the thermal field profile in a body under thermal excitation. The theory behind this computation begins with the calculation of the heat flow rate using Equation 3.23 presented in Chapter 3. The heat flux then is related to the temperature gradient using Fourier's law and this is shown as:

$$\{q\} = -[D_T]\{G\}T \quad (4.18)$$

where the conductivity matrix, $[D_T]$ and thermal gradient vector, $\{G\}T$ are defined as:

$$[D_T] = \begin{bmatrix} k_{xx} & 0 & 0 \\ 0 & k_{yy} & 0 \\ 0 & 0 & k_{zz} \end{bmatrix} \quad (4.19)$$

$$\{G\}T = \left[\frac{\partial T}{\partial x} \quad \frac{\partial T}{\partial y} \quad \frac{\partial T}{\partial z} \right]^T = [B_T]\{T_\varepsilon\} \quad (4.20)$$

where $[B_T]$ is the thermal strain-displacement matrix and $\{T_\varepsilon\}$ is the nodal temperature vector of element. Heat flux is further considered to determine heat energy and can be, written as following:

$$\ddot{q} = \rho c \left(\frac{\partial T}{\partial t} + \{y\}^T \{G\}T \right) + \{G\}^T \{q\} \quad (4.21)$$

where c and \ddot{q} are negligible for a steady-state analysis. The velocity vector for mass heat transportation, $\{y\}$ is defined as:

$$\{y\} = \begin{Bmatrix} y_x \\ y_y \\ y_z \end{Bmatrix} \quad (4.22)$$

4.2.3 Thermal-Structural Analysis

The consecutive equations for coupled thermal and structural analysis are expressed as:

$$\{\varepsilon\} = [D]^{-1} \{\sigma\} + \{\alpha\} \Delta T \quad (4.23)$$

$$S = \{\alpha\}^T \{\sigma\} + \frac{\rho C_p}{T_0} \Delta T \quad (4.24)$$

S , C_p , ρ and T_0 are the entropy density, specific heat at constant stress or pressure, density and absolute reference temperature, respectively. Thermoelastic strain is related to the corresponding stress as:

$$\{\sigma\} = [D] \{\varepsilon\} - \{\beta\} \Delta T \quad (4.25)$$

where $\{\beta\}$ is the vector of the thermoelastic coefficients. Based on the second law of thermodynamics the relationship between density entropy and heat density, Q is represented as:

$$Q = T_0 S \quad (4.26)$$

By substituting Equation 4.24 in Equation 4.26, the heat density equation produces:

$$Q = T_0 \{\beta\}^T \{\varepsilon\} + \rho C_v \Delta T \quad (4.27)$$

C_v refers to the specific heat at constant strain or volume. This equation is subsequently associated with the heat flow equation and it provides:

$$\frac{\partial Q}{\partial t} = T_0 \{\beta\}^T \frac{\partial \{\varepsilon\}}{\partial t} + \rho C_v \frac{\partial (\Delta T)}{\partial t} - [D_T] \nabla^2 T \quad (4.28)$$

where $\nabla^2 T$ is the thermal gradient.

The strain energy equation for static coupled thermo-elastic analysis is written as:

$$\check{U}_t = \frac{1}{2} \int_{\Lambda} \{\sigma\}^T \{\varepsilon\} d\{\Lambda\} \quad (4.29)$$

4.3 2-D ANALYSIS FOR THE OPTIMIZATION OF FGM DESIGN

The design of an FGM can be considered in different physical parameters, such as its thickness, the number of layers, grading index, grain size and porosity. Each of these parameters has its own significant effect on FGM design. In this study, the optimum thickness, number of layers and grading index of the cylindrical FGM specimen used in the experimental work were determined using a 2-D FE model. The effects of these parameters on the FGM were studied by evaluating the computed thermal residual stresses distribution of FGM structures with varying design parameters.

The development of the model began with the identification of the FGM's cross-sectional area in order to analyze and calculate the material properties at distinctive layers of the FGM structure. In this study, the cylindrical shape of the FGM specimen was transformed into 2-D axisymmetric model as depicted in Figure 4.2. In addition, by assuming that the two constituents' particles are well-dispersed and ideally joined, the position-dependent material properties were calculated based on a ROM formulation (see Equation 3.3). The geometry of the cross-sectional area selected for the analysis and the typical material properties at different FGM layers were defined as the inputs for the analysis. Before defining the boundary conditions, the model was discretised into 8-node SOLID273 elements, as defined in ANSYS library with a 0.1 mm mesh size. The configuration of the elements used in the analysis are shown in Figure 4.1(a). Although only the axisymmetric cross-sectional area of the cylindrical FGM was considered during the analysis, deformations at certain coordinates on the structure can

be non-axisymmetric. SOLID273 was selected for this analysis since it can support all nonlinearities existing in the analysis. In addition to the displacement boundary, thermal boundary conditions were also defined based on the assumption that the thermal residual stresses occurred during the cooling stage of the sintering process. Finally, by taking into account the behaviours of the metal and ceramic compositions in FGMs, the residual stresses were interpreted in terms of von-Mises and principal stresses. For the optimization of the FGM design parameters, the FE analysis had to be repeated with different design parameters as the inputs. The parameters used in the design of the FGM with the smallest thermal residual stress peak and the maximum relaxation in thermal residual stresses distribution were considered the optimum design parameters. The overall simulation method flow for the 2-D analysis is given in Figure 4.3.

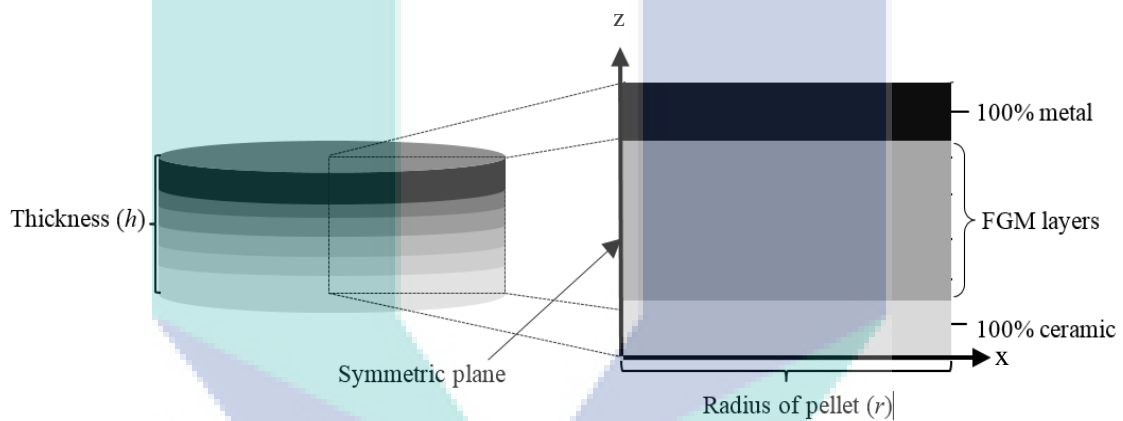


Figure 4.2: Transformation of the cylindrical FGM plate into a 2-D axisymmetric model

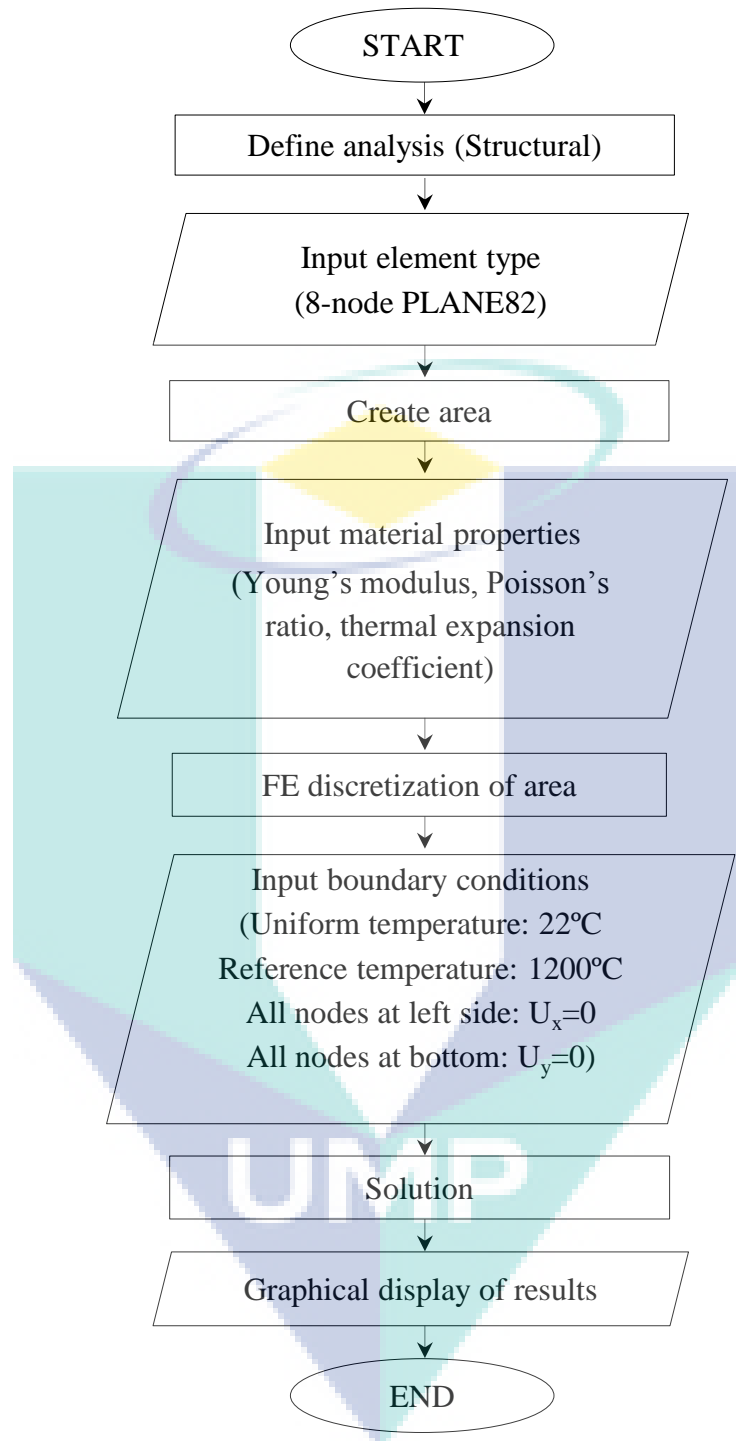


Figure 4.3: Flowchart of the 2-D FE optimization analysis

4.4 3-D ANALYSIS OF FGM PLATE RESPONSES

In addition to the main aim, which is to operate in a high temperature environment, FGMs are also constructed to be utilized in many applications where various energy sources affect the structures. In this study, the effects of mechanical, thermal and thermo-mechanical loadings on the responses of HA/Ti FGMs were calculated using a 3-D FE model. The numerical investigation started with an analysis of the FGM plate subjected to mechanical and thermal loadings, followed by thermo-mechanical loading. The responses of the FGM are examined for different loading conditions and different grading indices. A detailed explanation of the simulation method for each condition will be described in the following subsections.

4.4.1 Isothermal Loading

In this analysis, the FGM plate was subjected to uniform loading at the pure ceramic surface as shown in Figure 4.4. The model was designed to be in a cylindrical shape with eight overlapping layers. The elastic properties for each layer were calculated based on ROM, except Poisson's ratio, which is included as the input for the modelling. The Poisson's ratio was assumed to be constant and was calculated using Equation 3.4. The FGM cylindrical plate was then discretised into a 20-node Bricks quadratic (see Figure 4.1(b)) element with 0.1 mm mesh size. The boundary conditions of the model were defined based on simply supported circumstances. The mechanical load was then applied prior to the solution run.

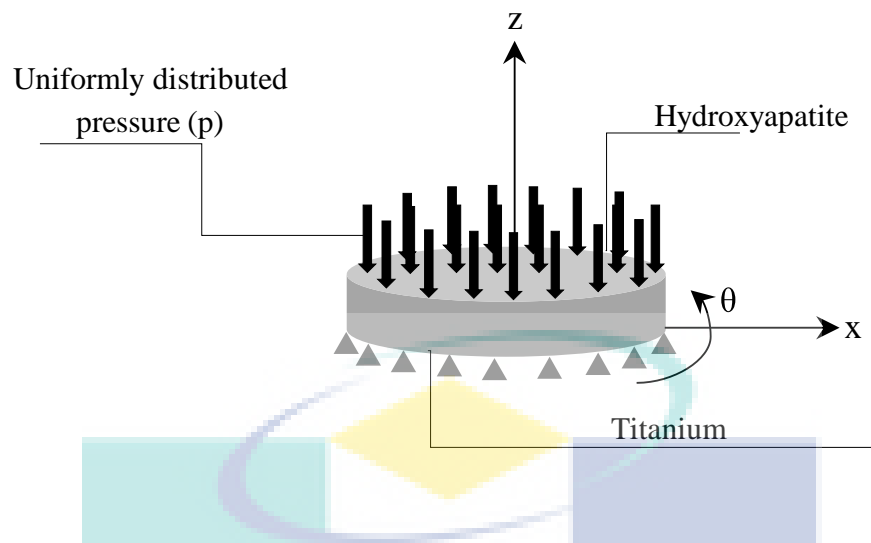


Figure 4.4: Schematic diagram of the FGM plate subjected to mechanical loading analysis

Among the results that could be obtained from the analysis were the displacements, stresses and strains of the FGM plate. The flow of the overall simulation method for investigating the mechanical characteristics of the FGM plate is illustrated in Figure 4.5.

UMP

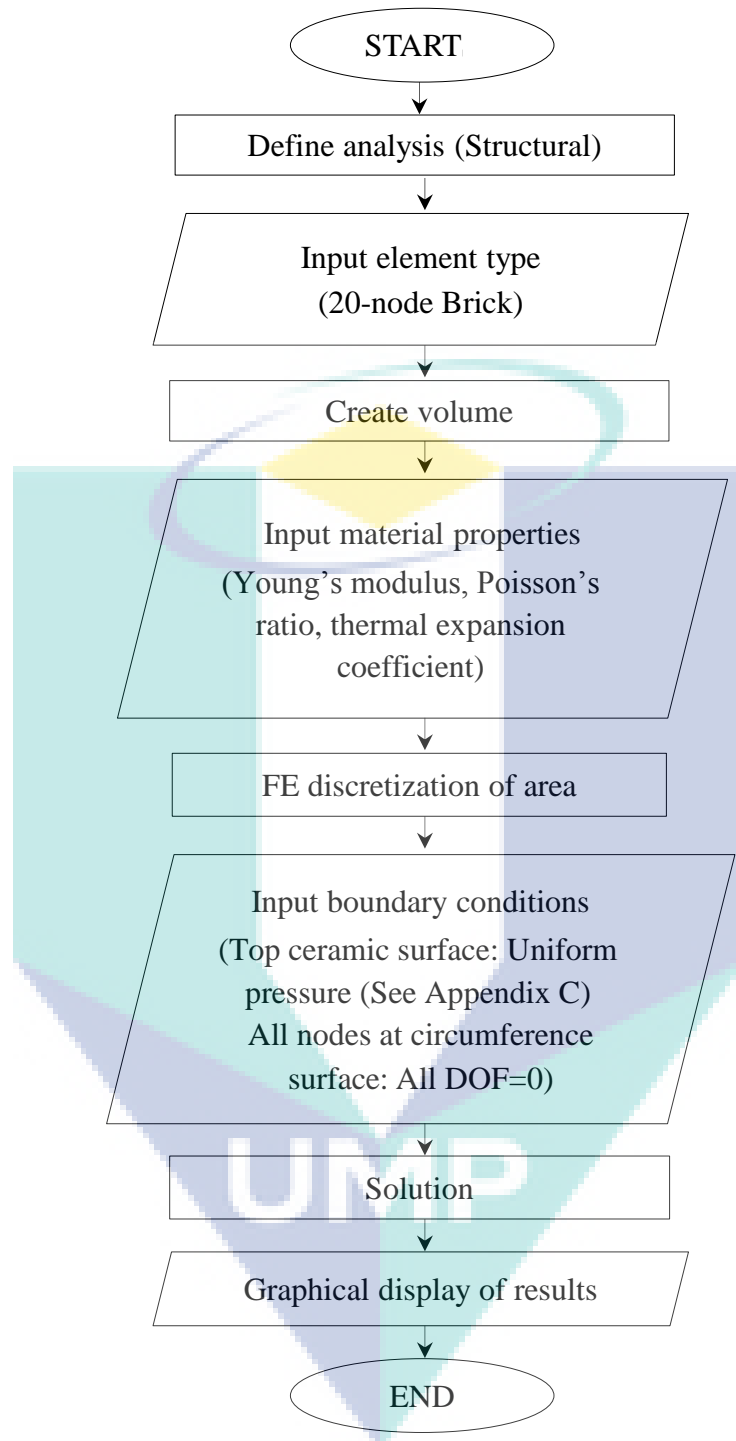


Figure 4.5: Flowchart of 3-D FE analysis of the FGM subjected to mechanical loading

4.4.2 Thermal Loading

The simulation of the FGM plate subjected to thermal loading started with a thermal analysis for the thermal field simulation and was followed by a structural analysis for the thermal stress responses. Figure 4.6 displays a schematic diagram of the FGM plate subjected to thermal loading analysis. It indicated that the pure ceramic phase surface was exposed to a higher temperature of 300°C while the pure metal phase surface remained at room temperature. The HA surface was subjected to the higher temperature because ceramics generally tend to resist high temperatures better than metals. In this analysis, most of the pre-processor definitions including element type, discretization parameters, structural boundary conditions and considered loading conditions were same as those used in the previous analysis of the FGM plate under mechanical loading. For the thermal characteristics of the FGM plate analysis, the boundary condition of thermal loading was required. Besides that, in order to get the structural responses resulting from thermal conduction activity, the thermal element was transformed into a structural element type. The result obtained from the thermal analysis was defined as the thermal boundary of the thermal loads in the structural analysis. The overall modelling method for the FGM plate subjected to thermal loading was presented in Figure 4.7. The temperature distribution, deflections, stresses and strains produced from the analysis could be used to determine the thermal behaviours of the FGM plate.

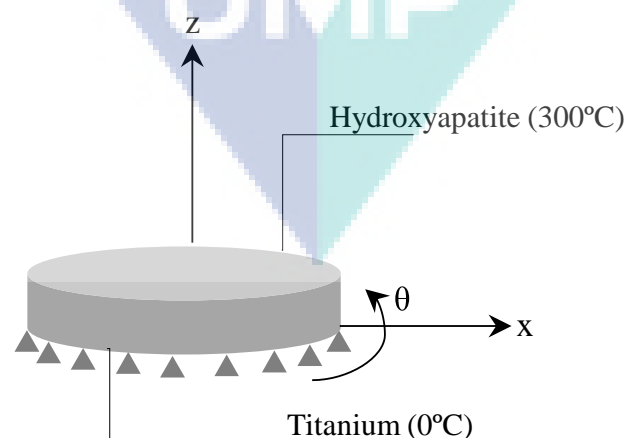


Figure 4.6: Schematic diagram of the FGM plate subjected to thermal loading analysis

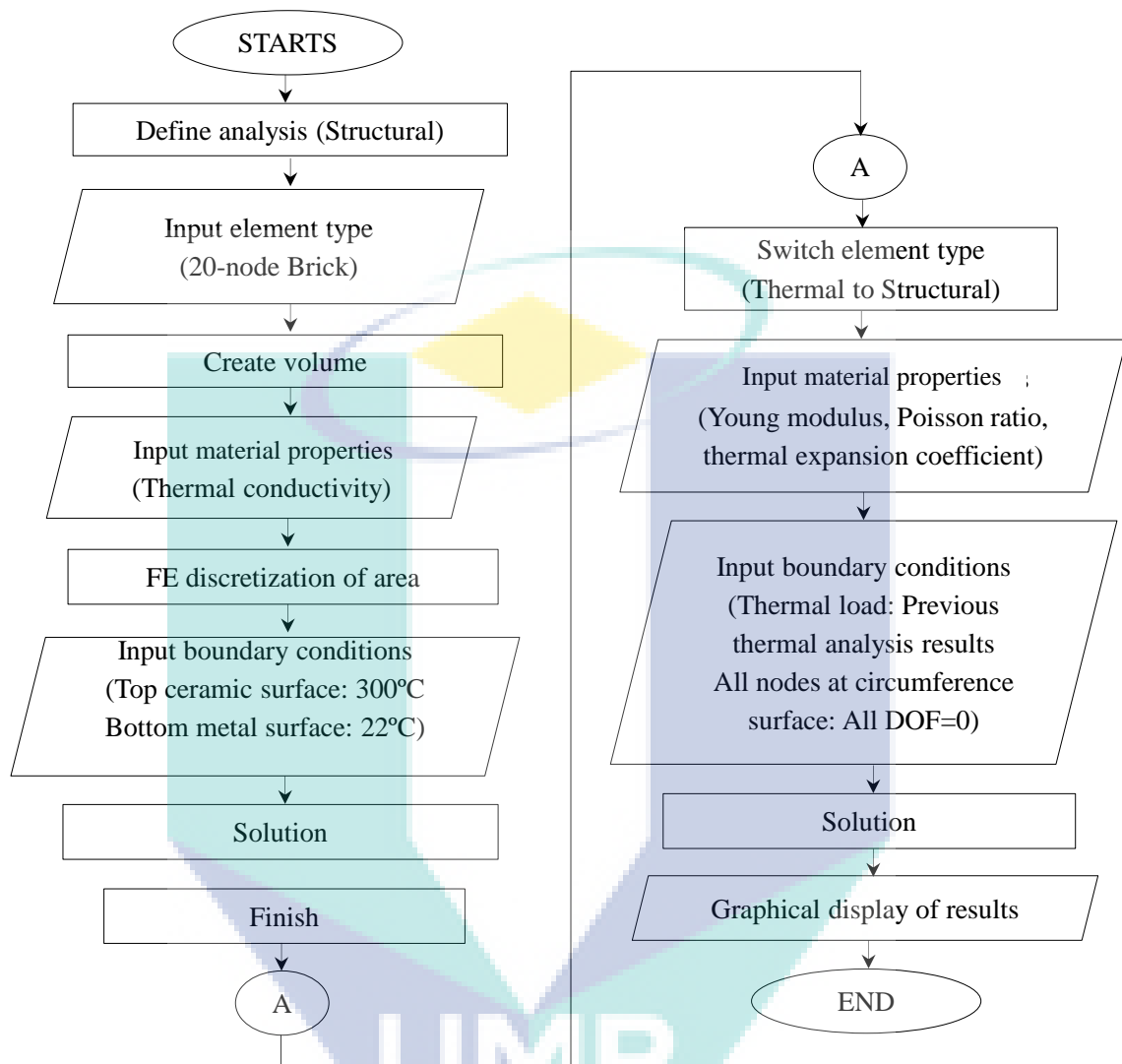


Figure 4.7: Flowchart of 3-D FE analysis of the FGM subjected to thermal loading

4.4.3 Thermo-mechanical Loading

The overall modelling setup for the thermo-mechanical problem analysis was similar to the thermal and mechanical analyses, except for the load boundary conditions. The simultaneously applied mechanical and thermal loadings on the HA surface created the coupled load boundary conditions for thermo-mechanical analysis. Figure 4.8 represents the schematic illustration of the analysis of thermo-mechanical problems in the FGM plate. During the analysis, the FGM plate was subjected to thermal loading at the same time as a uniform pressure which represented the mechanical load. The overall modelling method for the FGM plate subjected to thermo-mechanical loading is given in Figure 4.9. The results of the thermo-mechanical problems analysis in terms of temperature distribution, deflections, stresses and strains will be used to describe the thermo-mechanical behaviour of the FGM plate.

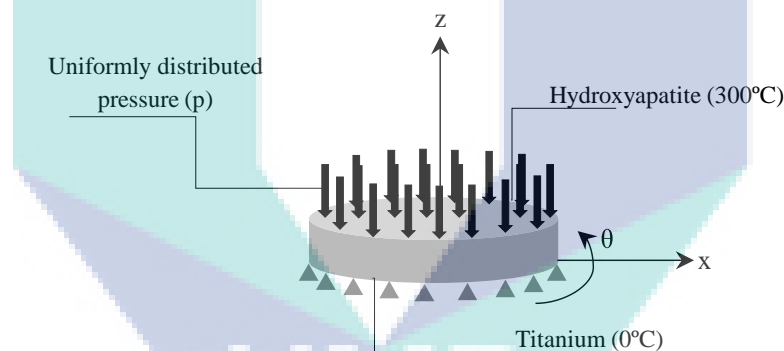


Figure 4.8: A simply supported FGM under thermo-mechanical loading

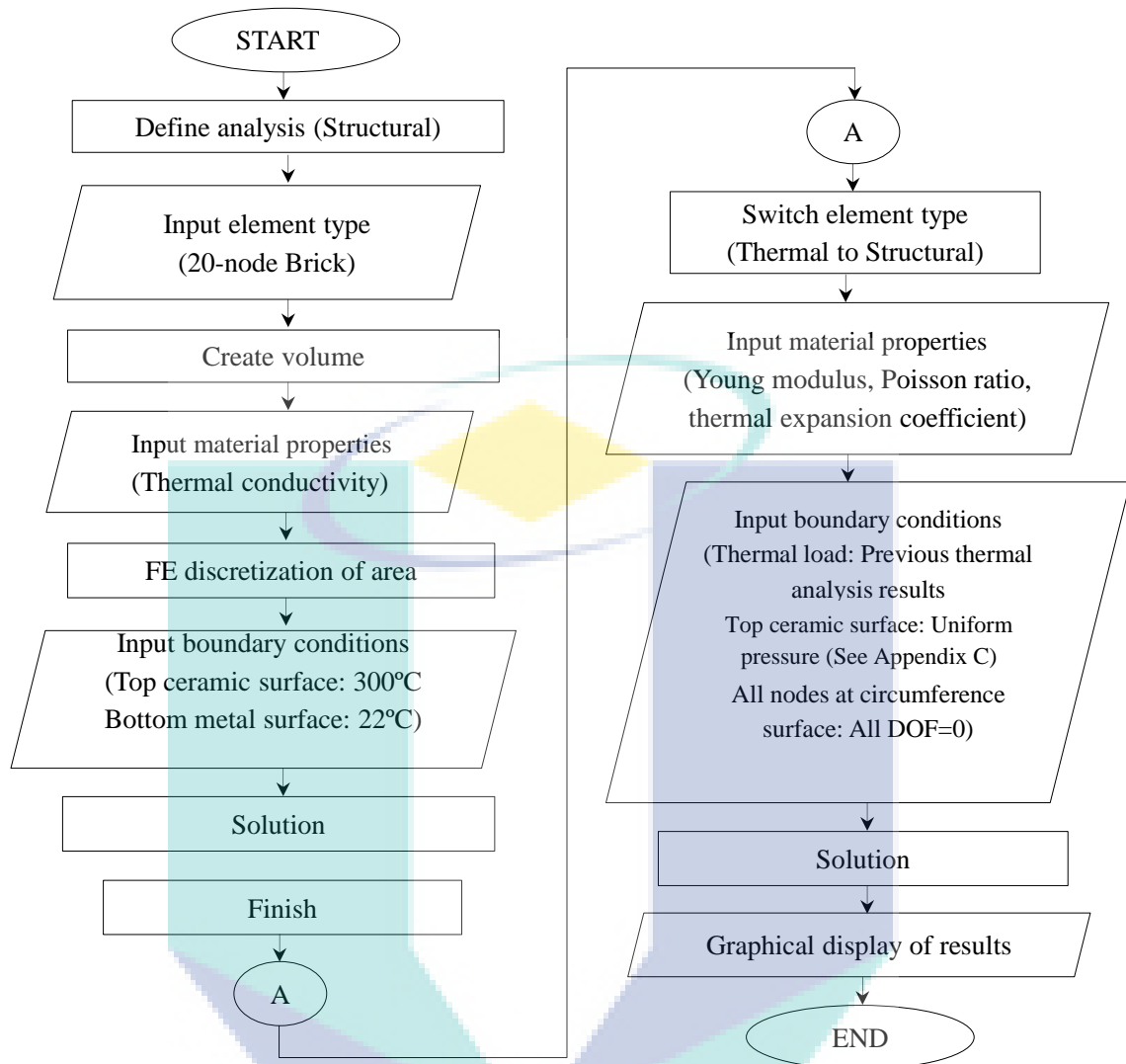


Figure 4.9: Flowchart of 3-D FE analysis of the FGM subjected to thermo-mechanical loading

In order to comprehensively present the responses of the FGM plate, the results achieved from the numerical calculations were transformed into dimensionless forms. The formulation of the dimensionless parameters involved in the present analysis are written as:

$$\bar{P} = \frac{d^2 p}{E_b h^4} \quad (4.30)$$

$$\bar{\omega} = \frac{\omega}{h} \quad (4.31)$$

$$\overline{\sigma_{xx}} = \sigma_{xx} \frac{h^2}{d^2 p} \quad (4.32)$$

$$\overline{\tau_{xz}} = \tau_{xz} \frac{h^2}{d^2} \quad (4.33)$$

$$\overline{K} = \frac{K}{\sigma_{xx} \sqrt{\pi z}} \quad (4.34)$$

$$\overline{x} = \frac{x}{d} \quad (4.35)$$

$$\overline{z} = \frac{z}{h} \quad (4.36)$$

4.5 MODEL VERIFICATION

In order to ensure the reliability of the FE models developed to predict the various characteristics of the FGM, verification of the FE calculations was obtained by comparing the present results with established results. The 2-D FE model for the FGM design optimization analysis was confirmed by taking into account the results reported by Park *et al.* (2009). This research team developed a crack-free Ni/Al₂O₃ FGM model with a total thickness of 26.1 mm and with 10 layers by considering the maximum principal stress theory. Figure 4.10 indicates the distribution of the first principal stress through the outer surface of the specimen simulated from both calculations.

In the analysis, the distribution of 1st principal stresses along the outer surface was analyzed within the distribution of the FGM strength to predict cracking in the structure. It is seen in Figure 4.10 that the peak principal stress occurred at an interface of 10 mm from the bottom surface, not exceed the corresponding critical failure strength. This result proved that there is no failure on the FGM. The numerical method was verified when the simulation results were matched by experimental observations.

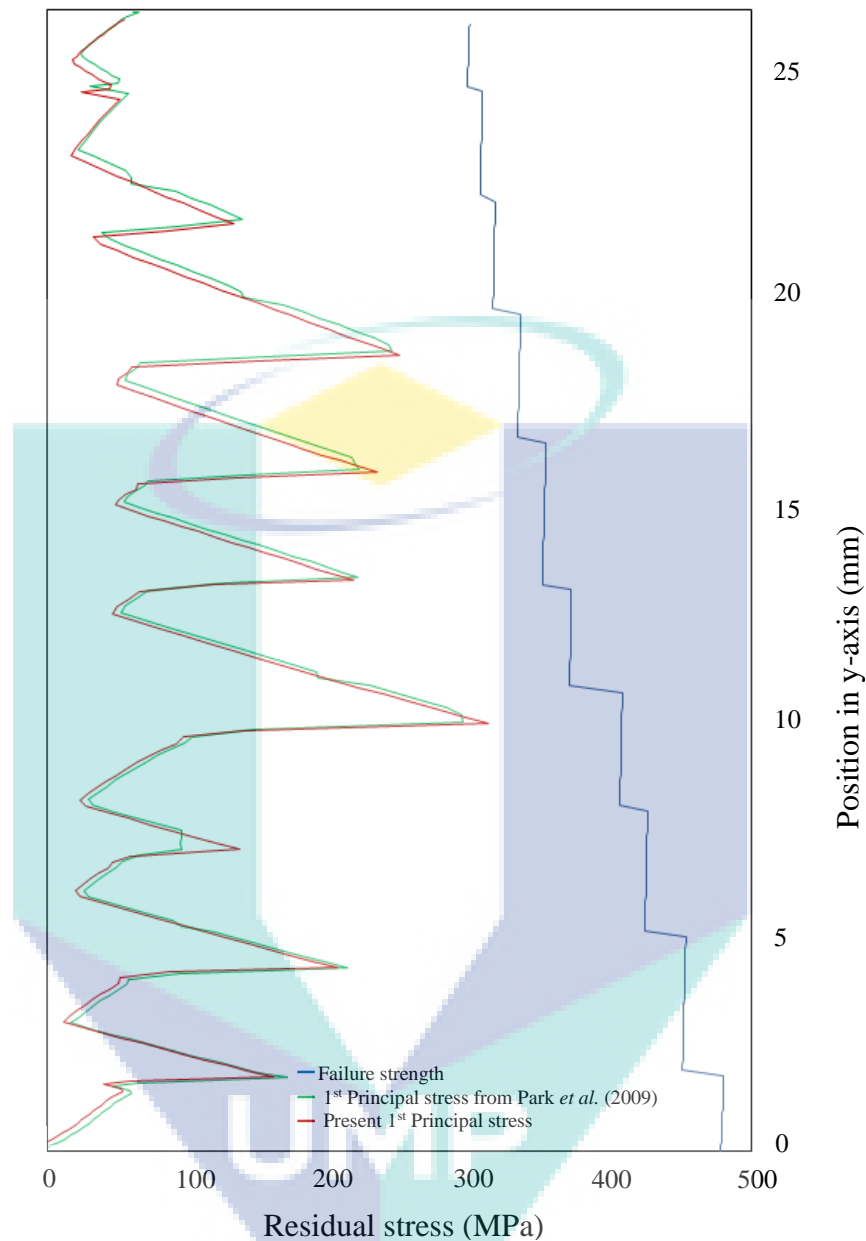


Figure 4.10: Verification of the 2-D modelling method

In addition to the 2-D model, the verification of the 3-D model was addressed in three stages. In the early stage of the verification process, the reliability of the steady-state thermal analysis method was confirmed because the present values of temperature distributions in Al/ZrO₂ (given in Figure 4.11) were highly consistent with those produced in the established research (Alshorbagy *et al.*, 2012). The thermal profile that resulted from the thermal analysis showed that homogeneous plates exhibited a higher temperature distribution in comparison to those belonging to FGM plates. The

dependence of the thermal conductivity properties of the constituents on the temperature distribution at the surfaces revealed that the grading parameter has a dominant role in the thermal characteristics of the FGM plates.

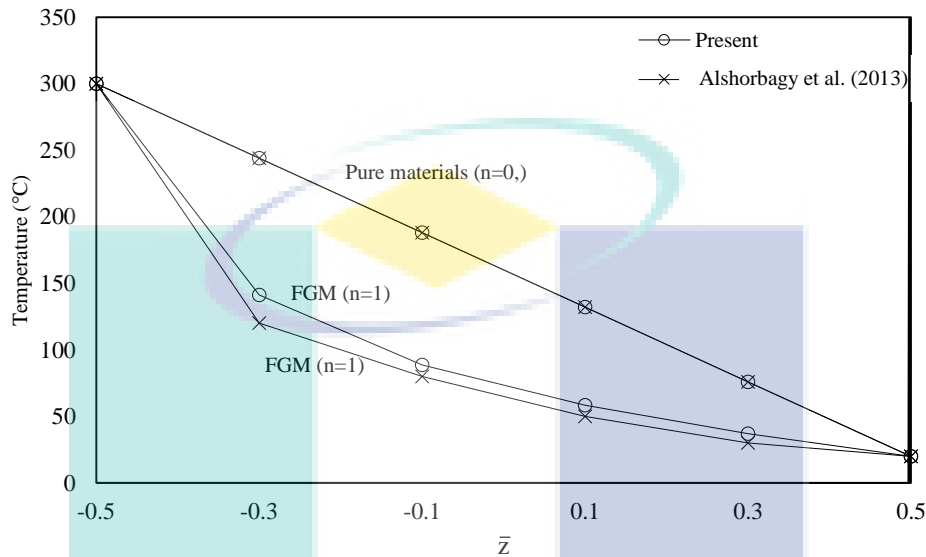


Figure 4.11: Temperature field distribution along the thickness of the FGM and pure plates

Then a convergence analysis of the fully discrete problem, where discretization parameters were completely determined by numerical solutions was performed on the Ni/ZrO₂ FGM. Nickel and zirconia were selected for the analysis since the results produced would be comparable to that reported in established work (Srinivas *et al.*, 2013) where similar constituents were used. When making a comparison between the present and the established cases, the results from both calculations matched each other and thus the simulation method is confirmed. The convergence studies of the simply supported Ni/ ZrO₂ FGM plate subjected to thermal loads and its comparison with established results are summarized in Tables 4.1 and 4.2, respectively.

Table 4.1: Convergence study of a simply supported Ni/ZrO₂ FGM plate subjected to thermal loadings with respect to different mesh divisions

Parameter	\bar{z}	Srinivas <i>et al.</i> (2013)	8x8	16x16	20x20	50x50	55x55
T	0.5	0.2432	0.2778	0.2779	0.2779	0.2779	0.2779
\bar{u}	0	0.0849	0.0432	0.0432	0.0432	0.0432	0.0432
	0.5	-0.7862	-0.6887	-0.6889	-0.6889	-0.6889	-0.6889
$\bar{\omega}$	1	-1.6990	-1.4560	-1.4560	-1.4560	-1.4560	-1.456
	0	5.5220	4.6320	4.6340	4.6340	4.6340	4.6340
$\bar{\sigma}_{xx}$	0.5	5.6350	4.7380	4.7390	4.7390	4.7390	4.7390
	1	6.0210	5.0700	5.0710	5.0710	5.0710	5.0710
$\bar{\sigma}_{zz}$	0	-75.780	-49.530	-48.580	-48.470	-48.300	-48.260
	0.5	-243.00	-299.70	-321.10	-320.30	-319.20	-318.90
$\bar{\tau}_{xz}$	1	-1006.0	-1120.2	-1099.9	-1097.4	-1093.6	-1092.6
	0.5	1.0150	0.8590	0.8454	0.8381	0.8318	0.8309
$\bar{\tau}_{xz}$	0.5	1.5830	2.2390	2.2370	2.2310	2.2240	2.2220

Table 4.2: Convergence study of simply supported Ni/ZrO₂ FGM plates subjected to thermal loadings with respect to different number of layers

Parameter	z/h	Srinivas <i>et al.</i> (2013)	6 Layers	8 Layers	9 Layers
T	0.5	0.2432	0.2844	0.2779	0.2769
\bar{u}	0	0.0849	0.0479	0.0432	0.0400
	0.5	-0.7862	-0.7106	-0.6889	-0.6822
$\bar{\omega}$	1	-1.6990	-1.5060	-1.4560	-1.4390
	0	5.5220	4.8010	4.6340	4.5100
$\bar{\sigma}_{xx}$	0.5	5.6350	4.9100	4.7390	4.6740
	1	6.0210	5.2520	5.0710	5.0030
$\bar{\sigma}_{zz}$	0	-75.780	-53.490	-48.260	-44.710
	0.5	-243.00	-331.20	-318.90	-304.40
$\bar{\tau}_{xz}$	1	-1006.0	-1106.0	-1093.0	-1078.0
	0.5	1.0150	0.9179	0.8309	0.7588
$\bar{\tau}_{xz}$	0.5	1.5830	2.4970	2.2220	1.9270

Tables 4.1 and 4.2 show that the responses of the FGMs converge within the arising mesh division and the number of layers. Since the results converge to less than a 20% error with a mesh division of 20x20 and with 8 layers, these discretization parameters were considered sufficient for the simulation.

The deflections of the Ni/ZrO₂ FGM plates subjected to mechanical loads calculated in the present simulation are listed in Table 4.3. In Table 4.3, the bolded numbers represent the established results. The simulation method is verified because the present values are highly consistent with those reported by Alshorbagy *et al.* (2013).

Table 4.3: Dimensionless central deflection of Al/ZrO₂ FGM plates subjected to mechanical loadings

\bar{P}	$\bar{\omega}$									
	Metal	n=0.5		n=1		n=2		Ceramic		
1	0.0449	0.0452	0.0264	0.0317	0.0297	0.0287	0.0326	0.0267	0.0208	0.0210
2	0.0897	0.0905	0.0528	0.0633	0.0594	0.0573	0.0652	0.0534	0.0416	0.0420
3	0.1346	0.1357	0.0792	0.0950	0.0891	0.0860	0.0978	0.0801	0.0623	0.0629
4	0.1794	0.1810	0.1056	0.1266	0.1192	0.1146	0.1304	0.1067	0.0832	0.0839
5	0.2243	0.2262	0.1320	0.1583	0.1486	0.1433	0.1631	0.1334	0.1040	0.1049
6	0.2692	0.2714	0.1584	0.1899	0.1782	0.1720	0.1957	0.1601	0.1248	0.1258
7	0.3140	0.3167	0.1848	0.2216	0.2080	0.2006	0.2283	0.1868	0.1456	0.1468
8	0.3589	0.3619	0.2112	0.2532	0.2377	0.2293	0.2609	0.2135	0.1664	0.1678
9	0.4038	0.4072	0.2376	0.2849	0.2674	0.2579	0.2935	0.2402	0.1872	0.1888
10	0.4486	0.4524	0.2640	0.3166	0.2971	0.2899	0.3261	0.2669	0.2080	0.2097
11	0.4935	0.4979	0.2903	0.3482	0.3269	0.3153	0.3587	0.2935	0.2288	0.2307
12	0.5384	0.5428	0.3167	0.3799	0.3566	0.3439	0.3913	0.3202	0.2496	0.2517

The thermo-mechanical model developed to estimate the thermo-elastic behaviours of FG plates were verified because the present results are in excellent agreement with those presented in Alshorbagy *et al.* (2013). In the simulation, the responses of the FG plates at the mid-plane are considered. The comparison between the present and established results (bolded numbers) are given in Table 4.4. With regard to simulation method verification, the FE formulation used in this study is considered valid to determine the solutions of thermo-mechanical problems in FGMs.

Table 4.4: Dimensionless deflection at the central point of Al/ZrO₂ FGM plates subjected to thermo-mechanical loadings

\bar{P}	$\bar{\omega}$							
	Metal		n=1		n=2		Ceramic	
1	-0.2015	-0.2050	-0.0527	-0.0665	-0.0580	-0.0547	-0.0860	-0.0879
2	-0.1567	-0.1598	-0.0230	-0.0379	-0.0250	-0.0280	-0.0650	-0.0669
3	-0.1119	-0.1146	0.0067	-0.0092	0.0072	-0.0013	-0.0440	-0.0459
4	-0.0671	-0.0690	0.0364	0.0195	0.0398	0.0254	-0.0240	-0.0250
5	-0.0223	-0.0240	0.0661	0.0481	0.0724	0.0521	-0.0030	-0.0040
6	0.0225	0.0210	0.0958	0.0768	0.1050	0.0788	0.0175	0.0170
7	0.0667	0.0660	0.1255	0.1054	0.1376	0.1054	0.0383	0.0380
8	0.1120	0.1115	0.1552	0.1341	0.1702	0.1321	0.0590	0.0589
9	0.1568	0.1568	0.1849	0.1628	0.2028	0.1588	0.0798	0.0799
10	0.2016	0.2020	0.2146	0.1914	0.2354	0.1855	0.1005	0.1009
11	0.2464	0.2473	0.2443	0.2201	0.2680	0.2122	0.1213	0.1219
12	0.2912	0.2925	0.2741	0.2487	0.3006	0.2389	0.1421	0.1428

4.6 CLOSURE

In this chapter, the finite element formulations and the solution methods for the analysis of HA/Ti FGM plates were presented and discussed. Basic FGM models were developed and verified with other published data. It was found that, in general, their agreement is excellent, which confirms the basis of these models. The results of the numerical works performed for the optimization of the grading index number, the number of layers and the thickness of the FGM plate and the modelling of various behaviours of the plate under isothermal, thermal and thermo-mechanical loadings is shown and discussed in the next chapter.

CHAPTER 5

NUMERICAL RESULTS AND DISCUSSION

5.1 INTRODUCTION

This chapter is primarily concerned with data predicted using FEA, which was presented in Chapter 4 and in the ANSYS model outlined in Appendix A. The computational work started with a 2-D FE analysis to optimize the grading parameters, the number of layers and the thickness parameters of a pre-designed HA/Ti FGM plate. The final section of this chapter focuses on a parametric study of the HA/Ti FGM using 3-D FE models. Its primary aim is to provide a greater understanding of the effects of some of the important influencing parameters on the behaviour of the FGM.

5.2 MATERIAL PROPERTIES

The typical properties of the base materials, HA and Ti, used throughout the numerical modelling are given in Table 5.1 (Chu *et al.*, 2003). The properties of the stepwise layers at intermediate locations on the FGM models were calculated based on a ROM formulation shown in Equation 3.3. When analyzing an FGM containing a HA constituent, it is important to realize that the elastic modulus of this material varies in a range between 73 to 120 MPa depending on the sintering temperature (Ruseska *et al.*, 2006). Therefore the selection of properties shown in Table 5.1 was made by taking into account the sintering temperature used for the preparation of the FGM samples, which is shown and discussed in the next chapter.

Table 5.1: Properties of materials

Material	(*) E (GPa)	(*) ν	(*) $\alpha \times 10^{-6}$ (/°C)	(**) k (W/mK)
HA	110.89	0.28	14.87	2.16
Ti	107.95	0.34	10.9	17.5293

Source: *Chu *et al.*, 2003; **Moroi *et al.*, 1993

Before the results of the numerical works present, it is important to show the impact of using different constituents' properties for modelling the models' responses. A through-the-thickness Young's modulus distribution of the FGM plates with two different HA constituents (given in Table 5.2) is presented in Figure 5.1. It can clearly be seen that the Young's modulus of the FGM plate with HA_{new} (Ruseska *et al.*, 2006) increased towards the Ti surface, while decreasing towards the same surface of the FGM plate with HA. In addition, the gap between the Young's modulus values of the adjacent layers of the FGM plate with HA_{new} is more significant when compared to that with HA.

Table 5.2: Properties of two different HAs

Material	(**) E (GPa)	(**) ν	(**) $\alpha \times 10^{-6}$ (/°C)	(***) k (W/mK)
HA_{new}	73.1*	0.28	14.87	2.16
HA	110.89**	0.28	14.87	2.16

Source: *Ruseska *et al.*, 2006; **Chu *et al.*, 2003; ***Moroi *et al.*, 1993

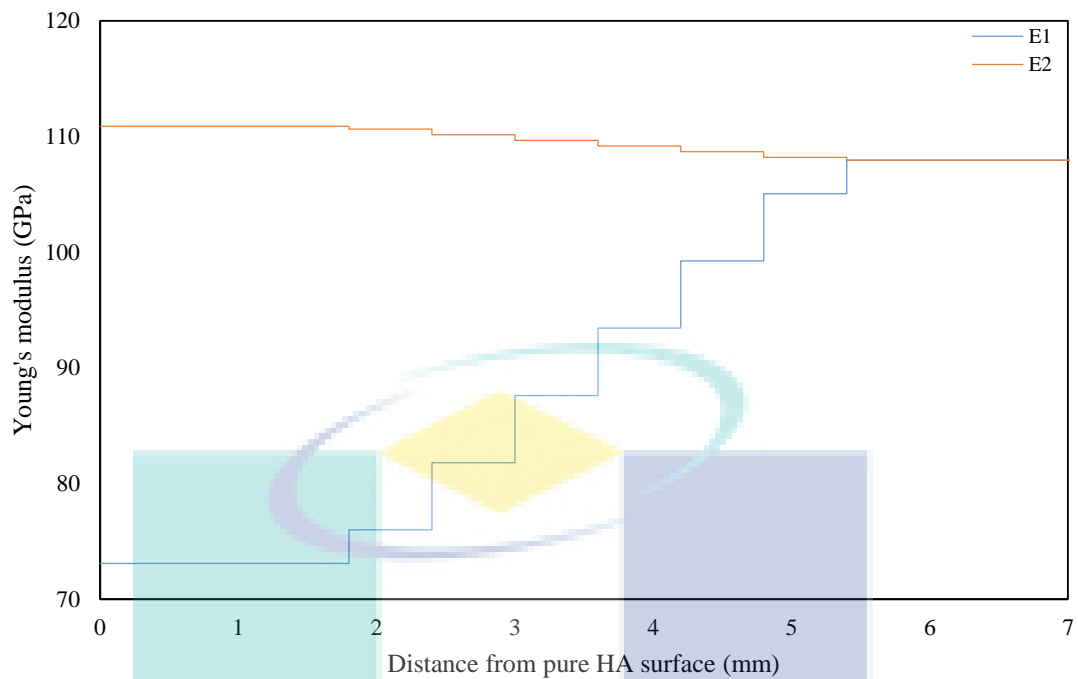


Figure 0.1: Young's modulus distribution along the thickness of the HA/Ti FGM plate with different HAs

Various response distributions, including deflection, normal stress and transverse shear stress of the FGM plate for different Young's modulus of HA constituents are shown in Figure 5.2. The lower central deflections found in the FGM plate with HA (Chu *et al.*, 2003) properties (illustrated in Figure 5.2(a)) show greater rigidity of the material due to the higher corresponding elastic modulus along the transverse plane of the plate. The small Young's modulus variation in the FGM plate with HA (Chu *et al.*, 2003) properties then becomes the main factor of the linear normal stress distribution presented in Figure 5.2(b). The less significant differences in the transverse Young's modulus profile also led to the decreasing corresponding transverse shear stress distribution at the intermediate FGM layers shown in Figure 5.2(c). For both FGM plates, the linear change in the plots represents the shear stress distribution along the pure Ti and the pure HA thicknesses. Since the shear stress values are negligibly small, the results shown in Figure 5.2(c) reveal that the transverse shear stress is not greatly affected by the loading.

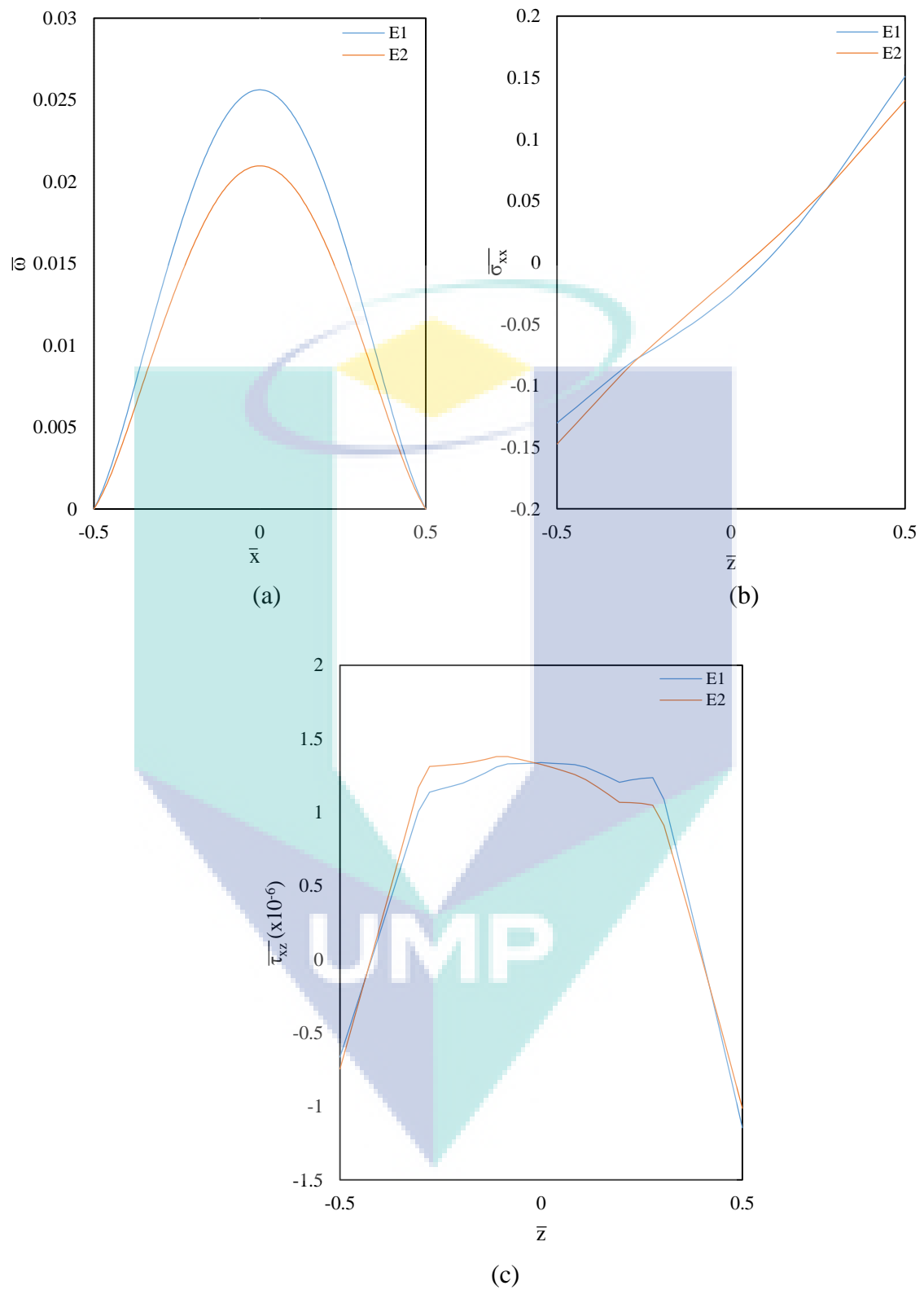


Figure 5.2: Responses of HA/Ti FGM plates with different Young's modulus of HA under mechanical loading ($\bar{P}=1$, $n=1$, $L=6$, $h=0.0072\text{m}$)

In addition to deflection, normal stress and shear stress, the stress intensity response is of particular importance since it contributes to the delamination failures of laminated structural elements. The stress intensity profile through the transverse and longitudinal directions of the FGM plates with different Young's modulus of HA under thermo-mechanical loading is given in Figures 5.3(a) and 5.3(b) respectively. Both illustrate that high stress intensity occurred at the end zones of the plate. The stress was obviously concentrated at the location where the highest Young's modulus represents a higher rigidity, as shown in Figure 5.3(a). The decreasing stress intensity within the larger ratio E_U/E_L is illustrated in Figure 5.3(b), which shows less rigidity of the materials due to a higher Young's modulus of the upper constituent. The results presented in Figures 5.2 and 5.3 revealed that the structural responses of the FGM plate were strongly affected by the elastic properties of the constituents. Thus using different properties in the computation definitely produces different results.

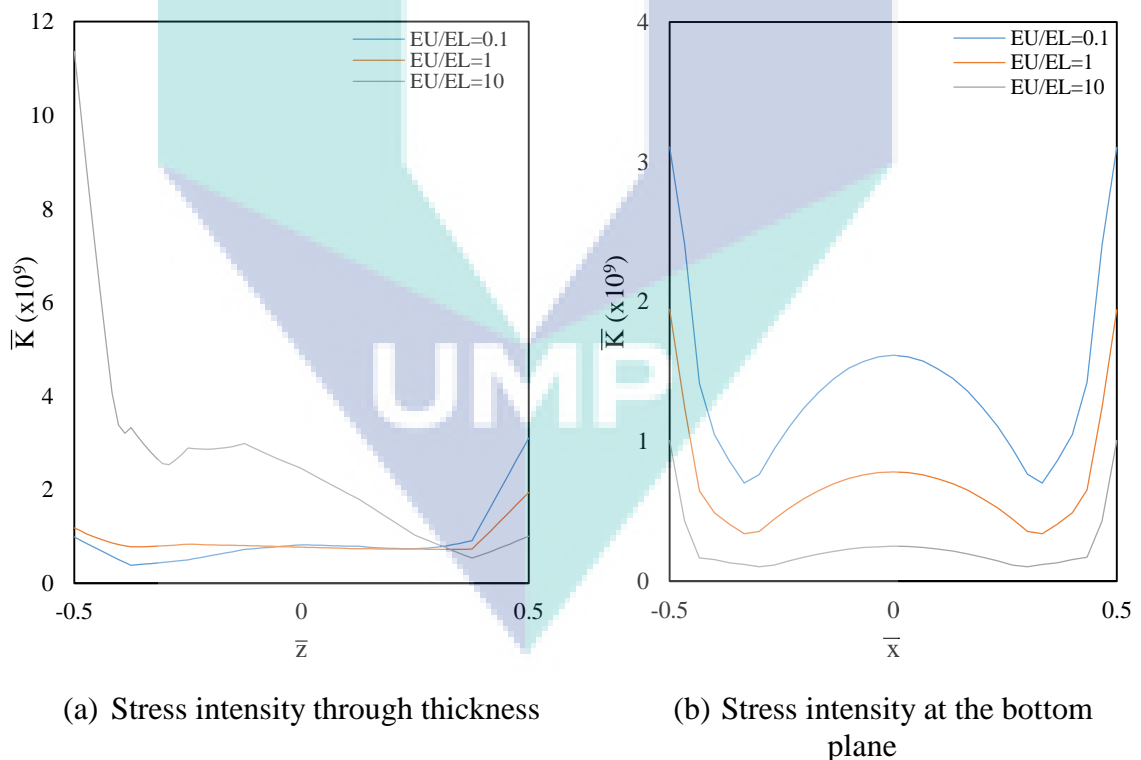


Figure 5.3: Effect of various Young's modulus of the base materials ratios on the stress intensity factor of a HA/Ti FGM plate under thermo-mechanical loading

5.3 2-D ANALYSIS: OPTIMIZATION OF DESIGN PARAMETERS

The optimization of design parameters, mentioned previously in Chapter 4 as the number of layers, grading index and thickness, was achieved through the evaluation of the residual stress distribution along the compositional gradient plane at the circumference surface of the cylindrical FGM plate. Optimization analysis was performed by assuming that the residual stress occurred because of a temperature drop during the sintering process due to a variation in the thermal and elastic properties along the transverse direction of the FGM structure. Since the effective properties vary with the variation in the number of layers, grading index and thickness of the FGM plate, an evaluation of the residual stress distribution was significant when determining the optimal geometrical parameters of the structure.

5.3.1 Evaluation of the Grading Index

The compositional distribution of the FGM plates with various grading indices is shown in Figure 5.4. The FGM plates with a grading index number $n=0$ and ∞ have homogeneous ceramic and metallic ingredients respectively. The properties' variation along the thickness direction of the plate is only possible when the grading parameter is between these two values. This parameter led to either ceramic or metal phase domination in terms of the volume fraction in the FGM plate. The grading parameter $n=1$ showed the balance or linear mixing ratio of the constituents' differences between adjacent FGM layers.

The residual stress distributions for different grading indices along the gradient plane of the FGM plates are represented by the teeterboard plots shown in Figure 5.5, where the lowest stress peak is found in the FGM plate with $n=1$. The linear variation in the compositional distribution of the constituents led to better stress relaxation in this plate. The higher stress peaks in the FGM plates with $n \neq 1$ need to be avoided in order to produce less stress intensity which cause failures in the FGM structure. The results shown in Figure 5.5 conclude that $n=1$ is the optimum grading index number for the pre-designed FGM plate analysed in this research.

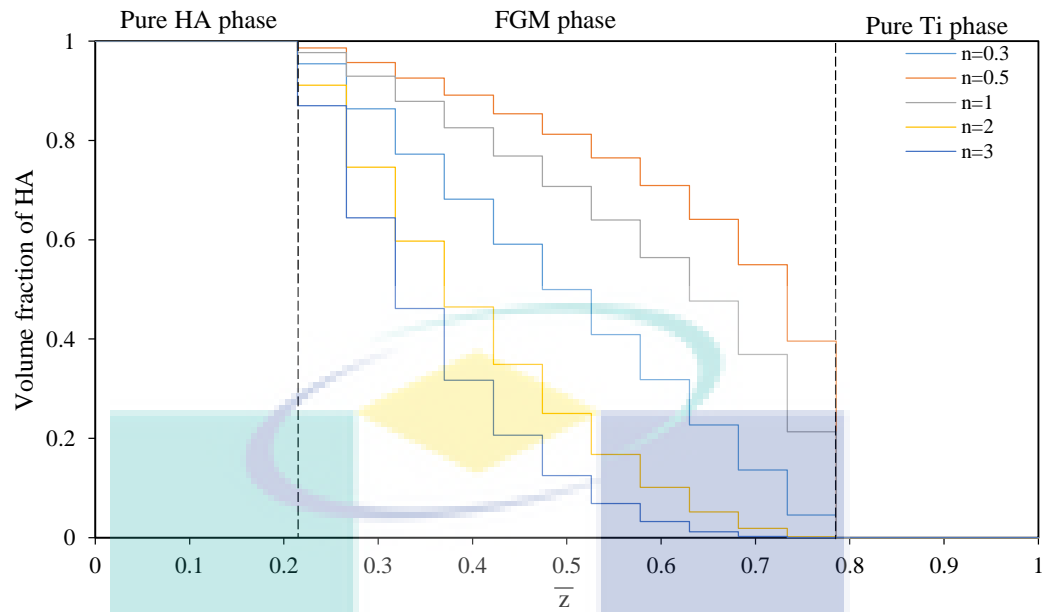


Figure 5.4: Compositional distribution profiles of the HA/Ti FGM plates with a variation of the grading parameter

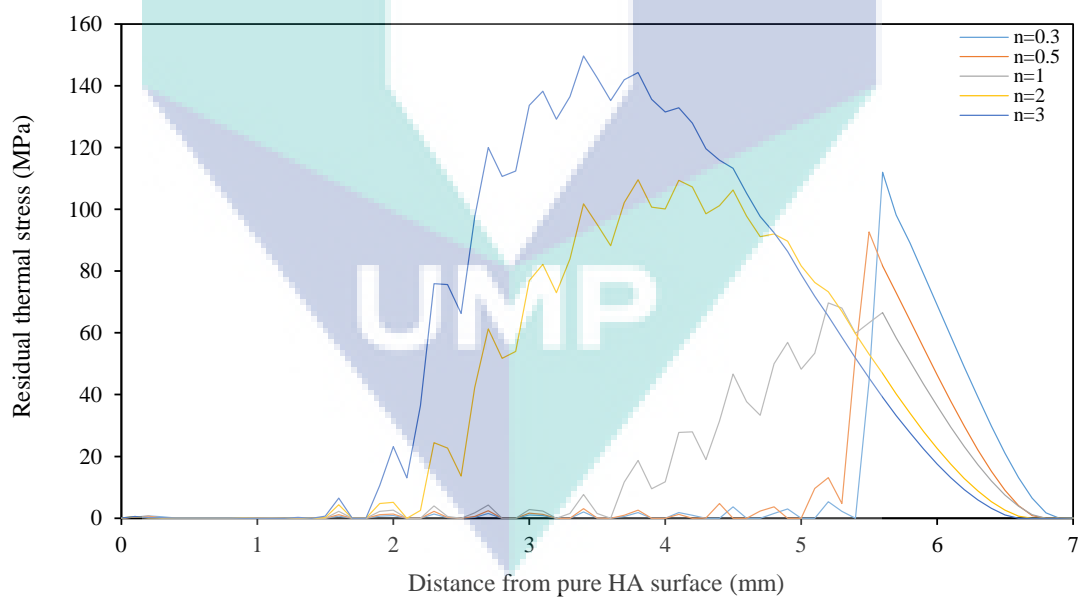


Figure 5.5: Residual thermal stress distribution along the thickness of the HA/Ti FGMs with various grading indices ($L=11$, thicknesses of pure Ti, FGM and pure HA layers: 1.5mm, 4mm, 1.5mm, respectively)

5.3.2 Evaluation of the Number of Layers

Figure 5.6 shows the residual stress distributions along the thickness of the HA/Ti FGM plates between 2 and 11 layers. The thermal relaxation in the FGM plates can be evaluated by considering the maximum residual stresses and the maximum stress peaks given in Table 5.3. The results indicate that with a higher number of layers inside the plate, the highest stress difference and highest residual stress of the respective FGM plates gradually reduced, most probably due to the lower significance of the component concentration variation between adjacent layers.

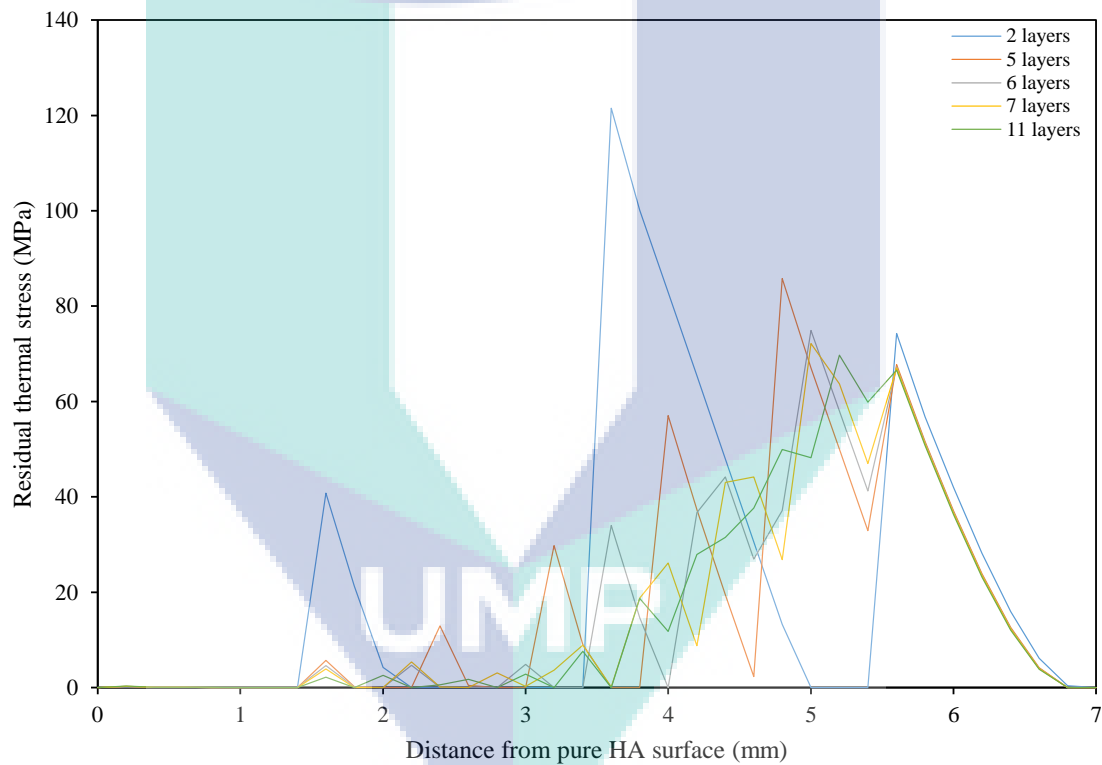


Figure 5.6: Residual thermal stress distribution along the thickness of HA/Ti FGM plates with various number of layers ($n=1$, thickness of pure layers, FGM layer: 1.5mm, 0.007m)

Table 5.3: Maximum thermal residual stress and the maximum thermal stresses differences of the HA/Ti FGM plates with different number of layers

Model	Maximum residual thermal stress (MPa)	Maximum thermal stress jump at the interfaces between the adjacent layers (MPa)
FGM 2 layers	121.49	121.49
FGM 5 layers	85.78	83.47
FGM 6 layers	74.89	53.67
FGM 7 layers	72.14	45.33
FGM 11 layers	68.04	27.75

Furthermore, the highest stress differences decreased rapidly when compared to the highest residual stresses. Since the worst bonding regions in the FGM plates are located at the interfaces, the drastic decrease in the highest stress differences is advantageous for the structural integrity of the plates. Even from a theoretical perspective, a greater number of layers is advantageous for the relaxation of the residual stresses (Zhang *et al.*, 2008). The decision whether to add more layers to the FGM plate should be included when considering fabrication. From this result the maximum residual stress relaxation was found on the FGM containing six layers. Thus $L \geq 6$ is selected as the optimum number of layers for the HA/Ti FGM.

5.3.3 Evaluation of the FGM's Thickness

A correlation between the FGM's thickness and the residual stress distribution was investigated for FGM plates with graded layers between 0.1 to 12 mm. The thickness of the upper and lower pure layers remained similar for all FGM plates. From Figure 5.7, it is evident that the stress peaks decrease within increasing thickness. For FGM plates with a thickness in the range 0.1mm to 2 mm, the residual stress increased rapidly from the pure HA surface before decreasing towards the pure Ti surface. The same trends were found in FGM plates with moderate thickness ($t=4, 6, 8$ mm) except in drastic stress differences. A gradual variation in the residual stress found in FGM plates with a moderate thickness still could be found in an FGM plate with greater thickness ($t=10, 12$ mm). However the stress kept increasing towards the pure Ti surfaces without decreasing back to the lowest value.

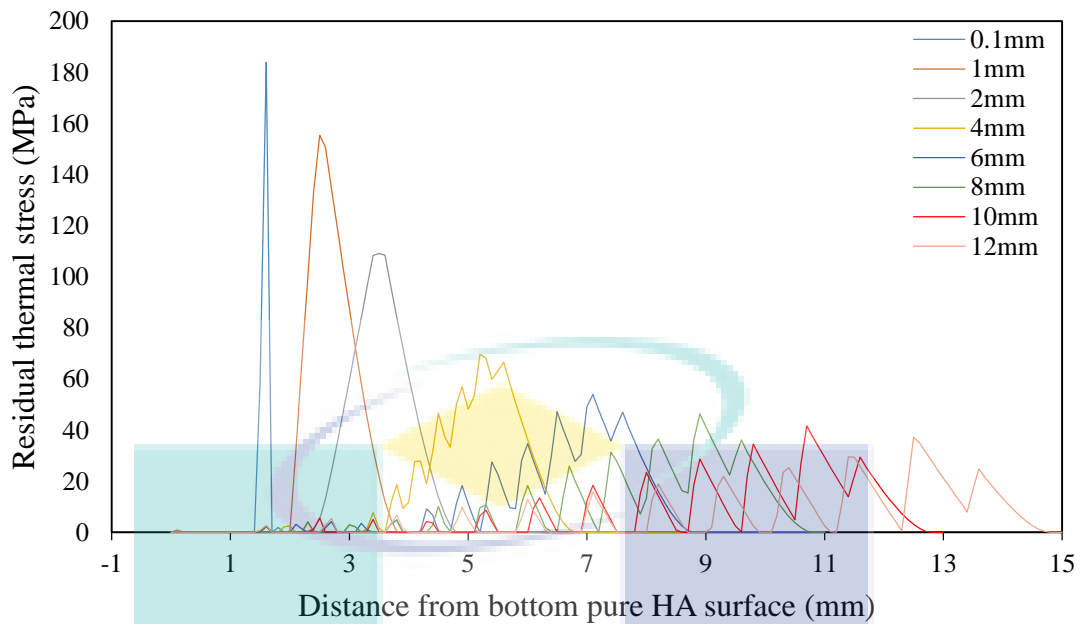


Figure 5.7: Residual thermal stress distribution of the HA/Ti FGM plates with various graded layers' thicknesses ($L=11$, $n=1$, thickness of the pure Ti and HA layers: 1.5mm)

In order to find the optimum thickness, the maximum residual stresses and the difference between the adjacent stress peaks of the FGM plates (given in Table 5.4) were considered. The minimum difference in the adjacent stress peaks of the FGM plate by thickness ($t=8$ mm) represented the greatest stress relaxation in this plate when compared to others. From this result, the optimum thickness of FGM layers was taken as $t=8$ mm. The optimum thickness of each layer inside the FGM plate can be calculated by dividing the FGM thickness by the number of layers inside the FGM plate. In the current case, the optimum thickness for the single FGM layer was ± 0.7 mm.

Table 5.4: Maximum thermal residual stresses and jumps in HA/Ti FGM plates with different thicknesses of the FGM phase

Thickness of FGM (mm)	Peak stress (MPa)	Different of current with previous peak stresses (MPa)
2	109.16	41.55
4	68.04	41.12
6	54	14.04
8	46.35	7.65
10	37.359	8.991
12	25.371	11.988

5.4 3-D ANALYSIS: RESPONSES OF FGMS UNDER VARIOUS LOADINGS

Numerical results achieved from the 3-D analysis performed on simply supported cylindrical HA/Ti FGM plates with optimal geometrical parameters obtained in the previous 2-D optimization analysis are presented and discussed in this section. The results are subsequently used to describe the effects of the number of layers, grading index number, and thickness parameters on the thermal and structural responses of FGM plates under isothermal, thermal and thermo-mechanical loading conditions. The thermal and mechanical properties of the constituents used in the present simulation were similar to that used in the 2-D analysis. The responses, in terms of temperature, displacement, normal stress, shear stress and stress intensity factor distributions, are presented throughout this subsection with the intention of using the HA/Ti FGM structure in thermal barrier applications.

5.4.1 Isothermal Loading

Figures 5.8(a) and 5.8(b) show the deflection colour contour images of the optimum FGM plate from two different views. The maximum deflection of 0.15 mm is represented by the red colour contour which can be observed in Figure 5.8(a) and is located at the centre of the plate. However the deflection decreased towards the outer radial surface because of the fixed zero degree of freedom boundary condition. In Figure 5.8(b), it is clear that the area of maximum deflection reduced towards the

bottom Ti surface. This revealed that the nodes located farther from the plane directed with the loading tended to deflect more than those that were closer.

The normal stress colour contour images for the optimum FGM plate (from similar views taken previously) are given in Figures 5.9(a) and 5.9(b) respectively. Figure 5.9(a) indicates that normal stress is the highest at the outer radial surface in the x-direction and that it decreases towards the centre of the FGM plate. The minimum normal stress can be found at the same location of the highest stress but on the bottom Ti plane, as shown in Figure 5.9(b). The normal stress at the centre of the bottom Ti plane is greater than that found on the top HA plane due to the higher tensile stress acting on it.

The corresponding transverse shear stress contour images for the optimum FGM plate are illustrated in Figure 5.10(a). This shows that the maximum shear stress appeared at the outer surface in the x-direction, where the minimum transverse shear stress was at the opposite side. This happens because the transverse shear stress distribution depends on both the circumference and thickness coordinates of the FGM plate. The moderate transverse shear stress distribution at the centre of the FGM plate (as shown in Figure 5.10(b)) revealed that the shear stress response is not greatly affected by the mechanical loading.

The stress intensity contours obtained from the analysis of the optimum FGM plate presented in Figure 5.11(a) shows the greatest stress intensity at the outer radial surface of the top HA plane. However the stress intensity distribution at the centre of the plate was less than that found at the circumference surface, as depicted in Figure 5.11(b). The stress intensity factor distribution, which is highly affected by the sample geometry, crack parameters and load distribution on the material, could be used to predict the magnitude of a crack-tip stress field or a crack initiation spot on the FGM plate. The area subjected to the high stress intensity factor distribution is the location in which the crack will be initiated.

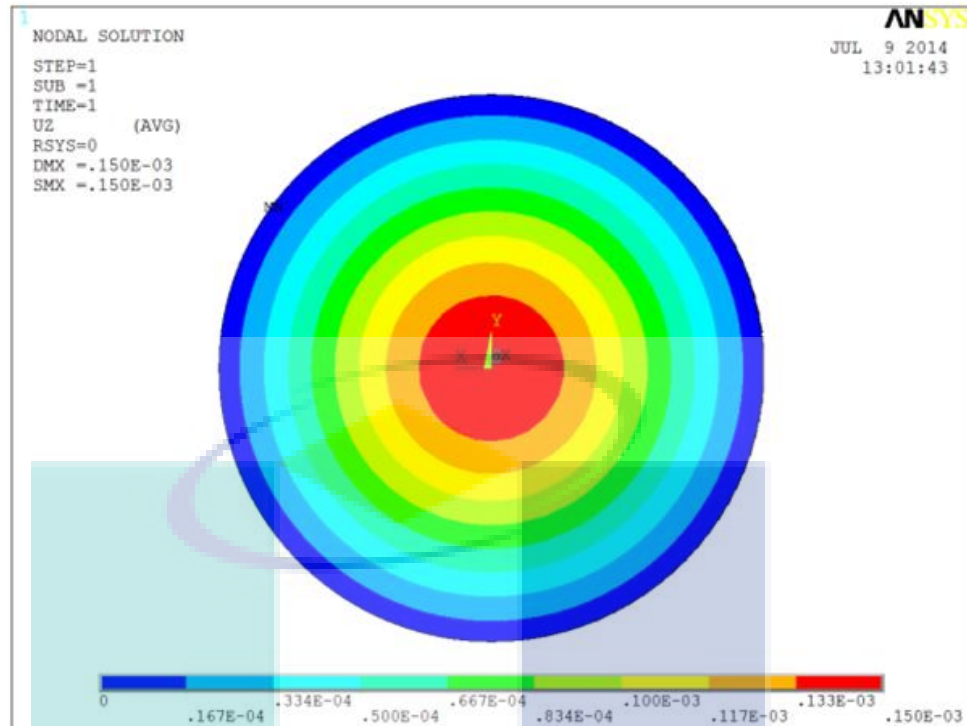
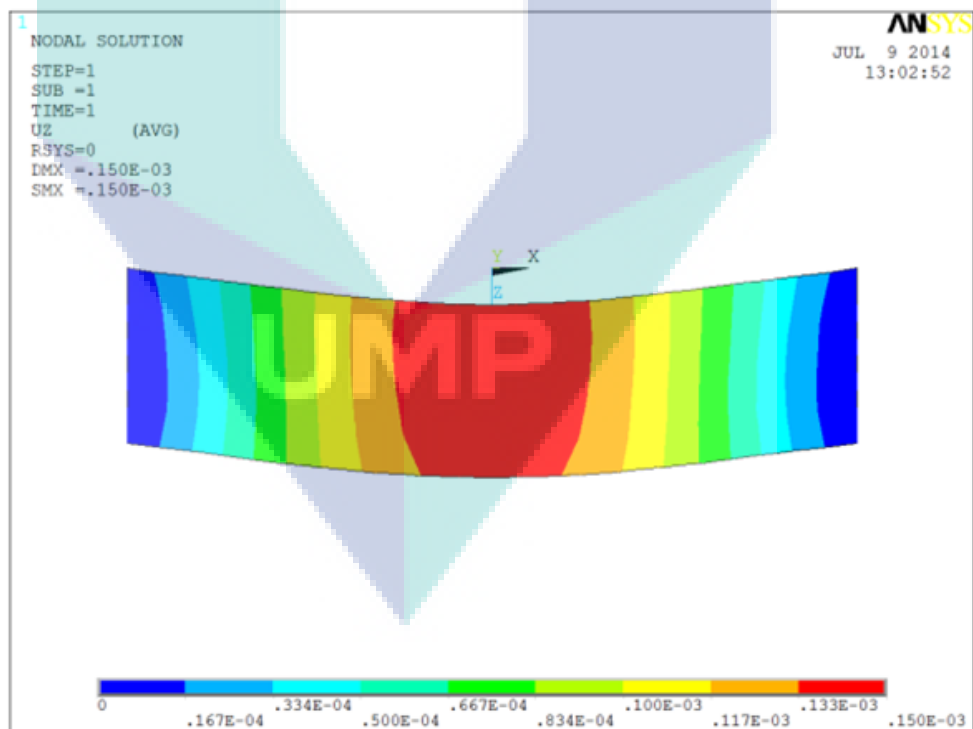
(a) δ_{zz} (top view)(b) δ_{zz} (mid-plane cross-section front view)

Figure 5.8: Deflection distribution of the HA/Ti FGM plates under isothermal conditions ($\bar{P}=1$, $n=1$, $L=6$, $h=0.0072\text{m}$)

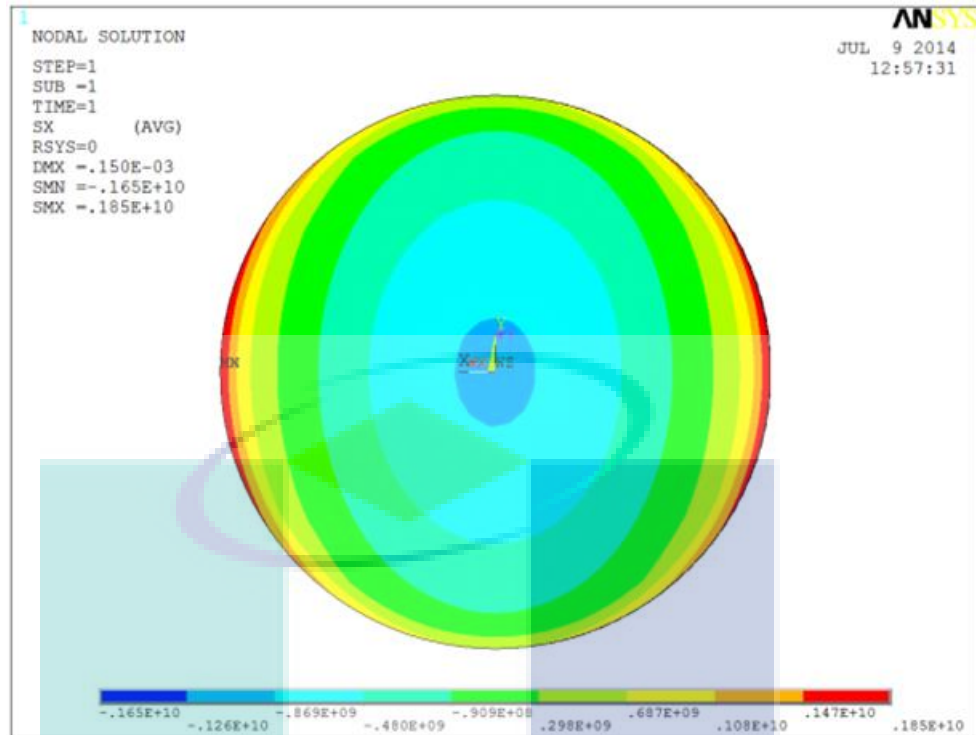
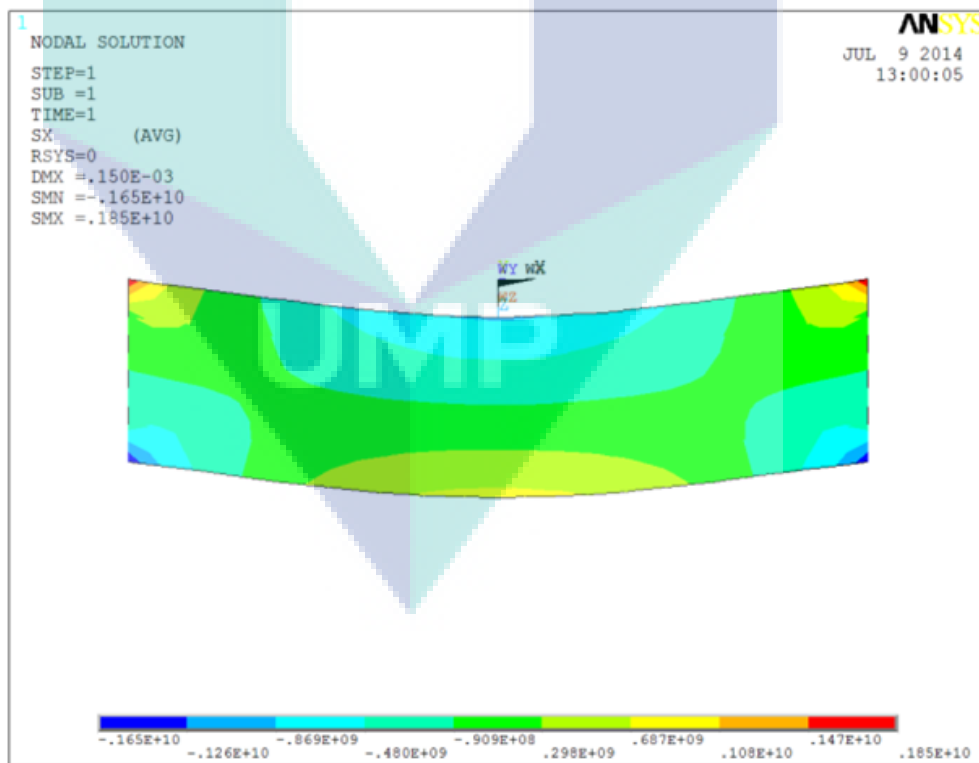
(a) σ_{xx} (top view)(b) σ_{xx} (mid-plane cross-section front view)

Figure 5.9: Normal stress distribution of the HA/Ti FGM plates under isothermal conditions ($\bar{P}=1$, $n=1$, $L=6$, $h=0.0072\text{m}$)

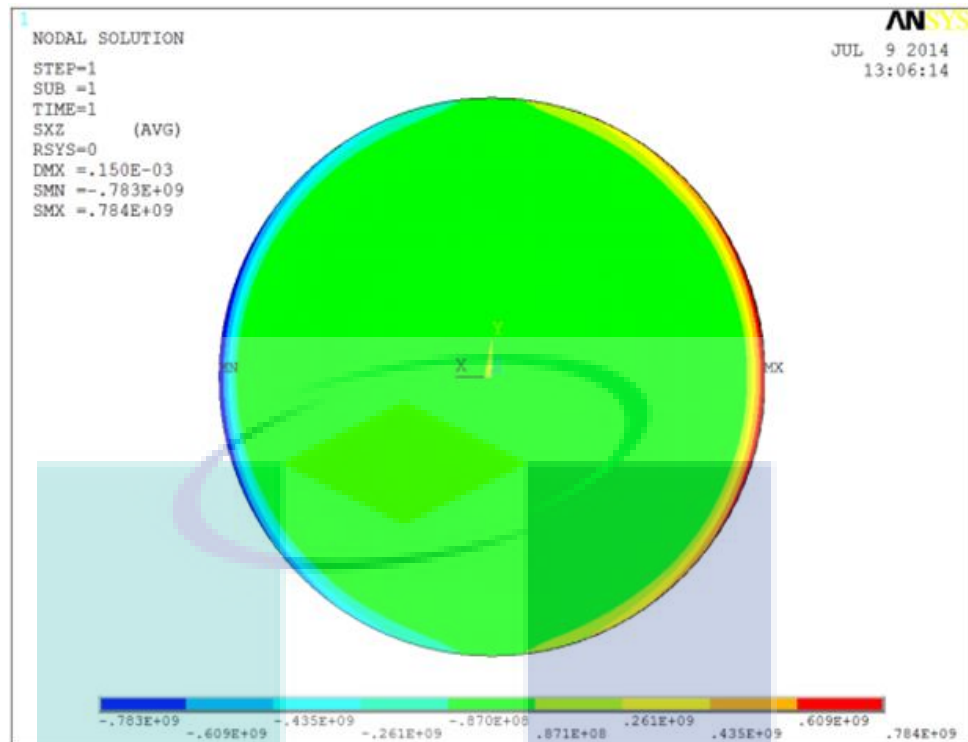
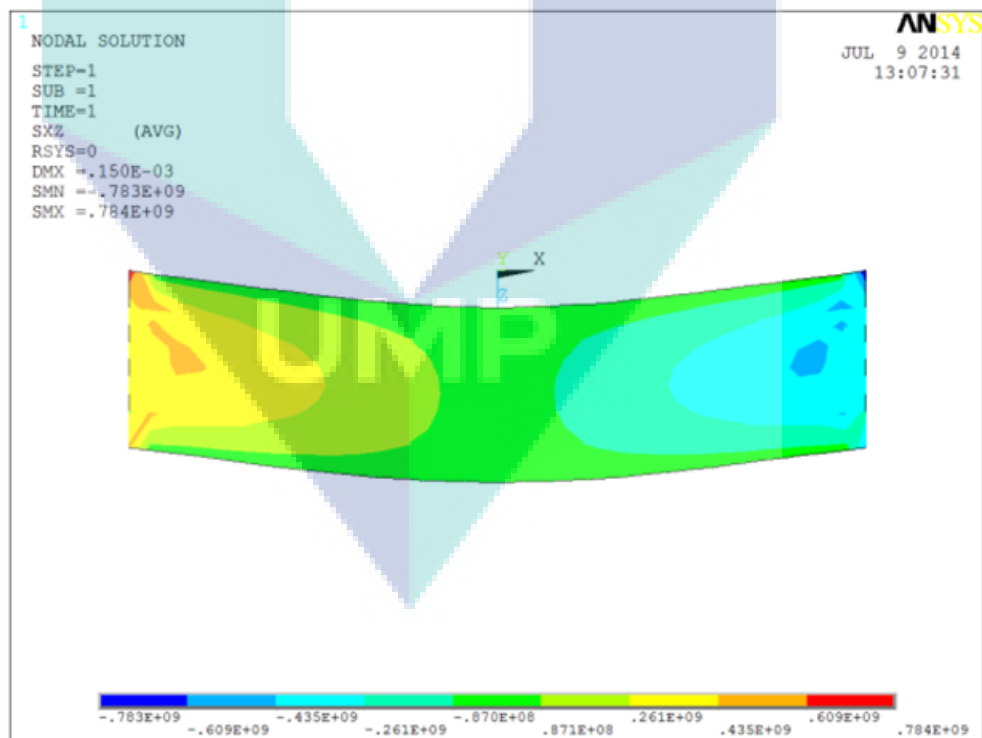
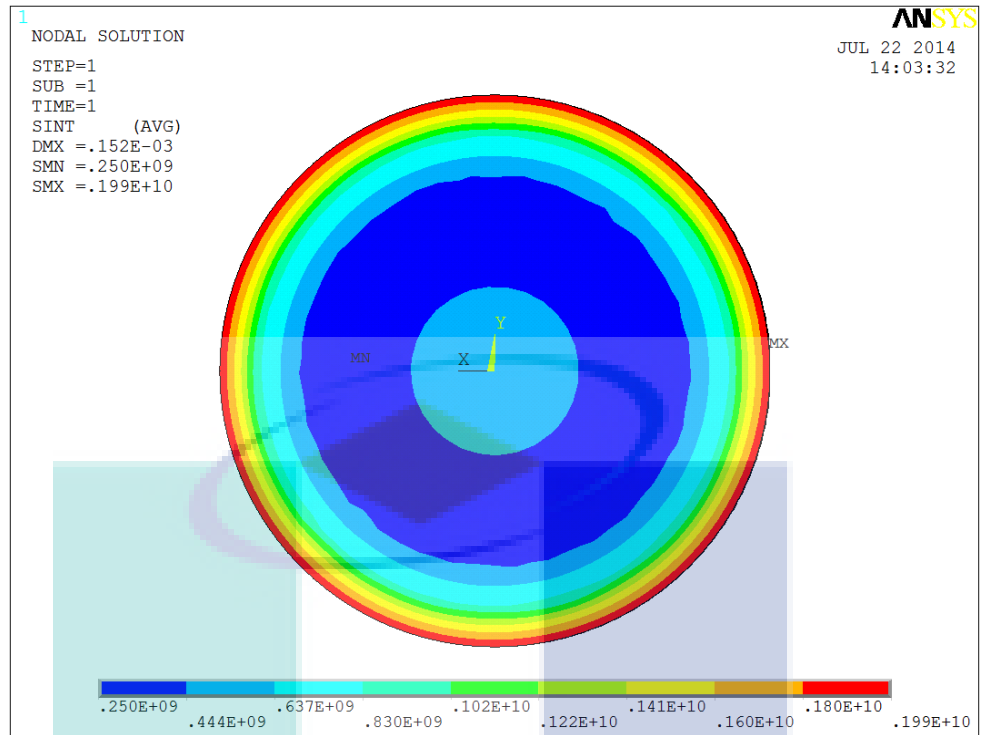
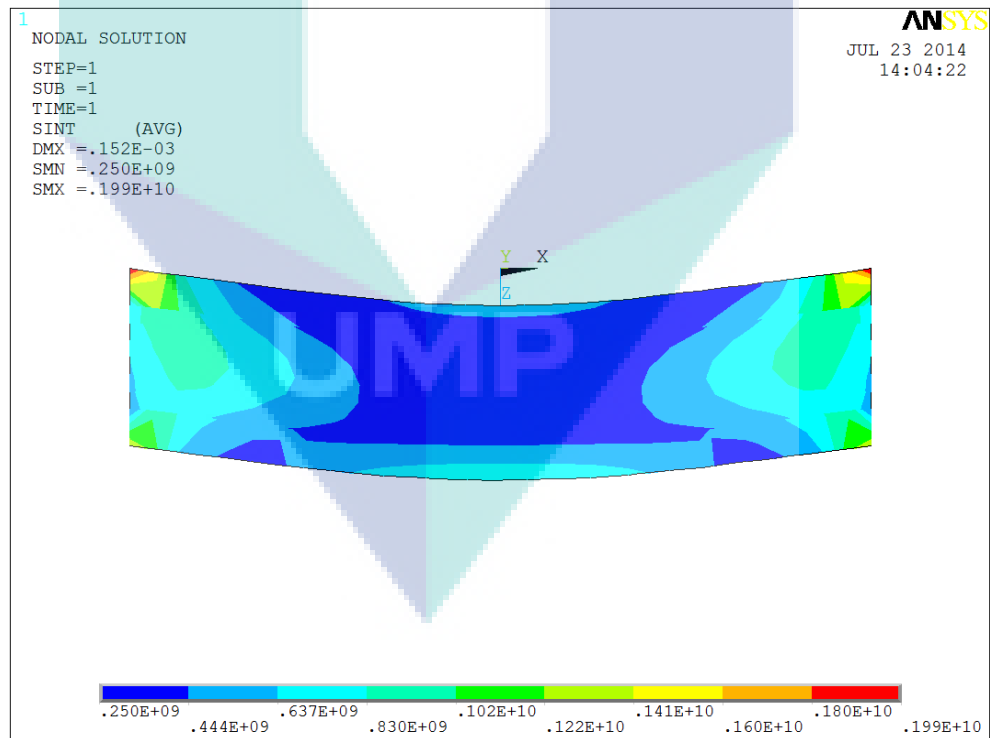
(a) τ_{xz} (top view)(b) τ_{xz} (mid-plane cross-section front view)

Figure 5.10: Transverse shear stress distribution of the HA/Ti FGM plates under isothermal conditions ($\bar{P}=1$, $n=1$, $L=6$, $h=0.0072\text{m}$)



(a) K (top view)



(b) K (mid-plane cross-section front view)

Figure 5.11: Stress intensity distribution of the HA/Ti FGM plates under isothermal conditions ($\bar{P}=1$, $n=1$, $L=6$, $h=0.0072\text{m}$)

The Effect of the Grading Index

Correlations between the dimensionless central deflection and the various grading indices ($n=0, 0.5, 1, 2, \infty$) of the FGM plates subjected to different load intensities taking place in the range [1, 12] are shown in Table 5.5. It is evident that for all plates the central deflection increased with a higher grading index number. In theory, the displacement change of a material strongly depends on the rigidity of its ingredient. Presently the FGM plates with a smaller grading index contain a higher compositional percentage of HA (ceramic), with a higher Young's modulus compared to that of Ti. Since the rigidity of a material increases with a greater Young's modulus, the FGM plates with a higher grading index tended to deflect more than that those with smaller grading index. The properties' gradation of a relatively isotropic nature of the FGM plates led to moderate deflections between the pure Ti and pure HA deflections. This proves the relevance of the consecutive property gradation based on ROM when producing an effective FGM.

Table 5.5: Dimensionless central deflection of FGM plates subjected to various load intensities

\bar{P}	\bar{w}				
	$n=0$	$n=0.5$	$n=1$	$n=2$	$n=\infty$
1	0.0207	0.0211	0.0210	0.0211	0.0212
2	0.0414	0.0417	0.0419	0.0422	0.0425
3	0.0622	0.0626	0.0629	0.0633	0.0637
4	0.0829	0.0834	0.0839	0.0843	0.0849
5	0.1036	0.1043	0.1048	0.1054	0.1062
6	0.1243	0.1252	0.1258	0.1265	0.1274
7	0.1450	0.1460	0.1467	0.1475	0.1486
8	0.1657	0.1668	0.1676	0.1686	0.1699
9	0.1864	0.1876	0.1886	0.1897	0.1910
10	0.2071	0.2086	0.2096	0.2108	0.2122
11	0.2278	0.2294	0.2306	0.2318	0.2335
12	0.2486	0.2503	0.2515	0.2529	0.2547

Plots in Figures 5.12(a) to 5.12(d) represent the dimensionless deflection, normal stress, transverse shear stress and stress intensity factor distributions of the FGM

plates under isothermal conditions. From Figure 5.12(a), it can clearly be seen that the intermediate deflections of the plates increased with a higher grading index number, due to their lower material rigidity. The deflection at the surfaces of all plates was equal to zero because the nodes at these locations were fixed for simply supported boundary conditions. The mechanical stress of the FGM plates did not vary significantly in comparison to homogeneous plates ($n=0, \infty$) as shown in Figure 5.12(b)) due to the small difference in the Young's modulus of the base materials. The normal stress distribution profile for all plates was almost a linear function of transverse coordinates. The properties' gradation resulted in more stress relaxation in FGM plates when compared to that in pure plates. These results revealed the importance of choosing base materials with significantly different Young's modulus.

The variation of transverse shear stresses along the transverse plane of FGM plates under isothermal conditions (shown in Figure 5.12(c)) showed that shear stress increased with a higher grading index number. The shear response of the FGM was highly related to the rigidity of the material, the same as deflection. The linear variation in the plots represented the shear stress distribution along the thicknesses of pure HA and Ti layers. The results shown in Figure 5.12(d) show that the stress intensity is distributed near the half-thickness position in all plates. However the stress intensity in FGM plates was less than that found in homogeneous plates due to the properties' gradation along the transverse plane of these plates. The most consistent stress intensity distribution was observed in an FGM plate with $n=1$. This strengthens the conclusion of the optimum grading index parameter made in previous 2-D analysis. The results presented in this section reveal the role of the grading index in the mechanical behaviours of the FGM plate. This parameter reflects the properties' distribution and the responses of the material.

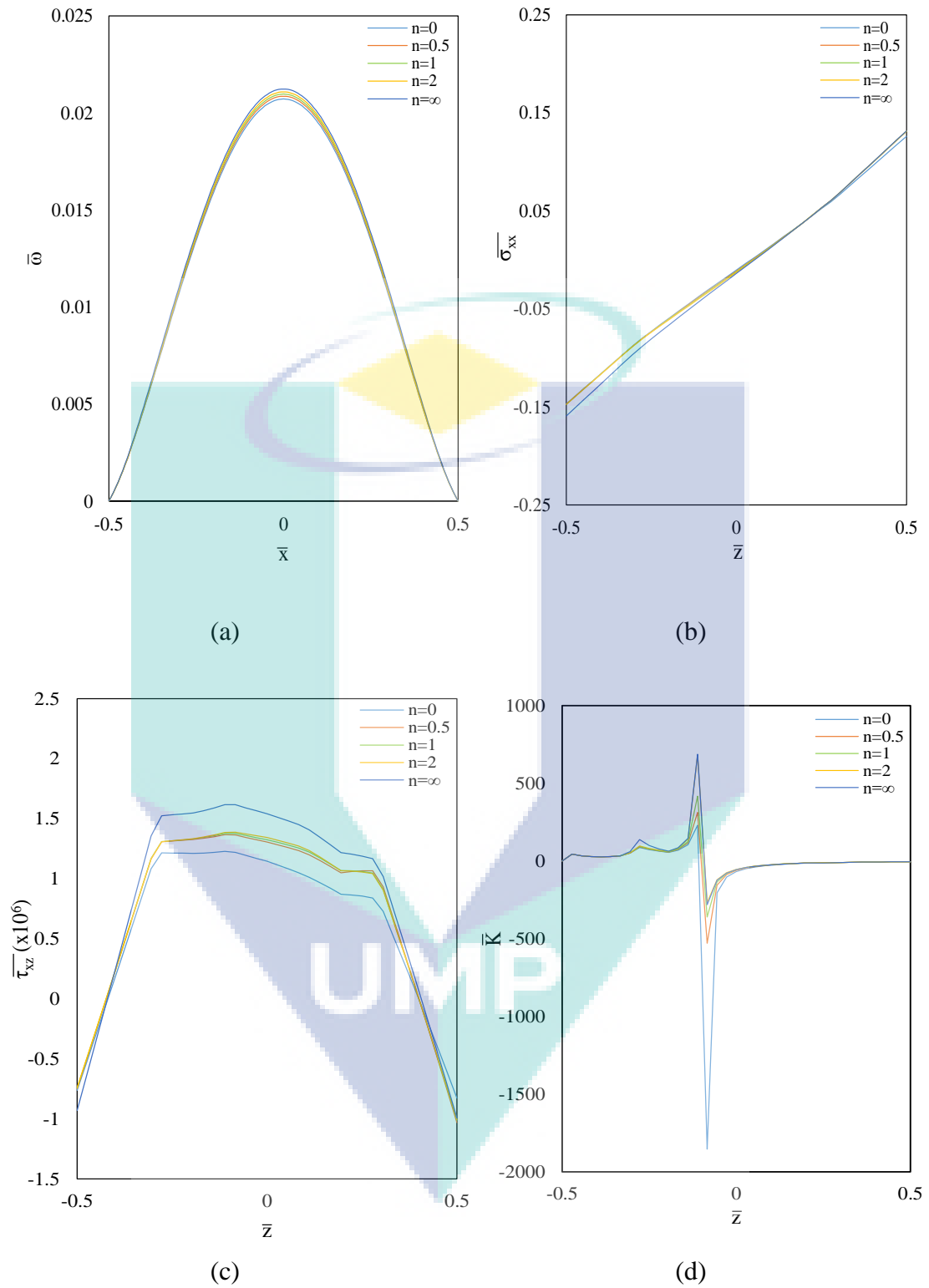


Figure 5.12: Variations of the various responses of the HA/Ti FGM plates under isothermal conditions, for various grading indices ($\bar{P}=1$, $L=6$, $h=0.0072\text{m}$)

The Effect of the Number of Layers

The variation of dimensionless deflection values along the longitudinal mid-plane of the FGM plates with different number of layers is given in Table 5.6. It is noticed in Table 5.6 that the deflection values of FGM plates with 9 layers are higher than those with 3 and 6 layers. This is due to the smoother variation of properties in the FGM plate with more layers. The approximately equal to zero deflection at the surfaces is because of the simply supported boundary conditions defined in the FGM models.

Table 5.6: Variation of deflection along the mid-plane of HA/Ti FGM plates under isothermal conditions for three different number of layers

\bar{x}	\bar{w}		
	3 Layers	6 Layers	9 Layers
-0.5	5.6213E-15	4.0283E-15	4.0356E-15
-0.4	4.7885E-03	4.7885E-03	4.7943E-03
-0.3	1.0805E-02	1.0805E-02	1.0813E-02
-0.2	1.6119E-02	1.6119E-02	1.6131E-02
-0.1	1.9708E-02	1.9708E-02	1.9721E-02
0	2.0972E-02	2.0972E-02	2.0985E-02
0.1	1.9708E-02	1.9708E-02	1.9721E-02
0.2	1.6121E-02	1.6121E-02	1.6132E-02
0.3	1.0806E-02	1.0806E-02	1.0814E-02
0.4	4.7903E-03	4.7904E-03	4.7960E-03
0.5	1.1310E-15	1.4982E-15	1.5022E-15

The small variation in the mechanical stress values of FGM plates with different numbers of layers (given in Table 5.7) shows the lower significance of the number of layers effect on the stress field. For all plates, the HA surface was subjected to the maximum compressive stress to react with the mechanical pressure applied on it. In addition the Ti surface was subjected to the maximum tensile stress because the plates were supported from the bottom surface. The mechanical stress of the FGM plate with 9 layers was the highest compared to the mechanical stress of others, probably because of the small thickness of the distinctive FGM layers.

Table 5.7: Normal stress along the thickness of HA/Ti FGM plates for three different number of layers subjected to mechanical loading

\bar{z}	3 Layers	$\overline{\sigma_{xx}}$ 6 Layers	9 Layers
-0.5	-0.1473	-0.1473	-0.1474
-0.4	-0.1170	-0.1169	-0.1170
-0.3	-0.0867	-0.0866	-0.0865
-0.2	-0.0612	-0.0608	-0.0609
-0.1	-0.0360	-0.0363	-0.0363
0	-0.0117	-0.0120	-0.0120
0.1	0.0128	0.0129	0.0129
0.2	0.0396	0.0391	0.0393
0.3	0.0669	0.0672	0.0673
0.4	0.0991	0.0992	0.0993
0.5	0.1313	0.1313	0.1313

Through-the-thickness variations of transverse shear stress and stress intensity factors for FGM plates with 3, 6 and 9 layers under isothermal conditions are shown in Figures 5.13(a) and 5.13(b) respectively. In Figure 5.13(a), it can clearly be seen that the minimum shear stress that appeared in the form of compression was located at the end surfaces of the FGM plates. Linear change in the plots represents the shear stress distribution along the thicknesses of the pure HA and Ti layers. The shear stress along the graded layers' thickness, which decreased with increasing number of layers, is due to the variation of the smoother properties along the thickness of the plates.

Extremely large compressive and tensile stress intensities occurred at the mid-thickness location of the FGM plate with 3 layers, as shown in Figure 5.13(b). This was due to the abrupt transition of properties in the plate. The lowest stress intensity distribution of the FGM plate with 6 layers was further evidence to support its selection as the optimum number of layers parameter in the previous 2-D analysis.

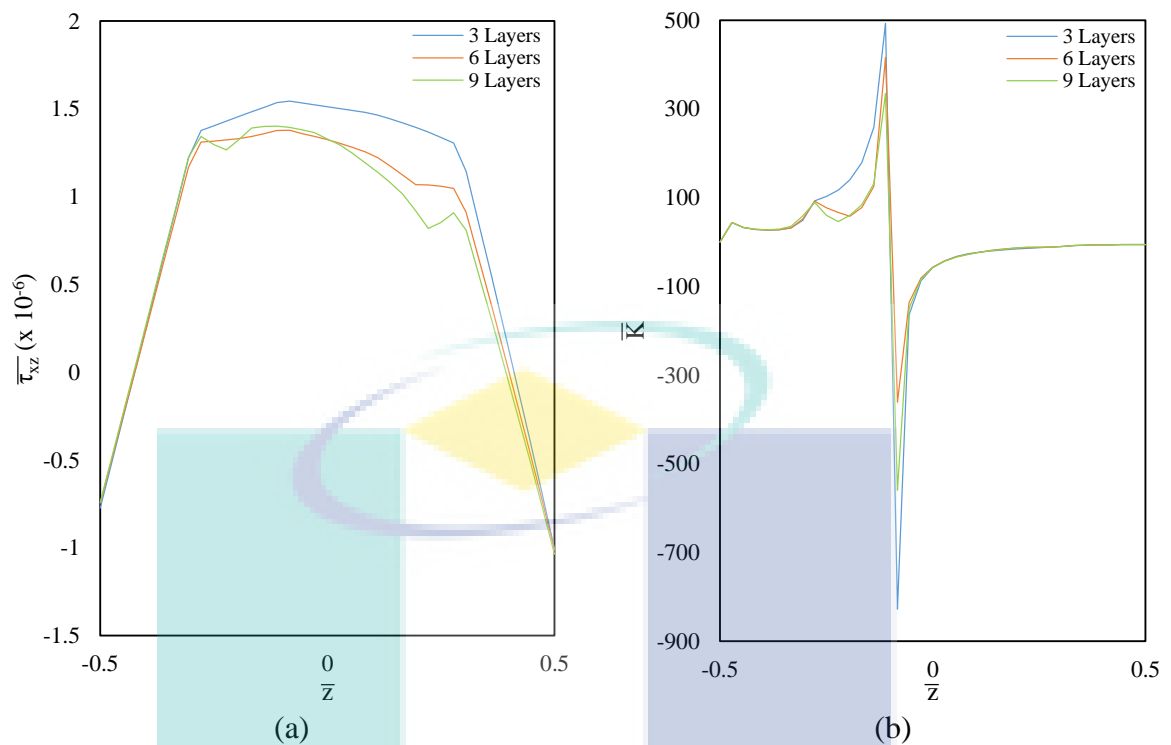


Figure 5.13: Variations of the various responses of the HA/Ti FGM plates under isothermal conditions, for various numbers of layers ($\bar{P}=1$, $n=1$, $h=0.0072\text{m}$)

The Effect of Thickness

The effect of the thickness parameter on the responses of FGM plates under isothermal loading were investigated by considering FGM plates with thicknesses in the range 0.006 to 0.0084 m. The variation of deflection, normal stress and transverse shear stress distributions of the FGM plate for different thicknesses are represented in Figures 5.14(a), 5.14(b) and 5.14(c) respectively. Figure 5.14(a) shows that the deflection of the FGM plates decreases within increasing thickness, because of the higher load intensity. This subsequently leads to a lower mechanical stress distribution as illustrated in Figure 5.14(b). For all FGM plates, the maximum compressive stress occurred at the surface where the load was applied (HA surface). The shear stress distribution given in Figure 5.14(c) was highly consistent with the deflection and normal stress distributions. The shear stress of the FGM plate with a higher thickness was greater than that with less thickness due to the high deflection of the structure.

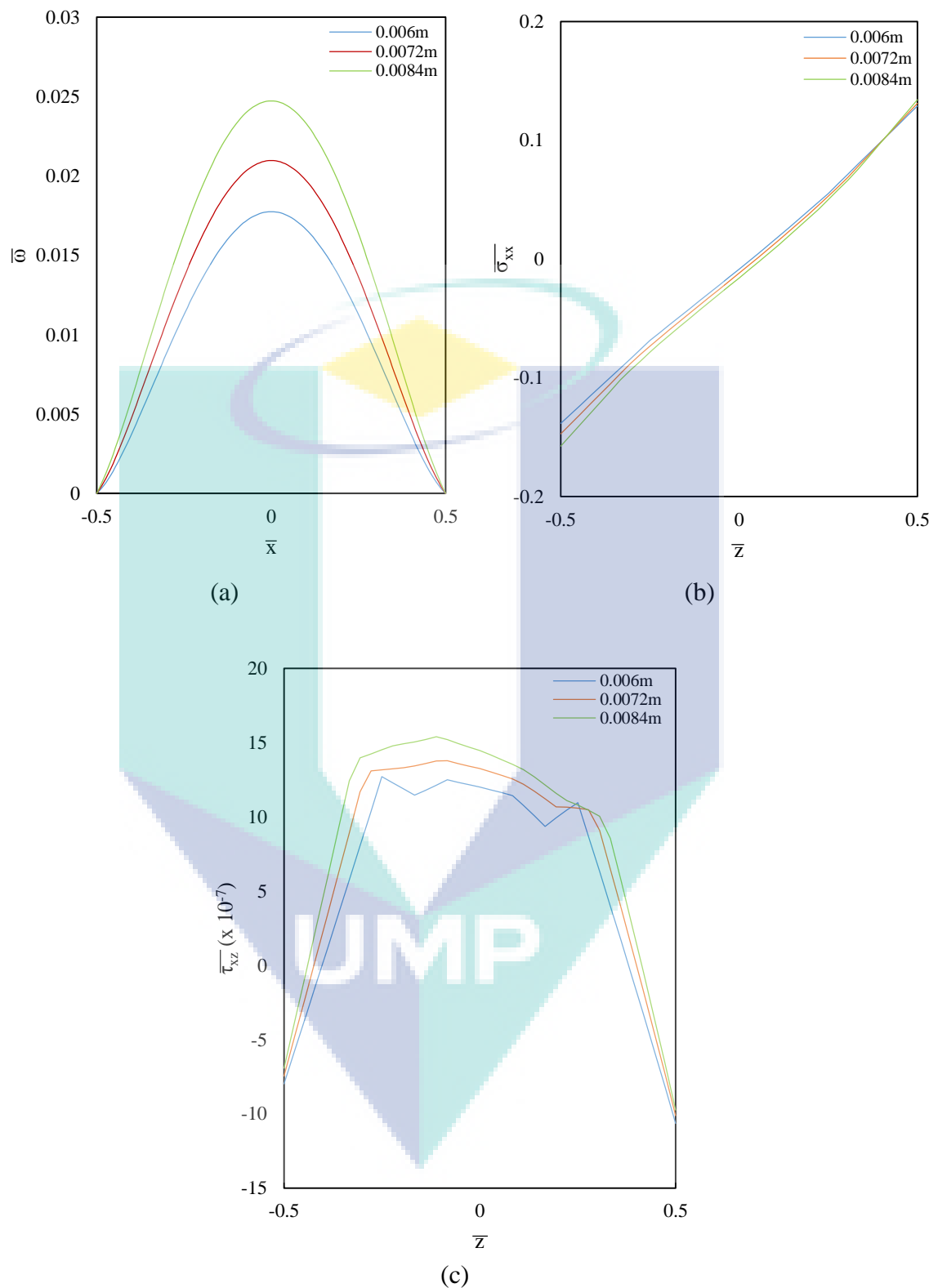


Figure 5.14: Variations of various responses of the HA/Ti FGM plates under isothermal conditions, for various thicknesses ($\bar{P}=1$, $n=1$, $L=6$)

5.4.2 Thermal Loading

As mentioned in the previous chapter, thermal loading was applied to the FGM plates by subjecting the top HA surface to a higher temperature of 300°C while maintaining the bottom Ti surface at room temperature (22°C). The thermal characteristics of the FGM plates were calculated by taking into account the effect of the geometrical design parameters considered in 2-D analysis on the responses of the plates, such as those made in previous subsection.

Colour contour images of the displacement distribution of the optimum FGM plate under thermal excitation from two different views was considered during isothermal analysis. This is shown in Figures 5.15(a) and 5.15(b) respectively. The decreasing deflection from the outer radial surface to the inner position of the top HA plane (shown in Figure 5.15(a)) represents the shrinkage phenomena in the structure, while the increasing deflection through the same direction of bottom Ti plane in Figure 5.15(b) shows the expansion of the structure. Both of these phenomena reflect the thermal loading applied to the FGM plates. The normal stress distribution contours from the top view shown in Figure 5.16(a) indicate that the maximum compressive stress occurs at the outer surface of the top HA surface of the FGM plate because of the simply supported boundary condition. The same reason causes the increasing tensile stress distribution from the half-thickness region to the bottom Ti surface, as shown in Figure 5.16(b).

Figure 5.17 shows the corresponding shear stress contour images of the optimum FGM plate under thermal excitation. The wide green colour distribution and small changes in the contours reveal that the FGM plate was subjected to moderate shear stress distribution which is not much affected by the thermal loading. The contour images shown in Figure 5.18 are in high agreement with the isothermal case when the maximum stress intensity is at the radial edge of the top HA surface. The stress intensity factor distribution was strongly affected by the normal stress response. The lower difference in normal stress distribution along the radial plane of the FGM plate under thermal loading led to the even stress intensity factor distribution of the plate.

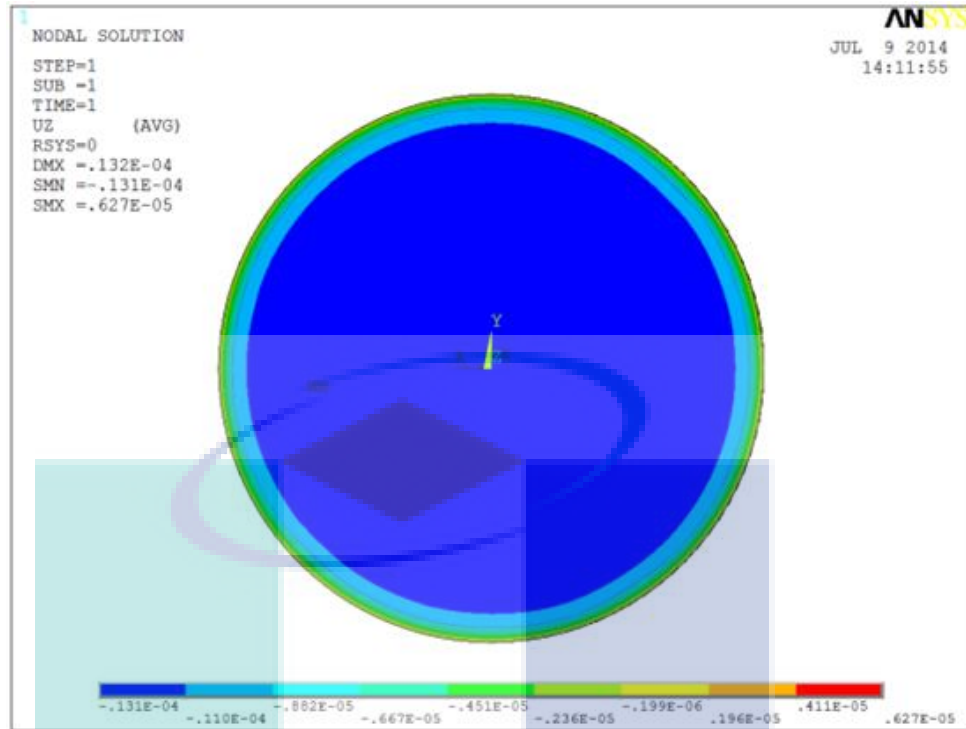
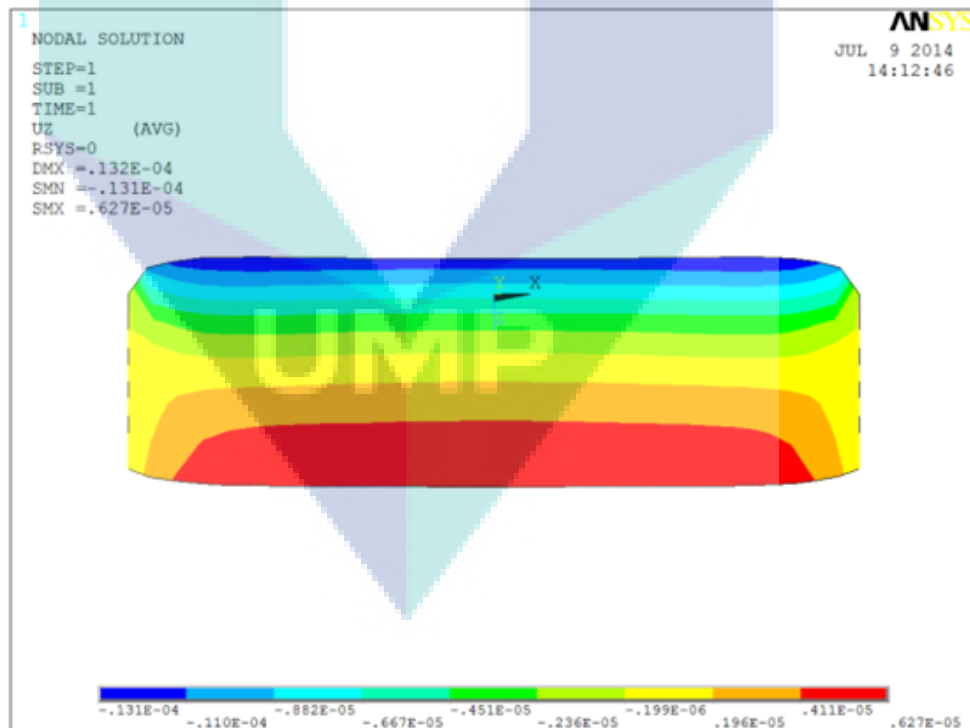
(a) δ_{zz} (top view)(b) δ_{zz} (mid-plane cross-section front view)

Figure 5.15: Deflection distribution of the HA/Ti FGM plates under thermal excitation ($\bar{P}=1$, $n=1$, $L=6$, $h=0.0072\text{m}$)

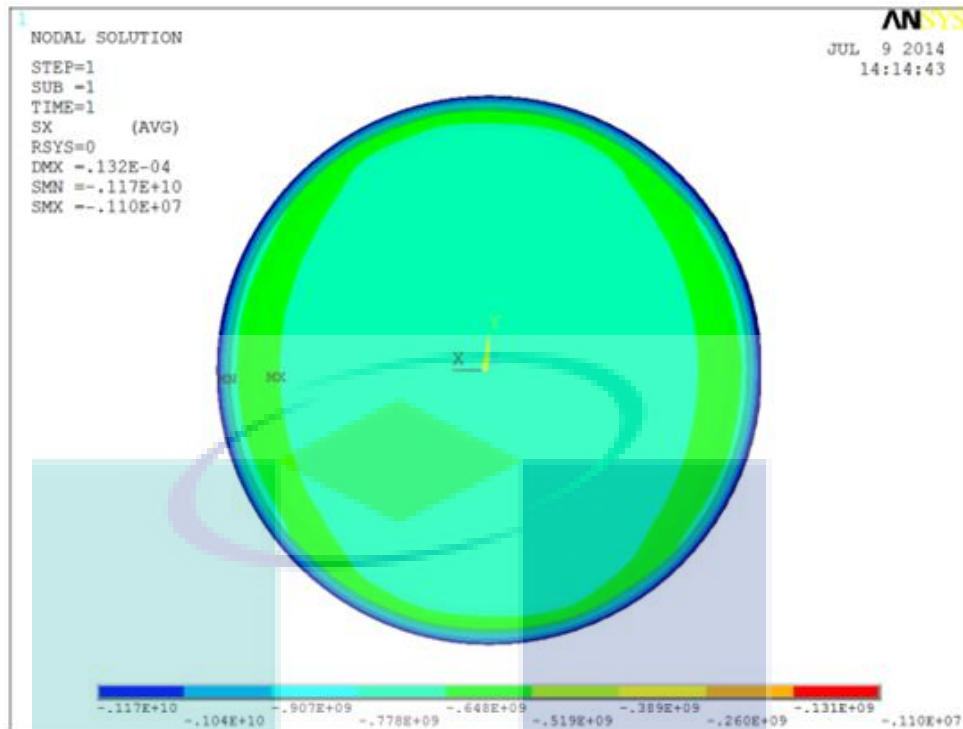
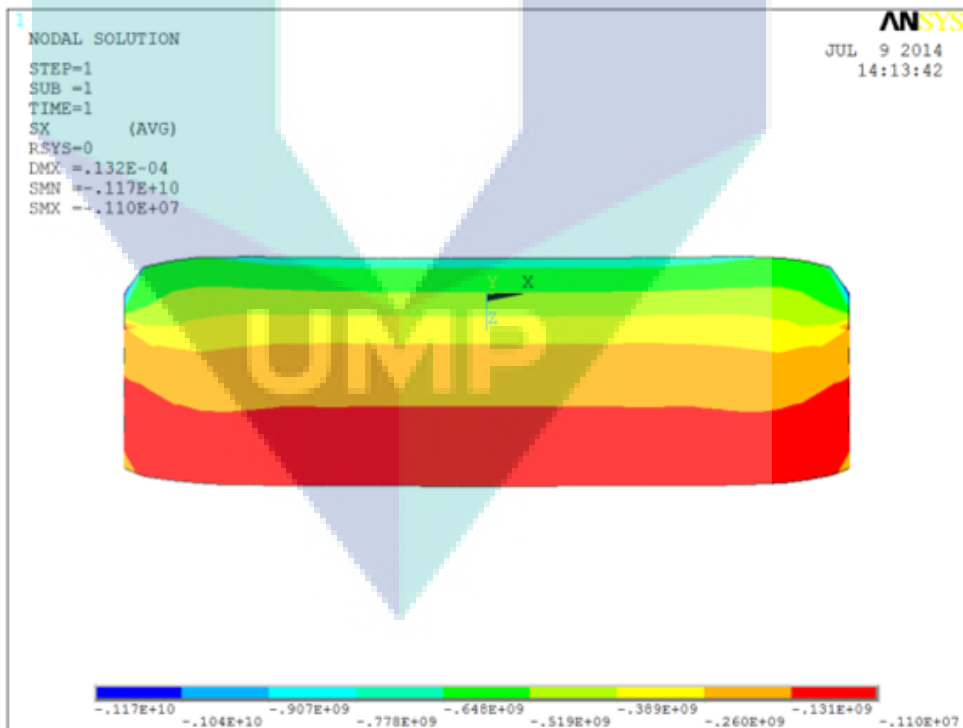
(a) σ_{xx} (top view)(b) σ_{xx} (mid-plane cross-section front view)

Figure 5.16: Normal stress distribution of the HA/Ti FGM plates under thermal excitation ($\bar{P}=1$, $n=1$, $L=6$, $h=0.0072\text{m}$)

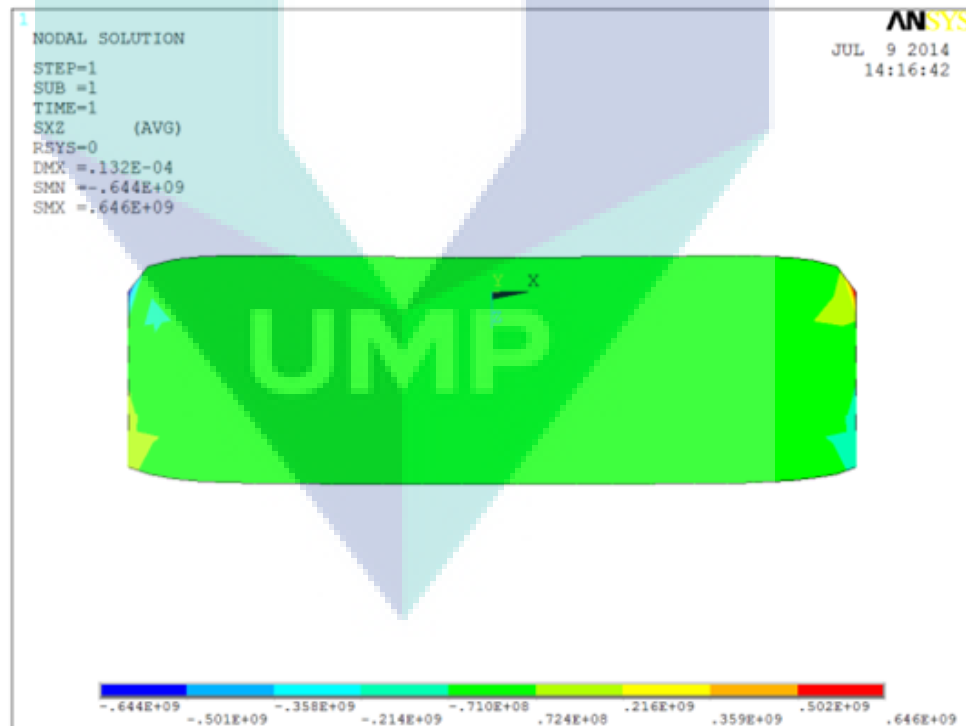
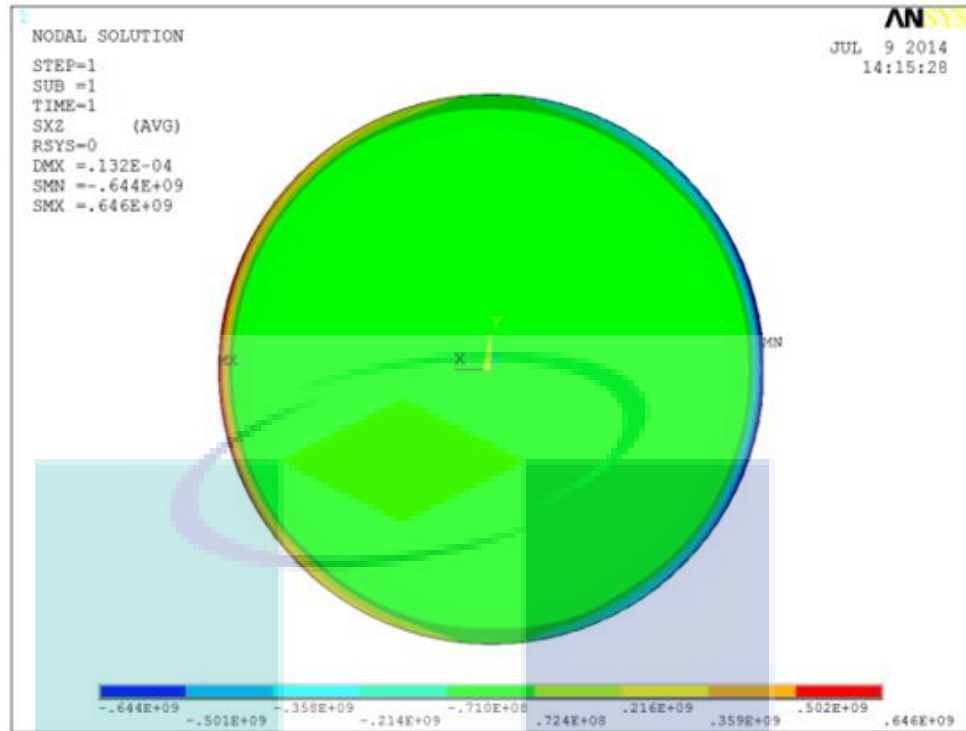
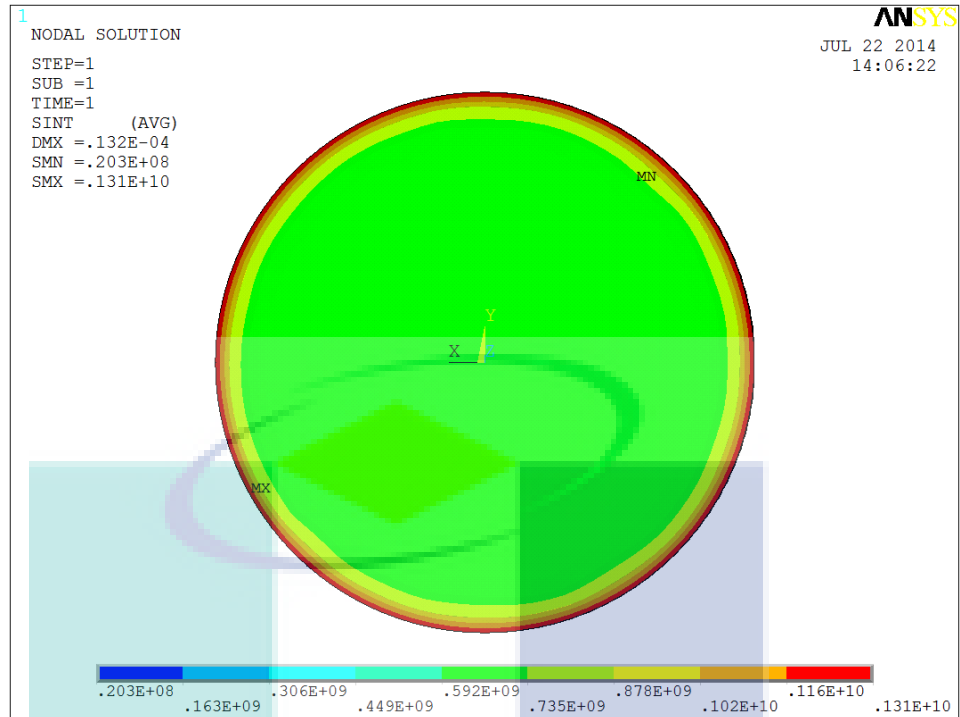
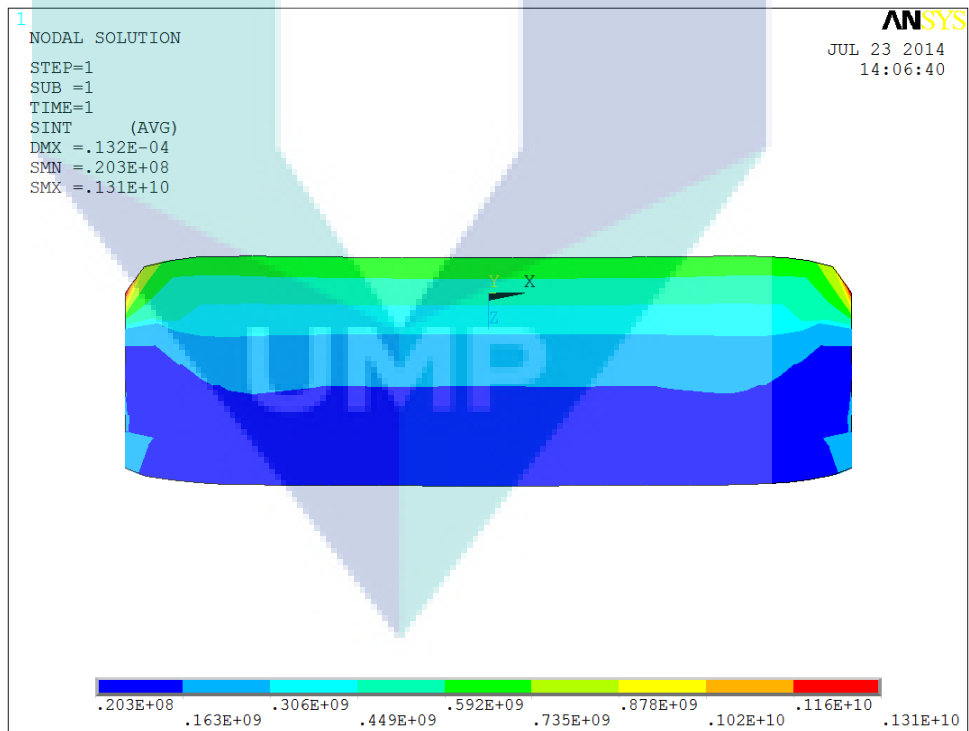


Figure 5.17: Transverse shear stress distribution of the HA/Ti FGM under thermal excitation ($\bar{P}=1$, $n=1$, $L=6$, $h=0.0072\text{m}$)



(a) K (top view)



(b) K (mid-plane cross-section front view)

Figure 5.18: Stress intensity distribution of the HA/Ti FGM plates under thermal excitation ($\bar{P}=1$, $n=1$, $L=6$, $h=0.0072\text{m}$)

The Effect of the Grading Index

The steady-state temperature distribution along the thickness direction of the FGM plates subjected to the higher temperature of 300°C at the top HA surface for various grading indices is given in Figure 5.19. It was observed that the temperature along the transverse plane of the FGM plates of HA and Ti constituents was always less than that corresponding to a purely Ti or HA plate. The temperature distribution for the isotropic materials is a linear function of the thickness direction. The temperature profile of the isotropic and FGM plates were different due to variation in the thermal conductivity of the laminated plates. This showed that the FGM plates are able to withstand high temperatures.

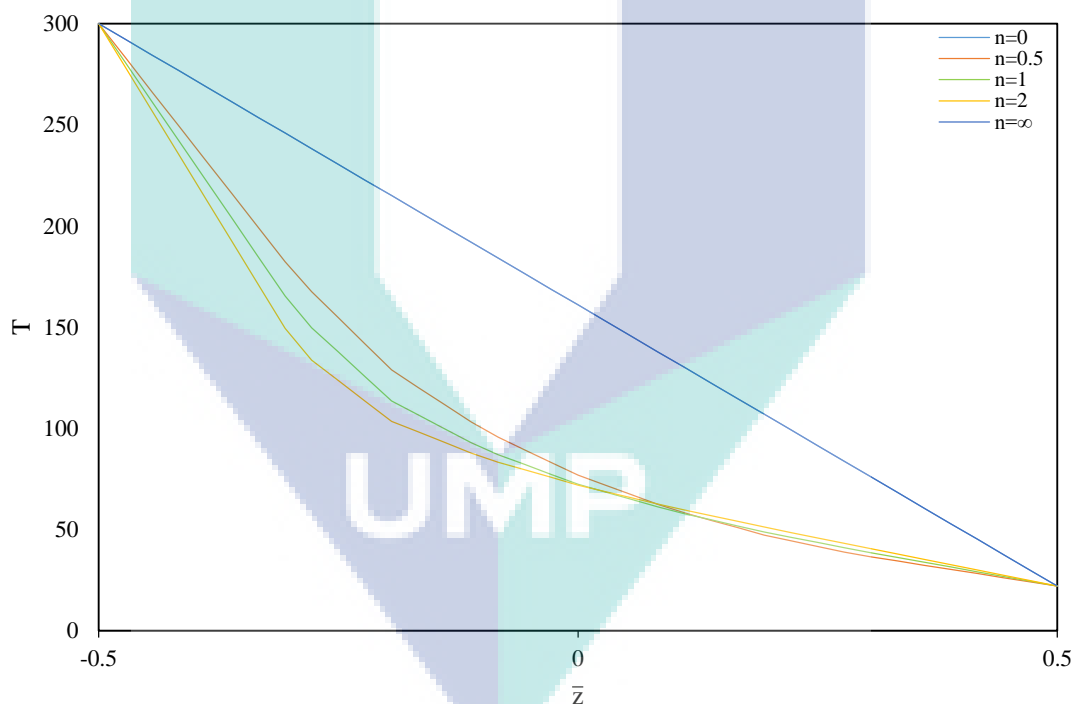


Figure 5.19: Temperature distribution along the thickness of the HA/Ti FGM subjected to thermal loading ($\bar{P}=1$, $L=6$, $h=0.0072\text{m}$)

The deflection distribution of the plates depended strongly on the temperature distribution as well as the thermal expansion coefficient of the material constituent. From Figure 5.20(a), it is clearly seen that the FGM plate with the higher temperature

distribution tends to deflect more than that with the lower temperature. The plate that exhibited the higher temperature distribution tended to deform (shrink or expand) more when compared to those with a lower temperature distribution. The higher deflection of the pure HA plate ($n=0$) compared to that of pure Ti plate ($n=\infty$) was due to the higher thermal expansion coefficient of the material.

The corresponding normal stress distribution of the FGM plates is shown in Figure 5.20(b). It can be seen that the thermal stress distribution of homogeneous plates ($n=0,\infty$) is a linear function of the thickness coordinate whereas that of FGM plates ($n \neq 0,\infty$) is a cubic function of the thickness coordinate. The pure HA plate ($n=0$) was subjected to larger thermal stresses because of its low thermal conductivity, while the Ti plate ($n=\infty$) was exposed to lower thermal stress than the HA material because of its high thermal conductivity. The moderate thermal conductivity of the FGM plates led to the lower thermal stress distribution in comparison to that of the homogeneous HA and Ti plates. The negative stress distribution seen in all nodes located along the thickness plane of all plates was subjected to compressive stress due to material expansion in the negative thickness direction while subjected to thermal excitation. For all plates, the neutral plane, where zero normal stress was found, was moved from the mid-plane to the bottom Ti surface. Figure 5.20(b) shows the capability of the HA/Ti FGM to resist high thermal stresses, which reflects its potential applications at elevated temperatures.

The increasing compressive shear stress distribution shown in Figure 5.20(c) represents the higher shear distortion of the intermediate FGM layers. The higher deflection of homogeneous HA and Ti plates led to a higher shear stress distribution. Figure 5.20(d) also shows that the material gradation does not affect the stress intensity factor distribution of the FGM plates.

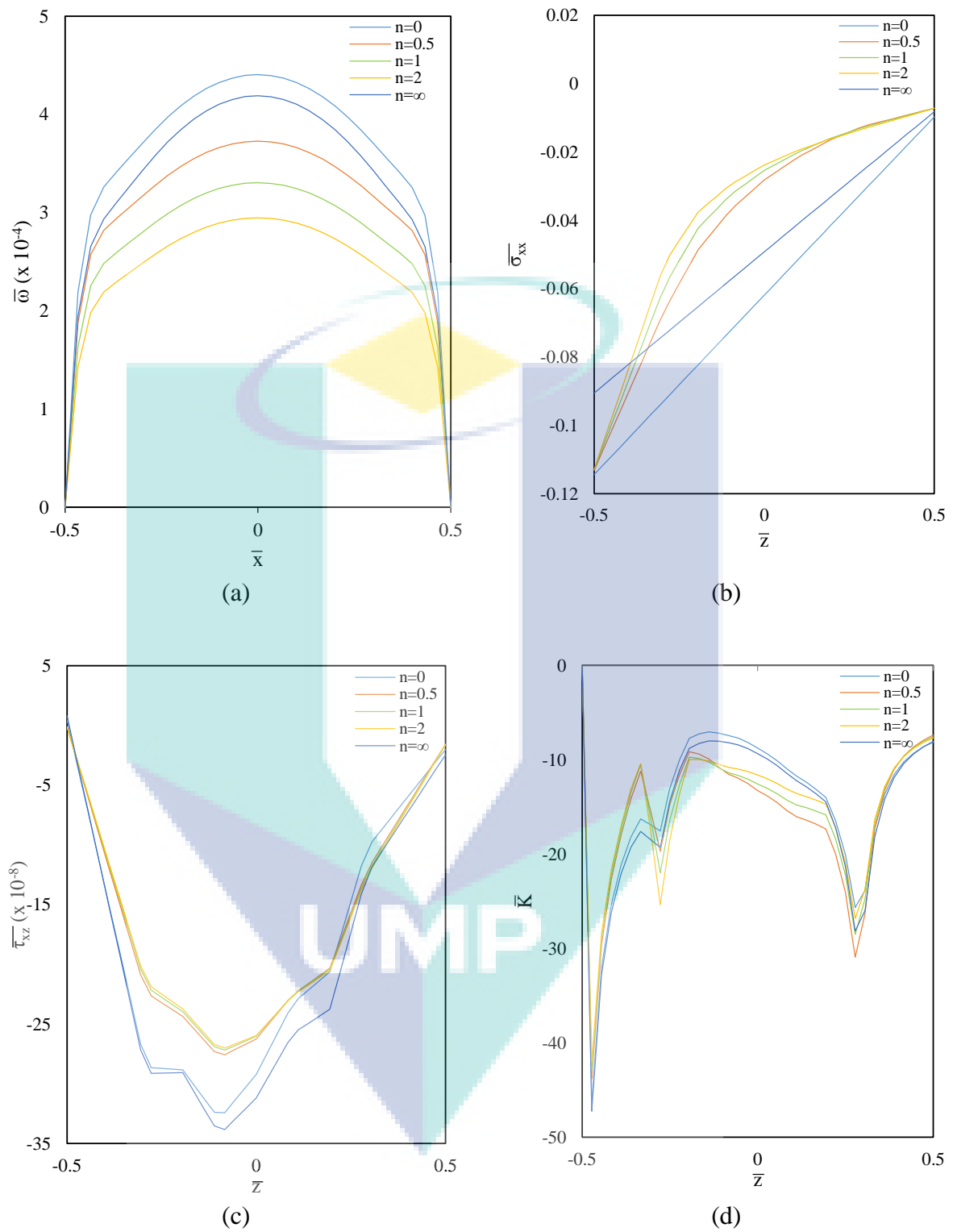


Figure 5.20: Responses of the FGM plates with different grading indices subjected to thermal loading ($\bar{P}=1, L=6, h=0.0072\text{m}$)

The Effect of the Number of Layers

The effect of the number of layers parameter on the structural responses of the FGM plate under thermal excitation can be seen in Figure 5.21. As indicated in Figure 5.21(a), the deflection at the intermediate thickness of the FGM plate which consists of more layers was lower than those with less layers. The displacement distribution led to a similar plot trend for the corresponding normal stress distribution shown in Figure 5.21(b), where the plate with less thickness was subjected to higher thermal stress. The variation in thermal conductivity and elastic properties along the thickness of the FGM plate with more layers produced more relaxation within the plate, thus the deflection and thermal stress were lower. However, the optimal or minimum number of layers needs to be determined to make the fabrication of the FGM possible. From the results shown in Figures 5.21(a) and 5.21(b), six layers was considered sufficient since the displacement and axial stress of all plates did not vary significantly. An FGM with nine layers is not recommended since it is subjected to higher shear distortion when compared to FGMs with three and six layers as shown in Figure 5.21(c). This result is reasonable since more shear stress is required to keep the laminated layers from slip past each other due to thermal excitation.

As noted in Figure 5.21(d), the compressive stress intensity peak appeared near the top HA surface for all FGM plates. The stress intensity accumulated at this location because of the extremely low thermal conductivity of HA. The much smaller stress intensity factor distribution of the present plate when compared to those shown in Figure 5.13(b) led to the conclusion that failures may occur due to mechanical loading rather than thermal loading.

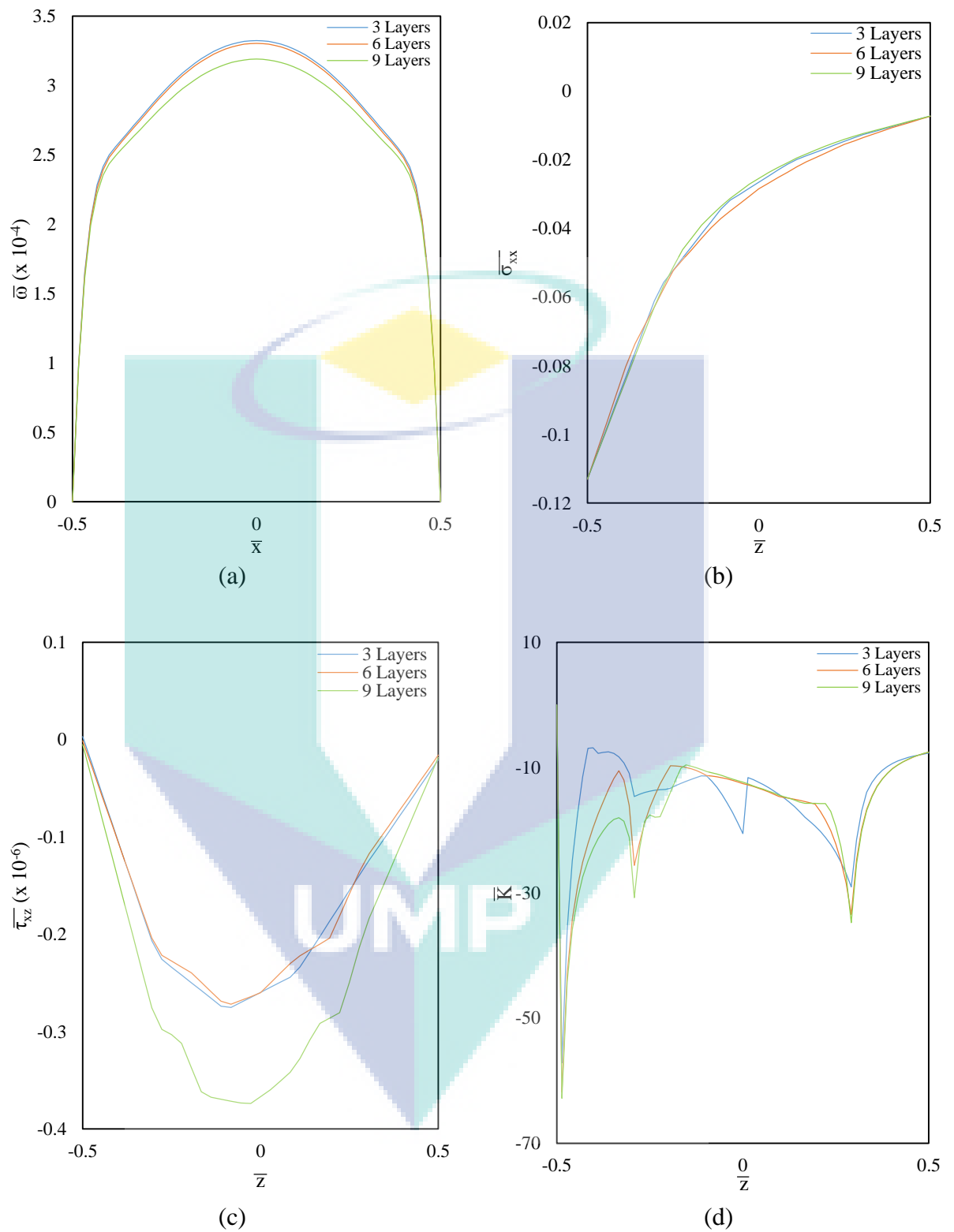


Figure 5.21: Responses of the HA/Ti FGM plates with different number of layers under thermal loading ($\bar{P}=1$, $n=1$, $h=0.0072\text{m}$)

The Effects of Thickness

Figure 5.22 shows the variation in various responses due to the thermal excitation of FGM plates with three different thicknesses. The extremely small responses deflection of the present FGM plate (shown in Figure 5.22(a)) when compared to those given in Figure 5.14(a) proves that the FGM plate tended to deflect more due to mechanical loading rather than thermal loading. The low temperature distribution of the FGM plate under thermal loading due to low thermal conductivity of the HA constituent led to the small deflection being interpreted in terms of the shrinkage and expansion of the material. These findings on the effect of the thermal conductivity are in agreement with established work (Alshorbagy *et al.*, 2013). The minimum deflection of the FGM plate with a thickness of 0.0072 m strengthens the conclusion of the optimum thickness made during 2-D optimization analysis.

Through-the-thickness variation in the normal stress of the HA/Ti FGM plates exposed to thermal excitation is illustrated in Figure 5.22(b) for different FGM thicknesses. The linear thermal stress distribution of the FGM plate with a thickness of 0.0084 m (shown in Figure 5.22(b)) showed that giving more thickness to the structure may eliminate the FGM behaviours. The FGM plate with the lowest thickness of 0.006 m however was subjected to greater thermal stress in comparison to those subjected to an FGM plate with a moderate thickness of 0.0072 m because of a drastic change in the properties' variation within the structure.

The corresponding transverse shear stress distribution illustrated in Figure 5.22(c) shows the maximum shear stress distribution at the intermediate thickness. This arose by decreasing the thickness of the FGM plate. The FGM plate with a thickness of 0.006 m is the highest when compared to others because the same reason caused the higher thermal stress distribution of the plate.

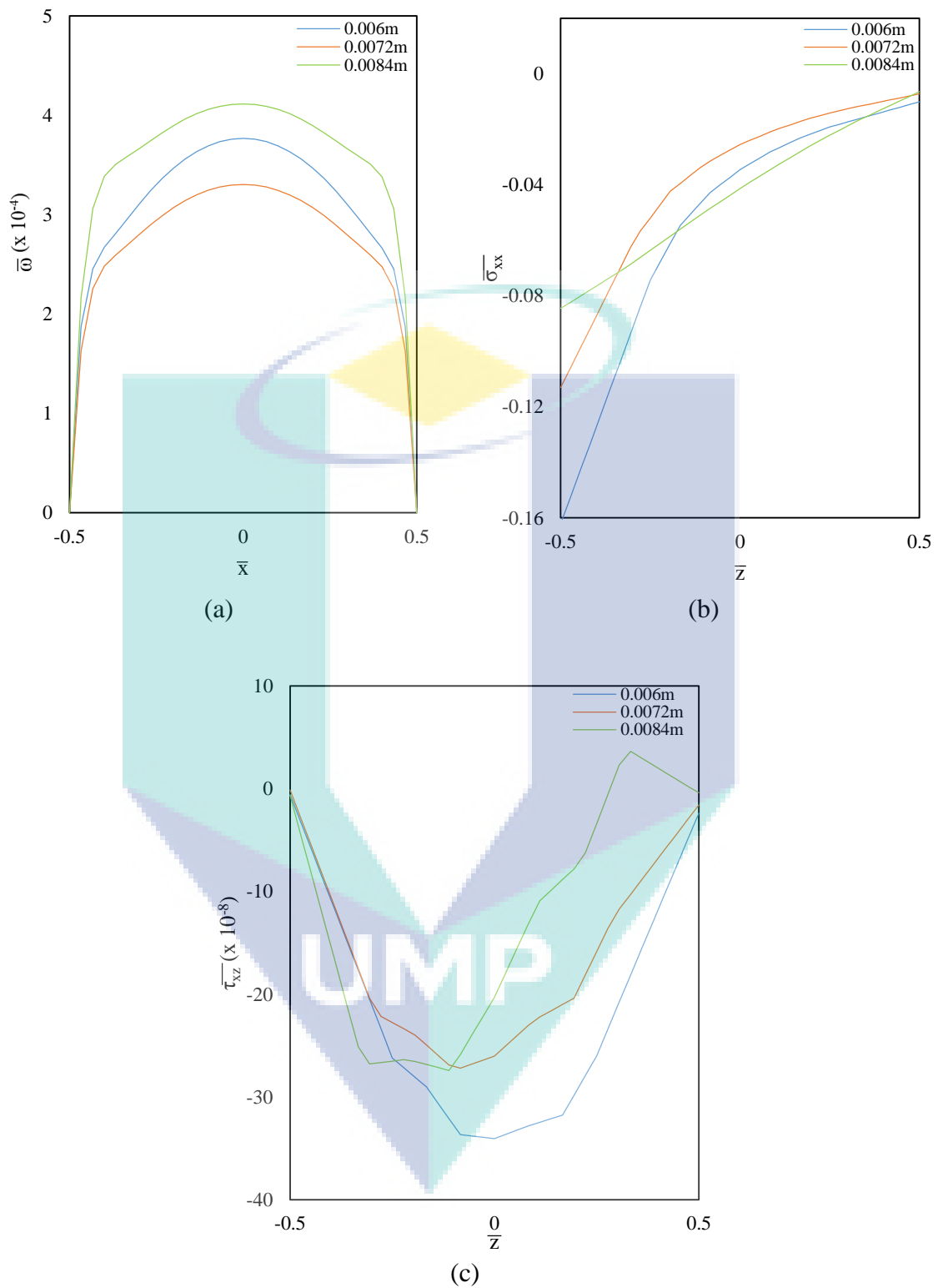


Figure 5.22: Responses of the FGM plates with different thicknesses of the FGM phase subjected to thermal loading ($\bar{P}=1$, $n=1$, $L=6$)

The Effect of Heat Generation

In order to determine the effect of heat generation on an FGM's thermal characteristics, an FGM plate under thermal excitation with a heat source ($\dot{q}=100 \times 10^6 \text{ watt/m}^3$) was considered. Initially, the temperature distribution along the transverse plane of the FGM plate was computed and is shown in Figure 5.23(a). From Figure 5.23(a), it was evident that the temperature of the pure HA plate was greater than the pure Ti and the FGM plates due to the low thermal conductivity (Alshorbagy *et al.*, 2013). The composition of HA in the FGM plates led to a slightly increased temperature near the top HA surface. This was confirmed when the temperature decreased with the increasing grading index number. The temperature distribution of the pure Ti plate was maintained as a linear function of the thickness coordinate due to the high thermal conductivity of this material. Obvious differences in the plots shown in Figures 5.23(b), 5.23(c) and 5.23(d) show the dominant role of heat generation on deflection, normal stress and transverse shear stress of the optimum FGM plate respectively. From Figure 5.23(b), it is indicated that the deflection of the FGM plate with heat generation is greater than that without heat generation. This is reasonable since heat generation leads to a higher temperature distribution through the thickness of the FGM plate. The same factor subsequently induced a higher compressive stress distribution and the sharp shear stress jump shown in Figures 5.23(c) and 5.23(d) respectively.

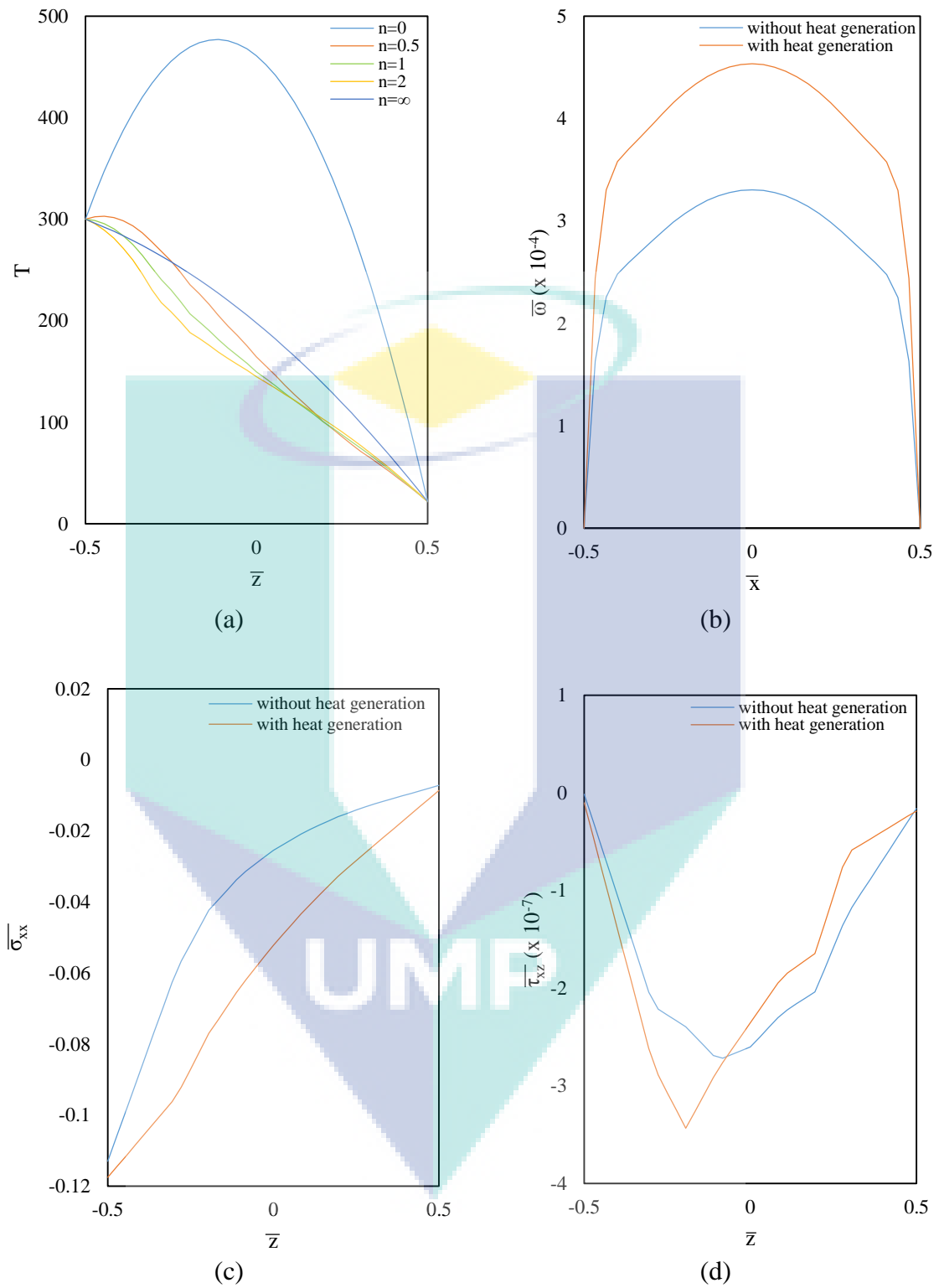
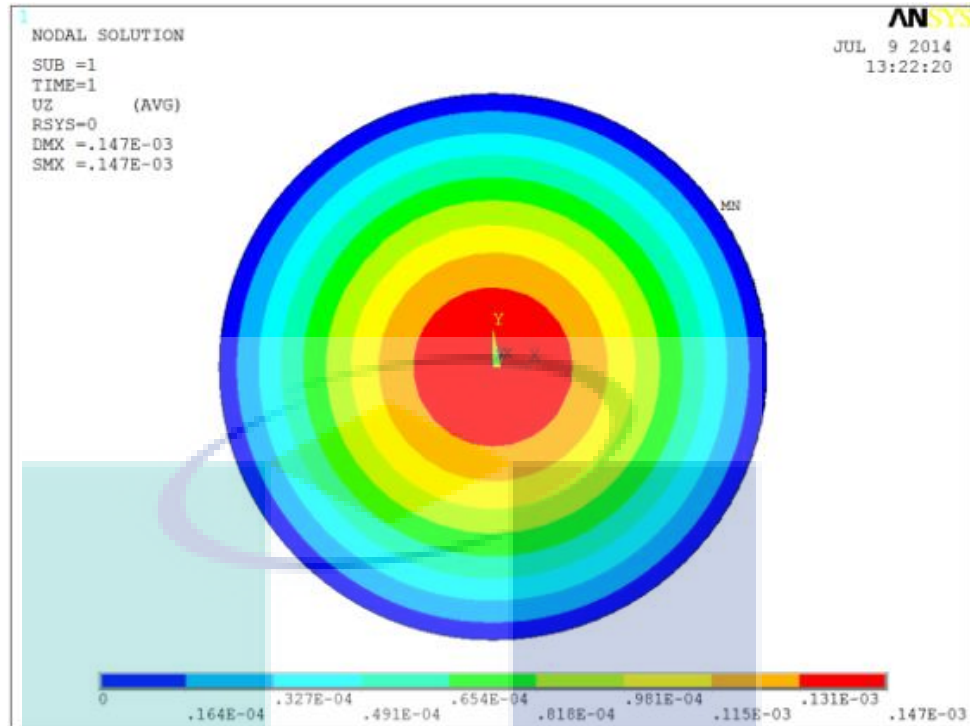
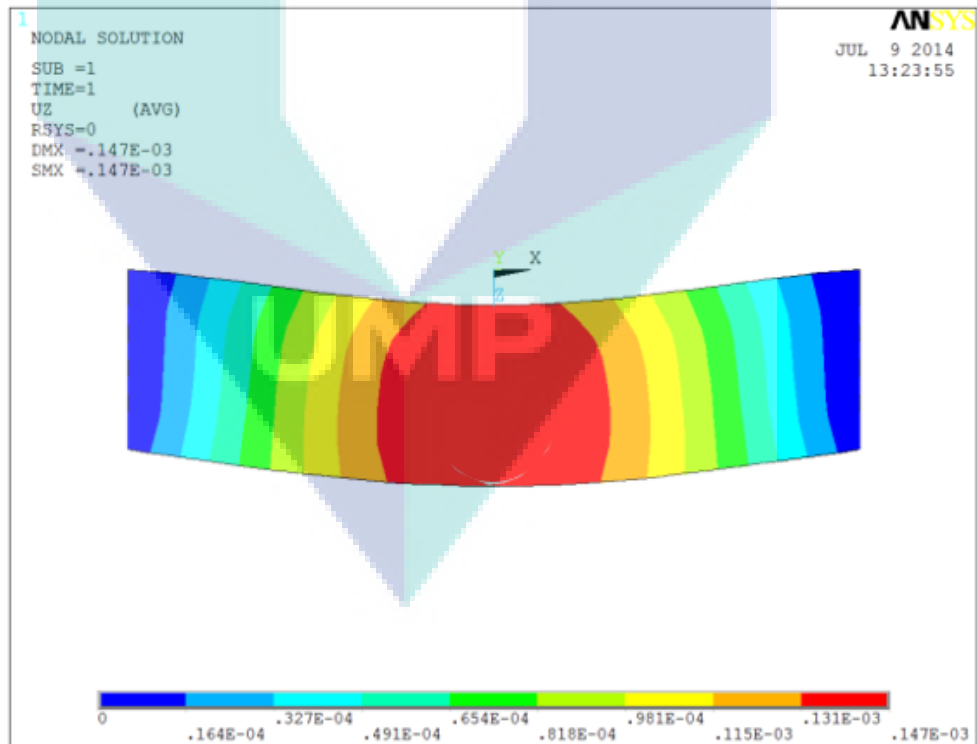


Figure 5.23: Responses of the FGM plates subjected to thermal loading with and without a heat source ($\bar{P}=1$, $n=1$, $L=6$, $h=0.0072\text{m}$)

5.4.3 Thermo-mechanical Loading

As described in Chapter 4, the modelling of thermo-mechanical problems was carried out by considering an HA/Ti FGM plate where the top HA surface was subjected to both mechanical and thermal loadings simultaneously. The effects of heat generated inside the FGM body on the behaviours of the plate when applying thermo-mechanical loading, were also included in this discussion to show the ability of the structure to withstand extreme and multiple loadings.

The deflection contours shown in Figures 5.24(a) and 5.24(b) are highly consistent with those found in FGM plates under isothermal loading, illustrated in Figure 5.9. The slightly different deflection distribution which was found in terms of a rising maximum deflection towards the bottom Ti surface of the present FGM plate showed the different effects of the coupled thermo-mechanical loading. Since the proximity of the deflection contours of this FGM plate was much closer to that under isothermal loading (rather than that under thermal excitation), this result found that the effects of mechanical loading on the plate was greater than that produced by thermal loading. The corresponding normal stress distributions of the optimum FGM plate given in Figures 5.25(a) and 5.25(b) are almost similar to that produced in the case of isothermal loading. The FGM plate was subjected to stress distribution under thermo-mechanical loading in a range that was lower than that subjected to isothermal loading because of the lower range of deflection responses. The same reason led to the differences in the corresponding shear stress and stress intensity factor distributions illustrated in Figures 5.26 and 5.27 respectively.

(a) δ_{zz} (top view)(b) δ_{zz} (mid-plane cross-section front view)**Figure 5.24:** Deflection of the HA/Ti FGM plates under thermo-mechanical loading

($\bar{P}=1$, $n=1$, $L=6$, $h=0.0072\text{m}$)

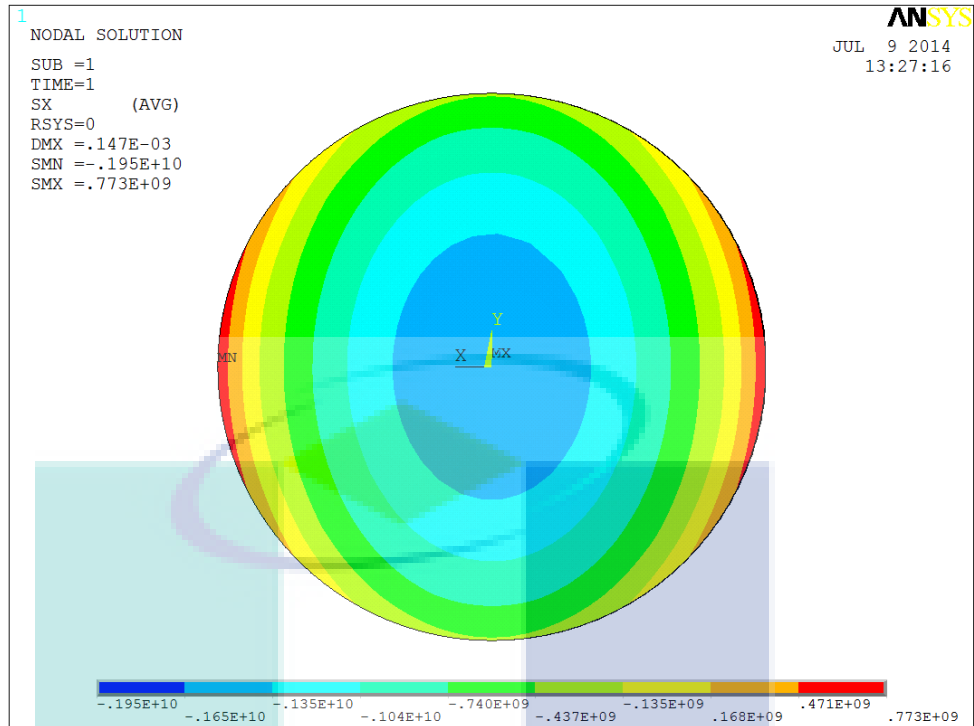
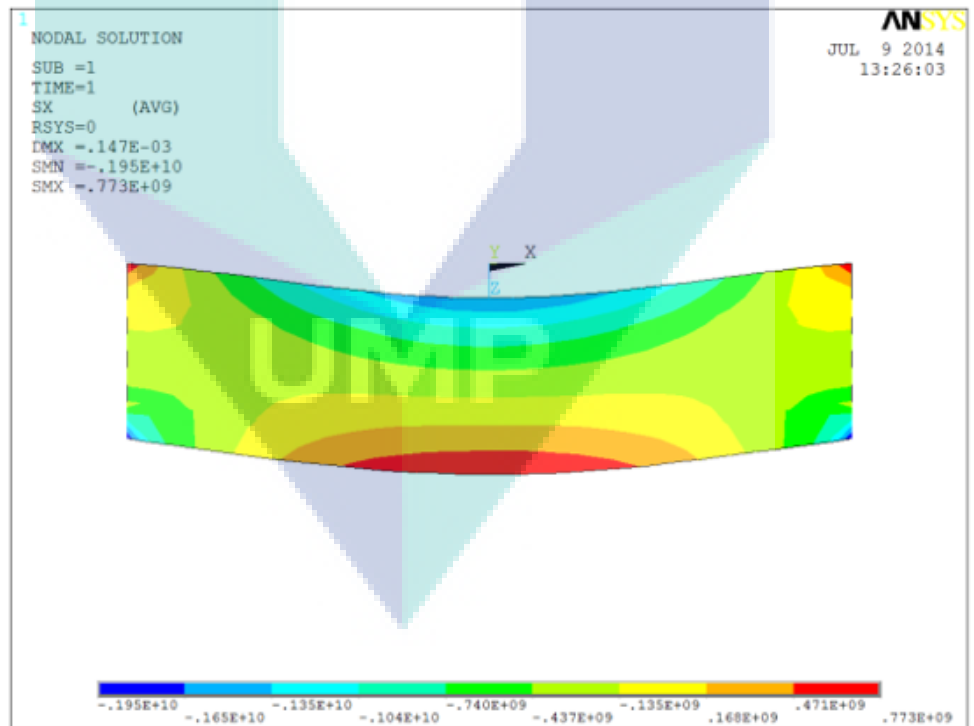
(a) σ_{xx} (top view)(b) σ_{xx} (mid-plane cross-section front view)

Figure 5.25: Normal stress distribution of the HA/Ti FGM plates under thermo-mechanical loading ($\bar{P}=1$, $n=1$, $L=6$, $h=0.0072\text{m}$)

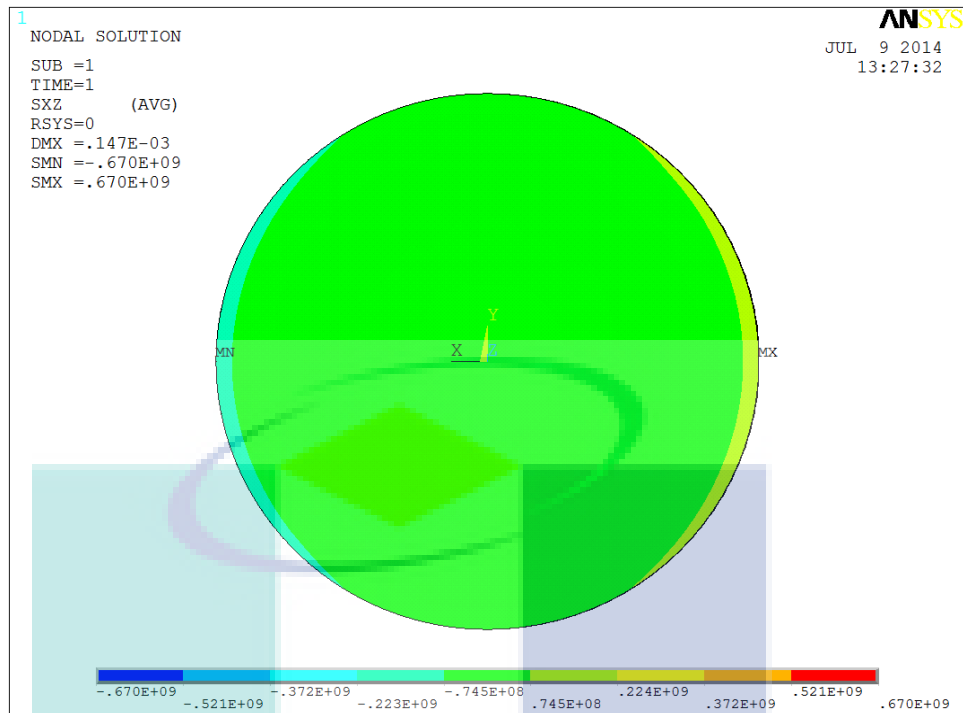
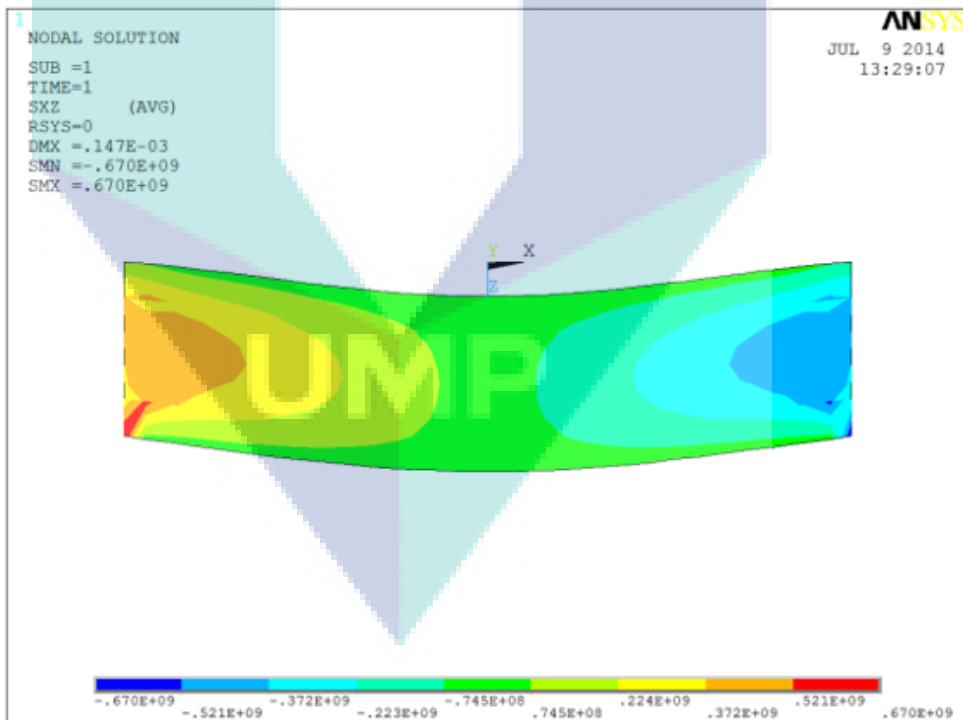
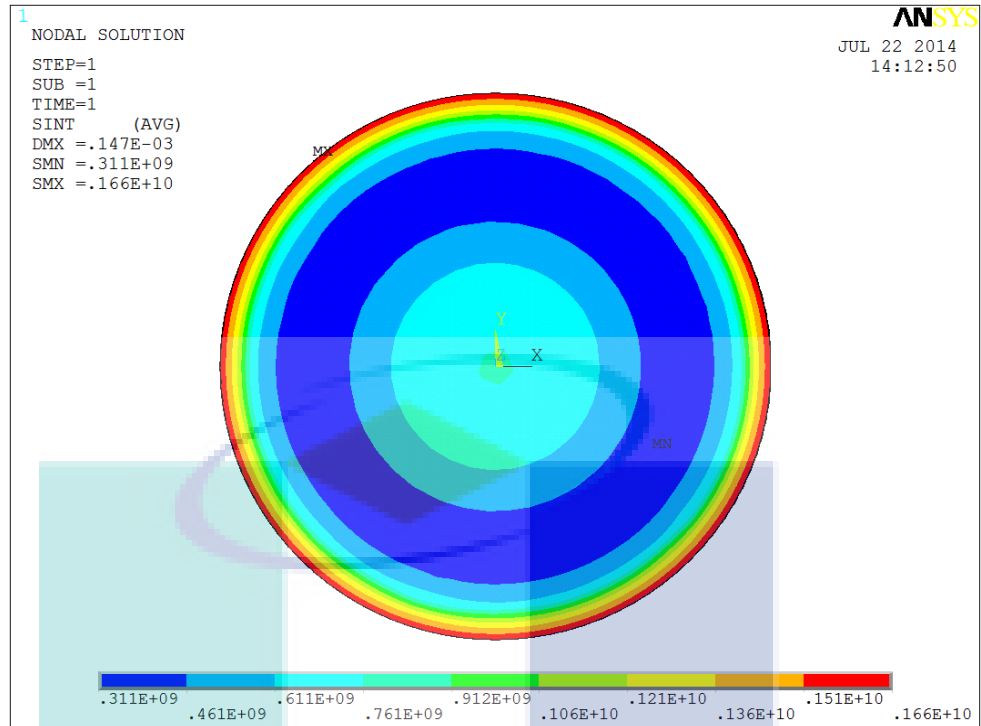
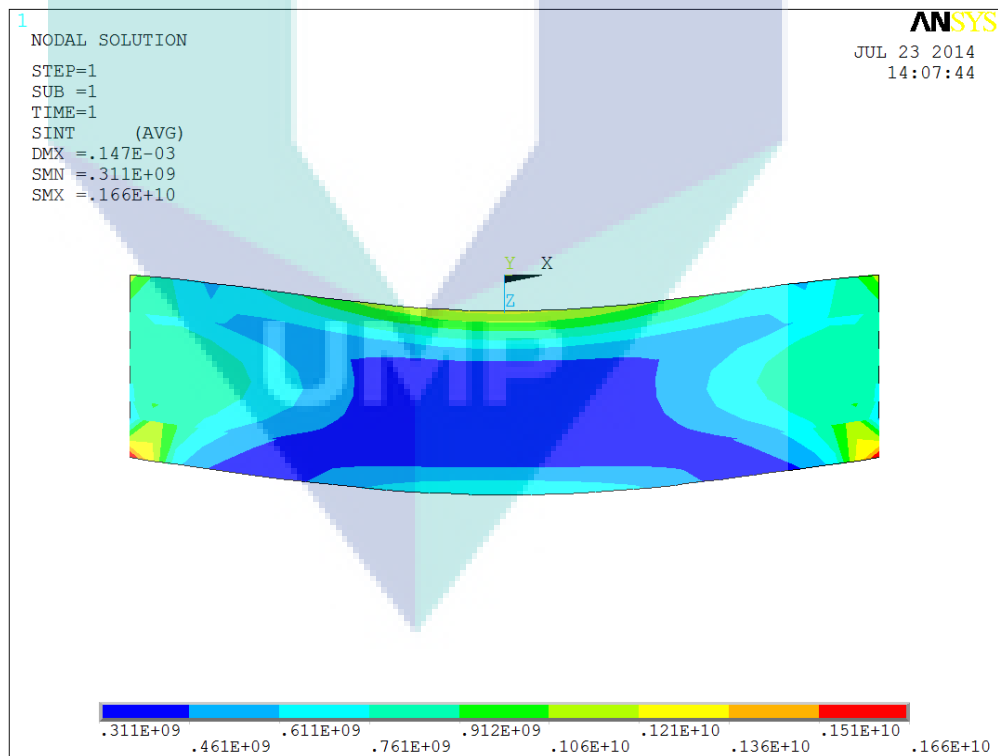
(a) τ_{xz} (top view)(b) τ_{xz} (mid-plane cross-section front view)

Figure 5.26: Transverse shear stress distribution of the HA/Ti FGM plates under thermo-mechanical loading ($\bar{P}=1$, $n=1$, $L=6$, $h=0.0072\text{m}$)



(a) K (bottom view)



(b) K (mid-plane cross-section front view)

Figure 5.27: Stress intensity distribution of the HA/Ti FGM plates under thermo-mechanical loading ($\bar{P}=1$, $n=1$, $L=6$, $h=0.0072\text{m}$)

The Effect of the Grading Index

Correlations between the grading parameter and various thermo-mechanical responses of the FGM plate were investigated by considering the previous grading index number in a range between 0 and ∞ . Table 5.8 shows the dimensionless central deflection of the FGM plates with various grading indices due to a corresponding dimensionless load intensity applied to the structure. Since the effects of mechanical loading on the structure's behaviour was greater than the thermal loading for the HA/Ti FGM plate, it was not surprising to see that the FGM plates experienced intermediate values of deflection, such as those found in the isothermal case (see Table 5.4). However the thermo-mechanical loading caused higher central deflections in all plates compared to those under isothermal conditions.

Table 5.8: Deflection of HA/Ti FG plates with various grading indices subjected to thermo-mechanical loading corresponding to various load intensities

P	\bar{w}				
	n=0	n=0.5	n=1	n=2	n= ∞
1	0.0212	0.0212	0.0213	0.0214	0.0216
2	0.0419	0.0421	0.0423	0.0425	0.0429
3	0.0626	0.0630	0.0632	0.0636	0.0641
4	0.0833	0.0838	0.0842	0.0846	0.0853
5	0.1040	0.1047	0.1052	0.1057	0.1066
6	0.1248	0.1255	0.1262	0.1268	0.1278
7	0.1454	0.1464	0.1471	0.1479	0.1490
8	0.1661	0.1672	0.1681	0.1689	0.1703
9	0.1868	0.1881	0.1890	0.1900	0.1914
10	0.2075	0.2089	0.2100	0.2111	0.2126
11	0.2283	0.2299	0.2310	0.2322	0.2339
12	0.2490	0.2507	0.2519	0.2533	0.2551

Figure 5.28 represents the dimensionless deflection, normal stress, transverse shear stress and the stress intensity factor distributions of the FGM plates under thermo-mechanical loading for different grading indices. It is evident in Figure 5.28(a) that the deflection of the homogeneous Ti plate ($n=\infty$) is much greater than the others. This can be explained by looking at the thermal conductivity as well as the thermal expansion

coefficient properties of the material. Although the temperature distribution profile of the pure HA plate was similar to that of the Ti plate (see Figure 5.19), the deflection remained as small as those of the FGM plates because of its small thermal conductivity (see Table 5.1).

The significant differences between the pure Ti plate responses distribution compared to the others were also clearly seen in normal stress, transverse shear stress and stress intensity factor distributions, shown in Figures 5.28(b), 5.28(c) and 5.28(d) respectively. As seen in Figure 5.28(b), the normal stress distribution of FGM plates which were previously linear under isothermal conditions changed to a cubic function of the thickness coordinates under thermo-mechanical effects. The thermo-mechanical stress of the FGM plates was lower than homogeneous plates due to the gradation of the material properties along the transverse plane of the plates (Alshorbagy *et al.*, 2013).

The extremely high shear stress of the pure Ti plate shown in Figure 5.28(c) is because of the high deflection of the structure. The shear stress that occurred in FGM plates was higher than those found in the pure HA plate because it needed to prevent the laminated layers from slipping past each other. The plots given in Figure 5.28(d) show that the stress intensity factor increased with the higher compositional percentage of Ti in the FGM plates. This supports the fact that the thermal conductivity of the ingredients inside the FGM plates had a dominant effect on the thermo-mechanical behaviour of the structures.

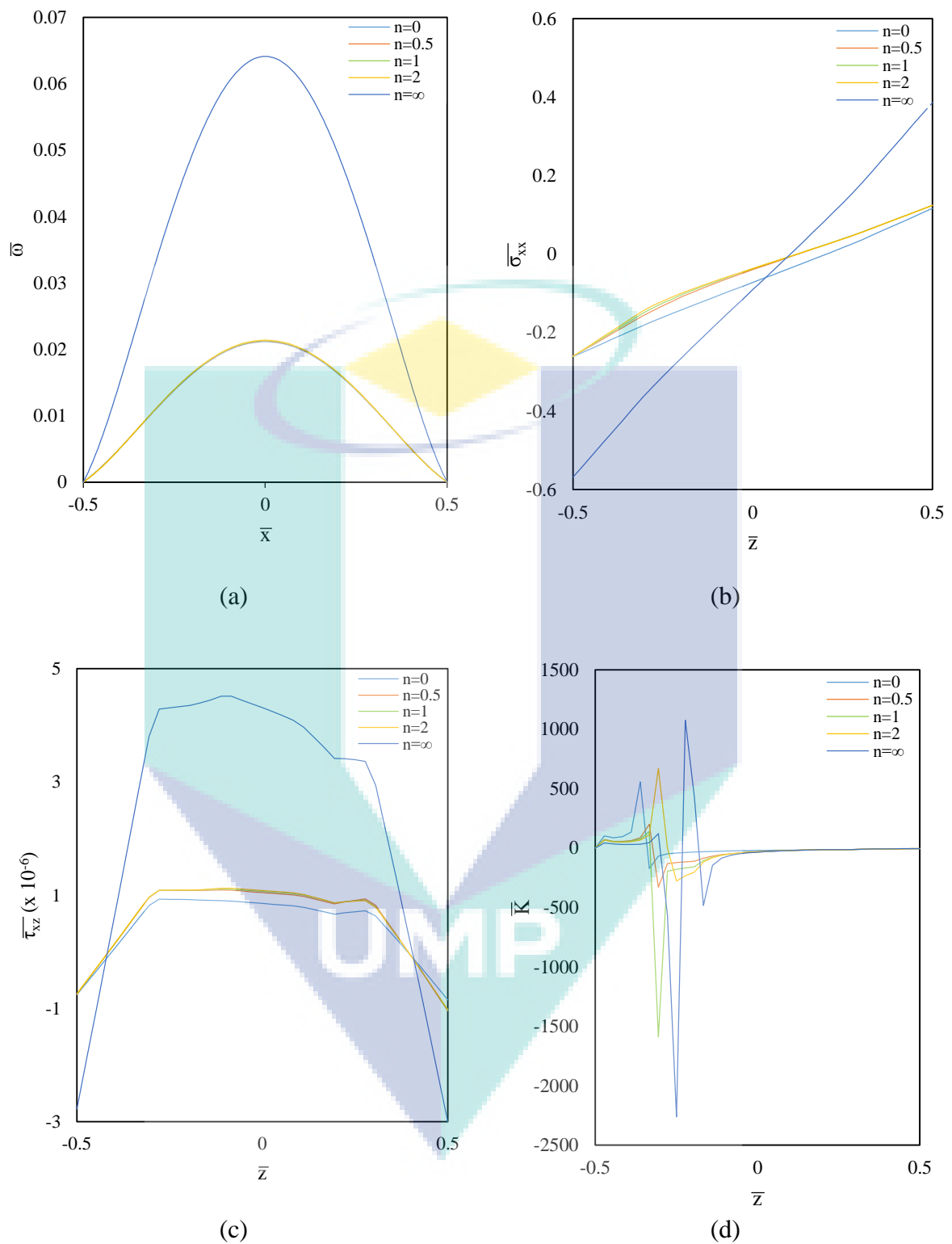


Figure 5.28: Variations of various responses of the HA/Ti FGM plates under thermo-mechanical loading, for various grading indices ($\bar{P}=1$, $L=6$, $h=0.0072\text{m}$)

The Effect of the Number of Layers

Table 5.9 shows slight differences in the deflection values along the mid-plane of the FGM plates with 5, 6 and 7 layers. Although the values were slightly higher due to thermo-mechanical loading effects, the variation in the deflection strongly corresponds with those induced by isothermal loading (refer to Table 5.6). In addition to the deflection response, the variation in the normal stress values and the transverse shear stress distribution (given in Table 5.10 and Figure 5.29(a) respectively) were also highly consistent with the case of isothermal loading. This leads to the conclusion that the effect of the number of layers parameter was similar in both the isothermal and thermo-mechanical behaviours of the FGM plates.

Table 5.9: Central deflections at the mid-plane of FGM plates with three different number of layers subjected to thermo-mechanical loading

\bar{x}	\bar{w}		
	3 Layers	6 Layers	9 Layers
-0.5	6.8315E-15	4.9092E-15	4.9136E-15
-0.4	5.0385E-03	5.0367E-03	5.0381E-03
-0.3	1.1087E-02	1.1085E-02	1.1086E-02
-0.2	1.6429E-02	1.6428E-02	1.6428E-02
-0.1	2.0035E-02	2.0033E-02	2.0035E-02
0	2.1304E-02	2.1303E-02	2.1304E-02
0.1	2.0035E-02	2.0033E-02	2.0035E-02
0.2	1.6431E-02	1.6428E-02	1.6429E-02
0.3	1.1088E-02	1.1086E-02	1.1087E-02
0.4	5.0399E-03	5.0382E-03	5.0393E-03
0.5	1.3737E-15	1.8258E-15	1.8290E-15

Table 5.10 lists some of the values of normal stress distributed along the thickness of the FGM plates with various grading indices that were subjected to thermo-mechanical loading. The change in the normal stress values was similar to that found in the deflection distribution of the FGM plates where normal stress decreased with the addition of the number of layers inside the FGM plates. This result strengthened the conclusion that a greater number of layers inside the FGM transition phase produced more relaxation in the stress distribution of the FGM plate.

Table 5.10: Normal stress values along the thickness of FGM plates with three different number of layers subjected to thermo-mechanical loading

\bar{z}	$\bar{\sigma}_{xx}$		
	3 Layers	6 Layers	9 Layers
-0.5	-2.6028E-01	-2.6030E-01	-2.6031E-01
-0.4	-2.0335E-01	-2.0401E-01	-2.0417E-01
-0.3	-1.4643E-01	-1.4771E-01	-1.4804E-01
-0.2	-1.0693E-01	-1.0403E-01	-1.0420E-01
-0.1	-6.9023E-02	-6.8899E-02	-6.8838E-02
0	-3.8174E-02	-3.7414E-02	-3.7414E-02
0.1	-7.5260E-03	-7.1797E-03	-7.1045E-03
0.2	2.3130E-02	2.3316E-02	2.3487E-02
0.3	5.4147E-02	5.4674E-02	5.4824E-02
0.4	8.9129E-02	8.9385E-02	8.9458E-02
0.5	1.2411E-01	1.2409E-01	1.2409E-01

Figure 5.29(a) shows the transverse shear stress distribution along the thickness of the FGM plates under thermo-mechanical loading for various numbers of layers. Figure 5.29(a) indicates that the shear stress distribution decreased with an increased number of layers, such as those induced by thermal and mechanical loadings. The result, showing the transverse shear stress distribution, reveals the ability of the FGM to withstand thermo-mechanical loading. Providing greater numbers of layers in the FGM however was not practical since it led to more complex fabrication requirements.

Figure 5.29(b) shows the variation in the stress concentration of the FGM plate when subjected to thermo-mechanical loading for various numbers of FGM transition layers. From Figure 5.29(b) it was evident that the obvious stress intensity peak was located at a quarter of the distance from the top of the HA surface of FGM plate with 6 layers. It was noted that the extreme change in the shear stress distribution was due to the inefficiency of the stepwise laminated layers arrangement. The peak stress intensity for the FGM plate with 3 layers occurred near the top of the HA surface because the elastic modulus of the lower Ti side of the plate was lower and it was less rigid.

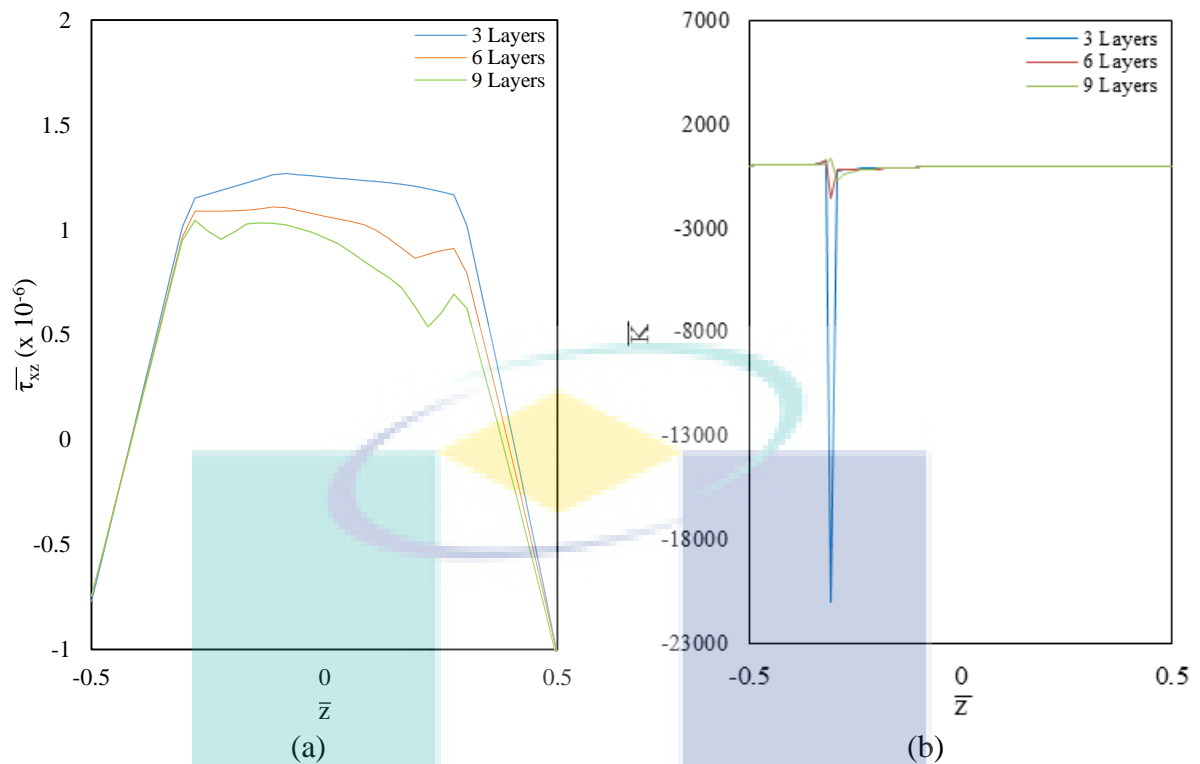


Figure 5.29: Transverse shear stress along the thickness of the HA/Ti FGM plates with a different number of layers under thermo-mechanical loading ($\bar{P}=1$, $n=1$, $h=0.0072\text{m}$)

The deflection distribution given in Figure 5.30(a) is highly consistent with that achieved in the isothermal case analysis shown in Figure 5.14(a). The negligibly small deflections induced by thermal loading when compared to mechanical loading is the main reason for the mechanical loading effect's domination. From Figure 5.30(b), it can be seen that the normal stress of the FGM plate, with a thickness of 0.006 m, was obviously greater than the others. This happened because the temperature changed more rapidly through the thickness of the thinner FGM plate. This factor led to the corresponding high transverse shear stress distribution given in Figure 5.30(c). These results reveal the importance of choosing the appropriate thickness of FGM plates so that they can withstand thermo-mechanical loadings.

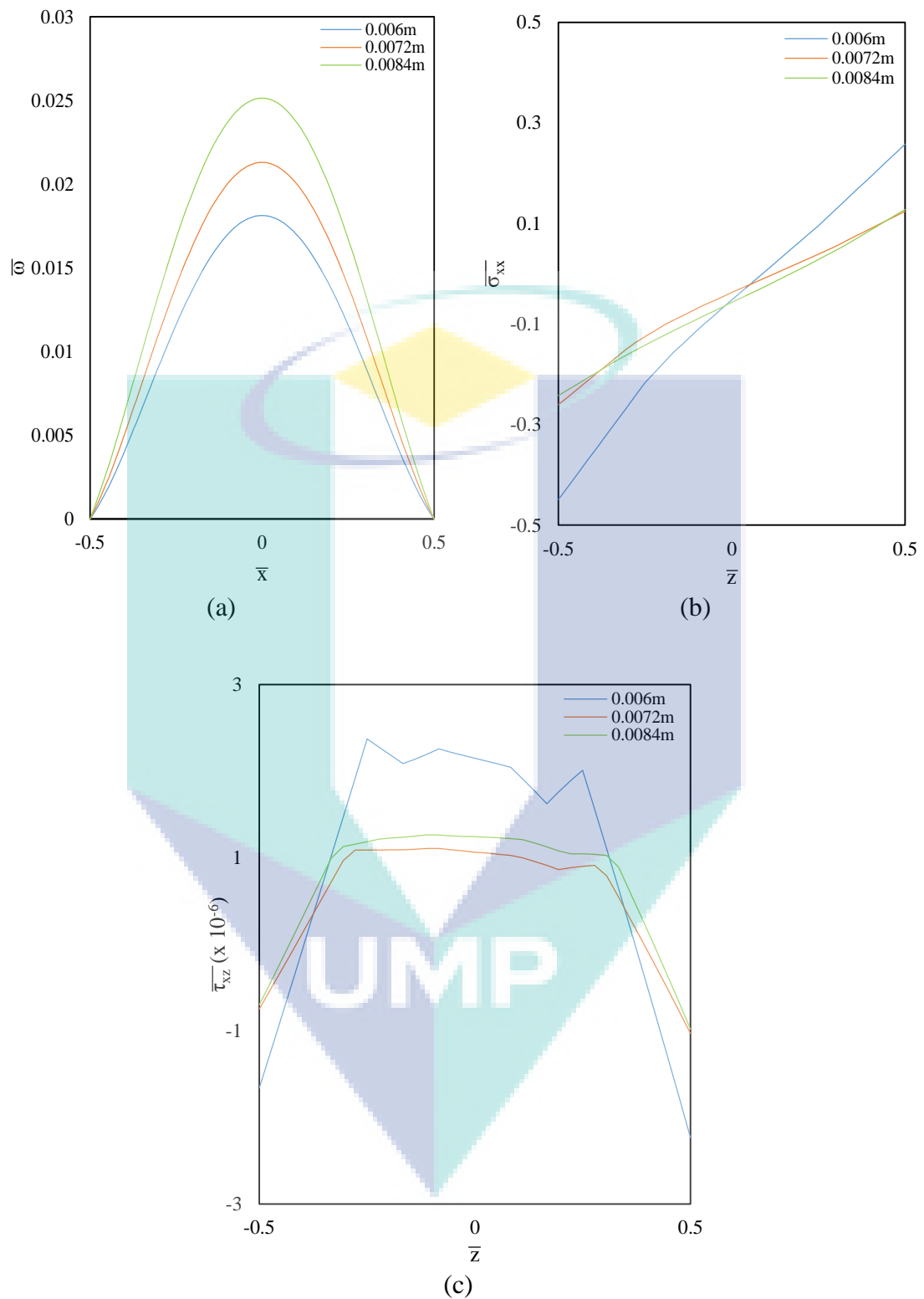


Figure 5.30: Responses of the FGM plates with different thicknesses subjected to thermo-mechanical loading ($\bar{P}=1$, $n=1$, $L=6$)

The Effect of Heat Generation

The effect of thermo-mechanical loading with heat generation was considered in a thermal analysis of the temperature profile as well as the structural responses of the HA/Ti FGM plate. During the thermal field computation, a heat source of $\dot{q}=100\times 10^6$ was generated in the FGM plate together with thermal loading (300°C at the top HA surface). The thermo-mechanical loading was defined in the FGM system by simultaneously applying the thermal excitation field calculated in thermal analysis and the mechanical pressure on the HA surface.

Figures 5.31-5.34 represent the deflection, normal stress, transverse shear stress and stress intensity factor distributions of the FGM plates subjected to thermo-mechanical loading with heat generated inside its body. It can clearly be observed from Figures 5.31(a) and 5.31(b) that the maximum deflection was no longer distributed at the top HA surface of the FGM plate. This happened because the expansion of the material due to heat generation led to a deflection towards the opposite end of the transverse loading direction. Due to the reduction of deflection on the top HA surface, the maximum normal stress occurred at the circumference area of the FGM plate analysed previously. Due to the reduction of the deflection on top HA surface, the maximum normal stress occurred at the circumference area of the FGM plate analysed previously is eliminated thus normal stress contours in Figure 5.32 is obtained.

The corresponding transverse shear stress and the stress intensity factor contour images of the present FGM plate are given in Figures 5.33 and 5.34 respectively. These responses were slightly different to those computed on FGM plates subjected to thermo-mechanical loading without heat generation (see Figures 5.26 and 5.27). These results indicated that the transverse shear stress (as well as stress intensity factor distributions) were not significantly affected by the heat generation inside the FGM plates. This was because the low thermal conductivity of the HA constituent inhibited temperature flow inside the FGM.

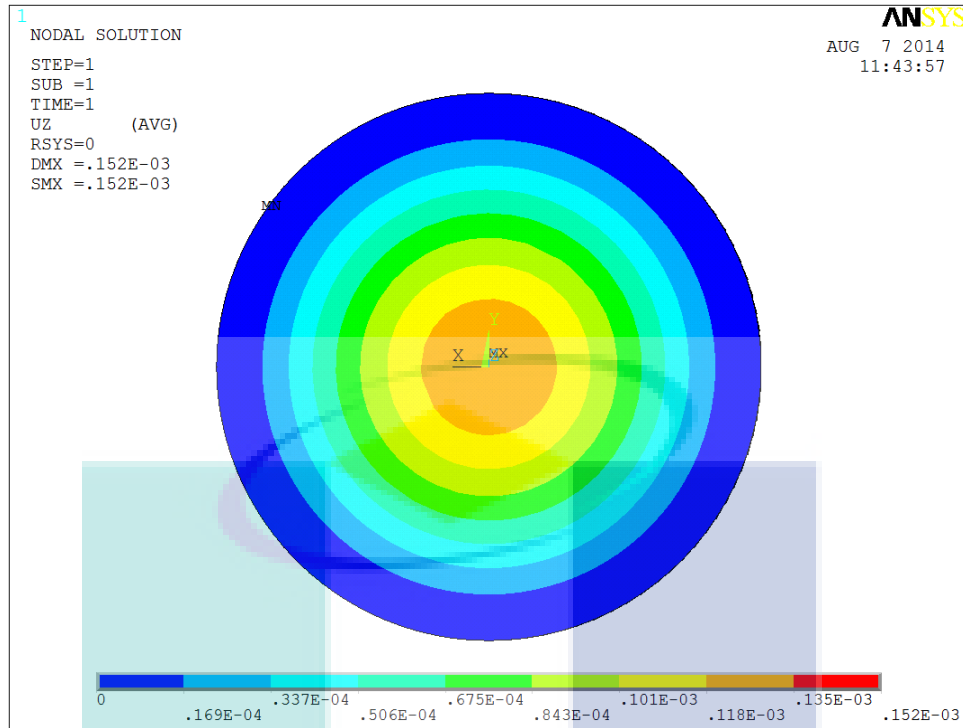
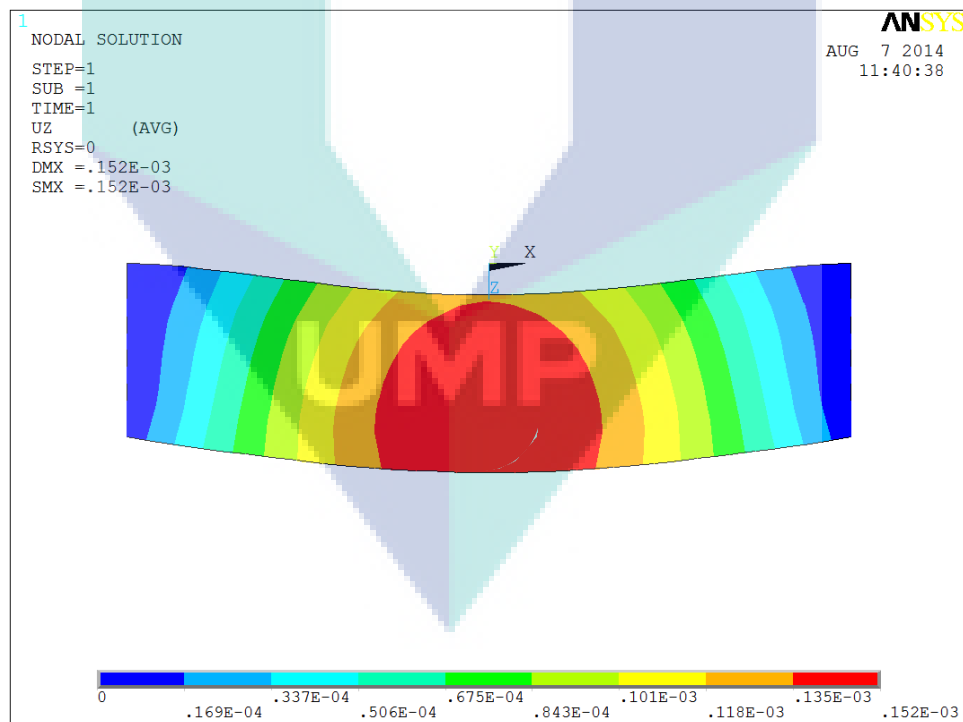
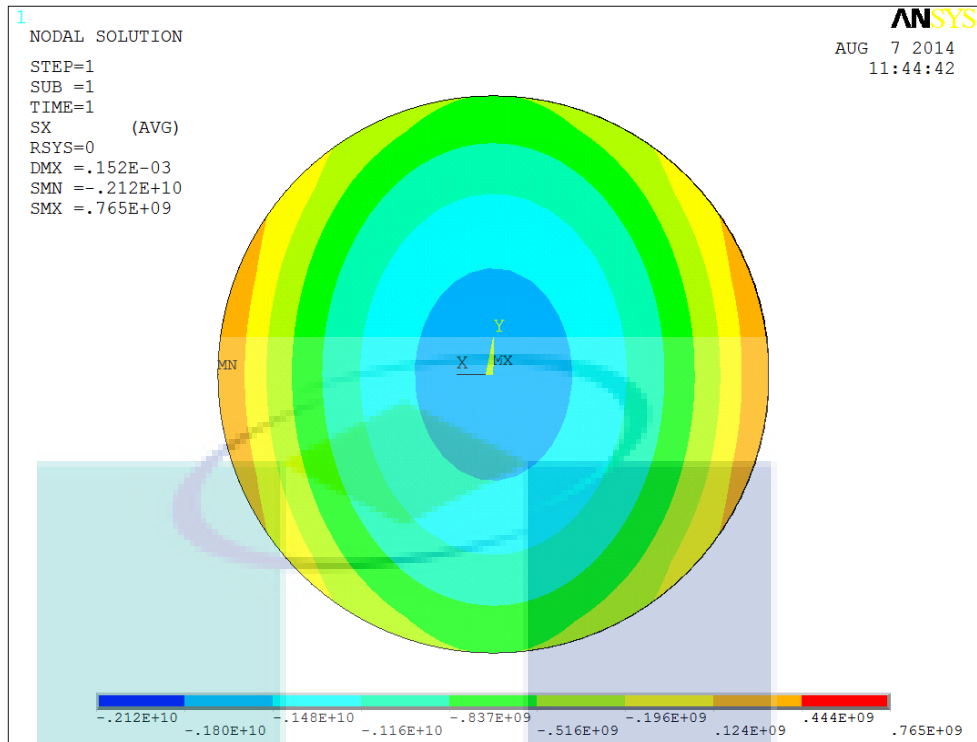
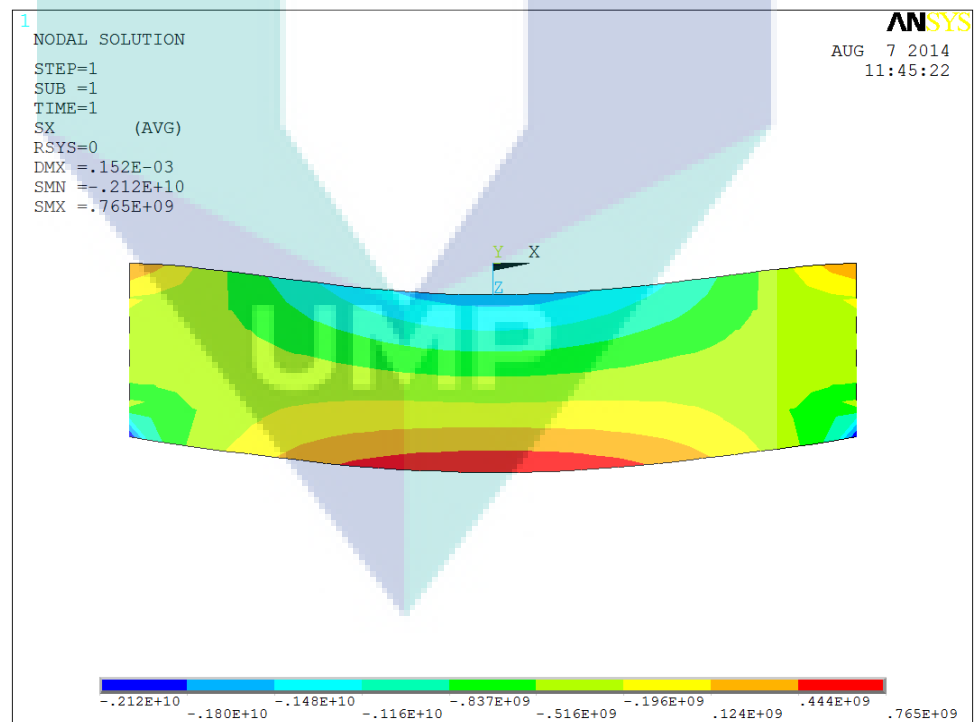
(a) δ_{zz} (top view)(b) δ_{zz} (mid-plane cross-section front view)

Figure 5.31: Deflection of the HA/Ti FGM plates under thermo-mechanical loading with a heat source ($\bar{P}=1$, $n=1$, $L=6$, $h=0.0072\text{m}$)



(a) σ_{xx} (top view)



(b) σ_{xx} (mid-plane cross-section front view)

Figure 5.32: Normal stress distribution of the HA/Ti FGM plate under thermo-mechanical loading with a heat source ($\bar{P}=1$, $n=1$, $L=6$, $h=0.0072\text{m}$)

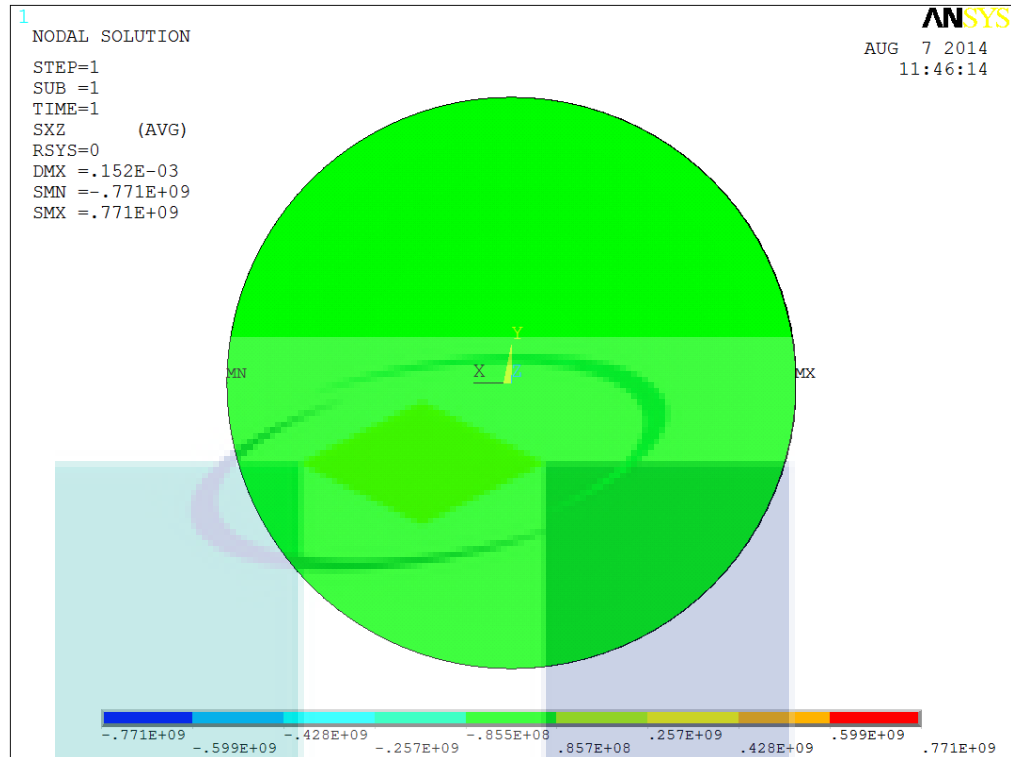
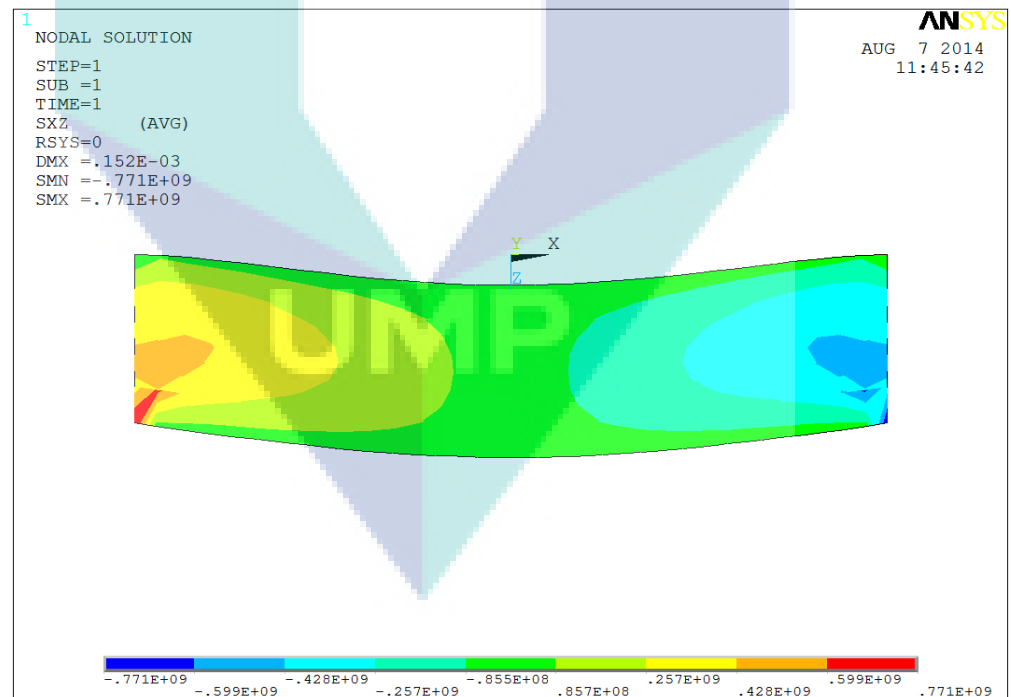
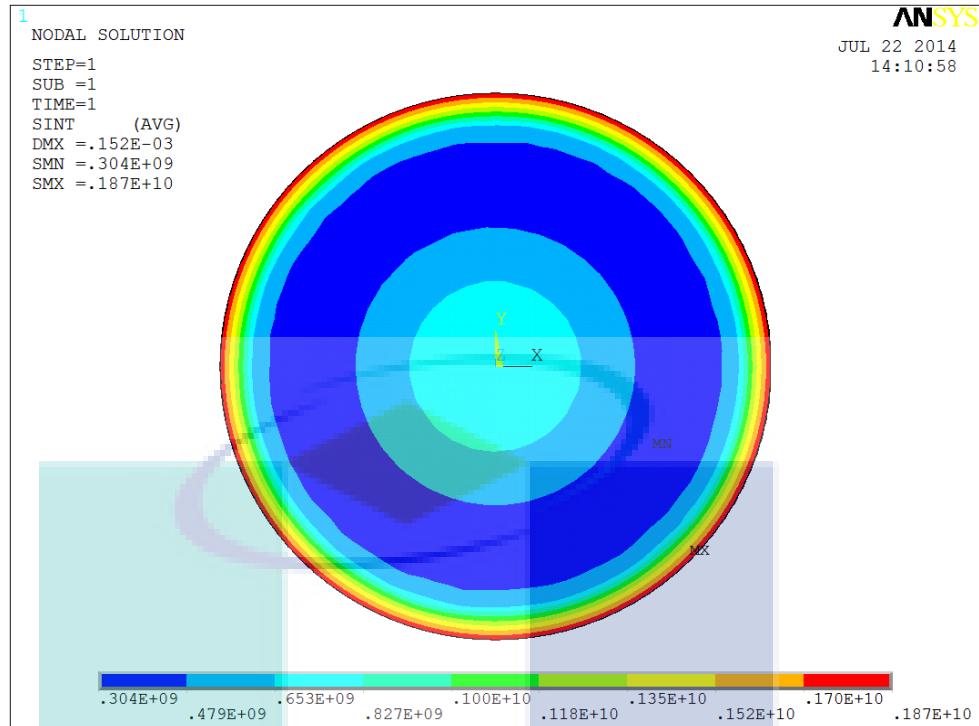
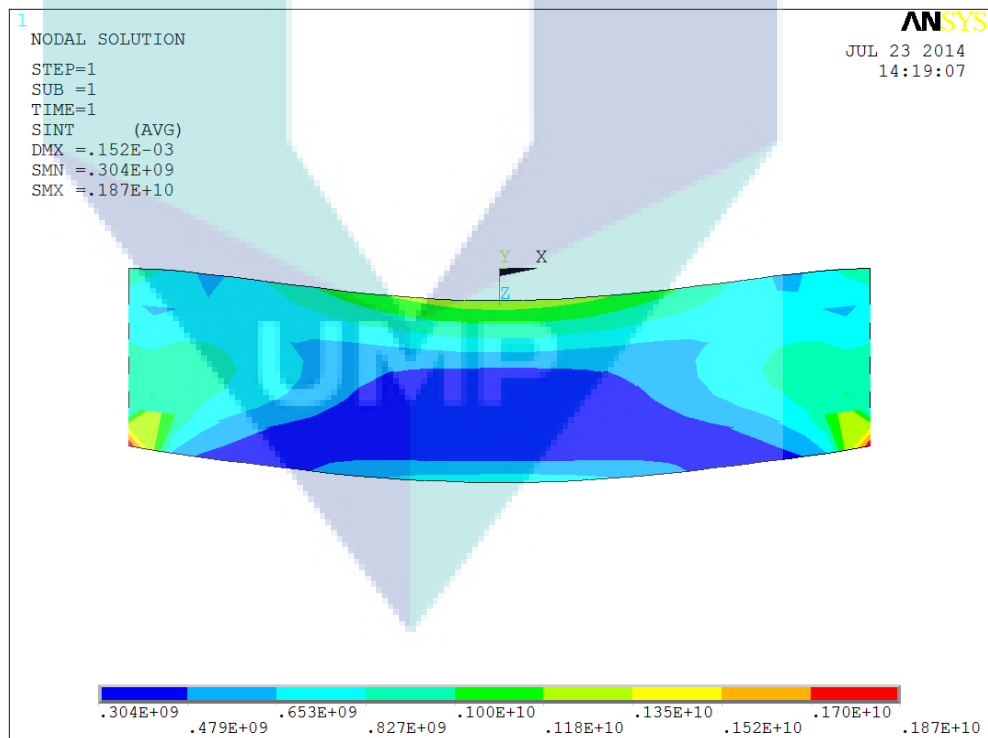
(a) τ_{xz} (top view)(b) τ_{xz} (mid-plane cross-section front view)

Figure 5.33: Transverse shear stress distribution of the HA/Ti FGM plate under thermo-mechanical loading with a heat source ($\bar{P}=1$, $n=1$, $L=6$, $h=0.0072\text{m}$)



(a) K (bottom view)



(b) K (mid-plane cross-section front view)

Figure 5.34: Stress intensity distribution of the HA/Ti FGM plate under thermo-mechanical loading with a heat source ($\bar{P}=1$, $n=1$, $L=6$, $h=0.0072\text{m}$)

Table 5.11 shows the dimensionless central deflection due to thermo-mechanical loadings with heat generation inside the FGM plate for various grading indices. The slightly higher deflection amounts of the present FGM plate when compared to those given in Table 5.8 reveal the less significance of the effect of heat generation on the deflection response. The small variation in the deflection of both plates can be clearly seen in Figure 5.35(a). Figure 5.35(b) shows that the top HA surface of the FGM plate with heat generation is subjected to higher compressive stress in comparison to those without heat generation. The transverse shear stress distributions of both plates do not vary significantly except along the intermediate FGM layers as shown in Figure 5.35(c). The less significant differences found in these plots led to the conclusion that the HA/Ti FGM plate is not greatly affected by heat generation in its body. Thus its ability to withstand extreme thermo-mechanical loading is revealed.

Table 5.11: Central deflections of the HA/Ti FGM plates subjected to thermo-mechanical loading with a heat source corresponding to various load intensities

P	\bar{w}				
	n=0	n=0.5	n=1	n=2	n=∞
1	0.02115	0.02138	0.02142	0.02149	0.02164
2	0.04188	0.04224	0.04239	0.04257	0.04288
3	0.06260	0.06311	0.06336	0.06365	0.06411
4	0.08331	0.08397	0.08433	0.08475	0.08535
5	0.10403	0.10483	0.10531	0.10583	0.10658
6	0.12475	0.12569	0.12628	0.12693	0.12781
7	0.14542	0.14653	0.14722	0.14792	0.14903
8	0.16611	0.16736	0.16819	0.16903	0.17028
9	0.18681	0.18819	0.18917	0.19014	0.19139
10	0.20750	0.20903	0.21014	0.21125	0.21264
11	0.22833	0.23000	0.23111	0.23236	0.23389
12	0.24903	0.25083	0.25208	0.25333	0.25514

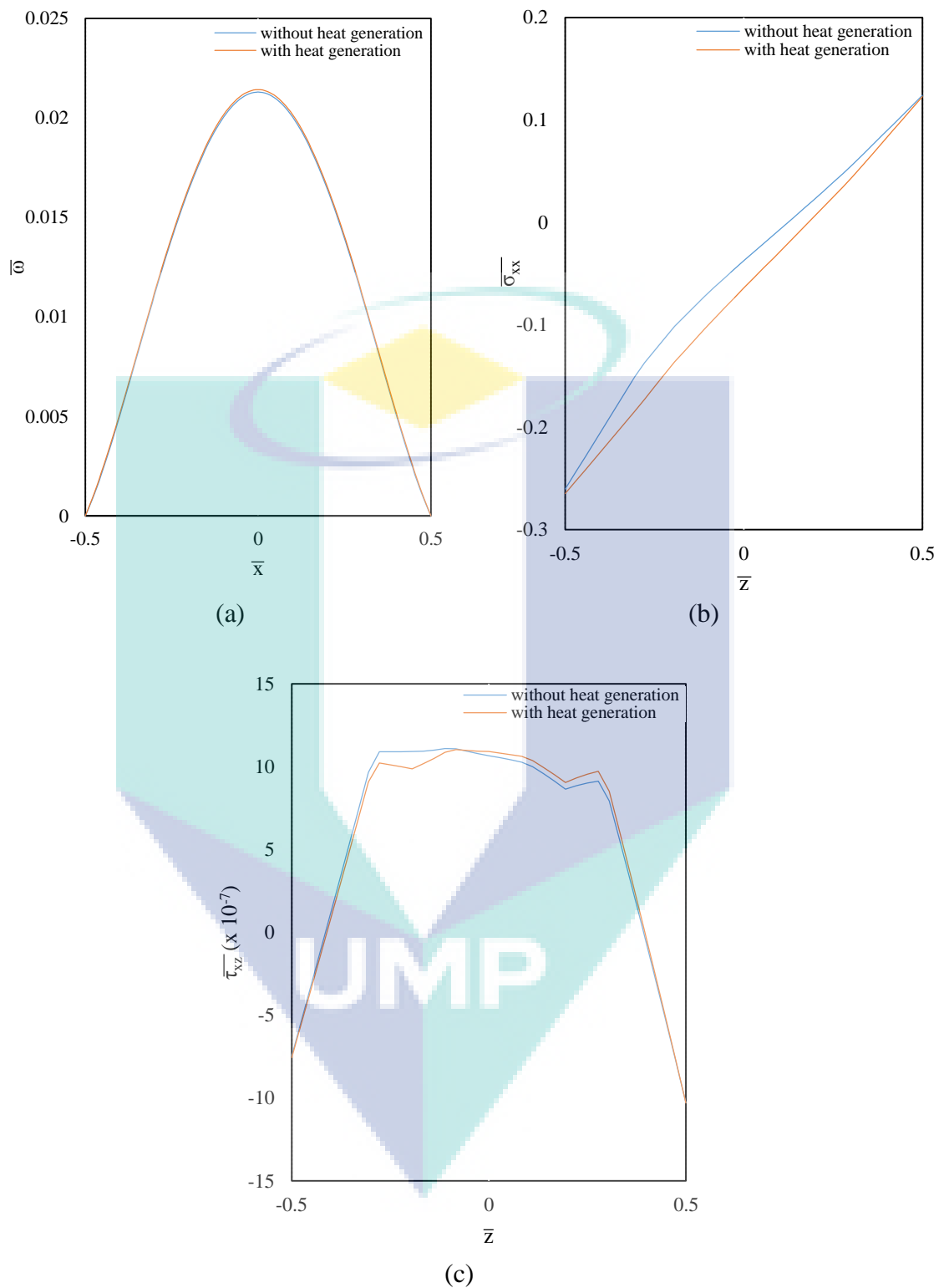


Figure 5.35: Responses of FGM plates under thermo-mechanical loading with and without a heat source ($\bar{P}=1$, $n=1$, $L=6$, $h=0.0072\text{m}$)

5.5 CLOSURE

The research work outlined in this chapter includes an in-depth FEA study into the effects of the parameters that influence the property distribution of the design and various responses of the HA/Ti FGM. The optimization of the grading index, the number of layers and the thickness acquired by the maximum residual stress relaxation have been successfully computed using a 2-D axisymmetric FE model. The results of the 2-D analysis showed that the optimum cylindrical HA/Ti FGM plate consisted of a minimum of six layers with linear property variation ($n=1$) and a specific thickness that can preserve the property gradation function. The parameters investigated in the 2-D analysis were further considered in the 3-D analysis for the parametric study on the characteristics of the FGM under isothermal, thermal and thermo-mechanical loading conditions. The results achieved from the study proved the ability of the HA/Ti FGM to withstand extreme temperatures, mechanical pressure and thermo-mechanical loading. This was confirmed because the temperature, deflection and stresses distributions in the FGM under thermal and thermo-mechanical conditions was lower than those found in homogeneous materials. The results showed the correlation between the effects of the design parameters on the characteristics of the FGM, highlighting the importance of optimizing the grading index, the number of layers and the thickness of the material for a practical fabrication process. The next chapter focuses on the experimental work used to explore the performance of the HA/Ti FGM. The effects of the parameters considered in this chapter on the FGM's behaviour are emphasized throughout this experimental work.

CHAPTER 6

EXPERIMENTAL PROGRAM, RESULTS AND DISCUSSION

6.1 INTRODUCTION

This chapter reports on the experimental phase of the research program that was designed essentially to provide an understanding of the fabrication of the HA/Ti FGM. Further aims are to provide quantitative data and additional information, to further understand the performance of the HA/Ti FGM in a real engineering application, and to supplement the limited amount of information available in the literature. The initial part of this chapter provides a basic explanation of the fabrication method via the powder metallurgy and cold sintering techniques of the cylindrical HA/Ti FGM samples. It is subsequently followed by a characterization of the metallurgical aspects of the samples using SEM, FTIR and XRD, as well as a measurement of their properties such as density and micro-hardness.

6.2 THE EXPERIMENTAL PROCESS

This section explains the fabrication of the sample using the cold processing of PM approach that is based on the optimum parameters predicted using 2-D FE analysis. This is followed by a measurement of its basic mechanical properties and a characterization of its morphology and composition. The relevance of using the PM method for the fabrication of various metal-ceramic FGMs has been highlighted in the literature (Jamaludin *et al.*, 2013). Since the operating limitation of different FGMs varies with the typical properties of the constituents, the parameters to be implemented in the fabrication of the HA/Ti FGM samples need to be determined based on the material properties listed by the manufacturers. The overall general flow of the fabrication work implemented and the manufacturer's specification for the HA (DTY-

CHEM, China) and Ti (Sigma Aldrich) raw materials are given in Figure 6.1 and in Table 6.1 respectively.

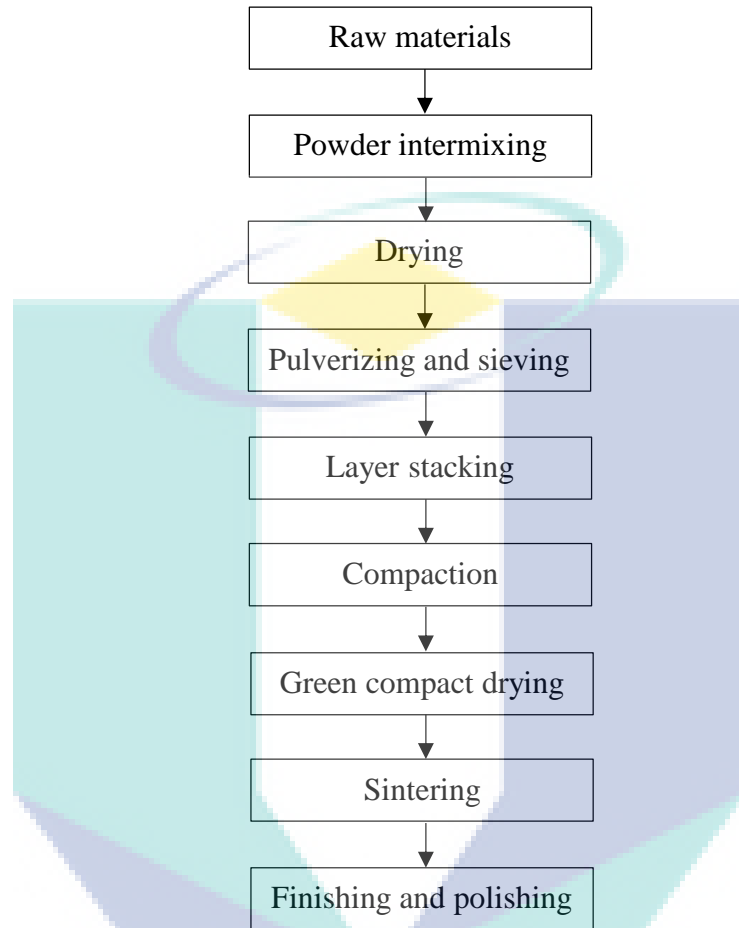


Figure 6.1: The powder metallurgy route

Table 6.1: The physical and chemical properties of the base materials (manufacturer's specifications)

Properties	HA	Ti
Purity (%)	Ca (minimum): 41.77	99.95
Molecular weight (g./mol.)	502.31	47.88
Composition	$\text{Ca}_5(\text{OH})(\text{PO}_4)_3$	Ti
Particle size (μm)	± 12	10-20
Specific gravity (g./cc.)	3.0-3.3	4.510
Melting point ($^{\circ}\text{C}$)	1760	1660

The fabrication of the FGM samples began with powder preparation, which included the weighing, blending, pulverizing and sieving processes. The determination of the percentage of powder in each distinctive FGM layer was based on the mixing ratio with respect to the molecular weight of the materials. In order to ensure the accuracy of the powder mass, the weighing of the powders was done using a closed digital analytical laboratory balance with an internal calibration weight (HR-250AZ). The calculation of the percentage weight for each constituent of each distinctive HA/Ti FGM configuration is shown in Table 6.2.

Table 6.2: Calculation of the weight percentage of powder mixtures

Layer	Phase Composition	Weight (g)
1	100% HA	1 x 502.3
2	80% HA + 20% Ti	$(0.8 \times 502.3) + (0.2 \times 47.88)$
3	60% HA + 40% Ti	$(0.6 \times 502.3) + (0.4 \times 47.88)$
4	40% HA + 60% Ti	$(0.4 \times 502.3) + (0.6 \times 47.88)$
5	20% HA + 80% Ti	$(0.2 \times 502.3) + (0.8 \times 47.88)$
6	100% Ti	1 x 47.88

The weighed powders were then mixed together according to the various pre-arranged compositions. The production of a homogeneous mixture of the elemental powders prior to the green compaction and firing treatment was one of great importance in the successful manufacture of the FGM. Here the satisfactory homogeneity of the mixed constituents was achieved using a ball milling method. Moderate success has been achieved in the appropriate mixing of Ti and HA mixtures using a planetary ball mills machine (Model PM100) shown in Figure 6.2. The blending process was performed in two stages. In the first stage, the pure powders were blended for 1hr at a speed of 300rpm to reduce the particle size. In the second stage, the two-phase powders were blended for 5hrs at the same rotating speed to ensure the effective dispersion and homogeneity of the mixtures.



Figure 6.2: Planetary ball mill machine - Faculty of Industrial Science and Technology (FIST) Laboratory, Universiti Malaysia Pahang (UMP)

In order to ensure the separation of the agglomerates and impurities that exist in the compounds, the blended powders then proceeded to the sieving process. Now the equal-size apertures of the HA/Ti mixtures were produced using a customized 100 μ m stainless steel sieve. To make the process more convenient, a coarse sieve was used first, followed by a fine sieve. The sieved powders were finally stored in an airtight container filled with silica gel to avoid moisture absorption.

Three customized steel compaction dies were machined to prepare some different shapes and sizes of the FGM pellets. The dies were used to prepare cylindrical FGM plates with diameters of 30mm and 15mm respectively. The aforementioned dies used to compact the FGM samples are shown in Figure 6.3.

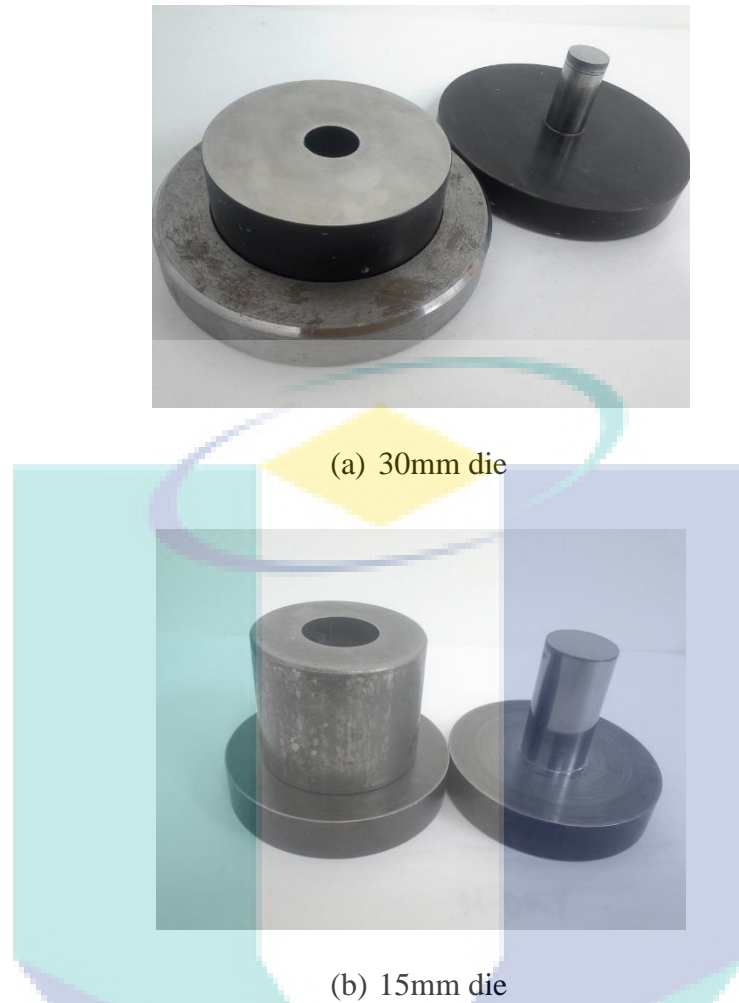


Figure 6.3: Customized dies for the compaction process

Figure 6.4 shows the configuration of a stepwise-built HA/Ti FGM sample fabricated in the present study. The configuration was developed by taking into account all the optimum geometrical parameters predicted in a previous 2-D simulation. The lay-up process prior to compaction was important in order to ensure that the distinctive graded layers were arranged properly in the FGM sample. The die-based layering process began by smearing the die surface that was in contact with the pre-compacted powders with alumina powder to avoid friction during compaction. In order to determine the mass of the powder to be added to the die, the final sintered volume of the layer was multiplied by the theoretical density of the powder composition based on the ROM formulation. The final sintered volume of the layer was calculated by multiplying the desired sintered layer thickness by the cross-sectional area of the die cavity. Once the appropriate mass of the powder was poured into the die cavity, the die punch was

lowered without additional pressure to flatten the surface of the powder. After the die punch was removed and a uniform surface was achieved, the next powder layer was added in a similar fashion. Once the layering of all the required powder compositions had been completed, the entire die assembly was prepared for the cold press process.

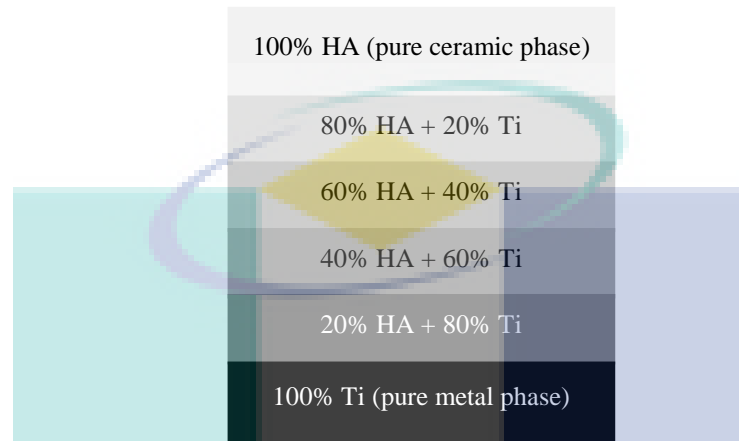


Figure 6.4: Cross-sectioned view of the stepwise HA/Ti FGM configuration

The cold press of the FGM sample was performed using a hydraulic press machine (refer to Figure 6.5) with a limited pressure of 30ton at room temperature. During the process, the pressure was increased slowly and gradually to avoid failures in structure. The compacted FGM sample and the cross-sectional illustration of its stepwise-built layers are shown in Figures 6.6(a) and 6.6(b) respectively.

The moisture content of the sample needed to be observed as it changed by uncertain amount when affected by the various conditions of shipping, storage and the natural reactions of the materials. The green compacts that entered the sintering furnace generally contained 0.5 to 1.5wt.% of moisture, which can lead to an abrupt structural change during heating. In order to avoid failures because of drastic heating during sintering, the FGM green compacts were dried in an oven (see Figure 6.7) at 40°C for at least 12hrs.



Figure 6.5: Hydraulic pressing machine



(a) The HA/Ti green compact



(b) Cross-sectional view of FGM green compact

Figure 6.6: The HA/Ti green compact



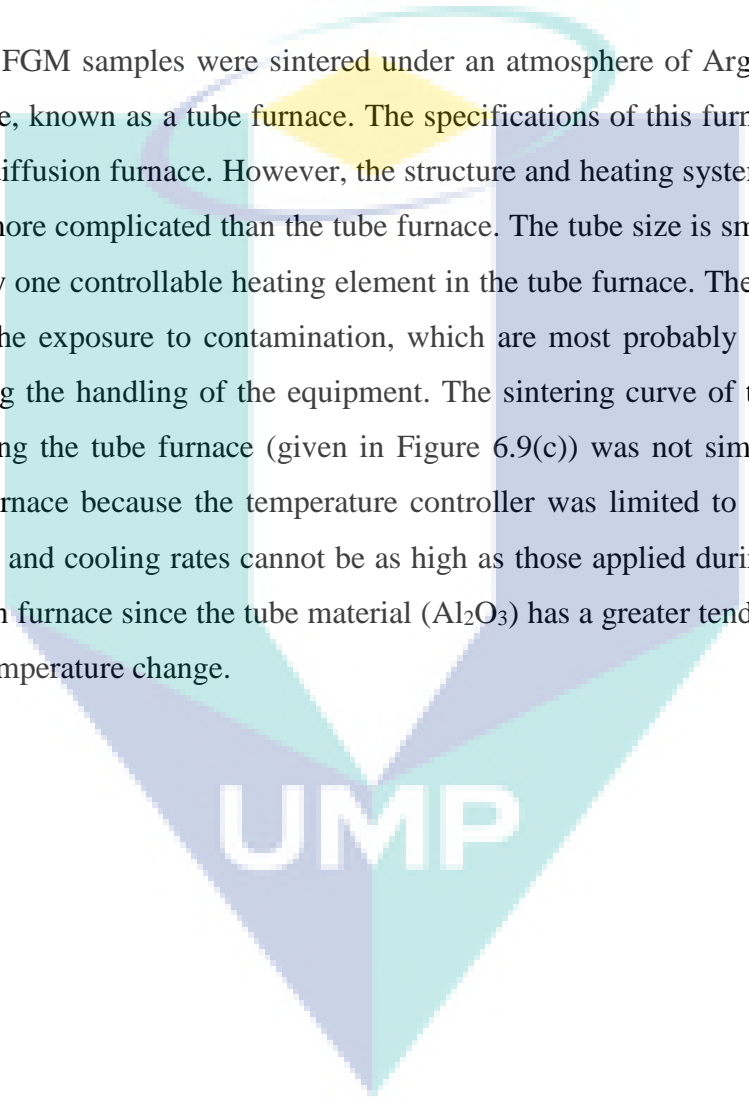
Figure 6.7: Vacuum oven used for drying the green compacts

The most challenging part of the fabrication of the FGM sample via the PM technique was the heat treatment process. There are no exact conditions reported for the heat treatment of HA/Ti FGM. Therefore, the appropriate circumstances for the sintering of this FGM was determined based on a trial and error approach. Three types of furnaces (shown in Figure 6.8) were used for the sintering process. The first type is called a muffle furnace and it is shown in Figure 6.8(a). This furnace is provided with three stage temperature controller system and has a maximum allowable temperature of 3000°C. This furnace has two limitations. The first is that the cooling rate cannot be programmed and the second is that the atmosphere inside the furnace cannot be controlled. The sintering curve for the heat treatment of the FGM samples using muffle furnace (given in Figure 6.9(a)) was based on established work (Shahrjerdi *et. al.*, 2011). The temperature controller of the furnace was set twice according to the Curve 1 and Curve 2 temperature setup because the controller was limited to only three stages of temperature change.

The specifications of the second furnace, which is called a diffusion furnace, are significantly different when compared to the first one. Although the maximum temperature is lower (at 1800°C), the cooling rate of the sintering process can be controlled. This makes the second furnace more appropriate for the heat treatment of the HA/Ti FGM samples in comparison to the muffle furnace. Three controllable heating

elements allow an even temperature distribution inside the diffusion furnace, which can ensure the homogeneous resistance of the samples. The FGM samples were sintered under forming (N_2+H_2) and N_2 gases using this furnace. The heat treatment process for the specimens was based on the manufacturer's default sintering curve (shown in Figure 6.9(b).) The reason for appointing more stages in the sintering curve was to ease the heating up and cooling down processes.

The FGM samples were sintered under an atmosphere of Argon (Ar) using the third furnace, known as a tube furnace. The specifications of this furnace are similar to that of the diffusion furnace. However, the structure and heating system of the diffusion furnace is more complicated than the tube furnace. The tube size is smaller (10 cm) and there is only one controllable heating element in the tube furnace. The limitation of this furnace is the exposure to contamination, which are most probably caused by human errors during the handling of the equipment. The sintering curve of the FGM samples sintered using the tube furnace (given in Figure 6.9(c)) was not similar to that of the diffusion furnace because the temperature controller was limited to only eight stages. The heating and cooling rates cannot be as high as those applied during sintering using the diffusion furnace since the tube material (Al_2O_3) has a greater tendency to crack due to drastic temperature change.

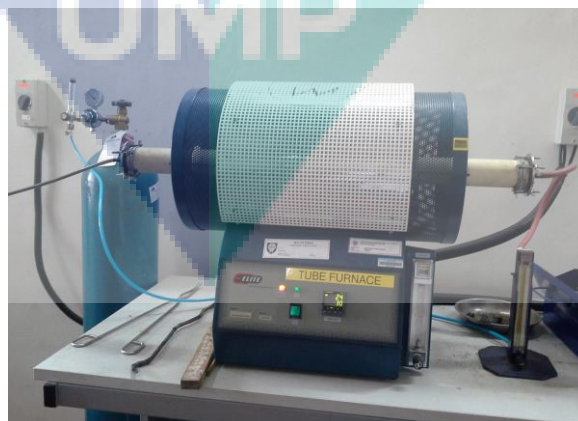
The logo for UMP (Universitas Muhammadiyah Purwokerto) is a large, stylized letter 'U' composed of four overlapping triangles in shades of teal and light blue. The letters 'UMP' are printed in white, bold, sans-serif font across the center of the 'U'.



(a) Box furnace (non-controllable atmosphere) – Material Laboratory Faculty of Manufacturing Engineering, Universiti Malaysia Pahang

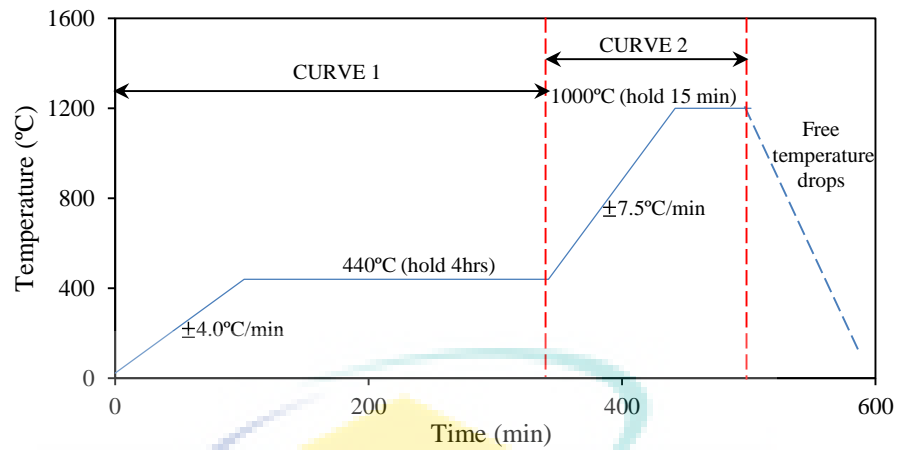


(b) Diffusion furnace (controllable atmosphere - N_2+H_2 and N_2 only) – Solar Energy Research and Innovation (SERI) Laboratory, Universiti Kebangsaan Malaysia

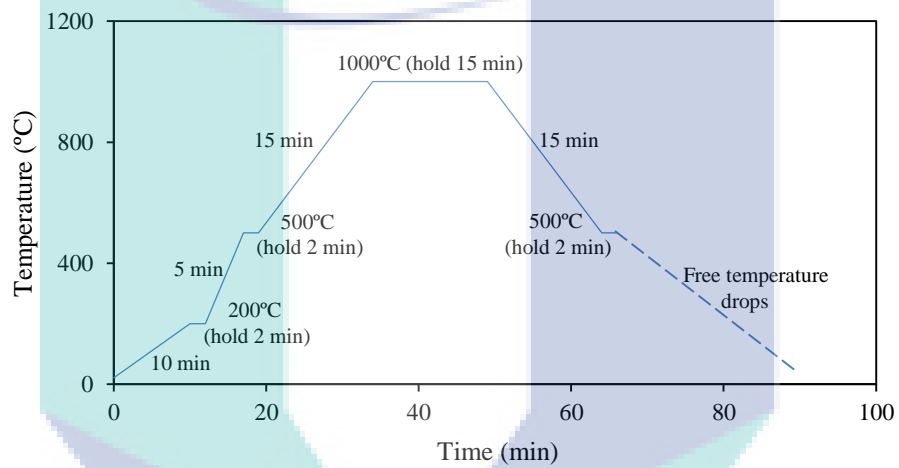


(c) Tube furnace (controllable atmosphere - Ar only) – Metallurgy Laboratory, Universiti Teknologi Tun Hussein Onn

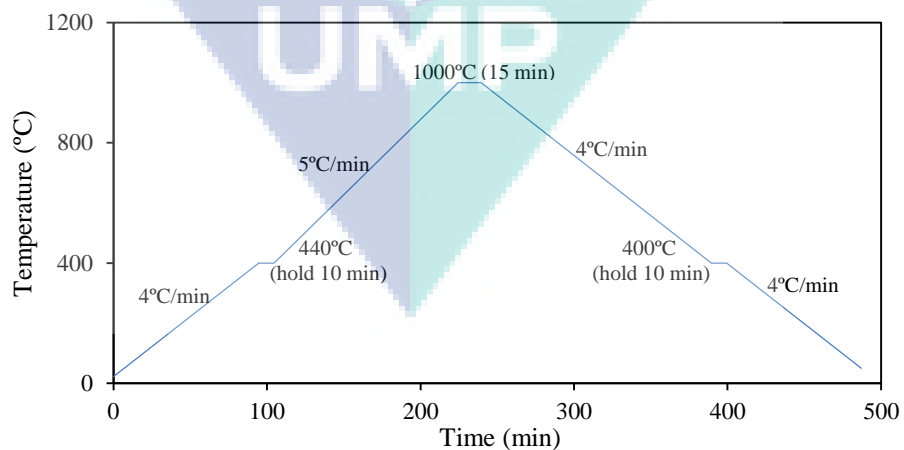
Figure 6.8: Furnaces used for the sintering process



(a) Sintering curve of the specimen sintered using the muffle furnace



(b) Sintering curve of the specimen sintered using the diffusion furnace



(c) Sintering curve of the specimen sintered using the tube furnace

Figure 6.9: Sintering curves applied during sintering using different furnaces

6.3 EXPERIMENTAL RESULTS AND DISCUSSION

This section provides and discusses the results of the experimental work. Initially, the qualitative results of the HA/Ti FGMs are presented for various processing parameters. Subsequent sections represent the quantitative results obtained by the characterization of the microstructure and the properties' characterization.

6.3.1 Qualitative Results

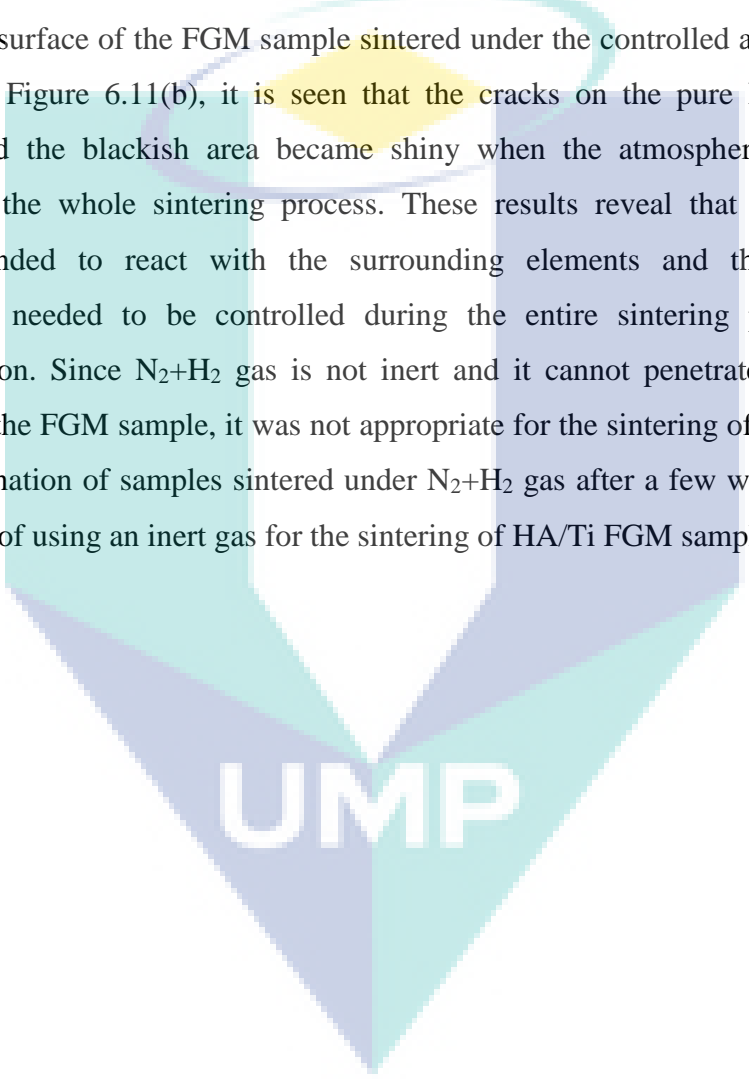
The qualitative results of the FGM samples with approximately 7mm green thickness were evaluated by considering various sintering atmospheres, compaction loads, drying processes, the direction of sample inside the furnace and the time of the flowing gas during sintering. These factors are among the parameters that influence the physical characteristics of the FGM samples.

The Effects of Flowing Gas

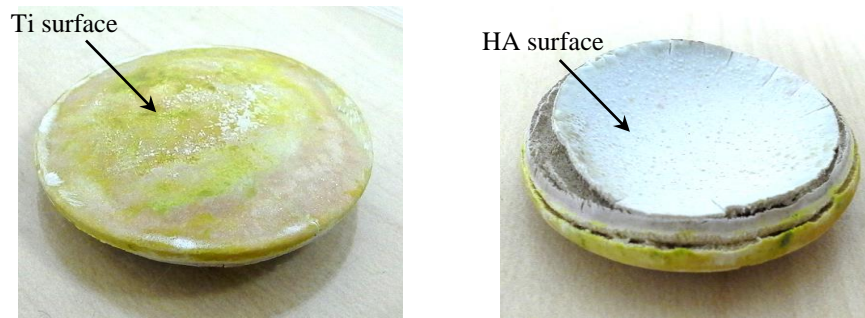
Figure 6.10 presents the results of the FGM samples compacted under a 10ton load for varying sintering atmospheres. The obvious difference observed in each sample were in terms of a colour change after the sintering process. The blackish colour of the pure Ti layer of the sample sintered under room atmosphere clearly changed to a greenish colour as shown in Figure 6.10(a). This shows that an O₂ atmosphere is totally unsuitable for the sintering of the HA/Ti FGM sample. The pure Ti layer of the sample sintered under flowing Ar gas turned a darker blackish colour with a whitish ring as illustrated in Figure 6.10(b), probably because of the existence of C and O₂ inside the tube furnace during sintering. For the samples sintered under flowing N₂+H₂ and N₂ gases, a shining area on the pure Ti surface gave an indication of the approximate completion of sintering process. These results revealed that the samples sintered using the diffusion furnace were exposed to less contamination in comparison to those sintered using the tube furnace. The observation of the FGM sample from the pure HA side shows cracks in each case, except for that sintered under flowing N₂+H₂ gas. The composition of the FGM layers and the dispersion of the constituents' particles need to

be improved because some of the adjacent FGM layers were observed as not bonding appropriately.

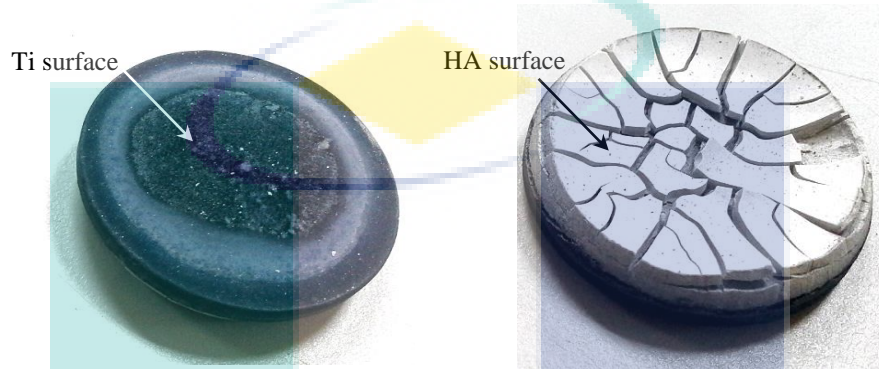
The FGM samples sintered under a controlled atmosphere during cooling, holding and the whole sintering process were compared in Figure 6.11 to study the effects of the flowing gas duration on the sintering performance of the samples. Figure 6.11(a) shows the crack formation on the pure HA surface and the pitch-black colour on the pure Ti surface of the FGM sample sintered under the controlled atmosphere during cooling. In Figure 6.11(b), it is seen that the cracks on the pure HA surface were reduced and the blackish area became shiny when the atmosphere was controlled throughout the whole sintering process. These results reveal that the HA/Ti FGM samples tended to react with the surrounding elements and thus the sintering atmosphere needed to be controlled during the entire sintering process to avoid contamination. Since N_2+H_2 gas is not inert and it cannot penetrate into the middle location of the FGM sample, it was not appropriate for the sintering of the HA/Ti FGM. The delamination of samples sintered under N_2+H_2 gas after a few weeks confirms the importance of using an inert gas for the sintering of HA/Ti FGM samples.

The logo of UMP (Universiti Malaysia Perlis) is a large, downward-pointing triangle composed of four smaller triangles meeting at the center. The top-left triangle is light blue, the top-right is light purple, the bottom-left is light green, and the bottom-right is light blue. The letters 'UMP' are written in white, bold, sans-serif font across the center of the triangle.

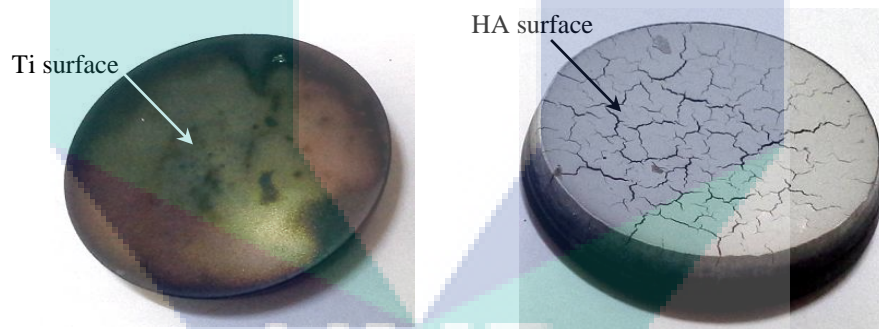
UMP



(a) O₂ atmosphere (sintered using the muffle furnace)



(b) Ar atmosphere (sintered using the tube furnace)



(c) N₂ atmosphere (sintered using the diffusion furnace)



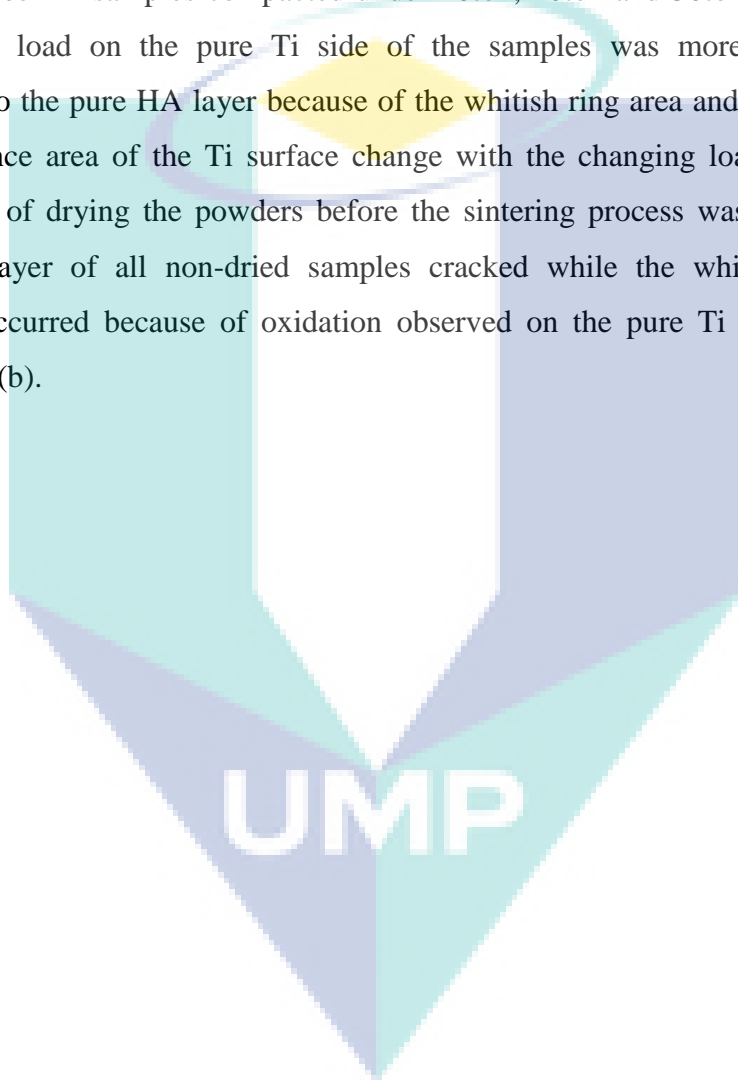
(d) N₂+H₂ gas atmosphere (sintered using the diffusion furnace)

Figure 6.10: Samples sintered under different sintering atmospheres

(L=6, T_s=1000°C, h=±7mm)

The Effects of the Drying Process

The effects of drying the powder before sintering and the various compaction loads on the FGM samples sintered under flowing N₂ gas during the cooling stage are shown in Figure 6.12. Figure 6.12(a) shows that the pure HA layer of sintered samples was not greatly affected by the compaction load since there was no significant difference seen in samples compacted under 10ton, 20ton and 30ton. The effect of the compaction load on the pure Ti side of the samples was more significant when compared to the pure HA layer because of the whitish ring area and the position at the circumference area of the Ti surface change with the changing load magnitude. The importance of drying the powders before the sintering process was proved when the pure HA layer of all non-dried samples cracked while the whitish region which probably occurred because of oxidation observed on the pure Ti layer as shown in Figure 6.12(b).



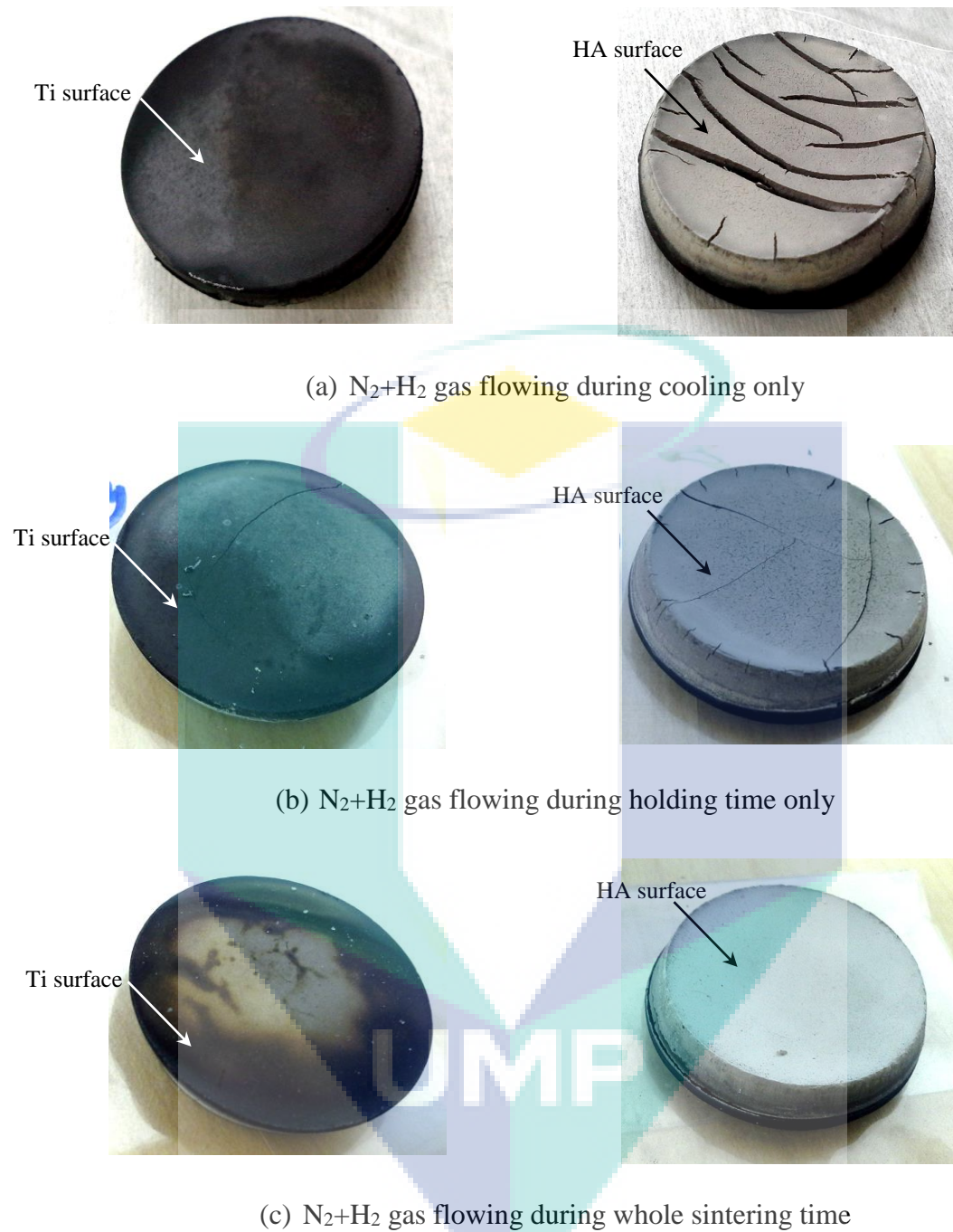


Figure 6.11: Effects of flowing gas duration during sintering on FGM samples ($L=6$, $T_s=1000^\circ\text{C}$, $h=\pm 7\text{mm}$)

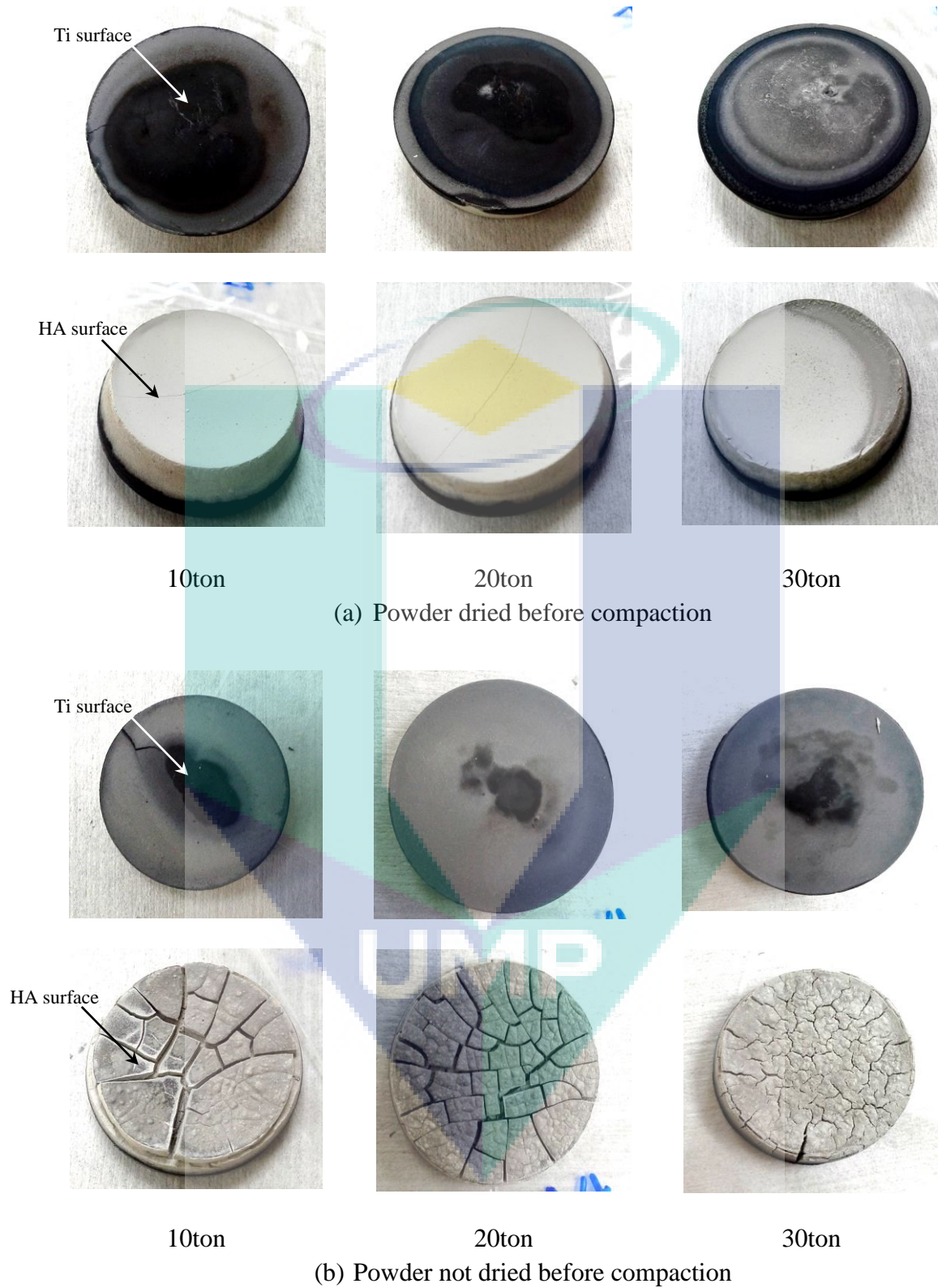
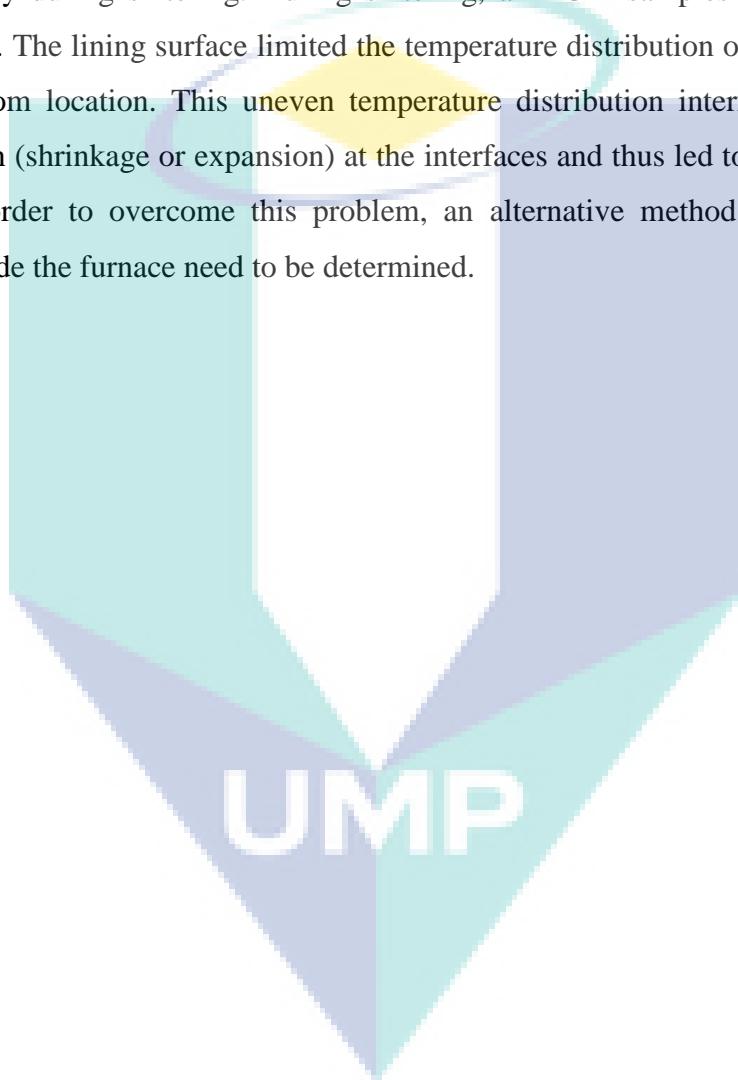


Figure 6.12: Effects of the drying process on FGM samples ($L=6$, $T_s=1000^\circ\text{C}$, $h=\pm 7\text{mm}$)

The Effects of Sample Direction during Sintering

The effects of the sample direction (HA or Ti at the top or bottom) during sintering are shown in Figure 6.13. The whitish ring on the pure Ti layers and the crack formation observed on the pure HA layers (shown in Figures 6.13(a) and 6.13(b) respectively) shows that the temperature was not evenly distributed across the whole sample body during sintering. During sintering, all FGM samples were located on a lining plate. The lining surface limited the temperature distribution on the FGM surface at the bottom location. This uneven temperature distribution interfered with gradual deformation (shrinkage or expansion) at the interfaces and thus led to the failures of the FGM. In order to overcome this problem, an alternative method of displaying the sample inside the furnace need to be determined.



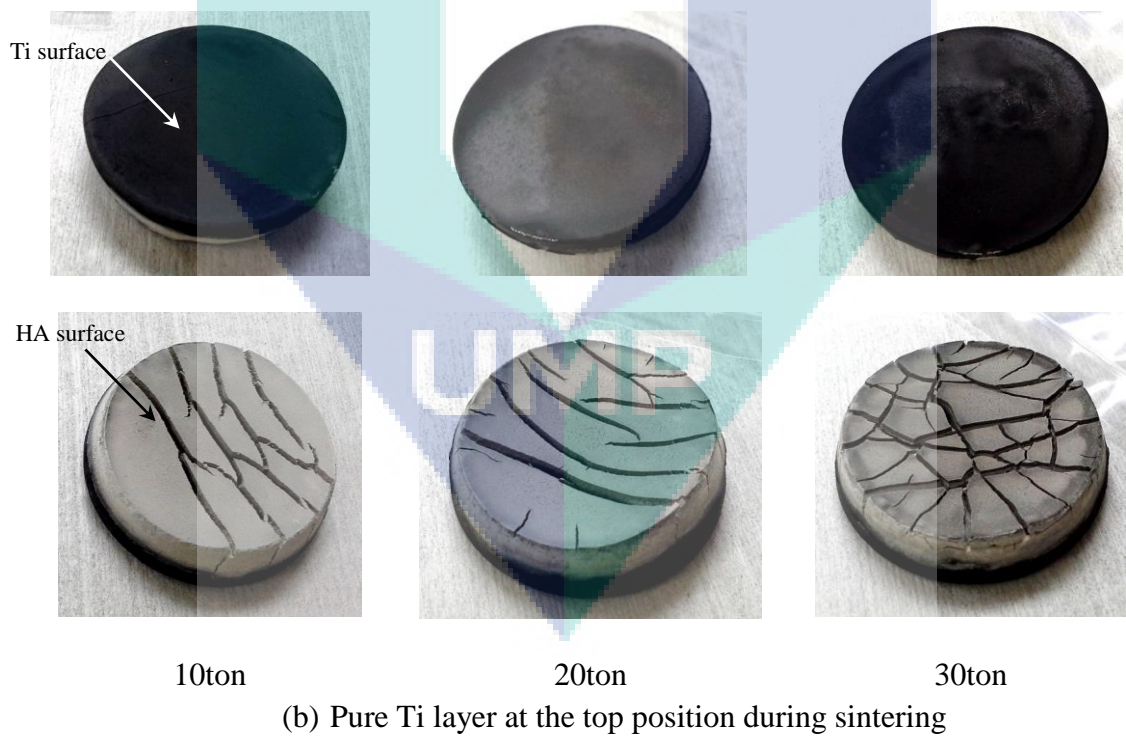
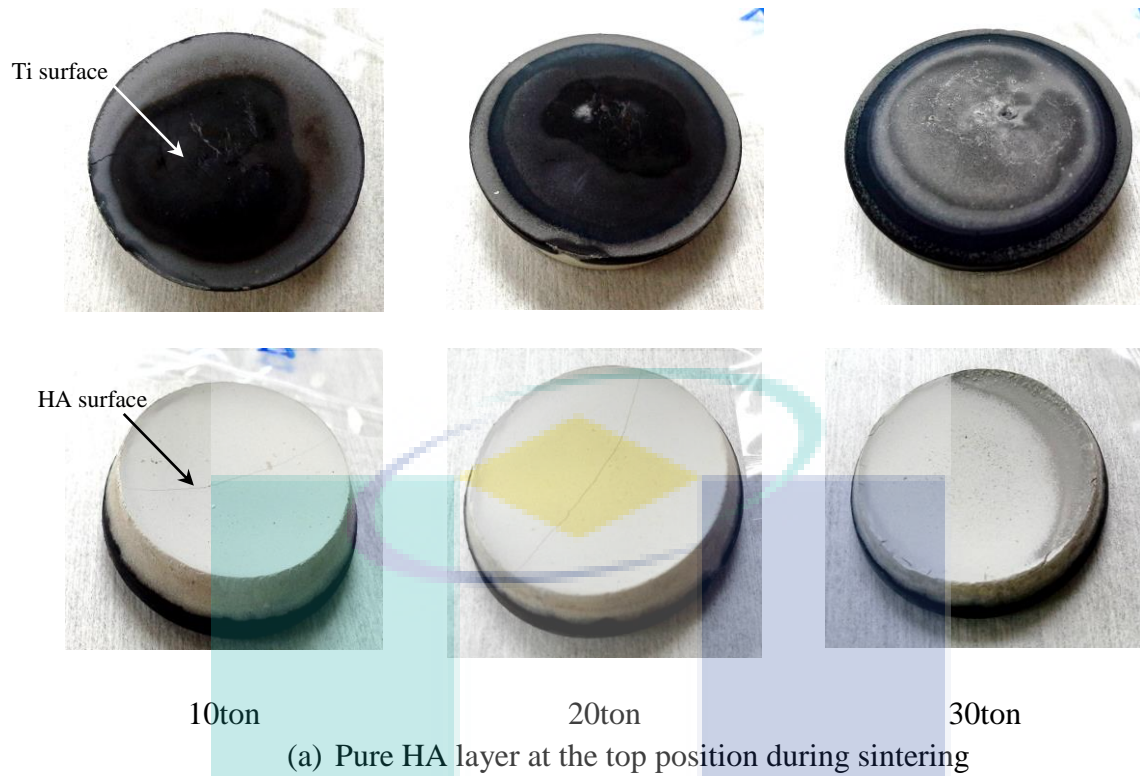


Figure 6.13: The effects of the sample's direction on FGM samples ($L=6$, $T_s=1000^\circ\text{C}$, $h=\pm 7\text{mm}$)

6.3.2 Basic Mechanical Properties

Density

As a part of physical characterization, the density variation within different percentages of the HA and Ti composition were measured via Archimedes' Method and compared with calculations based on ROM. Figures 6.14 and 6.15 show the variation of measurements using Archimedes' Method and the theoretically calculated densities of HA/Ti composites with various constituents' compositional percentages sintered under an oxygen atmosphere (muffle furnace) at 1100°C and 1200°C respectively.

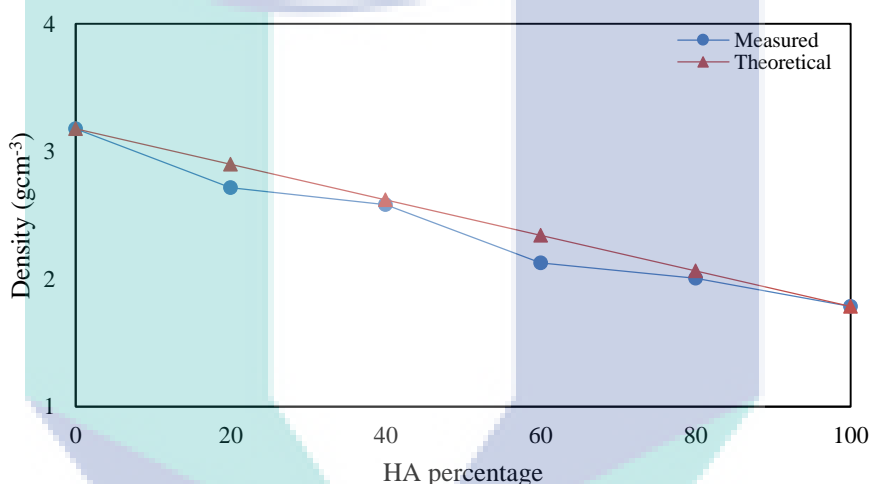


Figure 6.14: Measured and ROM-formulated densities of HA/Ti composites sintered at 1100°C under an O₂ atmosphere for various constituents' compositional percentages

Both Figures 6.14 and 6.15 indicate that the density is inversely proportional to the composition of HA. Besides that, the lower densities of distinctive HA/Ti composites sintered at 1200°C, in comparison to those sintered at 1100°C, show the dominant role of the sintering temperature on the sintering performance of the samples. From this result, a temperature of 1200°C can be taken as the better sintering temperature for the HA/Ti FGM since a minimal of density was often required to achieve or produce good material. This finding correlates highly with those established in the literature (Shahrjerdi *et al.*, 2011). The inequality of the measured and theoretically calculated densities was most probably due to the presence of impurities in

the composites, the unevenly heat-treated area of the samples and other technical errors that have been neglected by the theoretical formulation. The obvious difference between the theoretical and the measured densities of the 20%HA layer may be due to the transformation of Ti to TiO_2 after sintering in an O_2 atmosphere. The measured density was significantly lower than the theoretical density because the composition of the Ti element in this layer was higher when compared to other layers and the density of TiO_2 (Wells, 1984) is less than that of Ti (Lide, 2003).

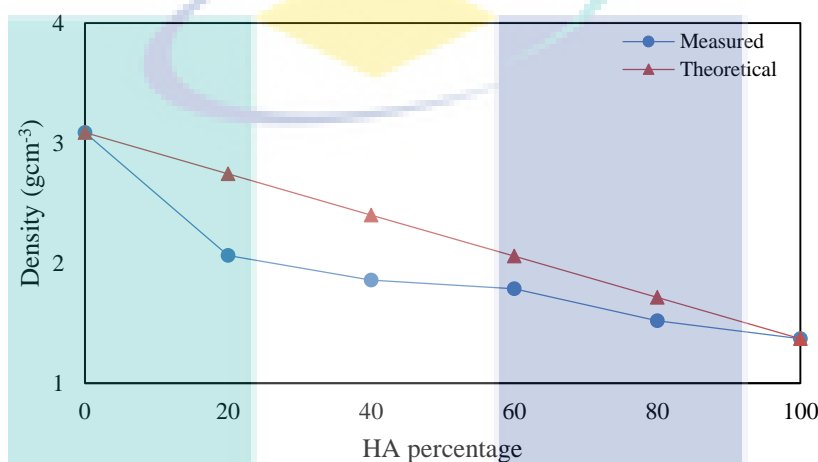


Figure 6.15: Measured and ROM-formulated densities of HA/Ti composites sintered at 1200°C under an O_2 atmosphere for various constituents' compositional percentages

Vicker's Micro-hardness

The micro-hardness test based on the ASTM E384 Standard (Severin *et al.*, 2011) was carried on the HA/Ti FGM samples by applying an indentation load of 0.3 kN using a micro-hardness tester (model-SHIMAZU). The average of at least three measurement values was taken as the main result to its accuracy. The micro-hardness in the FGM samples was measured at the polished cross-sectional surface of each distinctive layer. The variation of the micro-hardness through the thickness of the green FGM sample compacted under 10ton is given in Figure 6.16. The micro-hardness measurement of pure Ti layer was not included in the plot since no visible diamond indentation is obtained. This is most probably due to the uniaxial loading applied during compaction of the green sample which was not sufficient to achieve proper bonding of

Ti particulates. The hardness plotted in Figure 6.16 decreased within the increasing HA percentage except for layers containing 80%HA+20%Ti. This is probably due to the location of the layer closer to the surface on which the uniaxial load was applied.

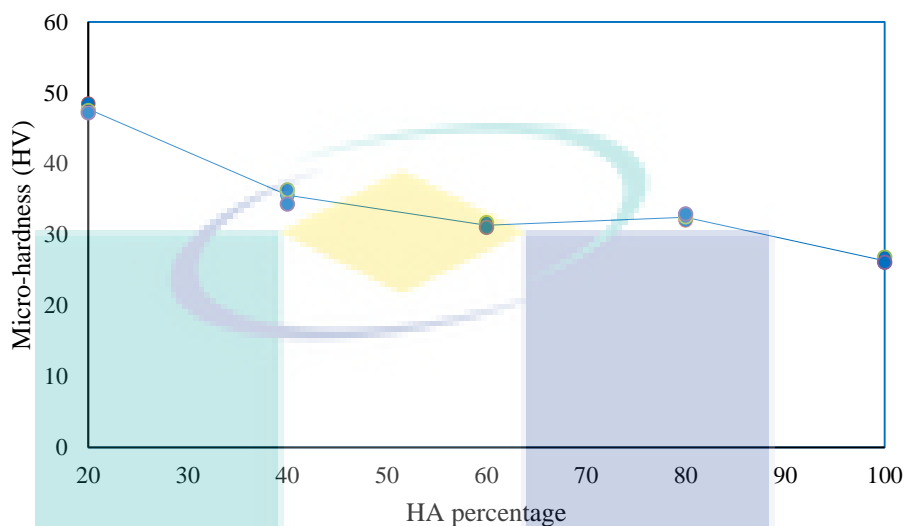


Figure 6.16: Vicker's micro-hardness distribution through the thickness of the green FGM sample compacted under 10ton of pressure ($L=6$, $h=\pm 7$ mm).

Figure 6.17 shows the effects of the compaction load magnitude on the micro-hardness distribution along the thickness of FGM samples sintered under Ar flowing at 1100°C. For FGM samples compacted under 20ton (refer to Figure 6.18(b)), the hardness at the surfaces was higher than those measured at an intermediate position. A similar finding on the relation between hardness and location along the thickness of the FGM sample was reported in Askari *et al.*, (2012). Although the hardness of the pure Ti surface of the FGM sample compacted under 30ton (refer to Figure 6.18(c)) was higher than that found at the inner thickness location, the hardness of the pure HA surface does not follow the same trend. The existence of severe cracks observed on this pure HA layer may be the main reason for the lower hardness compared to those measured at the intermediate thickness location of the sample. The hardness of the pure HA and Ti layers were not highly consistent with the established results (Singh *et al.*, 2011; Rocha *et al.*, 2006). Failures due to unsuitable processing conditions could be the main reason for this. The samples may contain impurities and could have become contaminated after sintering under an O₂ atmosphere. This will be confirmed by the chemical composition

characterization of the sintered samples using XRD and FTIR results, covered in the next section. The unsuitable sintering conditions could also be the reason for the unsuccessful measurement of the hardness at the intermediate layers of the FGM sample compacted under 15ton (refer to Figure 6.18(a)).

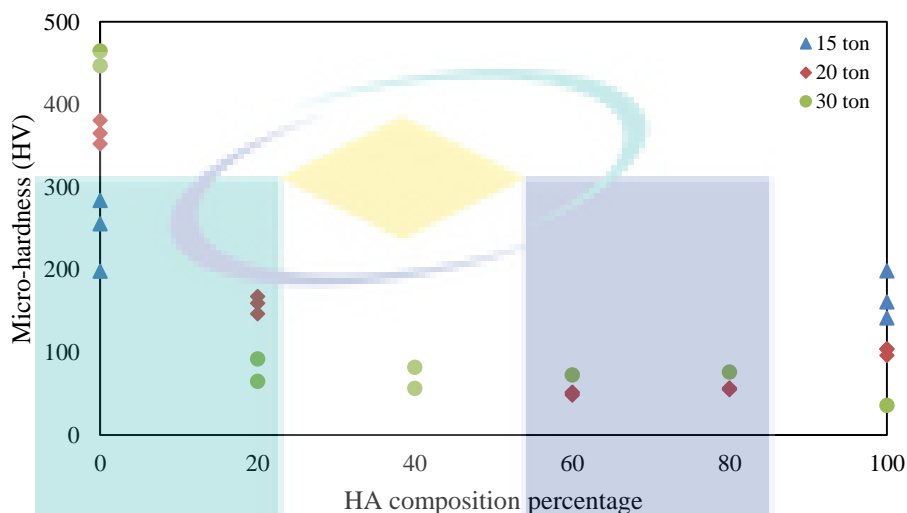


Figure 6.17: Vicker's micro-hardness distribution through the thickness of FGM samples for different compaction loads ($L=6$, $T_s=1100^\circ\text{C}$ (Ar), $h=\pm 7\text{mm}$).

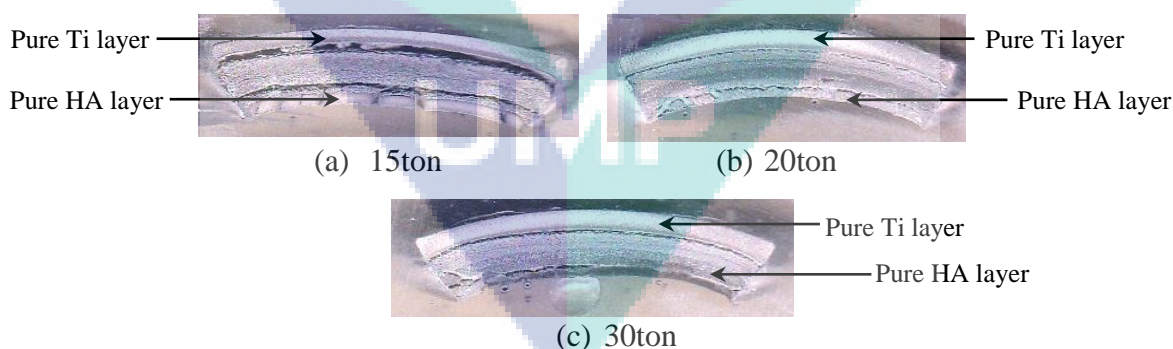


Figure 6.18: FGM samples sintered at 1100°C under an Ar atmosphere for different compaction loads ($L=6$, $h=\pm 7\text{mm}$)

The variation in hardness across the thickness of the FGM samples consisting of 8 layers (see Figure 6.19) with compositions 100HA, 90HA:10Ti, 75HA:25Ti, 60HA:40Ti, 40HA:60Ti, 25HA:75Ti, 10HA:90Ti, 100Ti is given in Figure 6.20. The hardness of the layer containing 60HA:40Ti was lowest when compared to other layers

because of a crack which most probably occurred during the compaction process. This shows the necessity of using a bonding agent which can bond the particulates while avoiding porosity and maintaining the solid structure of the FGM green compact after compaction.

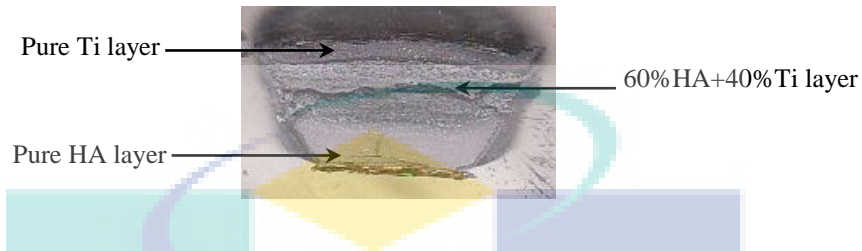


Figure 6.19: FGM sample with higher number of layers ($L=8$, $T_s=1100^\circ\text{C}$ (Ar), $p=10\text{ton}$, $\varnothing=15\text{mm}$, $h=\pm 7\text{mm}$)

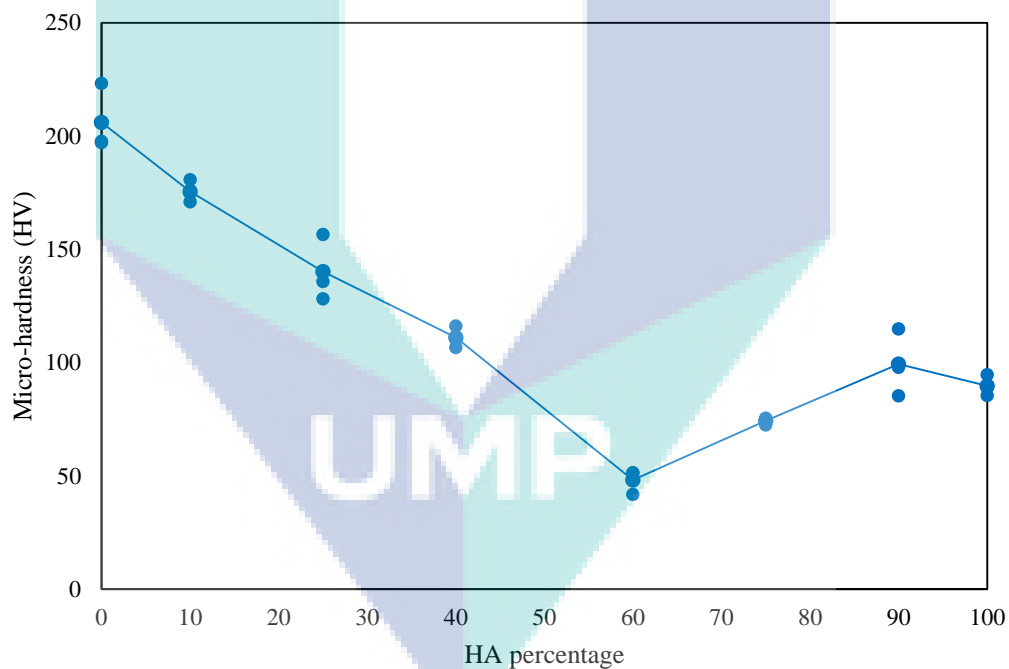


Figure 6.20: Vicker's micro-hardness distribution through the thickness of an FGM sample containing a higher number of layers ($L=8$, $T_s=1100^\circ\text{C}$ (Ar), $p=10\text{ton}$, $\varnothing=15\text{mm}$, $h=\pm 7\text{mm}$).

6.3.3 Metallurgical Characteristics

SEM

The morphological and microstructural characteristics of the FGM samples were observed by a SEM (Philips). Prior to scanning, the FGM samples were ground, polished, ultrasonically cleaned, dried and finally weighed. They were polished using a diamond liquid and the subsequent processes were performed to ensure that no scratches remained on the pre-analysed surface of the sample. The results of the SEM characterization performed on the ground green and sintered FGM samples are presented and discussed in this subsection. The effects of different compaction loads on the microstructure of the distinctive layers inside the FGM samples are given in tabulated form (shown in Figure 6.21.) The grey, white and dark elements (indicated as a, b and c, respectively) in the micrograph images represent the HA, Ti and the porosity profile of the samples. The obvious differences in the microstructure profile of each element within the distinctive layers confirmed the existence of six layers with different compositions inside the FGM sample. In addition to the three different element profiles, the SEM images also indicated that the FGM samples cracked (indicated as d) even before the sintering process. The dispersion of the constituents' particles were not evenly distributed. The reason why there was no obvious variation in the porosity size of the samples for various compaction loads was probably because the polishing process was skipped before characterization. Polishing the samples was impossible because the green compacts dissolve in liquid. However this limitation can be avoided when the samples have been through the sintering process successfully.

Figure 6.22 presents representative SEM micrographs of samples sintered under an N₂ atmosphere for various compaction loads. The pure HA layer of the sample was compacted under 30ton. It consisted of impurities and porosity that were represented by the darker and black elements (indicated as a and b) on the micrographs, respectively. The obvious existence of porosity can also be observed on the layers that contain 80%HA and 60%HA of the sample prepared using a 20ton compaction load. The non-bonded (indicated as c) irregular shape of the Ti particles observed on the pure Ti layer of all FGM samples showed that the layer was not successfully sintered. The N₂ gas

flowing during the sintering process was not helpful for reducing the surface energy of the adjacent Ti particles.

No significant difference was observed in the SEM micrographs of samples sintered under an N_2+H_2 atmosphere shown in Figure 6.23 in comparison to that sintered under flowing N_2 gas. The agglomerates (indicated as a) caused by non-uniform particle size distribution could be clearly seen in the microstructure profile of the layers containing 60%HA (10ton), 60%HA and 40%HA (20ton) and 40%HA (30ton). The uneven arrangement of the particles inside these structures led to difficulties completing the heat treatment process. This result revealed that N_2+H_2 gas was not appropriate for the sintering of HA/Ti FGM samples since most of the constituents' particles remained separate after the heat treatment process.

Figure 6.24 shows the SEM images of samples sintered under an Ar atmosphere using a tube furnace. As observed on the micrographs of samples sintered under N_2 and N_2+H_2 gases described previously, there was no significant difference in the microstructure images that showed the effects of different compaction loads. The main reason for the failures of the FGM samples seen in terms of agglomerates, impurities, non-bonded constituents' particles and pores (represented by arrows a, b, c and d, respectively), even after sintering under flowing Ar (inert) gas, was probably due to the contamination of the tube furnace.

A comparison of the microstructures of distinctive layers in the green and sintered FGM samples is shown in Figure 6.25. Fewer cracks (indicated as a) were observed on the surfaces of sintered FGM samples compared to those found on the green layers. The particle arrangements of the sintered samples were worse than the green compacts due to the failure of sintering process.

The effects of the drying process on the FGM samples sintered under flowing N_2+H_2 gas by cooling from the sintering temperature are shown in Figure 6.26. More agglomerates (represented by a) were found on the microstructure profiles of the non-dried sample in comparison to that of the dried sample. This result showed that the

existence of moisture between adjacent particles inside the FGM samples affected the sintering behaviour of those samples.

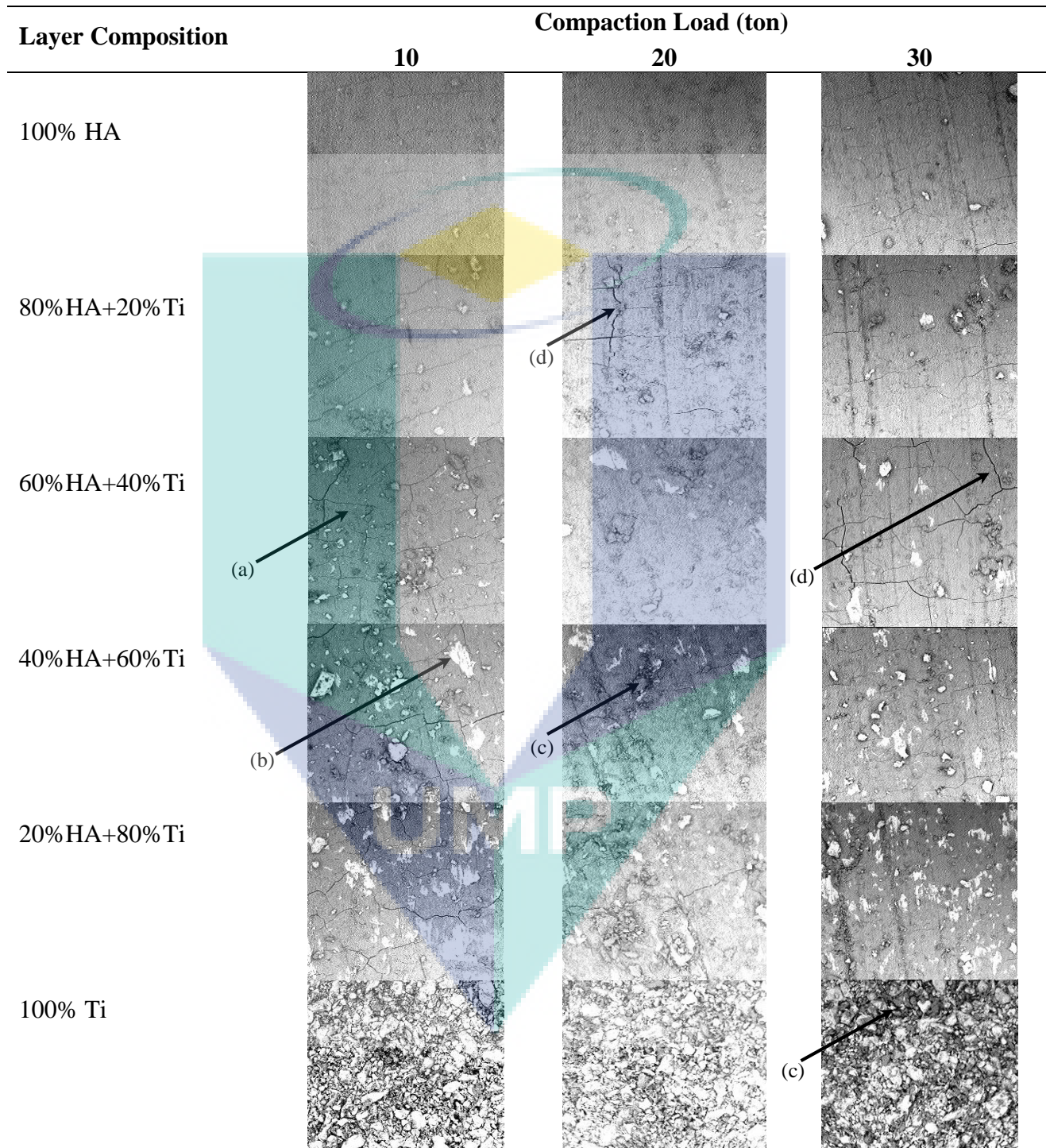


Figure 6.21: SEM images of FGM green samples for various compaction loads ($L=6$, $h=\pm 7\text{mm}$)

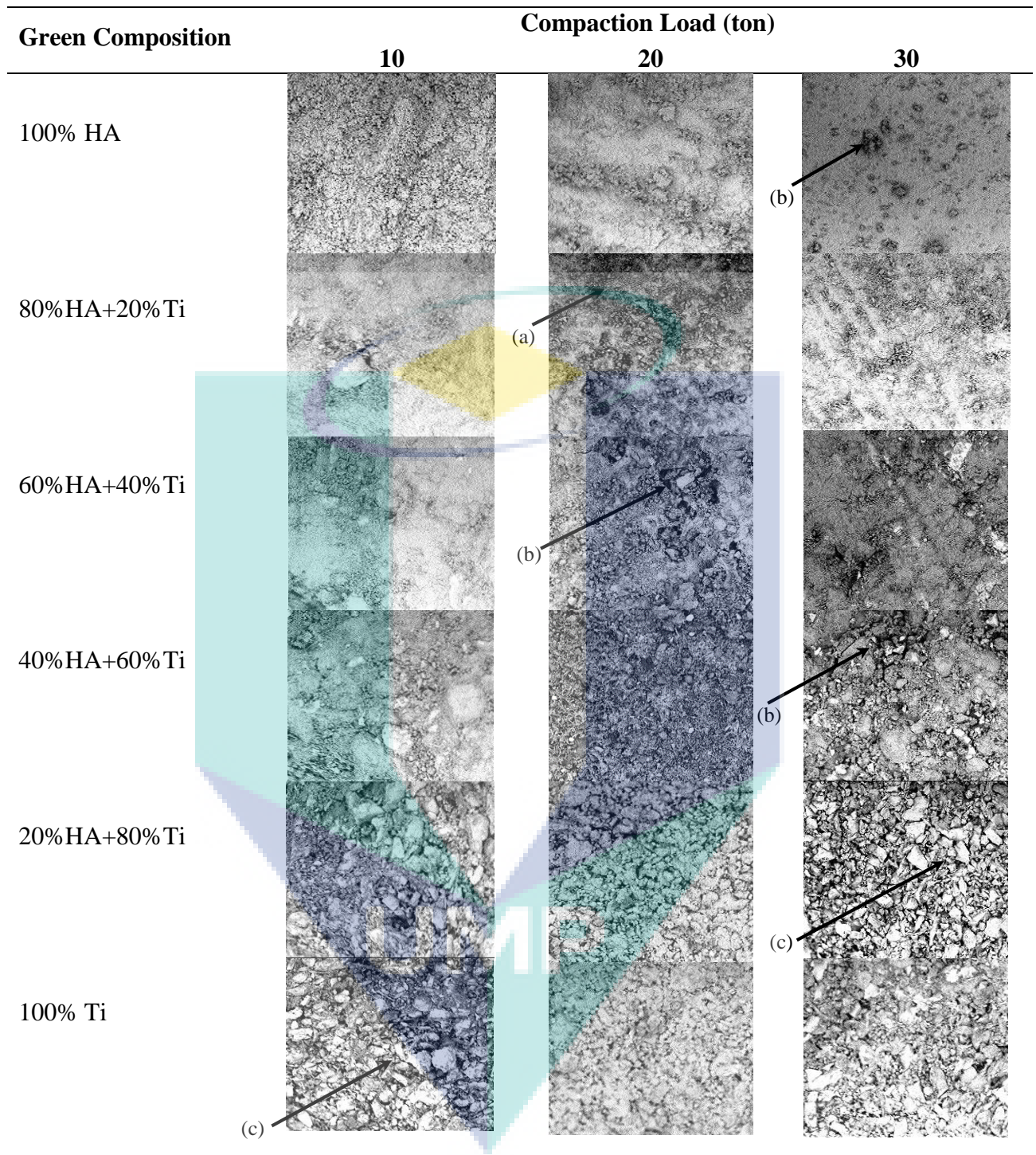


Figure 6.22: SEM images of FGM samples sintered under a N_2 atmosphere for various compaction loads ($L=6$, $T_s=1000^\circ C$, $h=\pm 7mm$)

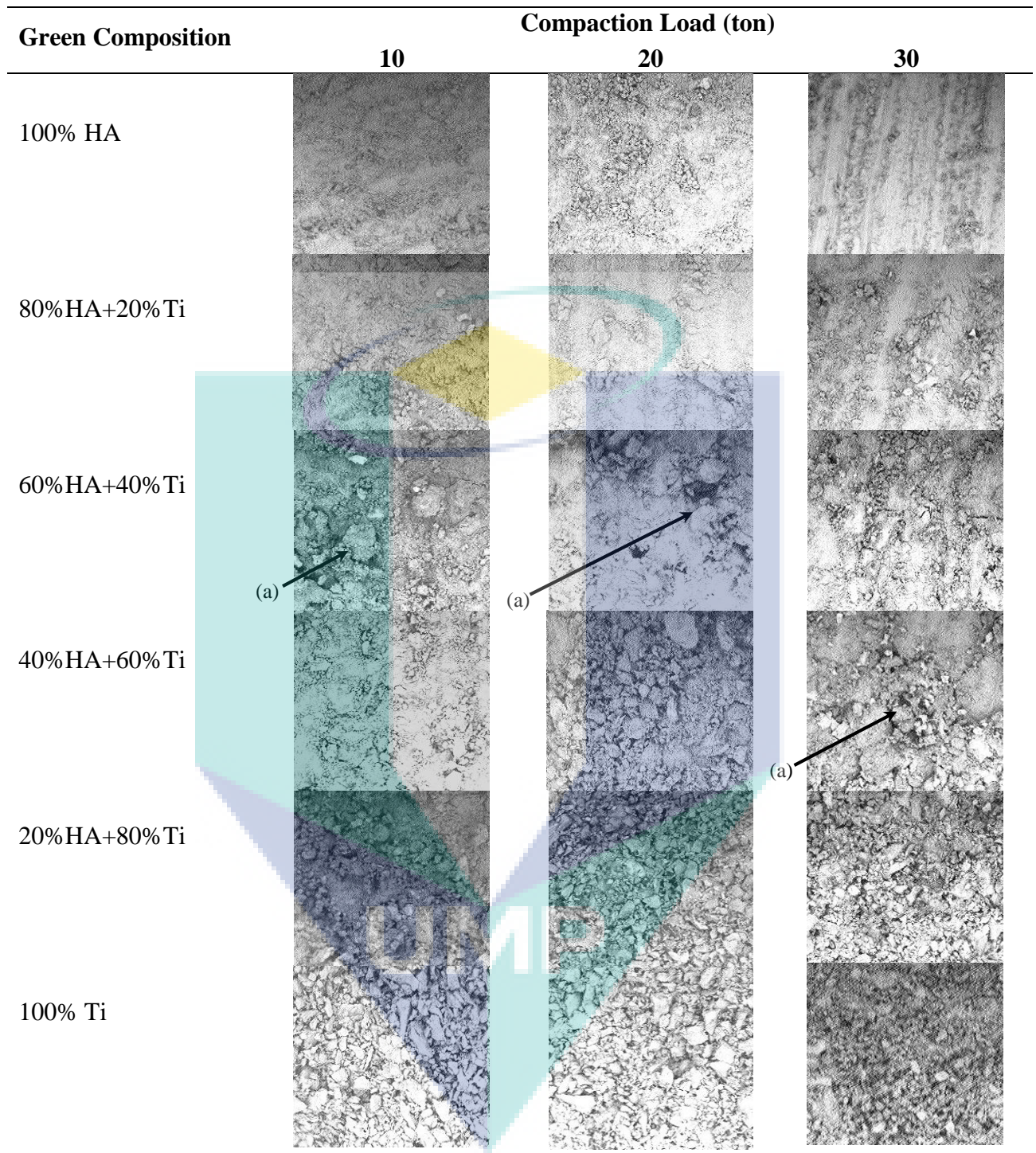


Figure 6.23: SEM images of FGM samples sintered under a N_2+H_2 atmosphere for various compaction loads ($L=6$, $T_s=1000^\circ C$, $h=\pm 7mm$)

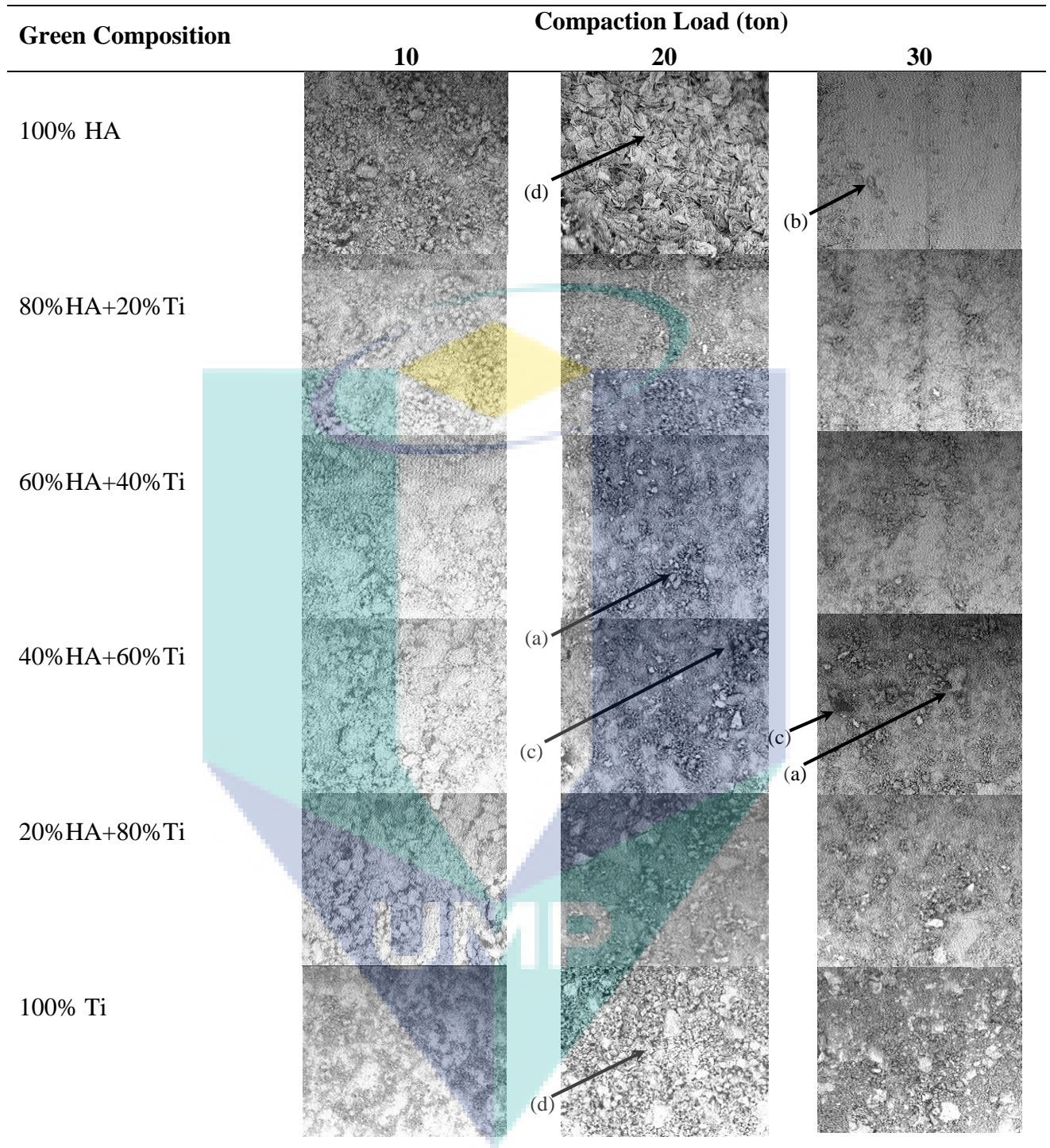


Figure 6.24: SEM images of FGM samples sintered under an Ar atmosphere for various compaction loads ($L=6$, $T_s=1000^\circ\text{C}$, $h=\pm 7\text{mm}$)

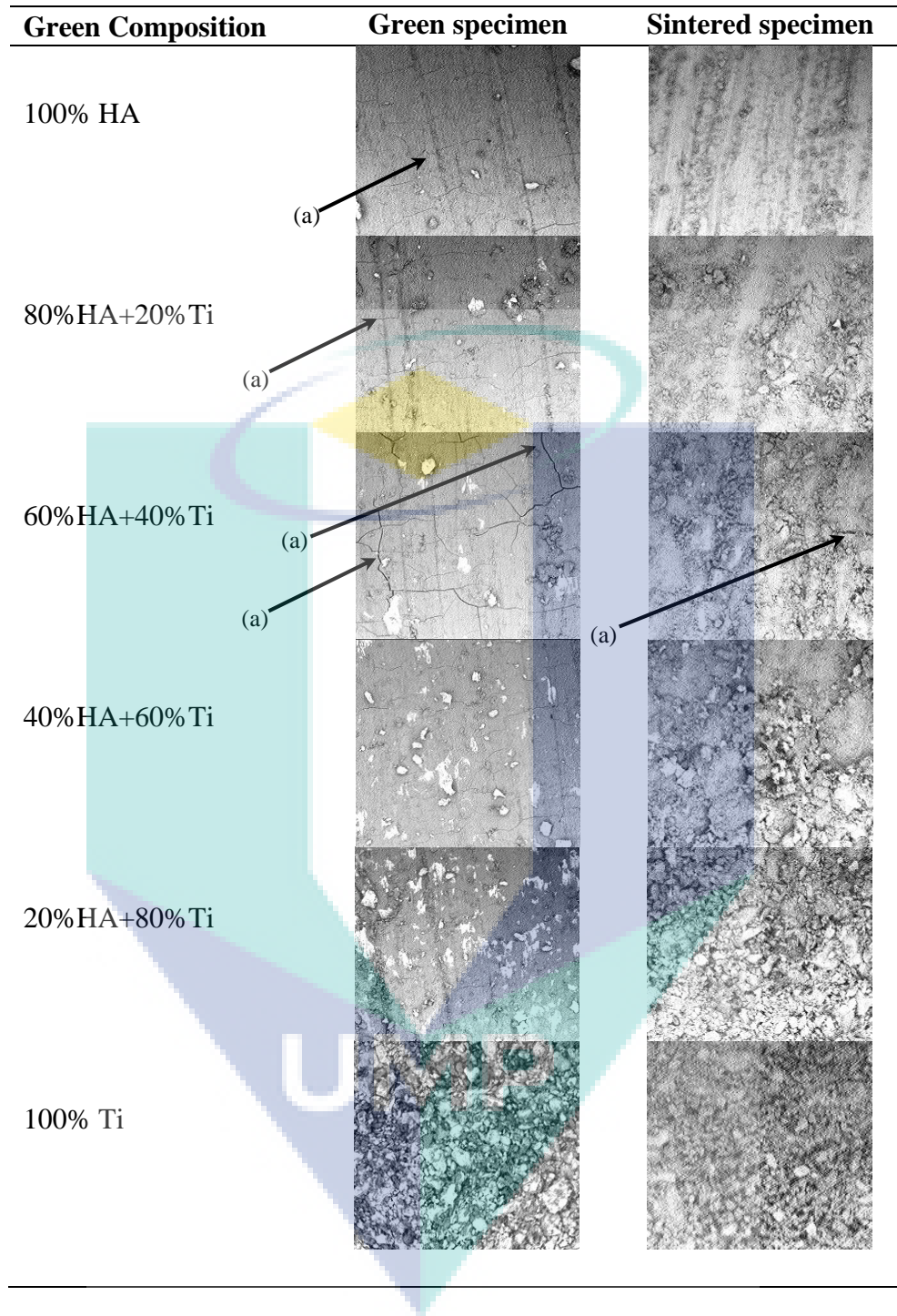


Figure 6.25: SEM images of green ($L=6$, $h=\pm 7\text{mm}$) and sintered FGM samples ($L=6$, $T_s=1000^\circ\text{C}$, $h=\pm 7\text{mm}$)

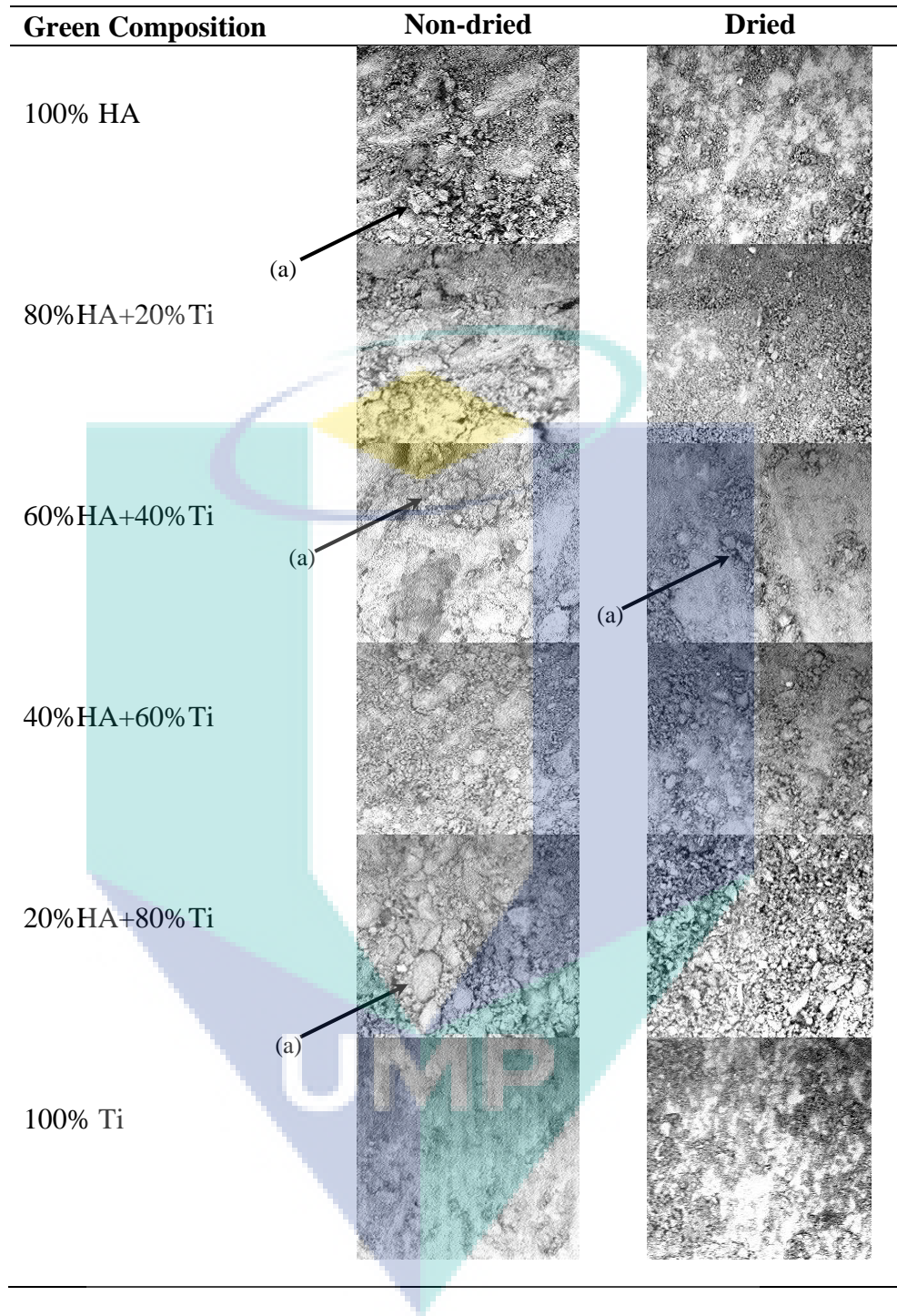


Figure 6.26: SEM images of non-dried and dried FGM samples before sintering ($L=6$, $T_s=1000^\circ\text{C}$, $h=\pm 7\text{mm}$)

FTIR

The objective of characterization using FTIR spectroscopy analysis was to identify the functional bonds present in the FGM samples. This analysis was carried out on the FGM samples using a Perkin Elmer Spectrum 100 FTIR machine. The sampling was prepared using a diamond with an attenuated total reflectance (ATR) crystal with a refractive index of 2.4. Figures 6.27-6.30 show all the functional bonds present in the pure Ti layer of the FGM samples sintered under various atmospheres, which are responsible for organic and inorganic molecules. The FTIR result for the sample sintered under an Ar atmosphere showed evidence of specific spectra for the whitish region on the pure Ti surface, indicated in Figure 6.27. FTIR studies confirmed the presence of medium amine bands (N-H) at 1649.47 cm^{-1} frequency. The titanium elements bonded to the N-H bands were also known as Titanium tetrachloride (TiCl_4). It can be produced by the chloride process when carbon and chlorine exist below a temperature of 900°C . The possibility of C and Cl elements existing inside the tube furnace used for sintering the FGM sample was high because the tube was not properly cleaned and chlorine sources are usually used for the cleaning process.

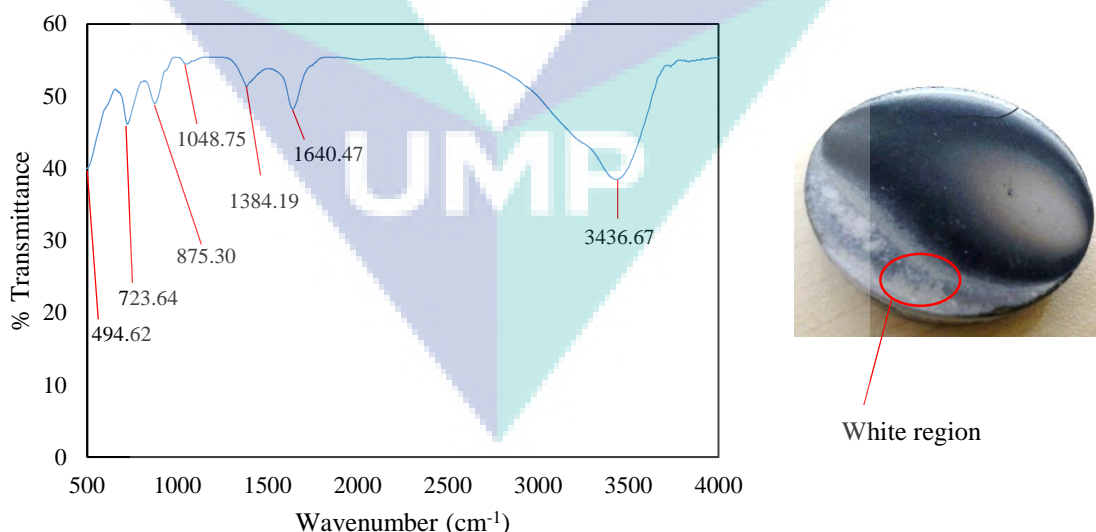


Figure 6.27: FTIR spectra in the white region of the Ti surface of the HA/Ti FGM sintered under an Ar atmosphere ($L=6$, $T_s=1000^\circ\text{C}$, $h=\pm 7\text{mm}$)

Figure 6.28 shows the presence of infrared (IR) bands obtained at the shining region located on the pure Ti layer of the FGM sample sintered under an N_2 atmosphere. The result shows the existence of medium alkyl halides (C-Br) and alkenes (-C=C-) stretches at a frequency of 608 cm^{-1} and 1644 cm^{-1} (respectively) on the sample, proving that the Ti has element reacted with the carbon content. Therefore, it was concluded that the carburization of the sample led to the failure of the sintering process. The C source came from the brick used as the lining of the sample during sintering.

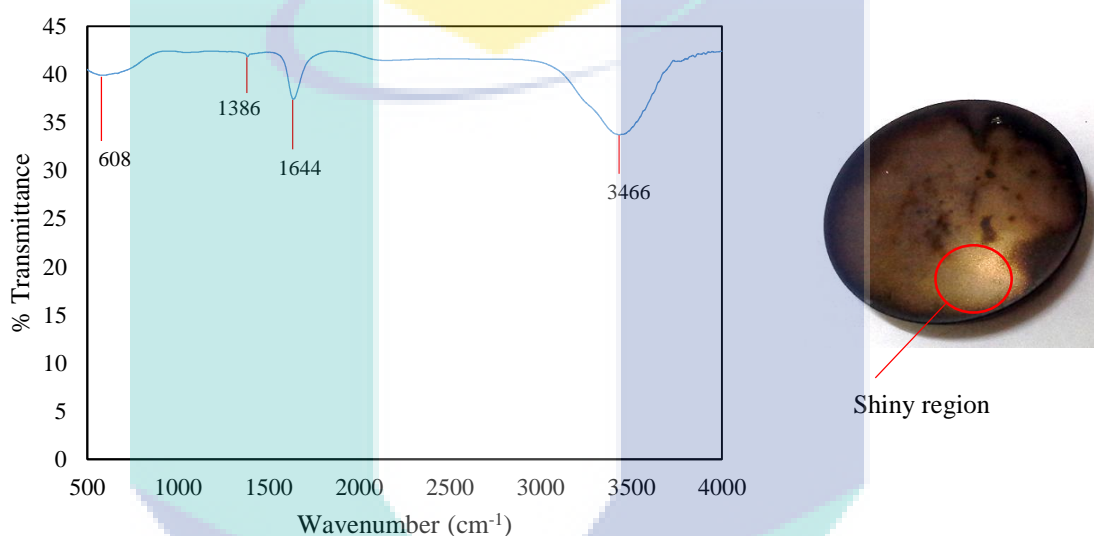


Figure 6.28: FTIR spectra at the shining region on the Ti surface of the HA/Ti FGM sintered under a N_2 atmosphere ($L=6$, $T_s=1000^\circ\text{C}$, $h=\pm 7\text{mm}$)

The FTIR spectra obtained at the greenish area on the pure Ti layer of the sample sintered using a muffle furnace is shown in Figure 6.29. The FTIR results reveal the presence of medium alkyl halides stretching at a frequency of 601.62 cm^{-1} . Aliphatic amines stretch at a frequency of 1043.02 cm^{-1} and amine bands at a frequency of 1634.63 cm^{-1} . The reaction between the pure Ti and O_2 , forming the TiO_2 compound, was confirmed when the present absorbance spectra matched approximately with FTIR results obtained in previous work (Mali *et al.*, 2012).

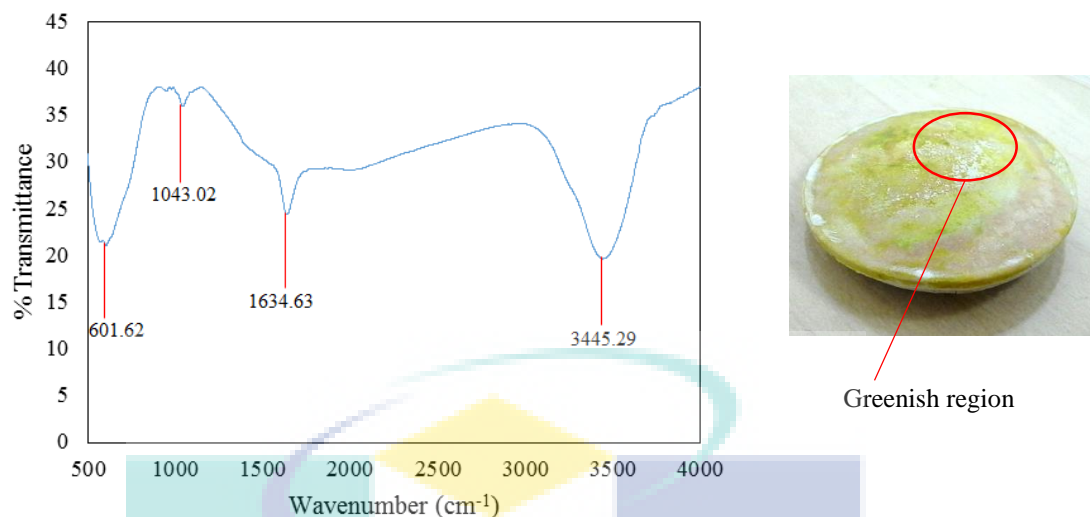


Figure 6.29: FTIR spectra at the greenish region on the Ti surface of the HA/Ti FGM sintered under an O₂ atmosphere (L=6, T_s=1000°C, h=±7mm)

Figure 6.30 shows the FTIR result of the black region on the pure Ti layer of the FGM sample sintered under an Ar atmosphere. The infrared spectra of this sample was highly similar to that obtained on the white region shown in Figure 6.27, where medium amine bands were detected at 1634.07. This result shows that the black coloured region represented the presence of C in the tested sample.

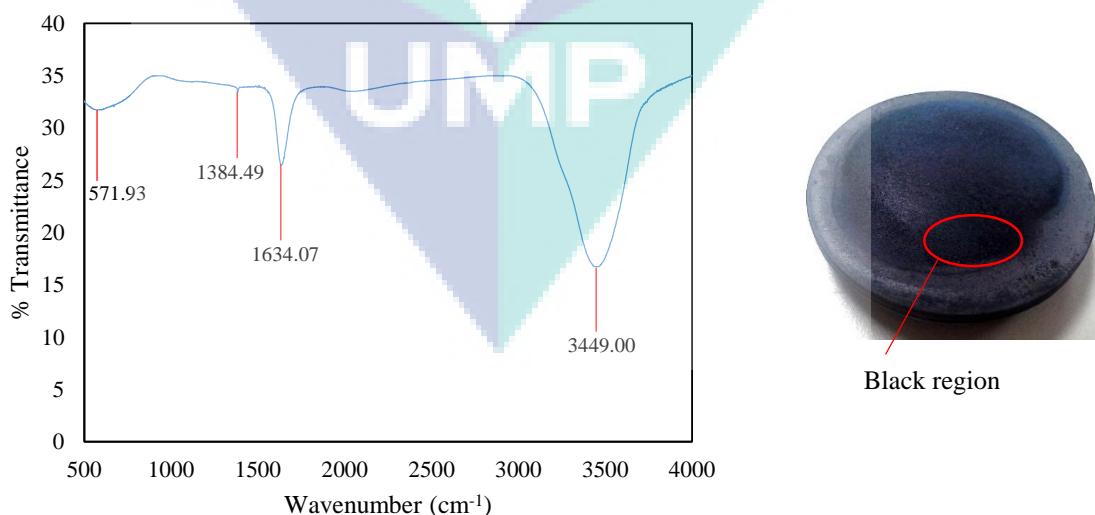


Figure 6.30: FTIR spectra at the black region on the Ti surface of the HA/Ti FGM sintered under an Ar atmosphere (L=6, T_s=1000°C, h=±7mm)

XRD

The detection of phase contamination in the FGM samples was performed using a Rigaku Miniflex X-ray Diffractometer. This machine is equipped with a 6-sample holder for maximum automation of sample measurements. The X-ray of the Cu K_a radiation, filtered by a Ni filter, has a wavelength of 1.54 Å. The Rigaku's full-function powder diffraction analysis package, which provided the Crystallography Open Database (COD) in this instrument, ensured accurate peak calculation and phase identification. This machine was used to measure the powdered FGM sample diffraction patterns from 3° to 80° in a two-theta scanning range.

In order to identify the original XRD patterns and to ensure that the raw materials were free from impurities, the base materials' powders were initially characterized using XRD analysis. The crystal structure of the pure Ti and the pure HA powders in terms of an XRD pattern are presented in Figures 6.31 (a) and 6.31(b) respectively. The phase name and the chemical formula of the inorganic compound HA used in the present study was detected as calcium phosphate hydroxide (Ca₅(OH)(PO₄)₃). Since only single element peaks are found in both XRD patterns, the purity of the base material is considered high.

The phase transformation of the FGM samples sintered under N₂+H₂ gas atmospheres, for different gas flowing durations during the heat treatment process is shown in Figure 6.32. The XRD patterns for all the FGM samples revealed that the samples were contaminated after the sintering process because there were some peaks referring to the existence of different elements in the XRD graphs. The XRD pattern shown in Figure 6.32(a) indicates the transformation of HA into apatite – the compound (CaF)(Ca₅(PO₄)₃F). The hydroxyl bond of the HA was probably broken due to a reaction with the H₂ in the N₂+H₂ gas. Even the O₂ can be eliminated due to its reaction with the O₂ gas remaining in the sintering tube during sintering.

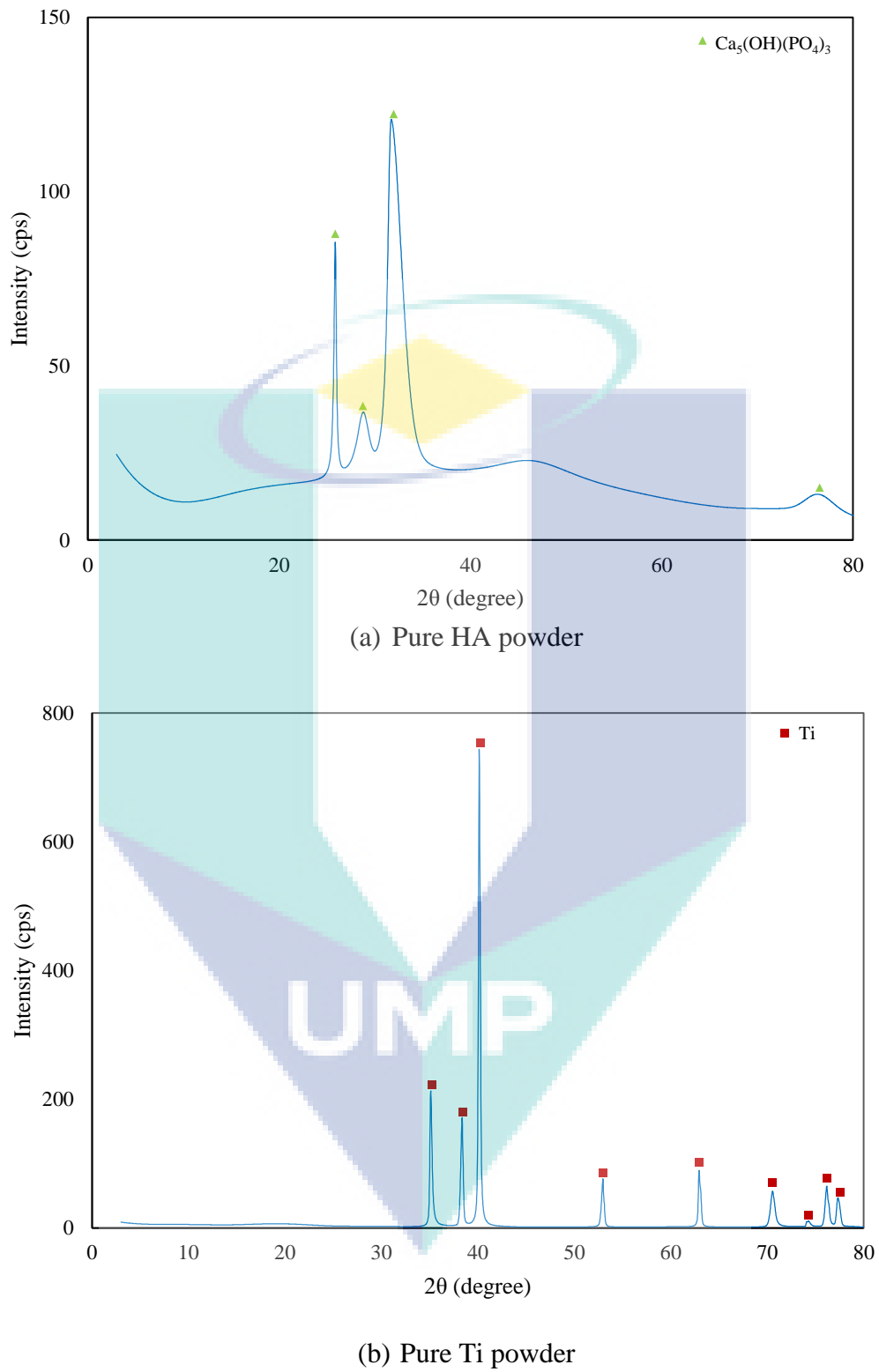


Figure 6.31: XRD pattern of the base materials

Figure 6.32(b) shows the presence of calcium chromium phosphate ($\text{CaCr}(\text{P}_2\text{O}_7)$) and sodium calcium magnesium carbonate phosphate hydroxide ($\text{Ca}_{3.892}\text{Na}_{0.087}\text{Mg}_{0.021}$) in the sintered FGM sample. As shown previously in Figure 6.32(a), the hydroxyl bond of HA is broken. The Cr element was detected because it was used as the XRD source. The presence of sodium (Na), Mg and carbonate in $\text{Ca}_{3.892}\text{Na}_{0.087}\text{Mg}_{0.021}$ are most probably due to the use of brick lining the sample during sintering. The XRD pattern of sample shown in Figure 6.32(c) shows the importance of controlling the atmosphere of the sintering process because XRD peaks for Ti remain. However the suitability of using N_2+H_2 gas for the sintering process needs to be investigated further since the N_2 and H_2 elements in the forming gas react with Ti and make its crystalline structure weak. The presence of a compound containing Ni in the sample is not surprising since it is one of the sources used for the XRD analysis.

The results of the XRD test performed on the dried and non-dried FGM green samples sintered under flowing N_2+H_2 gas during sintering, during the holding time, and under flowing N_2 during cooling, are given in Figure 6.33. The XRD pattern shown in Figure 6.33(a) confirmed the contamination of the FGM sample with the detection of CoO and dipotassium sodium trioxoferrate ($\text{K}_2\text{Na}(\text{FeO}_3)$). The existence of CoO represented the oxidation process which was probably due to the existence of moisture (H_2O) inside the sample. The production of $\text{K}_2\text{Na}(\text{FeO}_3)$ might be due to the brick lining used during sintering. The remaining chemical compositions of HA, inside the calcium hydrogen phosphate hydroxide ($\text{Ca}_9\text{HPO}_4(\text{PO}_4)_5\text{OH}$) as shown in Figure 6.33(b) strengthen the importance of drying process before the sintering process. The N_2 and N_2+H_2 atmospheres were not suitable for the sintering of structures containing HA because they reacted with this compound.

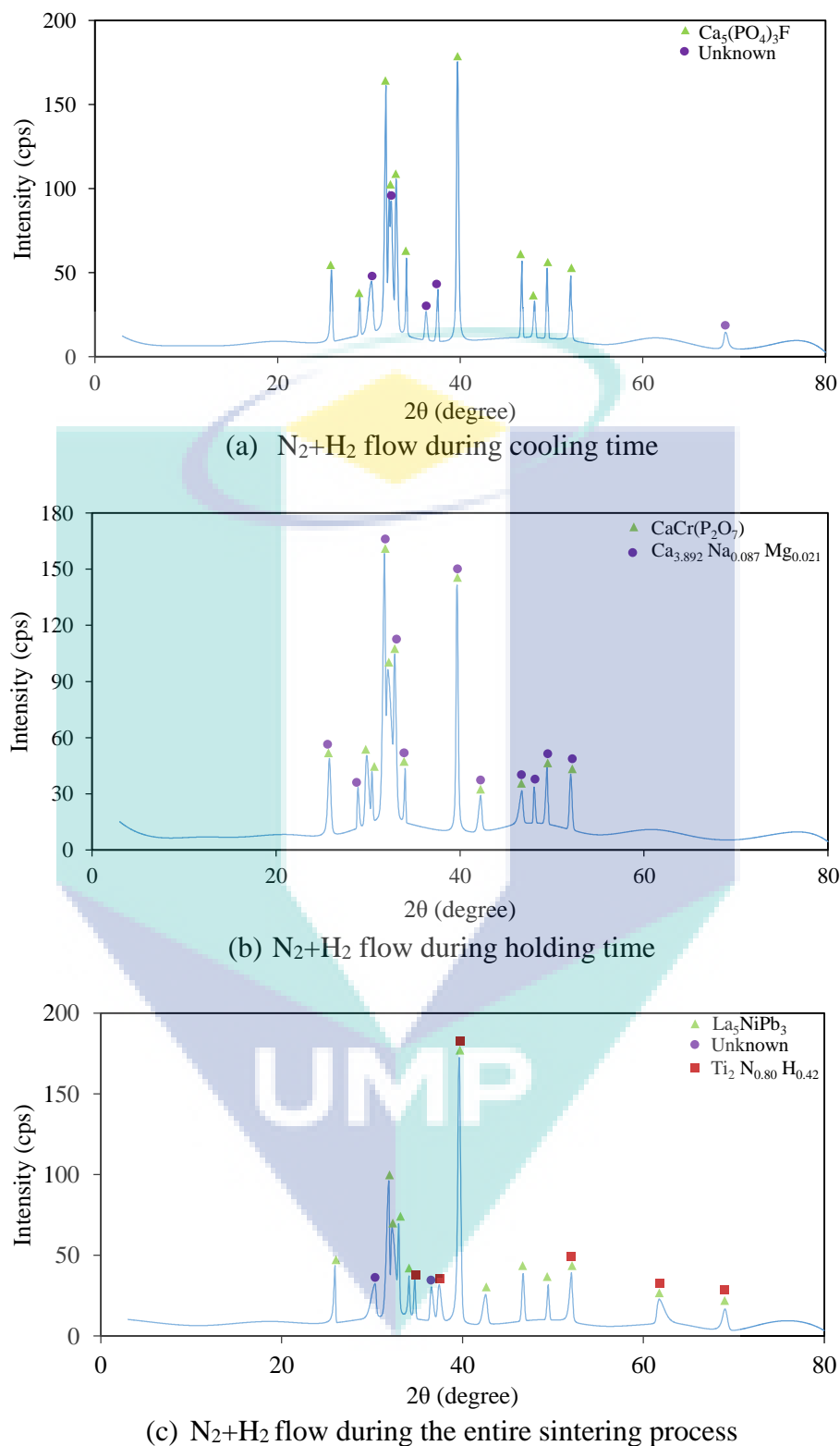


Figure 6.32: The XRD pattern of the FGM sintered under different N_2+H_2 flowing times ($L=6$, $T_s=1000^\circ\text{C}$, $h=\pm 7\text{mm}$)

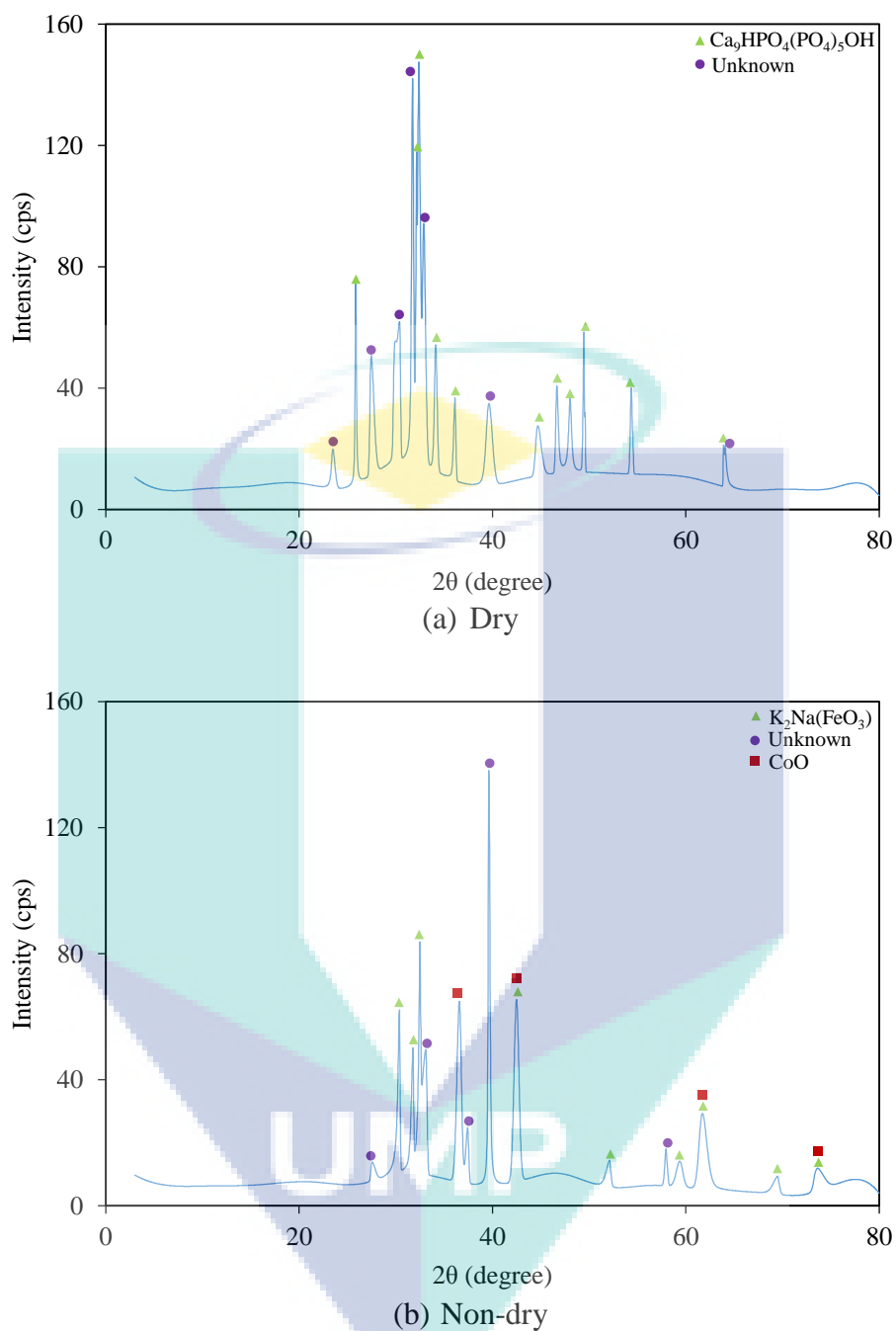
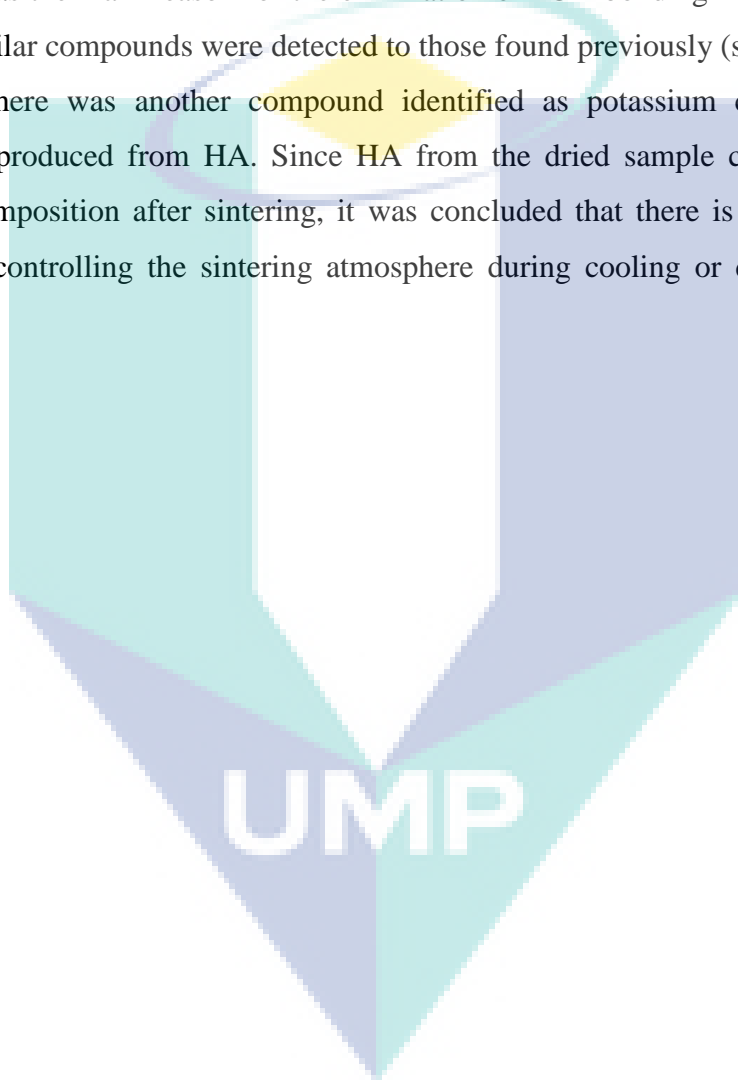


Figure 6.33: The XRD pattern of dried and non-dried FGMs sintered under N_2+H_2 atmosphere during the holding time and N_2 during the cooling time ($L=6$, $T_s=1000^\circ\text{C}$, $h=\pm 7\text{mm}$)

The phase transformations due to the green compact drying of the FGM samples sintered under flowing N_2+H_2 , during the holding period are presented in Figure 6.34. As shown in the XRD pattern of the non-dried sample, the presence of oxidation during the sintering process was confirmed by the detection of lead bismuth iron titanium oxide ($PbBi_{14}Fe_2Ti_{10}O_{45}$). The -OH elements bonded to the C and the phosphate elements of HA, producing calcium phosphate sulfide ($Ca_{10}(PO_4)6S_{0.95}$). The use of N_2+H_2 gas for sintering was the main reason for the elimination of -OH bonding in HA. For the dried sample similar compounds were detected to those found previously (see Figure 6.33(b)). However there was another compound identified as potassium calcium phosphate ($KCaPO_4$) produced from HA. Since HA from the dried sample cannot maintain its original composition after sintering, it was concluded that there is no significance in separately controlling the sintering atmosphere during cooling or during the holding time.



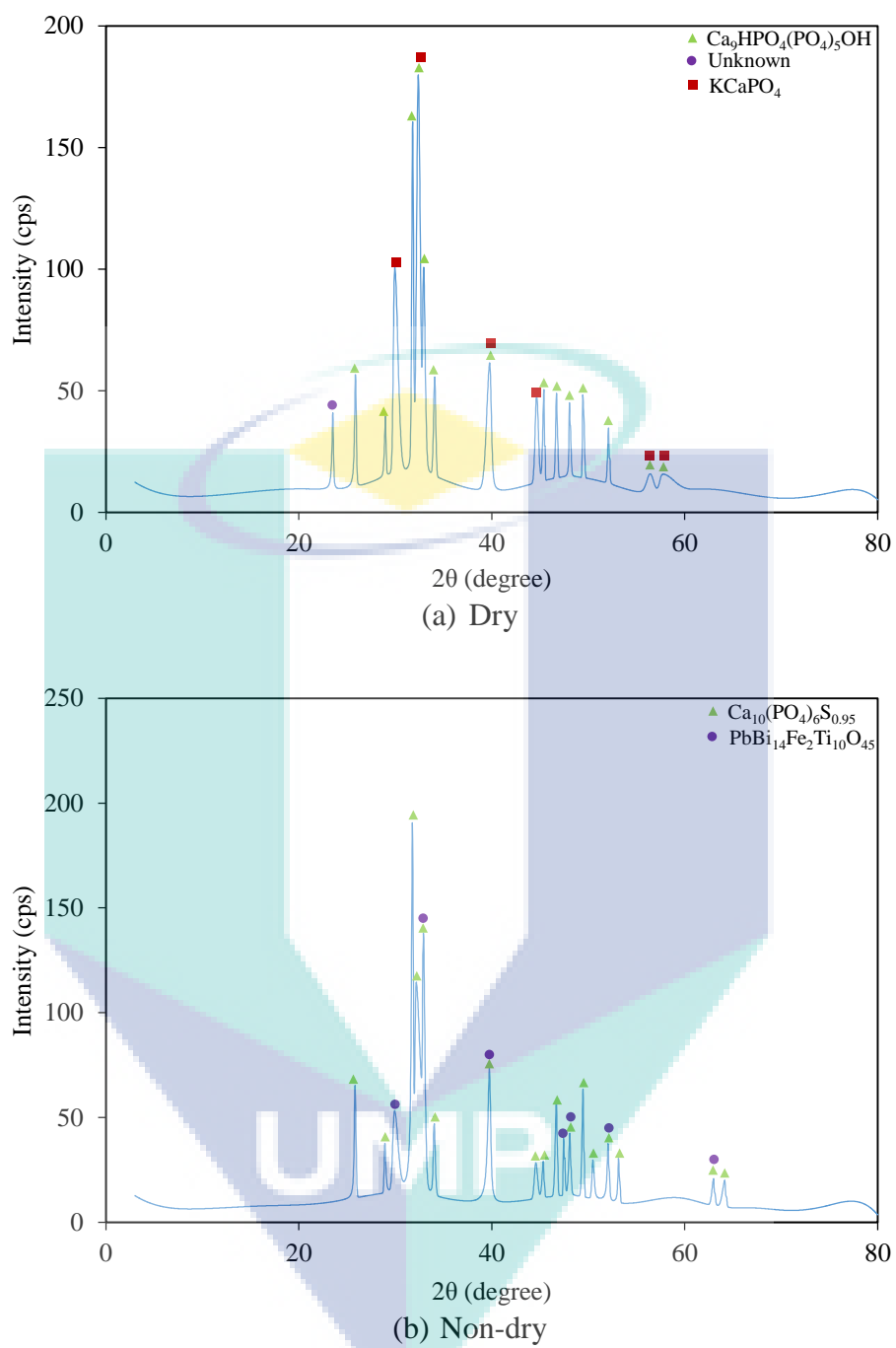
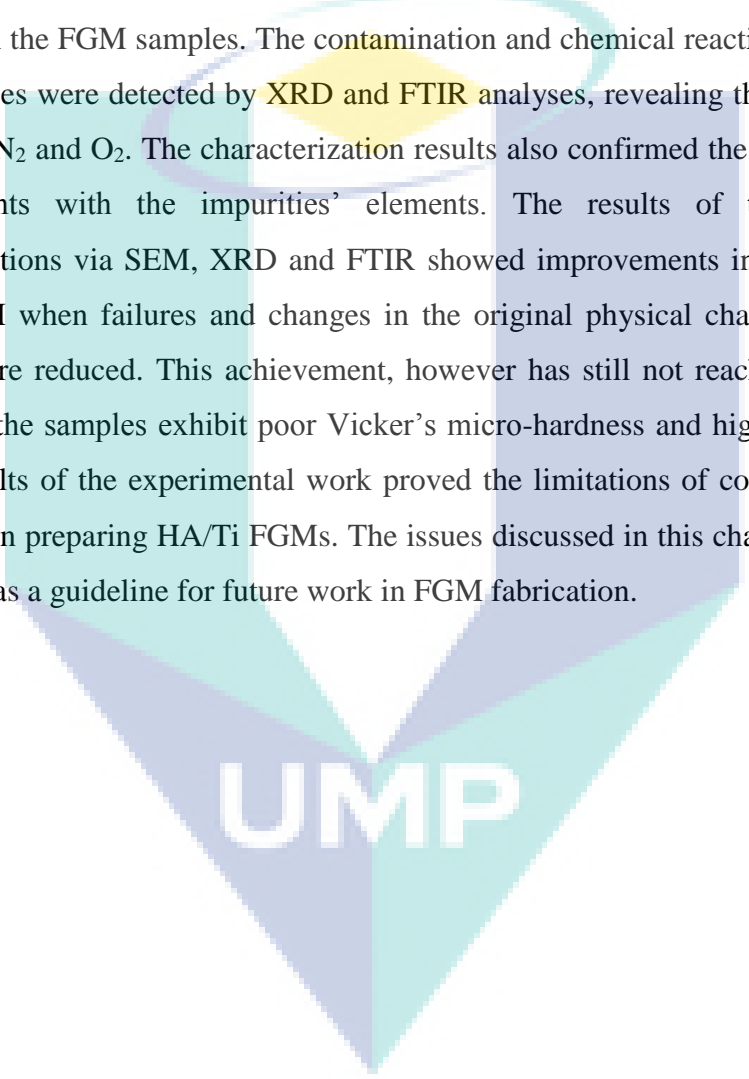


Figure 6.34: The XRD pattern of dried and non-dried FGMs sintered under N_2+H_2 atmosphere during the holding time only ($L=6$, $T_s=1000^\circ\text{C}$, $h=\pm 7\text{mm}$)

6.4 CLOSURE

This chapter combines the discussions on the experimental methodology and results of the analysis performed on the HA/Ti FGM. The powder metallurgy routes used for the FGM fabrication have been explained, together with the various cold PM processing parameters that were considered. Under SEM scanning, failures interpreted in terms of imperfect particulates bonding, impurities and cracking features were observed on the FGM samples. The contamination and chemical reaction of the sintered FGM samples were detected by XRD and FTIR analyses, revealing the high sensitivity of Ti to C, N₂ and O₂. The characterization results also confirmed the high reactivity of HA elements with the impurities' elements. The results of the metallurgical characterizations via SEM, XRD and FTIR showed improvements in the performance of the FGM when failures and changes in the original physical characteristics of the samples were reduced. This achievement, however has still not reached a satisfactory level since the samples exhibit poor Vicker's micro-hardness and high brittleness. The overall results of the experimental work proved the limitations of cold PM processing techniques in preparing HA/Ti FGMs. The issues discussed in this chapter however can be referred as a guideline for future work in FGM fabrication.

The logo for UMP (Universiti Malaysia Perlis) is a large, downward-pointing triangle composed of four smaller triangles meeting at the center. The top-left triangle is light blue, the top-right is light green, the bottom-left is light purple, and the bottom-right is light teal. The letters 'UMP' are written in white, bold, sans-serif font across the center of the triangle.

UMP

CHAPTER 7

CONCLUSIONS AND RECOMMENDATIONS FOR FUTURE WORK

7.1 CONCLUSIONS

In this thesis, the results of the comprehensive numerical and experimental study of the behavior of the HA/Ti FGM have been discussed. A review of the pertinent literature has shown that little effort has been put into the study of the HA/Ti FGM, particularly in the form of comprehensive parametric design data. This study has led to an improved understanding of the various characteristics and operating conditions of HA/Ti FGM. The objectives of the numerical work have been achieved in two ways. Its first achievement was the correlation between the parameters that affect the FGM property gradient and the FGM design performance, shown in terms of residual stresses distributions computed using 2-D FE computation. Another objective was achieved by understanding the various characteristics of the HA/Ti FGM under mechanical, thermal and thermo-mechanical loading effects, obtained using 3-D numerical calculations.

Unlike the theoretical findings, the achievement of the experimental work does not reach this level of satisfaction. Although various criteria were developed to determine the successful operating conditions of the HA/Ti FGM, these were neither suitable nor reliable enough for fabrication of the FGM. The main limitations included inappropriate facilities for fabrication, as well as a lack of information regarding processing. However because each unexpected and imperfect result was provided with a detail explanation, it is believed that the data and its limitations can be a basis for the successful processing of the HA/Ti FGM in the future.

Specific conclusions relating to the results obtained from the numerical and experimental studies are as follows:

1. A 2-D FE model was developed for the optimization of the geometrical design parameters for the pre-designed cylindrical HA/Ti FGM plate. Various grading indices, numbers of layers and FGM thickness were considered while determining the optimum FGM plate design. Consequently the correlation between these parameters and the residual stresses distribution of the structure were established. The results obtained confirmed that the grading index number, the number of layers and their thickness have significant effects on the stresses occurring due to changes in ambient temperature. Therefore, major consideration needs to be taken over these parameters in order to develop an essential design for the FGM.
2. The optimal graded compositional distribution exponent, the number of layers and the thickness of the FGM layers inserted between the pure constituents layers for the HA/Ti asymmetrical cylindrical FGM plate were acquired by the residual stresses relaxation design and structure optimization, and were found to be $n=1$, $L \geq 6$ and $t = \pm 8$ mm respectively.
3. The thermo-mechanical problems of the simply supported cylindrical HA/Ti FGM plate have been solved using a 3-D FE model. Various characteristics of the FGM under isothermal, thermal and thermo-mechanical loading conditions have been considered to gain better understanding of the capability of the advanced material. From the numerical results, it was observed that the thermo-mechanical responses in terms of deflection and various stresses were different compared to those subjected to either mechanical or thermal loading alone. The effects of thermo-mechanical loading were slightly greater than those induced by the uncoupled loading. The ability of the HA/Ti FGM to withstand extreme temperature, mechanical pressure and thermo-mechanical loading conditions revealed the potential of this material in applications such as aerospace engineering and the pressure vessel industry.
4. A parametric study of the various characteristics of the cylindrical HA/Ti FGM plate confirmed that the parameters that control the property gradation of the structure such as its grading index number, the number of layers and their

thickness have a dominant effect on the structural behaviors of the FGM subjected to various loadings. However the responses distribution varied in a sequential manner with respect to the effective properties, including Young's modulus, Poisson's ratio, the thermal expansion coefficient and the thermal conductivity of the constituents.

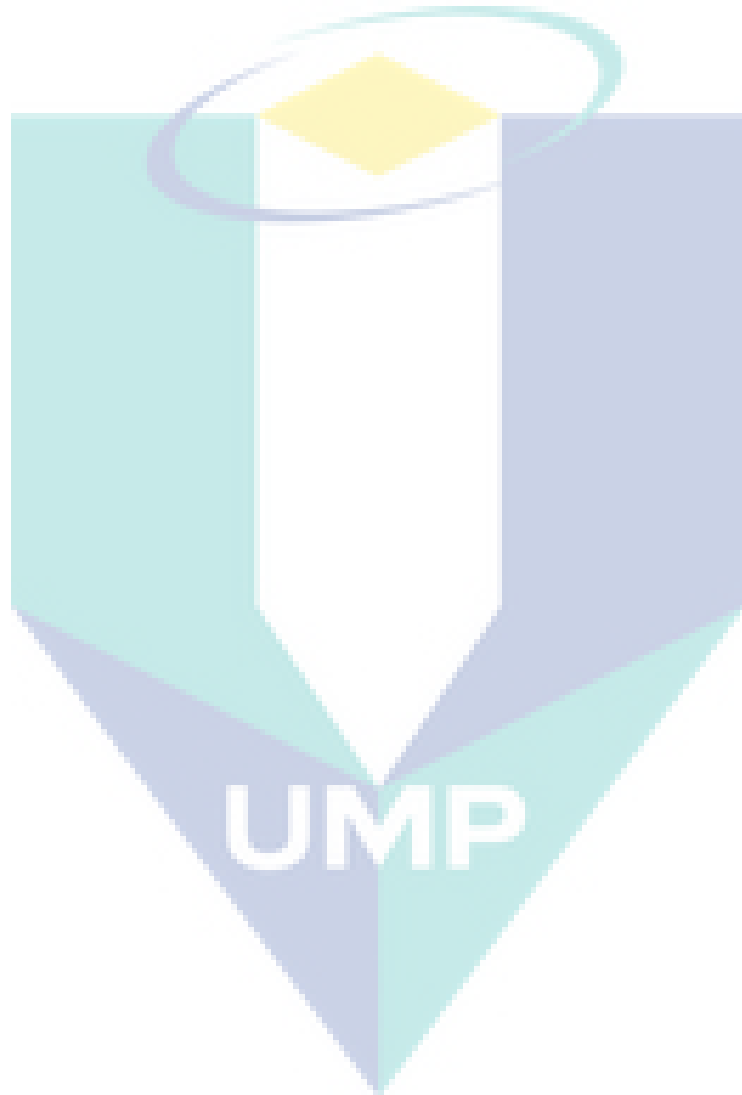
5. The powder metallurgy technique involving cold particulate processing was implemented in a proper sequence for the preparation of the HA/Ti FGM sample. Various operating parameters of the cold compaction and pressure-less sintering processing have been accounted for during the manufacturing process. Although the optimum condition for the fabrication of the FGM sample is yet to be determined, the effects and limitations of considered independent variables on the sample are clearly observable.
6. The SEM images consisting of the unaffiliated or unbonded particles of the sintered FGM reveal the unsatisfactory nature of the fabrication process. The different operating necessities of HA and Ti constituents led to difficulties in the fabrication of the HA/Ti FGM. The high tendency of Ti to react with the flowing gases (O_2 , N_2) and the sensitivity of HA to the presence of impurities during sintering of the FGM were confirmed by the XRD results.
7. Failures of the fabricated FGM specimen were not only caused by the limitations of the sintering process but might also be due to an improper powder processing technique and the compaction process. The significance of controlling the sintering atmosphere, preserving the particle binding of the green compact and assuring the proper particulate processing, revealed the sensitivity and complexity of both HA and Ti.

7.2 RECOMMENDATIONS FOR FUTURE WORK

Based on these numerical and experimental findings, few improvements can currently be made. The following are several recommendations for future work in the present study:

1. Numerical analysis of the comparison between various characteristics of the FGM with property gradients predicted on different established theories such as the modified rule of mixture (MROM), power law and exponential functions. The numerically predicted properties and behaviours of the FGM can be compared to those calculated using analytical models.
2. Extended failure analysis that investigates the effects of various modes of cracking on the HA/Ti FGM. The numerical crack analysis can be verified with experimental results of flexural strength measured via 3-point or 4-point bending testing. Otherwise the crack initiation in the structure can also be recorded by high speed camera and compared to those computed or predicted using a numerical model.
3. The fabrication of the HA/Ti FGM might be improved by applying a binding agent or adhesion compound either in between the distinctive FGM interfaces or to the whole of the mixed particulates. These elements can help to avoid delamination between the distinctive laminated layers as well as holding or strengthening the bonding of different constituent particulates until consolidation is completed. Another suggestion is the use of a sintering aid to minimize the required sintering time, while at the same time preserving the original characteristics of the constituents. A binding agent and sintering aid compatible with HA and Ti needs to be determined to ensure that no other chemical reactions are caused by the added compounds.
4. For the fabrication of the HA/Ti FGM, it could be suggested that either CIP or hot pressing techniques are utilised. The CIP technique could improve the bonding performance of the green compact since the pressure is applied simultaneously from all directions. A better bonding performance also could be

achieved by hot pressing. The simultaneously applied pressure and temperature during the process could preserve the particulates from debonding and at the same time facilitate the sintering activity.



REFERENCES

- Alibeigloo, A. 2010. Exact solution for thermo-elastic response of functionally graded rectangular plates. *Composite Structures*. **92**(1): 113-121.
- Alshorbagy, A.E., Alieldin, S.S., Shaat, M. and Mahmoud, F.F. 2013. Finite element analysis of the deformation of functionally graded plates under themomechanical loads. *Mathematical Problems in Engineering*. **2013** (Article ID 569781): 1-13.
- Askari, E., Mehrali, M., Metselaar, I.H.S.C., Kadri, N.A. and Rahman, M.M. 2012. Fabrication and mechanical properties of Al₂O₃/SiC/ZrO₂ functionally graded material by electrophoretic deposition. *Journal of Mechanical Behavior of Biomedical Materials*. **12**: 144-150.
- Bahr, H-A., Balke, H., Hofinger, I., Kirchhoff, G., Munz, D., Neubrand, A., Semenov, A.S., Weiss, H-J. and Yang, Y.Y. 2003. Cracks in functionally graded materials. *Materials Science and Engineering A*. **362**: 2-16.
- Balbinotti, P., Gemelli, E., Buerger, G., Lima, S.A., Jesus, J., Camargo, N.H.A., Henriques, V.A. and Soares, G.D.A. 2011. Microstructure development on sintered Ti/HA biocomposites produced by powder metallurgy. *Materials Research*. **14**(3): 384-393.
- Bao, G. and Wang, L. 1995. Multiple cracking in functionally graded ceramic/metal coatings. *International Journal of Solids Structures*. **32**(19): 2853-2871.
- Batin, G., Popa, C., Brandusan, L. and Vida-Simiti, I. 2011. Mechanical properties of Ti/HA functionally graded materials for hard tissue replacement. *Powder Metallurgy Progress*. **11**: 206-209.
- Beal, V.E., Erasenthiran, P., Hopkinson, N., Dickens, P. and Ahrens, C.H. 2006. The effect of scanning strategy on laser fusion of functionally graded H13/Cu materials. *International Journal of Advanced Manufacturing Technology*. **30**: 844-852.
- Bhangale, R.K. and Ganesan, N. 2006. Static analysis of simply supported functionally graded and layered magneto-electro-elastic plates. *International Journal of Solid and Structures*. **43**: 3230-3253.
- Bhattacharyya, M., Kumar, A.N. and Kapuria, S. 2008. Synthesis and characterization of Al/SiC and Ni/Al₂O₃ functionally graded materials. *Materials Science and Engineering A*. **487**: 524-535.
- Boucafa, A., Benzair, A., Tounsi, A., Draiche, K., Mechab, I. and Bedia, E.A. 2010. Analytical modeling of thermal residual stresses in exponential functionally graded material system. *Materials & Design*. **31**: 560-563.

- Bulbul, F. and Efeoglu, I. 2010. The effect of TiC transient layer on a DLC based functionally gradient coating prepared by closed field unbalanced magnetron sputtering plating system. *Metals and Materials International*. **16**(4): 573-580.
- Cannillo, V., Mazza, D., Siligardi, C. and Sola, A. 2008. Cobalt doped glass for the fabrication of percolated glass-alumina functionally graded materials. *Ceramics International*. **34**: 447-453.
- Chagnon, F. 2010. Effect of powder characteristics, mix formulation and compacting parameters on green density of PM parts. *Advances in Powder Metallurgy & Particulate Materials*. **1**(3): 1-11.
- Chan, Y-S., Paulino, G.H. and Fannjiang, A.C. 2008. Gradient elasticity theory for mode III fracture in functionally graded materials-Part II: Crack parallel to the material gradation. *Journal of Applied Mechanics*. **75**: 1-10.
- Chen, D.J. and Mayo, M.J. 1996. Rapid rate sintering of nanocrystalline ZrO_2 -3 mol% Y_2O_3 . *Journal of the American Ceramic Society*. **79**(4): 906-912.
- Chen, F. and Jie, W. 2007. Finite element design of MgO/Ni system functionally graded materials. *Journal of Materials Processing Technology*. **182**(1-3): 181-184.
- Chen, F. and Jie, W. 2007. Finite element design of MgO/Ni system functionally graded materials. *J. Mater. Process. Technol.* **182**(1-3): 181-184.
- Chen, F., Jianguang, X. and Hou, Z. 2012. In situ pressureless sintering of SiC/MoSi₂ composites. *Ceramics International*. **38**: 2767-2772.
- Cho, K-M., Choi, I-D. and Park, I. 2004. Thermal properties and fracture behaviour of compositionally graded Al-SiC_p composites. Designing, processing and properties of advanced engineering materials. *Materials Science Forum*. **449**: 621-624.
- Chu, C., Lin, P., Dong, Y., Xue, X., Zhu, J. and Yin, Z. 2002. Fabrication and characterization of hydroxyapatite reinforced with 20 vol % Ti particles for use as hard tissue replacement. *Journal of Materials Science. Materials in medicine*. **13**(10): 985-992.
- Chu, C., Xue, X., Zhu, J. and Yin, Z. 2006. In vivo study on biocompatibility and bonding strength of Ti/Ti-20 vol.% HA/Ti-40 vol.% HA functionally graded biomaterial with bone tissue in the rabbit. *Materials Science and Engineering A*. **429**: 18-24.
- Chu, C., Zhu, J., Yin, Z. and Lin, P. 2003. Optimal design and fabrication of hydroxyapatite-Ti asymmetrical functionally graded biomaterial. *Materials Science and Engineering A*. **348**: 244-250.
- Chung, Y.L. and Chi, S.H. 2001. The residual stress of functionally graded materials. *Journal of the Chinese Institute of Civil and Hydraulic Engineering*. **13**: 1-9.

- Cojocaru, C.V., Wang, Y., Moreau, C., Lima, R.S., Mesquita-Guimaraes, J., Garcia, E., Miranzo, P. and Osendi, M.I. 2010. Mechanical behavior of air plasma-sprayed YSZ functionally graded mullite coatings investigated via instrumented indentation. *Journal of Thermal Spray Technology*. **20**: 100-108.
- Delale, F. and Erdogan, F. 1983. The crack problem for a nonhomogeneous plane. *Journal of Applied Mechanics*. **50**(3): 609-614.
- Delale, F. and Erdogan, F. 1988. On the mechanical modeling of the interface region in bonded half-planes. *Journal of Applied Mechanics*. **55**: 317-324.
- Dobrzanski, L.A., Dolzanska, B., Golombek, G. and Matula, G. 2011. Characteristics of structure and properties of a sintered graded tool materials with cobalt matrix. *Archives of Materials Science and Engineering*. **47**(2): 69-76.
- Dobrzanski, L.A., Lukaszewicz, K. and Labisz, K. 2006. Structure of monolayer coatings deposited by PVD techniques. *Journal of Achievements in Materials and Manufacturing Engineering*. **18**(1-2): 271-274.
- El-Desouky, A.R. and El-Wazery, M.S. 2013. Mixed mode crack propagation of zirconia/nickel functionally graded materials. *International Journal of Engineering Transactions B: Application*. **26**(8): 885-894.
- El-Hadad, S., Sato, H., Muira-Fujiwara, E. and Watanabe, Y. 2009. Review fabrication of Al-Al₃Ti/Ti₃Al functionally graded materials under a centrifugal force. *Materials 2010*. **3**: 4639-4656.
- Elperin, T. and Rudin, G. 2007. "Thermal mirror" method for measuring physical properties of multilayers coatings. *International Journal of Thermophysics*. **28**(1): 60-82.
- El-Wezary, M.S. El-Desouky, A.R., Hamed, O.A., Mansour, N.A. and Hassan, A.A. 2012. Preparation and mechanical properties of zirconia/nickel functionally graded materials. *Arab Journal of Nuclear Sciences and Applications*. **45**(2): 435-446.
- Eriksson, M., Radwan, M. and Shen, Z. 2013. Spark plasma sintering of WC, cemented carbide and functional graded materials. *International Journal of Refractory Metals and Hard Materials*. **36**: 31-37.
- Fan, Z., Tsakiroopoulos, P. and Miodownik, A.P. 1994. A generalized law of mixtures. *Journal of Materials Science*. **29**:141-150.
- Fazarinc, M., Muhič, T., Šalej, A., Bombač, D., Fajfar, P., Terčelj, M. and Kugler, G. 2011. Thermal fatigue testing of bulk functionally graded materials. *Procedia Engineering*. **10**: 692-697.

- Fidancevska, E., Ruseska, G. and Bossert, J. 2007. Fabrication and characterization of porous bioceramic composites based on hydroxyapatite and titania. *Materials Chemistry and Physics*. **103**: 95-100.
- Fu, P.R.K., Gorin, A., Sujun, D. and Oo, Z. 2012. On the problem of novel composite materials development for car brake rotor. *International Journal of Engineering and Physical Sciences*. **6**: 333-336.
- Ganesh, P., Kaul, R., Mishra, S., Bhargava, P., Paul, C.P., Singh, C.P., Tiwari, P., Oak, S.M. and Prasad, R.C. 2009. Laser rapid manufacturing of bi-metallic tube with Stellite-21 and austenitic stainless steel. *Transaction of Indian Institute of Metals*. **62**(2): 169-174.
- Gasik, M.M., Zhang, B., Biest, O.V., Vleugels, J., Anne, G. and Put, S. 2003. Design and fabrication of symmetric FGM plates. *Materials Science Forum*. **423-425**: 23-28.
- Ge, C.C., Wu, A.H., Ling, Y.H., Cao, W.B., Li, J.T. and Shen, W.P. 2002. New progress of ceramic-based functionally graded plasma-facing materials in China. *Key Engineering Materials*. **224**(2): 459-464.
- German, R.M. 2001. Manipulation of strength during sintering as a basis for obtaining rapid densification without distortion. *Materials Transactions*. **42**(7): 1400-1410.
- Ghanbari, A. and Shafiee, S. 2013. Effect of functionally Poisson ratio on the stress and displacement of FGM cylindrical pressure vessels. *Advances in Agriculture, Science and Engineering*. **3**(10): 1235-1241.
- Gowtam, D.S., Rao, A.G., Mohape, M., Khatkar, V., Deshmukh, V.P. and Shah, A.K. 2008. Synthesis and characterization of in-situ reinforced Fe-TiC steel FGMs. *International Journal of Self-Propagating and High-Temperature Synthesis*. **17**(4): 227-232.
- Hashin, Z. and Shtrikman, S. 1963. A variational approach to the theory of the elastic behaviour of multiphase materials. *Journal of Mechanics and Physics of Solids*. **11**: 127-140.
- Hassannin, H. and Jiang, K. 2010. Infiltration-processed, functionally graded materials for microceramic components. *Micro Electro Mechanical System (MEMS) IEEE 23rd International Conference*, pp. 368-371.
- He, X., Du, H., Wang, W., Jing, W. and Liu, C. 2008. Fabrication of ZrO₂-SUS functionally graded materials by slip casting. *Key Engineering Materials*. **368-372**: 1823-1824.
- Henriques, B., Soares, D. and Silve, F.S. 2011. Optimization of bond strength between gold alloy and porcelain through a composite interlayer obtained by powder metallurgy. *Materials Science and Engineering A*. **528**: 1415-1420.

- Hilal, M.K., Shareef, M.Y., Maher, K.A. and Noort, R.V. 2012. Fabrication and characterisation of a calcium phosphate/zirconia composite. *International Research Journal of Biotechnology*. **3**(7): 112-119.
- Hill, R. 1963. Elastic properties of reinforced solids: Some theoretical principles. *Journal of Mechanics and Physics of Solids*. **11**: 357-372.
- Jamaludin, S.N.S., Mustapha, F., Nuruzzaman, D.M. and Basri, S. 2013. A review on the fabrication techniques of functionally graded ceramic-metallic materials in advanced composites. *Scientific Research and Essays*. **8**(21): 828-840.
- Jaworska, L., Rozmus, M., Królicka, B. and Twardowska, A. 2006. Functionally graded cermets. *ACI Materials Journal*. **17**(1-2): 73-76.
- Jiang, W., Nair, R. and Molian, P. 2005. Functionally graded mold inserts by laser-based flexible fabrication: Processing modeling, structural analysis, and performance evaluation. *Journal of Materials Processing Technology*. **166**(2): 286-293.
- Joshi, A., Patnaik, A., Gangil, B. and Kumar, S. 2012. Laser assisted rapid manufacturing technique for the manufacturing of functionally graded materials. *2012 Students Conference on Engineering and Systems (SCES 2012)*, pp. 1-3.
- Katayama, T., Sukenaga, S., Saito, N., Kagata, H. and Nakashima, K. 2011. Fabrication of Al₂O₃-W functionally graded materials by slip casting method. *Materials Science and Engineering*. **18**(20): 20-23.
- Kawasaki, A. and Watanabe, R. 2002. Thermal fracture behavior of metal/ceramic functionally graded materials. *Engineering Fracture Mechanics*. **69**: 1713-1728.
- Kiani, Y. and Eslami, M.R. 2013. Thermomechanical buckling of temperature-dependent FGM beams. *Latin American Journal of Solids and Structures*. **10**(2): 223-246.
- Kiebeck, B., Neubrand, A. and Riedel, H. 2003. Processing techniques for functionally graded materials. *Materials Science and Engineering A*. **362**: 81-105.
- Kim, J.H., Kim, M.C. and Park, C.G. 2003. Evaluation of functionally graded thermal barrier coatings fabricated by detonation gun spray technique. *Surface and Coatings Technology*. **168**: 275-280.
- Kim, J.I., Kim, W-J, Choi, D-J, Park, J.Y. and Ryu, W-S. 2003. C/SiC multilayer coating for the oxidation resistance of C-C composite by low pressure chemical vapor deposition. *International Journal of Modern Physics B*. **17**(8-9): 1223-1228.
- Kim, J.I., Kim, W-J., Choi, D-J., Park, J.Y. and Ryu, W-S. 2005. Design of a C/SiC functionally graded coating for the oxidation protection of C/C composites. *Carbon*. **43**(8): 1749-1757.

- Kohnke, P. 2013. ANSYS Mechanical APDL Theory Reference (online). <http://www.ansys.com> (11 December 2014)
- Kondo, H., Yokoyama, A., Omori, M., Ohkubo, A., Hirai, T., Watari, F., Uo, M. and Kawasaki, T. 2004. Fabrication of titanium nitride/apatite functionally graded implants by spark plasma sintering. *Materials Transactions*. **45**(11): 3156-3162.
- Kopeliovich, D. 2014. Substech Substances & Technologies: Hardness test methods (online). www.substech.com/dokuwiki/doku.php?id=hardness_test_methods (13 January 2015)
- Kumar, R.P. and Wang, M. 2002. Modulus and hardness evaluations of sintered bioceramic powders and functionally graded bioactive composites by nano-indentation technique. *Materials Science and Engineering A*. **338**: 230-236.
- Kursun, A., Topcu, M. and Tetik, T. 2011. Stress analysis of functionally graded disc under thermal and mechanical loads. *Procedia Engineering*. **10**: 2949-2954.
- Lakdawala, M. and Malik, G.M. 2013. Hydroxyapatite/titania coating on titanium strip by brush coating. *Archives of Applied Science Research*. **5**(3): 137-141.
- Larsson, C. and Oden, M. 2004. Hardness profile measurements in functionally graded WC-Co composites. *Materials Science and Engineering A*. **382**: 141-149.
- Lee, J.C., Park, J.H., Ryu, S.H., Hong, H.J., Riu, D.H., Ahn, S.H. and Lee, C.S. 2008. Reduction of functionally graded material layers for $\text{Si}_3\text{N}_4/\text{Al}_2\text{O}_3$ system using three-dimensional finite element modeling. *Materials Transaction*. **49**(4): 829-834.
- Lee, W.J., Yang, J.S., Park, Y.H., Park, B.G., Park, I.M. and Park, Y.H. 2009. Fabrication and residual stress characterization of squeeze infiltrated $\text{Al}_{18}\text{B}_4\text{O}_{33}/\text{Mg}$ functionally graded material. *International Journal of Modern Physics B*. **23**: 1485-1490.
- Li, J.Q., Zeng, X.R., Tang, J.N. and Xiao, P. 2003. Fabrication and thermal properties of a YSZ-NiCr joint with an interlayer of YSZ-NiCr functionally graded material. *Journal of European Ceramic Society*. **23**: 1847-1853.
- Li, J-F., Takagi, K., Ono, M., Pan, W. and Watanabe, R. 2003. Fabrication and evaluation of porous piezoelectric ceramics and porosity-graded piezoelectric actuators. *Journal of American Ceramic Society*. **86**(7): 1094-1098.
- Li, M., Song, Y., Cui, S., Hui, Z., Zhou, Z. and Lu, Y. 2005. Investigation on brass/W-Cu alloy functionally graded material (FGM) by infiltration diffusion method. *Chinese Journal of Rare Metals*. **2005**(5): 768-772.
- Lide, D.R. 2003. *CRC handbook of chemistry and physics*. 84th ed. Florida: CRC Press.

- Liew, K.M., Lei, Z.X., Yu, J.L. and Zhang, W. 2014. Postbuckling of carbon nanotube-reinforced functionally graded cylindrical panels under axial compression using meshless approach. *Computer Methods in Applied Mechanics and Engineering*. **268**: 1-17.
- Liu, J. and German, R.M. 1999. *Particle and particle systems characterization*. German: Wiley VCH.
- Liu, S., Shen, Q., Luo, G., Li, M. and Zhang, L. 2012. Calculation of tape thickness for ceramic tape casting. 7th China International Conference on High-Performance Ceramics, **512**: 328-333.
- Liu, X.Q., Wang, Y.S. and Zhu, J.H. 2004. Epoxy resin/polyurethane functionally graded material prepared by microwave irradiation. *Journal of Applied Polymer Science*. **94**(3): 994-999.
- Mahamood, R.M., Akinlabi, E.T., Shukla, M. and Pityana, S. 2012. Functionally graded material: An overview. *Proceedings of the World Congress on Engineering 2012*, **3**: 1-5.
- Mali, S.S., Betty, C.A., Bhosale, P.N. and Patil, P.S. 2012. Synthesis, characterization of hydrothermally grown MWCNT-TiO₂ photoelectrodes and their visible light absorption properties. *ECS Journal of Solid State Science and Technology*. **1**(2): 15-23.
- Marcelo, T.M., Livramento, V., Varella De Oliveira, M. and Carvalho, M.M. 2006. Microstructural characterization and interactions in Ti- and TiH₂-hydroxyapatite vacuum sintered composites. *Journal of Material Research*. **9**: 1516-1439.
- Martin, L.P. and Nguyen, J.H. 2005. Fabrication and characterization of graded impedance gas gun impactors from tape cast metal powders. *Materials Science and Engineering A*. **427**: 83-118.
- Matsunaga, H. 2009. Stress analysis of functionally graded plates subjected to thermal and mechanical loadings. *Composite Structures*. **87**(4): 344-357.
- Matula, G. and Dobrzanski, L.A. 2006. Structure and properties of FGM manufactured on the basis of HS6-5-2. *Journal of Achievements in Materials and Manufacturing Engineering*. **17**(1-2): 101-104.
- Menéndez, E., Salazar-Alvarez, G., Zhilyaev, A.P., Suriñach, S., Baró, M.D., Nogués, J. and Sort, J. 2008. Cold consolidation of metal-ceramic nanocomposite powders with large ceramic fractions. *Advanced Functional Materials*. **18**: 3293-3298.
- Michael, L.P. and Hugh, A.B. 2006. Pressure-less sintering of particle reinforced metal-ceramic composites for functionally graded materials: Part 1. Porosity reduction models. *Acta Materialia*. **54**: 1457-1465.

- Miyamoto, Y., Kaysser, W. A., Rabin, B. H., Kawasaki, A. and Ford, R. G. 1999. *Functionally graded materials: Design, processing and applications*. USA: Kluwer Academic Publishers.
- Mondal, A., Agrawal, D. and Upadhyaya, A. 2009. Microwave sintering of refractory metals/alloys: W, Mo, Re, W-Cu, W-Ni-Cu and W-Ni-Fe alloys. *Journal of Microwave Power & Electromagnetic Energy*. **44**(1): 28-44.
- Mori, T. and Tanaka, K. 1973. Average stress in matrix and average elastic energy of materials with misfitting inclusions. *Acta Metallurgica*. **21**(5): 571-574.
- Moroi, H.H., Okimoto, K., Moroi, R. and Terada, Y. 1993. Numeric approach to the biomechanical analysis of thermal effects in coated implants. *The International Journal of Prosthodontics*. **6**(6): 564-572.
- Mumtaz, K.A. and Hopkinson, N. 2007. Laser melting functionally graded composition of waspaloy and zirconia powders. *Journal of Materials Science*. **42**: 7647-7656.
- Munir, Z.A., Anselmi-Tamburini, U. and Ohyanagi, M. 2006. The effect of electric field and pressure on the synthesis and consolidation of materials: A review of the spark plasma sintering method. *Journal of Materials Science*. **41**: 763-777.
- Nan, C.W. 1993. Physics of inorganic inhomogeneous materials. *Progress in Materials Science*. **37**: 1-116.
- Neirinck, B., Mattheys, T., Braem, A., Fransaeer, J., Biestand, O.V. and Vleugels, J. 2009. Preparation of titanium foams by slip casting of particle stabilized emulsions. *Advanced Engineering Materials*. **1**(8): 633-636.
- Nomura, N., Sakamoto, K., Takahashi, K., Kato, S., Abe, Y., Doi, H., Tsutsumi, Y., Kobayashi, E., Kim, W-J., Kim, K-H. and Hanawa, T. 2010. Fabrication and mechanical properties of porous Ti/HA composites for bone fixation devices. *Materials Transactions*. **51**(8): 1449-1454.
- Nomura, T., Moriguchi, H., Tsuda, K., Isobe, K., Ikegaya, A. and Moriyama, K. 1999. Material design method for the functionally graded cemented carbide tool. *International Journal of Refractory Metals and Hard Materials*. **17**(6): 397-404.
- Ouyang, J.H., Mei, H. and Kovacevic, R. 2002. Rapid prototyping and characterization of a WC-(NiSiB alloy) cermet/tool steel functionally graded material (FGM) synthesized by laser cladding. *Proceedings of the TMS Fall Meeting*, pp. 77-93.
- Paggi, R.A., Beal, V.E. and Salmoria, G.V. 2012. Process optimization for PA12/MWCNT nanocomposite manufacturing by selective laser sintering. *International Journal of Advanced Manufacturing Technology*. **66**(9-12): 1977-1985.

- Park, J.H., Lee, J.C., Ryu, S.H., Jung, K.B., Song, H., Yun, J.C., Choa, Y.H., Ahn, S.H. and Lee, C.S. 2009. Crack-free joint in a Ni-Al₂O₃ FGM using three-dimensional modelling. *Materials Transactions*. **50**(7): 1875-1880.
- Parvin, N. and Rahimian, M. 2012. The characteristics of alumina particle reinforced pure Al matrix composite. *Acta Physica Polonica A*. **121**(1): 108-110.
- Pattanayak, D.K., Rao, B.T. and Rama Mohan TR. 2011. Calcium phosphate bioceramics and bioceramic composites. *Journal of Sol-Gel Science and Technology*. **59**(3): 432-447.
- Pines, M. and Bruck, H. 2006. Pressure-less sintering of particle-reinforced metal-ceramic composites for functionally graded materials: Part I. Porosity reduction models. *Acta Materialia*. **54**(6): 1457-1465.
- Pines, M. and Bruck, H. 2006. Pressure-less sintering of particle-reinforced metal-ceramic composites for functionally graded materials: Part II. Sintering model. *Acta Materialia*. **54**(6): 1467-1474.
- Preiss, A., Su, B., Collins, S. and Ellison, P. 2010. Fabrication of functionally graded ZTA ceramics using a novel combination of freeze casting and electrophoretic deposition. *Advances in Science and Technology*. **63**: 340-347.
- Raharijaona, J-J., Missiaen, J-M. and Mitteau, R. 2010. Coupling between sintering and liquid migration to process tungsten-copper functionally graded materials. *Advances in Sintering Science and Technology: Ceramic Transactions*. **209**: 321-332.
- Rajan, T.P.D and Pai, B.C. 2009. Formation of solidification microstructures in centrifugal cast functionally graded aluminum composites. *Transactions of the Indian Institute of Metals*. **62**(4-5): 383-389.
- Ramu, I. and Mohanty, S.C. 2014. Modal analysis of functionally graded material plates using finite element method. *Procedia Materials Science*. **6**: 460-467.
- Refugio-Garcia, E., Miranda-Hernandez, J.G., Rodriguez-Garcia, J.A. and Rocha-Rangel, E. 2011. Production of Al₂O₃/Ti/TiN functional materials by means of nitriding in ammonia salts of Al₂O₃/Ti composites. *Journal of Ceramic Processing Research*. **12**(3): 319-321.
- Rocha, S.S., Adabo, G.L., Henriques, G.E. and Nobilo, M.A. 2006. Vickers hardness of cast commercially pure titanium and Ti-6Al-4V alloy submitted to heat treatments. *Brazilian Dental Journal*. **17**(2): 126-129.
- Ruseska, G., Fidancevska, E. and Bossert, J. 2006. Mechanical and thermal-expansion characteristics of Ca₁₀(PO₄)₆(OH)₂-(PO₄)₂ composites. *Science of Sintering*. **38**: 245-253.

- Ryu, S., Park, J., Lee, C.S., Lee, J., Ahn, S. and Oh, S. 2009. Experimental measurement of coefficient of thermal expansion for graded layers in Ni-Al₂O₃ FGM joints for accurate residual stress analysis. *Materials Transactions*. **50**(6): 1553-1557.
- Sarikaya, O. and Celik, E. 2002. Effects of residual stress on thickness and interlayer of thermal barrier ceramic MgO-ZrO₂ coatings on Ni and AlSi substrates using finite element method. *Materials & Design*. **23**(7): 645-650.
- Sarkar, P. 2004. Synthesis and microstructural manipulation of ceramics by electrophoretic deposition. *Electrophoretic deposition: Fundamentals and applications*. *Journal of Materials Science*. **39**: 819-823.
- Schwartz, M. 2002. *Encyclopaedia of smart materials*. Vol.2. USA: Wiley.
- Sevcik, M., Hutar, P., Nahlik, L. and Knesl, Z. 2009. An evaluation of the stress intensity factor in functionally graded materials. *Applied and Computational Mechanics*. **3**: 401-410.
- Severin, T-L., Gutt, S., Gutt, G., Poroeh-Seritan, M. and Stroe, S-G. 2011. A study of the mechanical properties of the elements used in bearings construction according to various heat treatments. *Metal 2011*. **5**:18-20.
- Shahrjerdi, A., Mustapha, F., Bayat, M., Sapuan, S.M. and Majid, D.L.A. 2011. Fabrication of functionally graded hydroxyapatite-titanium by applying optimal sintering procedure and powder metallurgy. *International Journal of Physical Sciences*. **6**(9): 2258-2267.
- Shariyat, M. and Mohammadjani, R. 2013. Three-dimensional compatible finite element stress analysis of spinning two-dimensional FGM annular plates and disks with load and elastic foundation non-uniformities. *Latin American Journal of Solids and Structures*. **10**: 859-890.
- Shen, H-S. and Noda, N. 2005. Postbuckling of FGM cylindrical shells under combined axial and radial mechanical loads in thermal environments. *International Journal of Solids and Structures*. **42**(16-17): 4641-4662.
- Shen, Z., Johnsson, M., Zhou, Z. and Nygren, M. 2002. Spark plasma sintering of alumina. *Journal of American Ceramic Society*. **85**(8): 1921-1927.
- Shi, W., Kamiya, A., Zhu, J. and Watazu, A. 2002. Properties of titanium biomaterial fabricated by sinter-bonding of titanium/hydroxyapatite composite surface coated layer to pure bulk titanium. *Materials Science and Engineering A-Structure*. **337**: 104-109.
- Silva, A. and Carvalho, M.H. Atmosphere and constituent reaction effects on titanium-hydroxyapatite sintered composites (poster P3.21). In: Martins. R., Dias, C., Fortunato, E., Ferreira, I., Godinho, H. and Monteiro, R. 2003. *Materiais 2003 – a*

materials science forum. *Book of Abstracts of the XI Meeting of the Portuguese Materials Society*, pp. 1-175.

- Singh, G., Singh, S. and Prakash, S. 2011. Surface characterization of plasma sprayed pure and reinforced hydroxyapatite coating on Ti6Al4V alloy. *Surface & Coatings Technology*. **205**: 4814-4820.
- Slosarczyk, A., Zima, A., Paszkiewicz, Z., Szczepaniak, J., Aza, A.H. and Chroscicka, A. 2010. The influence of titanium on physicochemical properties of Ti-modified Hydroxyapatite materials. *Ceramic Materials*. **62**(3): 369-375.
- Srinivas, G., Prasad, S.U., Manikandan, M. and Kumar, P.A. 2013. Simulation of traditional composites under thermal loads. *Research Journal of Recent Sciences*. **2**: 273-278.
- Stanciu, L.A., Kodash, V.Y. and Groza, J.R. 2001. Effects of heating rate on densification and grain growth during field-assisted sintering of α -Al₂O₃ and MoSi₂ powders. *Metallurgical and Materials Transactions A*. **32A**: 2633-2638.
- Sun, L., Sneller, A. and Kwon, P. 2008. Fabrication of alumina/zirconia functionally graded material: From optimization of processing parameters to phenomenological consecutive models. *Materials Science and Engineering A*. **488**: 31-38.
- Tang, C.Y., Tsui, C.P., Guo, Y.Q., Gao, B. and Luan, R.H. 2012. Damage modeling of graded Ti-based composites using repeated unit cell approach. *International Journal of Material Science*. **2**(3): 63-66.
- Tilbrook, M.T., Rozenburg, K., Steffler, E.D., Rutgers, L. and Hoffman, M. 2006. Crack propagation paths in layered, graded composites. *Composites B*. **37**(6): 490-498.
- Tomota, Y., Kuroki, K., Mori, T. and Tamura, I. 1976. Tensile deformation of two-ductile-phase alloys: Flow curves of α/γ Fe-Cr-Ni alloys. *Materials Science and Engineering*. **24**: 85-94.
- Tsipas, S., Goodwin, P., McShane, H.B. and Rawlings, R.D. 2003. Effect of high energy ball milling on titanium-hydroxyapatite powders. *Powder Metallurgy*. **46**(1): 73-77.
- Velhinho, A., Vignoles, G.L., Cloetens, P., Thibault, X., Boller, E., Fernandes, F.B., Rocha, L.A. and Botas, J.D. 2005. Evaluation of SiC-particle connectivity in functionally graded Al/SiC_p composites by synchrotron radiation holographic microtomography. *Materials Science Forum*. **492-493**: 621-626.
- Wang, H., Yao, S. and Matsumura, S. 2004. Electrochemical preparation and characterization of Ni/SiC gradient deposit. *Journal of Materials Processing Technology*. **145**(3): 299-302.

- Wang, Y., Tao, J., Zhang, J. and Wang, T. 2011. Effects of addition of NH_4HCO_3 on pore characteristics and compressive properties of porous Ti-10%Mg composites. *Transactions of Nonferrous Metals Society of China*. **21**: 1074-1079.
- Watanabe, Y., Kim, I.S. and Fukui, Y. 2005. Microstructures of functionally graded materials fabricated by centrifugal solid-particle and in-situ methods. *Metals and Materials International*. **11**(5): 391-399.
- Watanabe, Y., Sato, H., Ogawa, T. and Kim, I-S. 2007. Density and hardness gradients of functionally graded material ring fabricated from Al-3mass%Cu alloy by a centrifugal in-situ method. *Materials Transactions*. **48**(11): 2945-2952.
- Watanabe, Y., Shibuya, M. and Sato, H. 2013. Fabrication of Al/diamond particles functionally graded materials by centrifuged sintered-casting method. *Journal of Physics*. **419**: 1-4.
- Watari, F., Kondo, H., Matsuo, S., Miyao, R., Yokoyama, A., Hirai, T., Tamura, Y., Uoa, M., Ohara, N. and Kawasaki, T. 2003. Development of functionally graded implant and dental post, for bio-medical application. *Materials Science Forum*. **423-425**: 321-326.
- Watari, F., Yokohama, A., Saso, F., Uo, M. and Kawasaki, T. 1997. Fabrication and properties of functionally graded dental implant. *Composites B*. **28B**: 5-11.
- Watari, F., Yokoyama, A., Omori, M., Hirai, T., Kondo, H., Uo, M. and Kawasaki, T. 2004. Biocompatibility of materials and development to functionally graded implant for bio-medical application. *Composites Science and Technology*. **64**: 893-908.
- Wells, A.F. 1984. *Structural Inorganic Chemistry*. 5th ed. UK: Oxford University Press.
- Willert-Porada, M., Grosse-Berg, J., Sen, I. and Park, H-S. 2005. Microwave sintering and infiltration of highly porous silicon nitride ceramics to form dense ceramics. *Key Engineering Materials*. **287**: 171-176.
- Wu, A.H., Cao, W.B., Ge, C.C., Li, J.E. and Kawasaki, A. 2005. Fabrication and characteristics of plasma facing SiC/C functionally graded composite material. *Materials Chemistry and Physics*. **91**(2-3): 545-550.
- Yakovlev, A., Trunova, E., Grevey, D. and Smurov, M. 2005. Laser-assisted direct manufacturing of functionally graded 3D objects. *Surface and Coatings Technology*. **190**(1): 15-24.
- Ye, F-X., Ohmori, A., Tsumura, T., Nakata, K. and Li, C-J. 2007. Microstructural analysis and photocatalytic activity of plasma-sprayed titania-hydroxyapatite coatings. *Journal of Thermal Spray Technology*. **16**(5-6): 776-782.

- Ye, H., Liu, X.Y. and Hong, H. 2009. Characterization of sintered titanium/hydroxyapatite biocomposite using FTIR spectroscopy. *Journal of Materials Science*. **20**: 843-850.
- Zhang, G., Guo, Q., Wang, K., Zhang, H., Song, Y., Shi, J. and Liu, L. 2008. Finite element design of SiC/C functionally graded materials for ablation resistance application. *Materials Science and Engineering A*. **488**:45-49.
- Zhang, L.W., Lei, Z.X., Liew, K.M. and Yu, J.L. 2014. Static and dynamic of carbon nanotube reinforced functionally graded cylindrical panels. *Composite Structures*. **111**: 205-212.
- Zhang, L.W., Zhu, P. and Liew, K.M. 2014. Thermal buckling of functionally graded plates using a local Kriging meshless method. *Composite Structures*. **108**: 472-492.
- Zhao, L., Bram, M., Buchkremer, H.P., Stover, D. and Li, Z. 2004. Preparation of TiO₂ composite microfiltration membranes by the wet powder spraying method. *Journal of Membrane Science*. **244**(1-2): 107-115.
- Zhou, Y.Z., Hirao, K., Yamauchi, Y. and Kansaki, S. 2003. Effects of heating rate and particle size on pulse electric current sintering of alumina. *Scripta Materialia*. **48**(12): 1631-1636.
- Zhou, Z-J., Song, S-X., Du, J., Zhong, Z-H. and Ge, C-C. 2007. Performance of W/Cu FGM based plasma facing components under high heat load test. *Journal of Nuclear Materials*. **363**: 1309-1314.
- Zhu, P., Zhang, L.W. and Liew, K.M. 2014. Geometrically nonlinear thermomechanical analysis of moderately thick functionally graded plates using a local Petrov-Galerkin approach with moving Kriging interpolation. *Composite Structures*. **107**: 298-314.

APPENDIX A-1

An example of ANSYS's Output File for Optimization 2-D Analysis

ANSYS Multiphysics

```
***** ANSYS COMMAND LINE ARGUMENTS *****
GRAPHICS DEVICE REQUESTED      = win32
GRAPHICAL ENTRY                = YES
LANGUAGE                       = en-us
00925682                      VERSION=WINDOWS x64      RELEASE= 13.0      UP20101012
CURRENT JOBNAME=n1 09:32:01 OCT 31, 2014 CP=          0.406
```

*** ANSYS GLOBAL STATUS ***

TITLE =OPTIMIZATION ANALYSIS

ANALYSIS TYPE = STATIC (STEADY-STATE)

NUMBER OF ELEMENT TYPES = 1

```
11100 ELEMENTS CURRENTLY SELECTED. MAX ELEMENT NUMBER = 11100
33749 NODES CURRENTLY SELECTED.    MAX NODE NUMBER   = 33749
28 KEYPOINTS CURRENTLY SELECTED.   MAX KEYPOINT NUMBER = 52
40 LINES CURRENTLY SELECTED.       MAX LINE NUMBER    = 76
13 AREAS CURRENTLY SELECTED.       MAX AREA NUMBER    = 25
MAXIMUM LINEAR PROPERTY NUMBER     = 13
ACTIVE COORDINATE SYSTEM           = 0 (CARTESIAN)
NUMBER OF SPECIFIED CONSTRAINTS     = 150
CURRENT LOAD CASE = 0 OF 0
LOAD SET = 1
SUBSTEP = 1
TIME/FREQ = 1.0000
```

LIST ALL SELECTED AREAS.

NUMBER	LOOP	LINES	AREA	ELEM SIZE	#NODES	#ELEM	MAT	REAL	TYP	ESYS	SECN
1	1	1 2 3 4	N/A	1.00E-04	6421	2250	-1	-1	-1	0	-1
14	1	3 53 7 54	N/A	1.00E-04	1493	600	-2	-1	-1	0	-1
15	1	7 55 11 56	N/A	1.00E-04	1493	600	-3	-1	-1	0	-1
16	1	11 57 15 58	N/A	1.00E-04	1493	600	-4	-1	-1	0	-1
17	1	15 59 19 60	N/A	1.00E-04	1493	600	-5	-1	-1	0	-1
18	1	19 61 23 62	N/A	1.00E-04	1493	600	-6	-1	-1	0	-1
19	1	23 63 27 64	N/A	1.00E-04	1493	600	-7	-1	-1	0	-1
20	1	27 65 31 66	N/A	1.00E-04	1493	600	-8	-1	-1	0	-1
21	1	31 67 35 68	N/A	1.00E-04	1493	600	-9	-1	-1	0	-1
22	1	35 69 39 70	N/A	1.00E-04	1493	600	-10	-1	-1	0	-1
23	1	39 71 43 72	N/A	1.00E-04	1493	600	-11	-1	-1	0	-1
24	1	43 73 47 74	N/A	1.00E-04	1493	600	-12	-1	-1	0	-1
25	1	47 75 51 76	N/A	1.00E-04	6421	2250	-13	-1	-1	0	-1

```
LIST ELEMENT TYPES FROM 1 TO 1 BY 1
ELEMENT TYPE 1 IS PLANE183 2-D 8-NODE PLANE STRS SOLID
KEYOPT( 1- 6)= 0 0 0 0 0 0
KEYOPT( 7-12)= 0 0 0 0 0 0
KEYOPT(13-18)= 0 0 0 0 0 0
CURRENT NODAL DOF SET IS UX UY
TWO-DIMENSIONAL MODEL
```

```
EVALUATE MATERIAL PROPERTIES FOR MATERIALS 1 TO 13 IN
INCREMENTS OF 1
MATERIAL NUMBER = 1 EVALUATED AT TEMPERATURE OF 22.000
```

EX = 0.11089E+12
 NUXY = 0.28000
 ALPX = 0.14870E-04
 PRXY = 0.28000
 MATERIAL NUMBER = 2 EVALUATED AT TEMPERATURE OF 22.000
 EX = 0.11076E+12
 NUXY = 0.28270
 ALPX = 0.14690E-04
 PRXY = 0.28270
 MATERIAL NUMBER = 3 EVALUATED AT TEMPERATURE OF 22.000
 EX = 0.11049E+12
 NUXY = 0.28820
 ALPX = 0.14329E-04
 PRXY = 0.28820
 MATERIAL NUMBER = 4 EVALUATED AT TEMPERATURE OF 22.000
 EX = 0.11022E+12
 NUXY = 0.29360
 ALPX = 0.13968E-04
 PRXY = 0.29360
 MATERIAL NUMBER = 5 EVALUATED AT TEMPERATURE OF 22.000
 EX = 0.10995E+12
 NUXY = 0.29910
 ALPX = 0.13607E-04
 PRXY = 0.29910
 MATERIAL NUMBER = 6 EVALUATED AT TEMPERATURE OF 22.000
 EX = 0.10969E+12
 NUXY = 0.30450
 ALPX = 0.13246E-04
 PRXY = 0.30450
 MATERIAL NUMBER = 7 EVALUATED AT TEMPERATURE OF 22.000
 EX = 0.10942E+12
 NUXY = 0.31000
 ALPX = 0.12885E-04
 PRXY = 0.31000
 MATERIAL NUMBER = 8 EVALUATED AT TEMPERATURE OF 22.000
 EX = 0.10915E+12
 NUXY = 0.31550
 ALPX = 0.12524E-04
 PRXY = 0.31550
 MATERIAL NUMBER = 9 EVALUATED AT TEMPERATURE OF 22.000
 EX = 0.10889E+12
 NUXY = 0.32090
 ALPX = 0.12163E-04
 PRXY = 0.32090
 MATERIAL NUMBER = 10 EVALUATED AT TEMPERATURE OF 22.000
 EX = 0.10862E+12
 NUXY = 0.32640
 ALPX = 0.11802E-04
 PRXY = 0.32640
 MATERIAL NUMBER = 11 EVALUATED AT TEMPERATURE OF 22.000
 EX = 0.10835E+12
 NUXY = 0.33180
 ALPX = 0.11441E-04
 PRXY = 0.33180
 MATERIAL NUMBER = 12 EVALUATED AT TEMPERATURE OF 22.000
 EX = 0.10808E+12
 NUXY = 0.33730
 ALPX = 0.11080E-04
 PRXY = 0.33730
 MATERIAL NUMBER = 13 EVALUATED AT TEMPERATURE OF 22.000

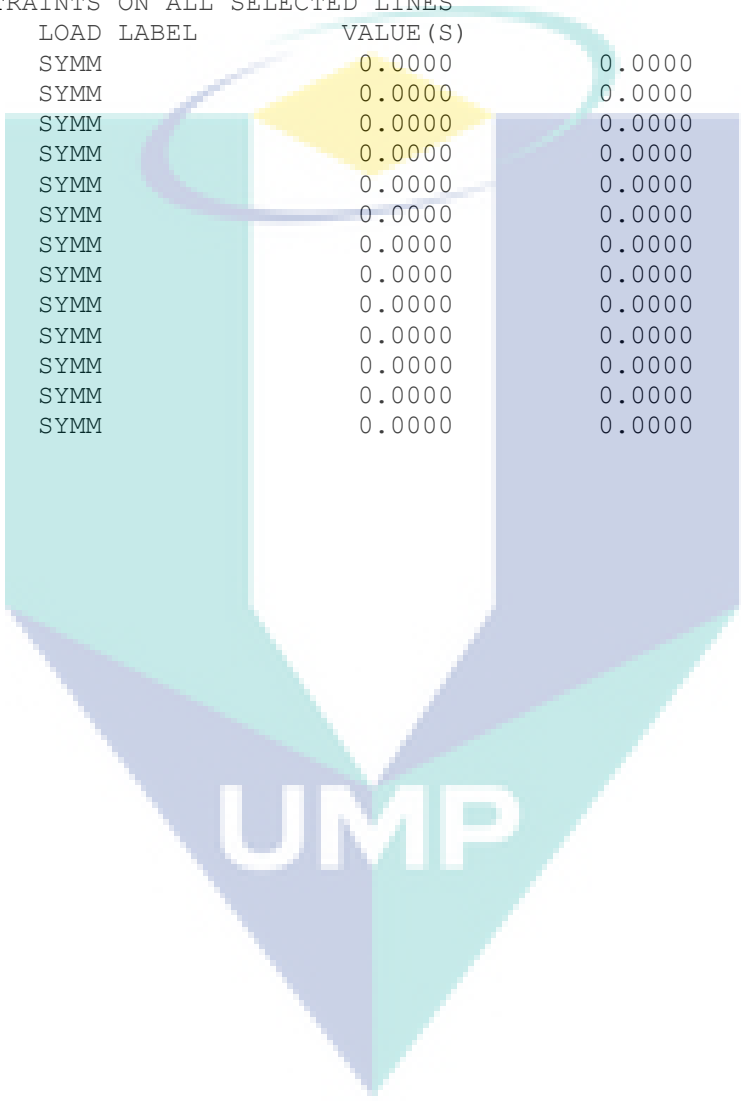
EX = 0.10795E+12
 NUXY = 0.34000
 ALPX = 0.10900E-04
 PRXY = 0.34000

LIST SELECTED DOF CONSTRAINTS ON ALL SELECTED KEYPOINTS
 CURRENTLY SELECTED DOF SET= UX UY

KEYPOINT	LOAD LABEL	VALUE (S)	EXP	KEY
1	UX	0.0000	0.0000	0
1	UY	0.0000	0.0000	0

LIST CONSTRAINTS ON ALL SELECTED LINES

LINE	LOAD LABEL	VALUE (S)	NAREA
4	SYMM	0.0000	1
54	SYMM	0.0000	14
56	SYMM	0.0000	15
58	SYMM	0.0000	16
60	SYMM	0.0000	17
62	SYMM	0.0000	18
64	SYMM	0.0000	19
66	SYMM	0.0000	20
68	SYMM	0.0000	21
70	SYMM	0.0000	22
72	SYMM	0.0000	23
74	SYMM	0.0000	24
76	SYMM	0.0000	25



UMP

APPENDIX A-2

An example of ANSYS's Output File for Mechanical Field 3-D Analysis

```

ANSYS Multiphysics
***** ANSYS COMMAND LINE ARGUMENTS *****
GRAPHICS DEVICE REQUESTED      = win32
GRAPHICAL ENTRY                 = YES
LANGUAGE                        = en-us
00925682                       VERSION=WINDOWS x64      RELEASE= 13.0      UP20101012
CURRENT JOBNAME=P1 12:20:08 OCT 31, 2014 CP=          0.391

```

```

*** ANSYS GLOBAL STATUS ***
TITLE = STRUCTURAL ANALYSIS (ISOTHERMAL)
ANALYSIS TYPE = STATIC (STEADY-STATE)
NUMBER OF ELEMENT TYPES =      2
    6256 ELEMENTS CURRENTLY SELECTED. MAX ELEMENT NUMBER =    12512
    28609 NODES CURRENTLY SELECTED.   MAX NODE NUMBER =      28609
    36 KEYPOINTS CURRENTLY SELECTED.  MAX KEYPOINT NUMBER =     64
    52 LINES CURRENTLY SELECTED.     MAX LINE NUMBER =      104
    25 AREAS CURRENTLY SELECTED.     MAX AREA NUMBER =     50
    8 VOLUMES CURRENTLY SELECTED.    MAX VOL. NUMBER =     16
MAXIMUM LINEAR PROPERTY NUMBER      =      8
ACTIVE COORDINATE SYSTEM             =      0 (CARTESIAN)
NUMBER OF SPECIFIED CONSTRAINTS     =    7488
NUMBER OF SPECIFIED SURFACE LOADS   =     782
CURRENT LOAD CASE =      0 OF      0
LOAD SET =      1
SUBSTEP =      1
TIME/FREQ =     1.0000

```

LIST ALL SELECTED VOLUMES.

NO.	SHEL	AREAS	VOLU	#NODES	#ELEM	MAT	REAL	TYP	ESYS	SECN
1	1	1 2 3	4 N/A	734	782	-1	-1	-1	0	0
10	1	2 6 37	38 N/A	734	782	-2	-1	-1	0	0
11	1	6 10 39	40 N/A	734	782	-3	-1	-1	0	0
12	1	10 14 41	42 N/A	734	782	-4	-1	-1	0	0
13	1	14 18 43	44 N/A	734	782	-5	-1	-1	0	0
14	1	18 22 45	46 N/A	734	782	-6	-1	-1	0	0
15	1	22 26 47	48 N/A	734	782	-7	-1	-1	0	0
16	1	26 30 49	50 N/A	734	782	-8	-1	-1	0	0

```

LIST ELEMENT TYPES FROM      1 TO      2 BY      1
ELEMENT TYPE      1 IS SOLID186      3-D 20-NODE STRUCTURAL SOLID
  KEYOPT( 1- 6)=      0      0      0      0      0      0
  KEYOPT( 7-12)=      0      0      0      0      0      0
  KEYOPT(13-18)=      0      0      0      0      0      0
ELEMENT TYPE      2 IS MESH200      8-NODE QUAD MESHING FACET
  KEYOPT( 1- 6)=      7      0      0      0      0      0
  KEYOPT( 7-12)=      0      0      0      0      0      0
  KEYOPT(13-18)=      0      0      0      0      0      0
CURRENT NODAL DOF SET IS  UX      UY      UZ
THREE-DIMENSIONAL MODEL

```

```

EVALUATE MATERIAL PROPERTIES FOR MATERIALS 1 TO 8 IN INCREMENTS OF      1
MATERIAL NUMBER =      1 EVALUATED AT TEMPERATURE OF      0.0000
EX = 0.11089E+12

```

NUXY = 0.28000
 ALPX = 0.14870E-04
 PRXY = 0.28000
 MATERIAL NUMBER = 2 EVALUATED AT TEMPERATURE OF 0.0000
 EX = 0.11065E+12
 NUXY = 0.28500
 ALPX = 0.14539E-04
 PRXY = 0.28500
 MATERIAL NUMBER = 3 EVALUATED AT TEMPERATURE OF 0.0000
 EX = 0.11016E+12
 NUXY = 0.29500
 ALPX = 0.13878E-04
 PRXY = 0.29500
 MATERIAL NUMBER = 4 EVALUATED AT TEMPERATURE OF 0.0000
 EX = 0.10967E+12
 NUXY = 0.30500
 ALPX = 0.13216E-04
 PRXY = 0.30500
 MATERIAL NUMBER = 5 EVALUATED AT TEMPERATURE OF 0.0000
 EX = 0.10918E+12
 NUXY = 0.31500
 ALPX = 0.12554E-04
 PRXY = 0.31500
 MATERIAL NUMBER = 6 EVALUATED AT TEMPERATURE OF 0.0000
 EX = 0.10869E+12
 NUXY = 0.32500
 ALPX = 0.11893E-04
 PRXY = 0.32500
 MATERIAL NUMBER = 7 EVALUATED AT TEMPERATURE OF 0.0000
 EX = 0.10820E+12
 NUXY = 0.33500
 ALPX = 0.11231E-04
 PRXY = 0.33500
 MATERIAL NUMBER = 8 EVALUATED AT TEMPERATURE OF 0.0000
 EX = 0.10795E+12
 NUXY = 0.34000
 ALPX = 0.10900E-04
 PRXY = 0.34000

LIST CONSTRAINTS ON ALL SELECTED AREAS

AREA	LOAD LABEL	VALUE (S)	
3	UX	0.0000	0.0000
3	UY	0.0000	0.0000
3	UZ	0.0000	0.0000
4	UX	0.0000	0.0000
4	UY	0.0000	0.0000
4	UZ	0.0000	0.0000
37	UX	0.0000	0.0000
37	UY	0.0000	0.0000
37	UZ	0.0000	0.0000
38	UX	0.0000	0.0000
38	UY	0.0000	0.0000
38	UZ	0.0000	0.0000
39	UX	0.0000	0.0000
39	UY	0.0000	0.0000
39	UZ	0.0000	0.0000
40	UX	0.0000	0.0000
40	UY	0.0000	0.0000
40	UZ	0.0000	0.0000
41	UX	0.0000	0.0000

41	UY	0.0000	0.0000
AREA	LOAD LABEL	VALUE (S)	
41	UZ	0.0000	0.0000
42	UX	0.0000	0.0000
42	UY	0.0000	0.0000
42	UZ	0.0000	0.0000
43	UX	0.0000	0.0000
43	UY	0.0000	0.0000
43	UZ	0.0000	0.0000
44	UX	0.0000	0.0000
44	UY	0.0000	0.0000
44	UZ	0.0000	0.0000
45	UX	0.0000	0.0000
45	UY	0.0000	0.0000
45	UZ	0.0000	0.0000
46	UX	0.0000	0.0000
46	UY	0.0000	0.0000
46	UZ	0.0000	0.0000
47	UX	0.0000	0.0000
47	UY	0.0000	0.0000
47	UZ	0.0000	0.0000
48	UX	0.0000	0.0000
AREA	LOAD LABEL	VALUE (S)	
48	UY	0.0000	0.0000
48	UZ	0.0000	0.0000
49	UX	0.0000	0.0000
49	UY	0.0000	0.0000
49	UZ	0.0000	0.0000
50	UX	0.0000	0.0000
50	UY	0.0000	0.0000
50	UZ	0.0000	0.0000

LIST SURFACE LOADS ON ALL SELECTED AREAS

AREA	LKEY	LOAD LABEL	VALUE (S)	REAL
1	1	PRES	P1	3.58152E+08

*** NOTE *** CP = 3.859 TIME= 12:28:37
No nodal body forces to list.

UMP

APPENDIX A-3

An example of ANSYS's Output File for Thermal Field 3-D Analysis

```

ANSYS Multiphysics
***** ANSYS COMMAND LINE ARGUMENTS *****
GRAPHICS DEVICE REQUESTED      = win32
GRAPHICAL ENTRY                = YES
LANGUAGE                        = en-us
00925682                      VERSION=WINDOWS x64      RELEASE= 13.0      UP20101012
CURRENT JOBNAME=T300 12:44:50 OCT 31, 2014 CP=        0.406

*** ANSYS GLOBAL STATUS ***
TITLE =THERMAL-STRUCTURAL ANALYSIS (THERMAL)
ANALYSIS TYPE = STATIC (STEADY-STATE)
NUMBER OF ELEMENT TYPES =      2
    6256 ELEMENTS CURRENTLY SELECTED.  MAX ELEMENT NUMBER =    12512
    28609 NODES CURRENTLY SELECTED.    MAX NODE NUMBER =      28609
    36 KEYPOINTS CURRENTLY SELECTED.   MAX KEYPOINT NUMBER =     64
    52 LINES CURRENTLY SELECTED.      MAX LINE NUMBER =      104
    25 AREAS CURRENTLY SELECTED.      MAX AREA NUMBER =       50
    8 VOLUMES CURRENTLY SELECTED.     MAX VOL. NUMBER =       16
MAXIMUM LINEAR PROPERTY NUMBER      =      8
ACTIVE COORDINATE SYSTEM             =      0 (CARTESIAN)
NUMBER OF SPECIFIED CONSTRAINTS     =    12370
CURRENT LOAD CASE =      0 OF      0
LOAD SET =      1
SUBSTEP =      1
TIME/FREQ =      1.0000

LIST ALL SELECTED VOLUMES.
NO.  SHEL  AREAS  VOLU  #NODES  #ELEM  MAT  REAL  TYP  ESYS  SECN
   1   1   1   2   3   4  N/A    734   782  -1   -1   -1    0    0
  10   1   2   6  37  38  N/A    734   782  -2   -1  -1    0    0
  11   1   6  10  39  40  N/A    734   782  -3   -1  -1    0    0
  12   1  10  14  41  42  N/A    734   782  -4   -1  -1    0    0
  13   1  14  18  43  44  N/A    734   782  -5   -1  -1    0    0
  14   1  18  22  45  46  N/A    734   782  -6   -1  -1    0    0
  15   1  22  26  47  48  N/A    734   782  -7   -1  -1    0    0
  16   1  26  30  49  50  N/A    734   782  -8   -1  -1    0    0

LIST ELEMENT TYPES FROM      1 TO      2 BY      1
ELEMENT TYPE      1 IS SOLID186      3-D 20-NODE STRUCTURAL SOLID
  KEYOPT( 1- 6)=      0      0      0      0      0      0
  KEYOPT( 7-12)=      0      0      0      0      0      0
  KEYOPT(13-18)=      0      0      0      0      0      0
ELEMENT TYPE      2 IS MESH200      8-NODE QUAD MESHING FACET
  KEYOPT( 1- 6)=      7      0      0      0      0      0
  KEYOPT( 7-12)=      0      0      0      0      0      0
  KEYOPT(13-18)=      0      0      0      0      0      0
CURRENT NODAL DOF SET IS  UX    UY    UZ
THREE-DIMENSIONAL MODEL

EVALUATE MATERIAL PROPERTIES FOR MATERIALS      1 TO      8 IN INCREMENTS
OF      1
MATERIAL NUMBER =      1 EVALUATED AT TEMPERATURE OF      0.0000
EX = 0.11089E+12

```

NUXY = 0.28000
 ALPX = 0.14870E-04
 KXX = 2.1600
 PRXY = 0.28000
 MATERIAL NUMBER = 2 EVALUATED AT TEMPERATURE OF 0.0000
 EX = 0.11065E+12
 NUXY = 0.28500
 ALPX = 0.14539E-04
 KXX = 3.4408
 PRXY = 0.28500
 MATERIAL NUMBER = 3 EVALUATED AT TEMPERATURE OF 0.0000
 EX = 0.11016E+12
 NUXY = 0.29500
 ALPX = 0.13878E-04
 KXX = 6.0023
 PRXY = 0.29500
 MATERIAL NUMBER = 4 EVALUATED AT TEMPERATURE OF 0.0000
 EX = 0.10967E+12
 NUXY = 0.30500
 ALPX = 0.13216E-04
 KXX = 8.5639
 PRXY = 0.30500
 MATERIAL NUMBER = 5 EVALUATED AT TEMPERATURE OF 0.0000
 EX = 0.10918E+12
 NUXY = 0.31500
 ALPX = 0.12554E-04
 KXX = 11.125
 PRXY = 0.31500
 MATERIAL NUMBER = 6 EVALUATED AT TEMPERATURE OF 0.0000
 EX = 0.10869E+12
 NUXY = 0.32500
 ALPX = 0.11893E-04
 KXX = 13.687
 PRXY = 0.32500
 MATERIAL NUMBER = 7 EVALUATED AT TEMPERATURE OF 0.0000
 EX = 0.10820E+12
 NUXY = 0.33500
 ALPX = 0.11231E-04
 KXX = 16.248
 PRXY = 0.33500
 MATERIAL NUMBER = 8 EVALUATED AT TEMPERATURE OF 0.0000
 EX = 0.10795E+12
 NUXY = 0.34000
 ALPX = 0.10900E-04
 KXX = 17.529
 PRXY = 0.34000

LIST CONSTRAINTS ON ALL SELECTED AREAS

AREA	LOAD LABEL	VALUE (S)	
3	UX	0.0000	0.0000
3	UY	0.0000	0.0000
3	UZ	0.0000	0.0000
4	UX	0.0000	0.0000
4	UY	0.0000	0.0000
4	UZ	0.0000	0.0000
37	UX	0.0000	0.0000
37	UY	0.0000	0.0000
37	UZ	0.0000	0.0000
38	UX	0.0000	0.0000
38	UY	0.0000	0.0000

38	UZ	0.0000	0.0000
39	UX	0.0000	0.0000
39	UY	0.0000	0.0000
39	UZ	0.0000	0.0000
40	UX	0.0000	0.0000
40	UY	0.0000	0.0000
40	UZ	0.0000	0.0000
41	UX	0.0000	0.0000
41	UY	0.0000	0.0000
AREA	LOAD LABEL	VALUE (S)	
41	UZ	0.0000	0.0000
42	UX	0.0000	0.0000
42	UY	0.0000	0.0000
42	UZ	0.0000	0.0000
43	UX	0.0000	0.0000
43	UY	0.0000	0.0000
43	UZ	0.0000	0.0000
44	UX	0.0000	0.0000
44	UY	0.0000	0.0000
44	UZ	0.0000	0.0000
45	UX	0.0000	0.0000
45	UY	0.0000	0.0000
45	UZ	0.0000	0.0000
46	UX	0.0000	0.0000
46	UY	0.0000	0.0000
46	UZ	0.0000	0.0000
47	UX	0.0000	0.0000
47	UY	0.0000	0.0000
47	UZ	0.0000	0.0000
48	UX	0.0000	0.0000
AREA	LOAD LABEL	VALUE (S)	
48	UY	0.0000	0.0000
48	UZ	0.0000	0.0000
49	UX	0.0000	0.0000
49	UY	0.0000	0.0000
49	UZ	0.0000	0.0000
50	UX	0.0000	0.0000
50	UY	0.0000	0.0000
50	UZ	0.0000	0.0000

LIST NODAL TEMPERATURES FOR ALL SELECTED NODES

NODE	TEMPERATURE
1	300.000000
2	300.000000
3	300.000000
4	300.000000
5	300.000000
6	300.000000
7	300.000000
8	300.000000
9	300.000000
10	300.000000
11	300.000000
12	300.000000
13	300.000000
14	300.000000
15	300.000000
16	300.000000
17	300.000000
18	300.000000

```

19      300.000000
.
.
.
2433    300.000000
2434    300.000000
2435    300.000000
2436    300.000000
2437    300.000000
2438    300.000000
2439    300.000000
2440    300.000000
2441    300.000000
2442    155.816855
2443    155.816836
2444    155.816788
2445    155.816807
2446    155.816846
2447    155.816812
2448    155.816797
2449    155.816831
2450    155.816837
2451    155.816809
.
.
.
28596   30.8832884
28597   30.8832880
28598   30.8832904
28599   30.8832903
28600   30.8832828
28601   30.8832876
28602   30.8832886
28603   30.8832886
28604   30.8832857
28605   30.8832880
28606   30.8832906
28607   30.8832884
28608   30.8832895
28609   30.8832886

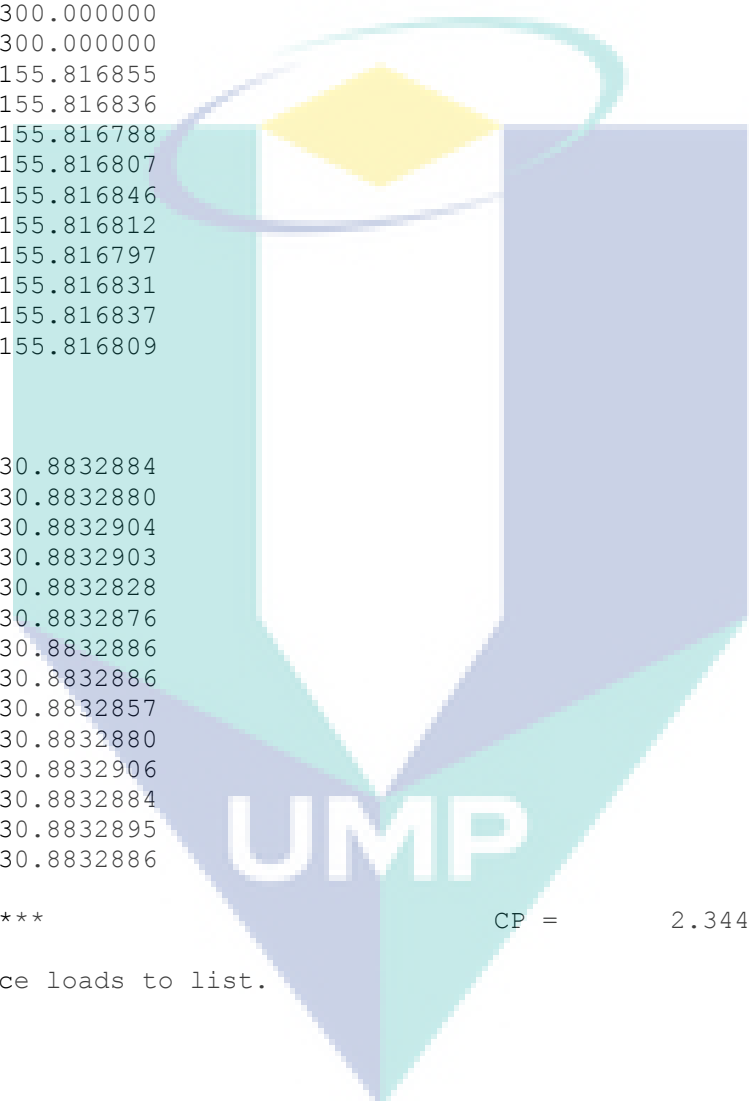
```

*** NOTE ***

12:48:36

No surface loads to list.

CP = 2.344 TIME=



UMP

APPENDIX A-4

An example of ANSYS's Output File for Thermo-mechanical Field 3-D Analysis

```

ANSYS Multiphysics
***** ANSYS COMMAND LINE ARGUMENTS *****
GRAPHICS DEVICE REQUESTED      = win32
GRAPHICAL ENTRY                 = YES
LANGUAGE                         = en-us
00925682          VERSION=WINDOWS x64          RELEASE= 13.0          UP20101012
CURRENT JOBNAME=300P1  11:33:16  OCT 31, 2014 CP=          0.422

*** ANSYS GLOBAL STATUS ***
TITLE =THERMAL-STRUCTURAL ANALYSIS (THERMO-MECHANICAL)
ANALYSIS TYPE =  STATIC (STEADY-STATE)
NUMBER OF ELEMENT TYPES =          2
    6256 ELEMENTS CURRENTLY SELECTED.  MAX ELEMENT NUMBER =      12512
    28609 NODES CURRENTLY SELECTED.    MAX NODE NUMBER =
    28609
    36 KEYPOINTS CURRENTLY SELECTED.  MAX KEYPOINT NUMBER =      64
    52 LINES CURRENTLY SELECTED.      MAX LINE NUMBER =      104
    25 AREAS CURRENTLY SELECTED.      MAX AREA NUMBER =      50
    8 VOLUMES CURRENTLY SELECTED.     MAX VOL. NUMBER =      16
MAXIMUM LINEAR PROPERTY NUMBER      =          8
ACTIVE COORDINATE SYSTEM             =          0  (CARTESIAN)
NUMBER OF SPECIFIED CONSTRAINTS      =     12370
NUMBER OF SPECIFIED SURFACE LOADS    =          782
CURRENT LOAD CASE =          0 OF      0
LOAD SET =          1
SUBSTEP =          1
TIME/FREQ =          1.0000

LIST ALL SELECTED VOLUMES.
NO.   SHEL  AREAS  VOLU  #NODES  #ELEM  MAT  REAL  TYP  ESYS  SECN
   1   1    1    2    3    4  N/A    734   782  -1    -1   -1    0    0
  10   1    2    6   37   38  N/A    734   782  -2    -1   -1    0    0
  11   1    6   10   39   40  N/A    734   782  -3    -1   -1    0    0
  12   1   10   14   41   42  N/A    734   782  -4    -1   -1    0    0
  13   1   14   18   43   44  N/A    734   782  -5    -1   -1    0    0
  14   1   18   22   45   46  N/A    734   782  -6    -1   -1    0    0
  15   1   22   26   47   48  N/A    734   782  -7    -1   -1    0    0
  16   1   26   30   49   50  N/A    734   782  -8    -1   -1    0    0

LIST ELEMENT TYPES FROM          1 TO          2 BY          1
ELEMENT TYPE          1 IS SOLID186          3-D 20-NODE STRUCTURAL SOLID
  KEYOPT( 1- 6)=          0          0          0          0          0
  KEYOPT( 7-12)=          0          0          0          0          0
  KEYOPT(13-18)=          0          0          0          0          0
ELEMENT TYPE          2 IS MESH200          8-NODE QUAD MESHING FACET
  KEYOPT( 1- 6)=          7          0          0          0          0
  KEYOPT( 7-12)=          0          0          0          0          0
  KEYOPT(13-18)=          0          0          0          0          0
CURRENT NODAL DOF SET IS  UX    UY    UZ
THREE-DIMENSIONAL MODEL

EVALUATE MATERIAL PROPERTIES FOR MATERIALS  1 TO  8 IN INCREMENTS
OF          1

```

MATERIAL NUMBER = 1 EVALUATED AT TEMPERATURE OF 0.0000
 EX = 0.11089E+12
 NUXY = 0.28000
 ALPX = 0.14870E-04
 KXX = 2.1600
 PRXY = 0.28000
 MATERIAL NUMBER = 2 EVALUATED AT TEMPERATURE OF 0.0000
 EX = 0.11065E+12
 NUXY = 0.28500
 ALPX = 0.14539E-04
 KXX = 3.4408
 PRXY = 0.28500
 MATERIAL NUMBER = 3 EVALUATED AT TEMPERATURE OF 0.0000
 EX = 0.11016E+12
 NUXY = 0.29500
 ALPX = 0.13878E-04
 KXX = 6.0023
 PRXY = 0.29500
 MATERIAL NUMBER = 4 EVALUATED AT TEMPERATURE OF 0.0000
 EX = 0.10967E+12
 NUXY = 0.30500
 ALPX = 0.13216E-04
 KXX = 8.5639
 PRXY = 0.30500
 MATERIAL NUMBER = 5 EVALUATED AT TEMPERATURE OF 0.0000
 EX = 0.10918E+12
 NUXY = 0.31500
 ALPX = 0.12554E-04
 KXX = 11.125
 PRXY = 0.31500
 MATERIAL NUMBER = 6 EVALUATED AT TEMPERATURE OF 0.0000
 EX = 0.10869E+12
 NUXY = 0.32500
 ALPX = 0.11893E-04
 KXX = 13.687
 PRXY = 0.32500
 MATERIAL NUMBER = 7 EVALUATED AT TEMPERATURE OF 0.0000
 EX = 0.10820E+12
 NUXY = 0.33500
 ALPX = 0.11231E-04
 KXX = 16.248
 PRXY = 0.33500
 MATERIAL NUMBER = 8 EVALUATED AT TEMPERATURE OF 0.0000
 EX = 0.10795E+12
 NUXY = 0.34000
 ALPX = 0.10900E-04
 KXX = 17.529
 PRXY = 0.34000

LIST CONSTRAINTS ON ALL SELECTED AREAS

AREA	LOAD LABEL	VALUE (S)	
3	UX	0.0000	0.0000
3	UY	0.0000	0.0000
3	UZ	0.0000	0.0000
4	UX	0.0000	0.0000
4	UY	0.0000	0.0000
4	UZ	0.0000	0.0000
37	UX	0.0000	0.0000
37	UY	0.0000	0.0000
37	UZ	0.0000	0.0000

38	UX	0.0000	0.0000
38	UY	0.0000	0.0000
38	UZ	0.0000	0.0000
39	UX	0.0000	0.0000
39	UY	0.0000	0.0000
39	UZ	0.0000	0.0000
40	UX	0.0000	0.0000
40	UY	0.0000	0.0000
40	UZ	0.0000	0.0000
41	UX	0.0000	0.0000
41	UY	0.0000	0.0000
AREA	LOAD LABEL	VALUE (S)	
41	UZ	0.0000	0.0000
42	UX	0.0000	0.0000
42	UY	0.0000	0.0000
42	UZ	0.0000	0.0000
43	UX	0.0000	0.0000
43	UY	0.0000	0.0000
43	UZ	0.0000	0.0000
44	UX	0.0000	0.0000
44	UY	0.0000	0.0000
44	UZ	0.0000	0.0000
45	UX	0.0000	0.0000
45	UY	0.0000	0.0000
45	UZ	0.0000	0.0000
46	UX	0.0000	0.0000
46	UY	0.0000	0.0000
46	UZ	0.0000	0.0000
47	UX	0.0000	0.0000
47	UY	0.0000	0.0000
47	UZ	0.0000	0.0000
48	UX	0.0000	0.0000
AREA	LOAD LABEL	VALUE (S)	
48	UY	0.0000	0.0000
48	UZ	0.0000	0.0000
49	UX	0.0000	0.0000
49	UY	0.0000	0.0000
49	UZ	0.0000	0.0000
50	UX	0.0000	0.0000
50	UY	0.0000	0.0000
50	UZ	0.0000	0.0000

LIST NODAL TEMPERATURES FOR ALL SELECTED NODES

NODE	TEMPERATURE
1	300.000000
2	300.000000
3	300.000000
4	300.000000
5	300.000000
6	300.000000
7	300.000000
8	300.000000
9	300.000000
10	300.000000
11	300.000000
12	300.000000
13	300.000000
14	300.000000
15	300.000000
16	300.000000

```

17      300.000000
18      300.000000
19      300.000000
.
.
.
2433    300.000000
2434    300.000000
2435    300.000000
2436    300.000000
2437    300.000000
2438    300.000000
2439    300.000000
2440    300.000000
2441    300.000000
2442    155.816855
2443    155.816836
2444    155.816788
2445    155.816807
2446    155.816846
2447    155.816812
2448    155.816797
2449    155.816831
2450    155.816837
2451    155.816809
.
.
.
28596   30.8832884
28597   30.8832880
28598   30.8832904
28599   30.8832903
28600   30.8832828
28601   30.8832876
28602   30.8832886
28603   30.8832886
28604   30.8832857
28605   30.8832880
28606   30.8832906
28607   30.8832884
28608   30.8832895
28609   30.8832886

```

LIST SURFACE LOADS ON ALL SELECTED AREAS

AREA	LKEY	LOAD LABEL	VALUE (S)	REAL
1	1	PRES	P1	3.58152E+08

APPENDIX B-1

An example ANSYS's Optimization Analysis Results

PRINT ALONG PATH DEFINED BY LPATH COMMAND. DSYS= 0
 ***** PATH VARIABLE SUMMARY *****

X	Y	S1	S2	S3	SEQV
1.50E-02	0	6395.6	0	-32842	36463
1.50E-02	2.00E-05	91659	0	-14009	99407
1.50E-02	4.00E-05	1.84E+05	0	-1947.2	184680
1.50E-02	6.00E-05	2.77E+05	9289.1	0	272030
1.50E-02	8.00E-05	3.70E+05	20278	0	359950
1.50E-02	1.00E-04	4.63E+05	31160	0	448110
1.50E-02	1.20E-04	4.30E+05	38821	0	412310
1.50E-02	1.40E-04	3.98E+05	46407	0	376830
1.50E-02	1.60E-04	3.66E+05	53890	0	341780
1.50E-02	1.80E-04	3.33E+05	61225	0	307310
1.50E-02	2.00E-04	3.01E+05	68336	0	273630
1.50E-02	2.20E-04	89845	0	-15377	98438
1.50E-02	2.40E-04	80424	0	-301150	348390
1.50E-02	2.60E-04	80369	0	-596290	640270
1.50E-02	2.80E-04	81236	0	-892350	935610
1.50E-02	3.00E-04	82380	0	-1188700	1231900
1.50E-02	3.20E-04	80500	0	-1733600	1775200
1.50E-02	3.40E-04	78628	0	-2278500	2318800
1.50E-02	3.60E-04	76760	0	-2823400	2862500
1.50E-02	3.80E-04	74894	0	-3368300	3406400
1.50E-02	4.00E-04	73029	0	-3913200	3950200
1.50E-02	4.20E-04	70948	0	-4669400	4705300
1.50E-02	4.40E-04	68871	0	-5425700	5460500
1.50E-02	4.60E-04	66795	0	-6181900	6215600
1.50E-02	4.80E-04	64721	0	-6938200	6970800
1.50E-02	5.00E-04	62648	0	-7694400	7726000
1.50E-02	5.20E-04	60555	0	-8626900	8657400
1.50E-02	5.40E-04	58465	0	-9559400	9588800
1.50E-02	5.60E-04	56378	0	-10492000	10520000
1.50E-02	5.80E-04	54293	0	-11424000	11452000
1.50E-02	6.00E-04	52209	0	-12357000	12383000
1.50E-02	6.20E-04	50308	0	-13436000	13461000
1.50E-02	6.40E-04	48408	0	-14515000	14539000
1.50E-02	6.60E-04	46511	0	-15593000	15617000
1.50E-02	6.80E-04	44615	0	-16672000	16694000
1.50E-02	7.00E-04	42721	0	-17751000	17772000
1.50E-02	7.20E-04	40873	0	-18951000	18972000
1.50E-02	7.40E-04	39028	0	-20152000	20171000
1.50E-02	7.60E-04	37183	0	-21352000	21371000
1.50E-02	7.80E-04	35339	0	-22552000	22570000
1.50E-02	8.00E-04	33497	0	-23753000	23769000

1.50E-02	8.20E-04	31994	0	-25054000	25070000
1.50E-02	8.40E-04	30492	0	-26356000	26371000
1.50E-02	8.60E-04	28990	0	-27657000	27672000
1.50E-02	8.80E-04	27489	0	-28959000	28973000
1.50E-02	9.00E-04	25988	0	-30261000	30274000
1.50E-02	9.20E-04	22978	0	-31647000	31659000
1.50E-02	9.40E-04	19968	0	-33034000	33044000
1.50E-02	9.60E-04	16958	0	-34420000	34429000
1.50E-02	9.80E-04	13948	0	-35807000	35814000
1.50E-02	1.00E-03	10939	0	-37193000	37199000
1.50E-02	1.02E-03	12506	0	-38649000	38656000
1.50E-02	1.04E-03	14073	0	-40105000	40112000
1.50E-02	1.06E-03	15640	0	-41561000	41569000
1.50E-02	1.08E-03	17207	0	-43017000	43025000
1.50E-02	1.10E-03	18774	0	-44472000	44482000
1.50E-02	1.12E-03	0	-4651.4	-45991000	45989000
1.50E-02	1.14E-03	0	-28077	-47509000	47495000
1.50E-02	1.16E-03	0	-51503	-49028000	49002000
1.50E-02	1.18E-03	0	-74928	-50546000	50509000
1.50E-02	1.20E-03	0	-98354	-52065000	52016000
1.50E-02	1.22E-03	0	-61326	-53613000	53582000
1.50E-02	1.24E-03	0	-24218	-55161000	55149000
1.50E-02	1.26E-03	12963	0	-56709000	56715000
1.50E-02	1.28E-03	50212	0	-58257000	58282000
1.50E-02	1.30E-03	87522	0	-59805000	59849000
1.50E-02	1.32E-03	0	-430790	-61500000	61286000
1.50E-02	1.34E-03	0	-948380	-63196000	62727000
1.50E-02	1.36E-03	0	-1465300	-64892000	64172000
1.50E-02	1.38E-03	0	-1981600	-66589000	65621000
1.50E-02	1.40E-03	0	-2497300	-68287000	67073000
1.50E-02	1.42E-03	0	-2071300	-67527000	66516000
1.50E-02	1.44E-03	0	-1615800	-66797000	66004000
1.50E-02	1.46E-03	0	-1130400	-66096000	65538000
1.50E-02	1.48E-03	0	-614930	-65426000	65121000
1.50E-02	1.50E-03	0	-69048	-64786000	64751000
1.50E-02	1.52E-03	4.09E+05	0	-63759000	63964000
1.50E-02	1.54E-03	9.25E+05	0	-62771000	63238000
1.50E-02	1.56E-03	1.48E+06	0	-61822000	62575000
1.50E-02	1.58E-03	2.08E+06	0	-60913000	61977000
1.50E-02	1.60E-03	2.19E+06	0	-61198000	62320000
1.50E-02	1.62E-03	1.68E+06	0	-62879000	63735000
1.50E-02	1.64E-03	1.17E+06	0	-64561000	65155000
1.50E-02	1.66E-03	6.65E+05	0	-66242000	66577000
1.50E-02	1.68E-03	1.59E+05	0	-67924000	68004000
1.50E-02	1.70E-03	0	-921180	-69699000	69243000
1.50E-02	1.72E-03	0	-2056300	-71486000	70480000
1.50E-02	1.74E-03	0	-3189000	-73276000	71734000

1.50E-02	1.76E-03	0	-4319200	-75067000	73004000
1.50E-02	1.78E-03	0	-4677100	-74915000	72689000
1.50E-02	1.80E-03	0	-3591100	-71450000	69724000
1.50E-02	1.82E-03	0	-2354300	-68135000	66989000
1.50E-02	1.84E-03	0	-951850	-64986000	64516000
1.50E-02	1.86E-03	6.30E+05	0	-62017000	62334000
1.50E-02	1.88E-03	1.45E+06	0	-58325000	59064000
1.50E-02	1.90E-03	2.20E+06	0	-54571000	55706000
1.50E-02	1.92E-03	3.11E+06	0	-50973000	52600000
1.50E-02	1.94E-03	4.20E+06	0	-47558000	49793000
1.50E-02	1.96E-03	4.82E+06	0	-45681000	48272000
1.50E-02	1.98E-03	3.70E+06	0	-47445000	49397000
1.50E-02	2.00E-03	2.58E+06	0	-49212000	50550000
1.50E-02	2.02E-03	1.46E+06	0	-50982000	51727000
1.50E-02	2.04E-03	3.43E+05	0	-52755000	52928000
1.50E-02	2.06E-03	0	-743390	-54563000	54195000
1.50E-02	2.08E-03	0	-1818700	-56385000	55498000
1.50E-02	2.10E-03	0	-2892100	-58203000	56818000
1.50E-02	2.12E-03	0	-3963600	-60034000	58154000
1.50E-02	2.14E-03	0	-4676600	-60885000	58687000
1.50E-02	2.16E-03	0	-3680100	-57434000	55685000
1.50E-02	2.18E-03	0	-2496400	-54169000	52965000
1.50E-02	2.20E-03	0	-1102300	-51116000	50574000
1.50E-02	2.22E-03	5.24E+05	0	-48294000	48558000
1.50E-02	2.24E-03	1.49E+06	0	-44819000	45585000
1.50E-02	2.26E-03	2.12E+06	0	-41003000	42104000
1.50E-02	2.28E-03	2.94E+06	0	-37376000	38928000
1.50E-02	2.30E-03	3.99E+06	0	-33981000	36138000
1.50E-02	2.32E-03	5.07E+06	0	-31293000	34114000
1.50E-02	2.34E-03	3.94E+06	0	-33081000	35218000
1.50E-02	2.36E-03	2.81E+06	0	-34874000	36363000
1.50E-02	2.38E-03	1.69E+06	0	-36671000	37546000
1.50E-02	2.40E-03	5.73E+05	0	-38473000	38763000
1.50E-02	2.42E-03	0	-515940	-40307000	40051000
1.50E-02	2.44E-03	0	-1580200	-42166000	41398000
1.50E-02	2.46E-03	0	-2642200	-44028000	42768000
1.50E-02	2.48E-03	0	-3702100	-45891000	44157000
1.50E-02	2.50E-03	0	-4760000	-47757000	45564000
1.50E-02	2.52E-03	0	-3846300	-44281000	42488000
1.50E-02	2.54E-03	0	-2690500	-41043000	39766000
1.50E-02	2.56E-03	0	-1252600	-38087000	37477000
1.50E-02	2.58E-03	5.03E+05	0	-35449000	35704000
1.50E-02	2.60E-03	1.74E+06	0	-32290000	33193000
1.50E-02	2.62E-03	2.16E+06	0	-28314000	29450000
1.50E-02	2.64E-03	2.80E+06	0	-24564000	26077000
1.50E-02	2.66E-03	3.76E+06	0	-21127000	23234000
1.50E-02	2.68E-03	5.13E+06	0	-18102000	21137000

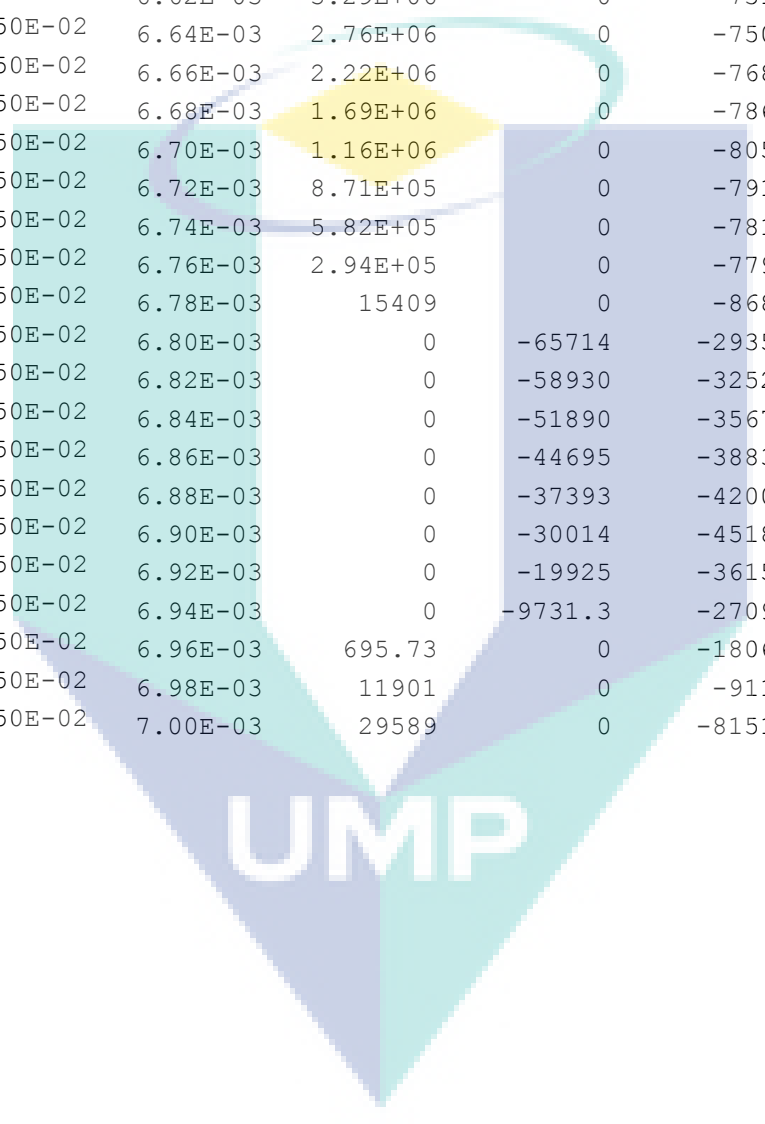
1.50E-02	2.70E-03	4.23E+06	0	-19467000	21889000
1.50E-02	2.72E-03	3.08E+06	0	-21256000	22953000
1.50E-02	2.74E-03	1.95E+06	0	-23053000	24085000
1.50E-02	2.76E-03	8.17E+05	0	-24858000	25276000
1.50E-02	2.78E-03	0	-279590	-26694000	26556000
1.50E-02	2.80E-03	0	-1328700	-28578000	27938000
1.50E-02	2.82E-03	0	-2375200	-30465000	29350000
1.50E-02	2.84E-03	0	-3419300	-32354000	30787000
1.50E-02	2.86E-03	0	-4461200	-34245000	32247000
1.50E-02	2.88E-03	0	-3994100	-31688000	29892000
1.50E-02	2.90E-03	0	-2882500	-28445000	27119000
1.50E-02	2.92E-03	0	-1349000	-25624000	24977000
1.50E-02	2.94E-03	6.75E+05	0	-23294000	23638000
1.50E-02	2.96E-03	2.46E+06	0	-20725000	22059000
1.50E-02	2.98E-03	2.52E+06	0	-16428000	17824000
1.50E-02	3.00E-03	2.81E+06	0	-12357000	13975000
1.50E-02	3.02E-03	3.53E+06	0	-8724600	10928000
1.50E-02	3.04E-03	5.06E+06	0	-5891400	9491100
1.50E-02	3.06E-03	4.75E+06	0	-6527500	9809900
1.50E-02	3.08E-03	3.53E+06	0	-8238100	10460000
1.50E-02	3.10E-03	2.33E+06	0	-9973400	11320000
1.50E-02	3.12E-03	1.15E+06	0	-11730000	12348000
1.50E-02	3.14E-03	18428	0	-13529000	13538000
1.50E-02	3.16E-03	0	-1004700	-15437000	14960000
1.50E-02	3.18E-03	0	-2025500	-17348000	16429000
1.50E-02	3.20E-03	0	-3044200	-19260000	17933000
1.50E-02	3.22E-03	0	-4061300	-21175000	19464000
1.50E-02	3.24E-03	0	-4078800	-19476000	17791000
1.50E-02	3.26E-03	0	-3068100	-16161000	14866000
1.50E-02	3.28E-03	0	-1234600	-13668000	13094000
1.50E-02	3.30E-03	1.54E+06	0	-12118000	12958000
1.50E-02	3.32E-03	4.69E+06	0	-10936000	13886000
1.50E-02	3.34E-03	4.38E+06	0	-6300200	9301200
1.50E-02	3.36E-03	4.08E+06	0	-1667700	5123600
1.50E-02	3.38E-03	3.84E+06	2905200	0	3469200
1.50E-02	3.40E-03	7.64E+06	3443100	0	6622900
1.50E-02	3.42E-03	8.72E+06	2734000	0	7729400
1.50E-02	3.44E-03	6.87E+06	1663700	0	6207800
1.50E-02	3.46E-03	5.04E+06	567530	0	4782900
1.50E-02	3.48E-03	3.25E+06	0	-569510	3572300
1.50E-02	3.50E-03	1.53E+06	0	-1771700	2862400
1.50E-02	3.52E-03	3.78E+05	0	-3538800	3741900
1.50E-02	3.54E-03	0	-722840	-5358300	5036000
1.50E-02	3.56E-03	0	-1792000	-7209200	6501200
1.50E-02	3.58E-03	0	-2841500	-9079700	8044600
1.50E-02	3.60E-03	0	-3530200	-8033800	6974400
1.50E-02	3.62E-03	0	-3068400	-4188800	3756100

1.50E-02	3.64E-03	1.29E+06	0	-4243000	5015700
1.50E-02	3.66E-03	5.88E+06	0	-4528700	9043900
1.50E-02	3.68E-03	1.05E+07	0	-4827800	13565000
1.50E-02	3.70E-03	1.16E+07	0	-1644900	12525000
1.50E-02	3.72E-03	1.31E+07	1184000	0	12557000
1.50E-02	3.74E-03	1.56E+07	3042100	0	14287000
1.50E-02	3.76E-03	1.89E+07	4046000	0	17211000
1.50E-02	3.78E-03	2.06E+07	4022800	0	18906000
1.50E-02	3.80E-03	1.87E+07	3012600	0	17387000
1.50E-02	3.82E-03	1.68E+07	2000700	0	15896000
1.50E-02	3.84E-03	1.49E+07	986940	0	14440000
1.50E-02	3.86E-03	1.30E+07	0	-29158	13031000
1.50E-02	3.88E-03	1.12E+07	0	-1148800	11851000
1.50E-02	3.90E-03	9.49E+06	0	-2309000	10835000
1.50E-02	3.92E-03	7.78E+06	0	-3491600	9991300
1.50E-02	3.94E-03	6.09E+06	0	-4699800	9365600
1.50E-02	3.96E-03	5.44E+06	0	-4996600	9037000
1.50E-02	3.98E-03	8.21E+06	0	-3475300	10393000
1.50E-02	4.00E-03	1.18E+07	0	-2770700	13404000
1.50E-02	4.02E-03	1.58E+07	0	-2504700	17222000
1.50E-02	4.04E-03	2.01E+07	0	-2459900	21419000
1.50E-02	4.06E-03	2.26E+07	0	-694090	22976000
1.50E-02	4.08E-03	2.49E+07	1311700	0	24292000
1.50E-02	4.10E-03	2.77E+07	2826100	0	26413000
1.50E-02	4.12E-03	3.09E+07	3918600	0	29164000
1.50E-02	4.14E-03	3.35E+07	4377800	0	31515000
1.50E-02	4.16E-03	3.16E+07	3354000	0	30081000
1.50E-02	4.18E-03	2.98E+07	2328000	0	28669000
1.50E-02	4.20E-03	2.79E+07	1299800	0	27283000
1.50E-02	4.22E-03	2.61E+07	269010	0	25926000
1.50E-02	4.24E-03	2.43E+07	0	-800150	24663000
1.50E-02	4.26E-03	2.25E+07	0	-1895900	23483000
1.50E-02	4.28E-03	2.07E+07	0	-2998900	22360000
1.50E-02	4.30E-03	1.89E+07	0	-4109900	21303000
1.50E-02	4.32E-03	1.76E+07	0	-4986400	20547000
1.50E-02	4.34E-03	2.06E+07	0	-3650700	22602000
1.50E-02	4.36E-03	2.39E+07	0	-2720600	25389000
1.50E-02	4.38E-03	2.76E+07	0	-2096600	28695000
1.50E-02	4.40E-03	3.15E+07	0	-1694500	32363000
1.50E-02	4.42E-03	3.46E+07	0	-498080	34839000
1.50E-02	4.44E-03	3.72E+07	1210000	0	36596000
1.50E-02	4.46E-03	4.01E+07	2606900	0	38859000
1.50E-02	4.48E-03	4.33E+07	3728400	0	41544000
1.50E-02	4.50E-03	4.67E+07	4614900	0	44576000
1.50E-02	4.52E-03	4.49E+07	3590100	0	43212000
1.50E-02	4.54E-03	4.31E+07	2560800	0	41860000
1.50E-02	4.56E-03	4.13E+07	1529500	0	40526000

1.50E-02	4.58E-03	3.95E+07	496160	0	39213000
1.50E-02	4.60E-03	3.77E+07	0	-554580	37952000
1.50E-02	4.62E-03	3.59E+07	0	-1627100	36754000
1.50E-02	4.64E-03	3.42E+07	0	-2703500	35589000
1.50E-02	4.66E-03	3.24E+07	0	-3784100	34458000
1.50E-02	4.68E-03	3.07E+07	0	-4869200	33367000
1.50E-02	4.70E-03	3.33E+07	0	-3827200	35339000
1.50E-02	4.72E-03	3.66E+07	0	-2819900	38057000
1.50E-02	4.74E-03	4.01E+07	0	-2034600	41146000
1.50E-02	4.76E-03	4.38E+07	0	-1431100	44527000
1.50E-02	4.78E-03	4.72E+07	0	-502550	47432000
1.50E-02	4.80E-03	4.99E+07	1055400	0	49424000
1.50E-02	4.82E-03	5.29E+07	2391000	0	51777000
1.50E-02	4.84E-03	5.61E+07	3525000	0	54444000
1.50E-02	4.86E-03	5.95E+07	4480200	0	57380000
1.50E-02	4.88E-03	5.87E+07	3799200	0	56879000
1.50E-02	4.90E-03	5.69E+07	2770700	0	55587000
1.50E-02	4.92E-03	5.52E+07	1740600	0	54310000
1.50E-02	4.94E-03	5.34E+07	708770	0	53048000
1.50E-02	4.96E-03	5.17E+07	0	-330150	51818000
1.50E-02	4.98E-03	4.99E+07	0	-1385500	50642000
1.50E-02	5.00E-03	4.82E+07	0	-2443400	49489000
1.50E-02	5.02E-03	4.65E+07	0	-3503900	48358000
1.50E-02	5.04E-03	4.48E+07	0	-4567100	47251000
1.50E-02	5.06E-03	4.66E+07	0	-3987400	48720000
1.50E-02	5.08E-03	4.99E+07	0	-2951500	51438000
1.50E-02	5.10E-03	5.34E+07	0	-2086500	54437000
1.50E-02	5.12E-03	5.70E+07	0	-1369400	57675000
1.50E-02	5.14E-03	6.05E+07	0	-589600	60835000
1.50E-02	5.16E-03	6.34E+07	903080	0	62978000
1.50E-02	5.18E-03	6.65E+07	2226800	0	65396000
1.50E-02	5.20E-03	6.97E+07	3394800	0	68059000
1.50E-02	5.22E-03	7.30E+07	4421000	0	70939000
1.50E-02	5.24E-03	7.32E+07	4090300	0	71252000
1.50E-02	5.26E-03	7.15E+07	3027600	0	70020000
1.50E-02	5.28E-03	6.98E+07	1962700	0	68802000
1.50E-02	5.30E-03	6.80E+07	895690	0	67599000
1.50E-02	5.32E-03	6.63E+07	0	-121270	66393000
1.50E-02	5.34E-03	6.47E+07	0	-603820	65011000
1.50E-02	5.36E-03	6.31E+07	0	-1086600	63633000
1.50E-02	5.38E-03	6.15E+07	0	-1569600	62257000
1.50E-02	5.40E-03	5.98E+07	0	-2052800	60885000
1.50E-02	5.42E-03	5.95E+07	0	-1953300	60547000
1.50E-02	5.44E-03	6.04E+07	0	-1393400	61121000
1.50E-02	5.46E-03	6.13E+07	0	-870630	61756000
1.50E-02	5.48E-03	6.23E+07	0	-384430	62450000
1.50E-02	5.50E-03	6.32E+07	66006	0	63199000

1.50E-02	5.52E-03	6.38E+07	577140	0	63555000
1.50E-02	5.54E-03	6.45E+07	1060200	0	63955000
1.50E-02	5.56E-03	6.51E+07	1515100	0	64400000
1.50E-02	5.58E-03	6.58E+07	1942300	0	64888000
1.50E-02	5.60E-03	6.66E+07	2342000	0	65418000
1.50E-02	5.62E-03	6.49E+07	1867100	0	64002000
1.50E-02	5.64E-03	6.33E+07	1389900	0	62585000
1.50E-02	5.66E-03	6.16E+07	912090	0	61171000
1.50E-02	5.68E-03	6.00E+07	433710	0	59761000
1.50E-02	5.70E-03	5.83E+07	0	-45300	58354000
1.50E-02	5.72E-03	5.68E+07	0	-19458	56834000
1.50E-02	5.74E-03	5.53E+07	7334.6	0	55314000
1.50E-02	5.76E-03	5.38E+07	34061	0	53794000
1.50E-02	5.78E-03	5.23E+07	60716	0	52275000
1.50E-02	5.80E-03	5.08E+07	87291	0	50755000
1.50E-02	5.82E-03	4.93E+07	66790	0	49285000
1.50E-02	5.84E-03	4.78E+07	46194	0	47816000
1.50E-02	5.86E-03	4.64E+07	25598	0	46346000
1.50E-02	5.88E-03	4.49E+07	5001.4	0	44876000
1.50E-02	5.90E-03	4.34E+07	0	-15595	43407000
1.50E-02	5.92E-03	4.20E+07	0	-14785	41987000
1.50E-02	5.94E-03	4.06E+07	0	-13932	40567000
1.50E-02	5.96E-03	3.91E+07	0	-13079	39147000
1.50E-02	5.98E-03	3.77E+07	0	-12226	37727000
1.50E-02	6.00E-03	3.63E+07	0	-11373	36307000
1.50E-02	6.02E-03	3.49E+07	0	-14112	34955000
1.50E-02	6.04E-03	3.36E+07	0	-16859	33604000
1.50E-02	6.06E-03	3.22E+07	0	-19605	32253000
1.50E-02	6.08E-03	3.09E+07	0	-22351	30902000
1.50E-02	6.10E-03	2.95E+07	0	-25098	29551000
1.50E-02	6.12E-03	2.83E+07	0	-26623	28281000
1.50E-02	6.14E-03	2.70E+07	0	-28146	27012000
1.50E-02	6.16E-03	2.57E+07	0	-29669	25742000
1.50E-02	6.18E-03	2.45E+07	0	-31193	24473000
1.50E-02	6.20E-03	2.32E+07	0	-32717	23204000
1.50E-02	6.22E-03	2.20E+07	0	-34505	22033000
1.50E-02	6.24E-03	2.08E+07	0	-36294	20862000
1.50E-02	6.26E-03	1.97E+07	0	-38084	19692000
1.50E-02	6.28E-03	1.85E+07	0	-39875	18521000
1.50E-02	6.30E-03	1.73E+07	0	-41668	17351000
1.50E-02	6.32E-03	1.63E+07	0	-43526	16298000
1.50E-02	6.34E-03	1.52E+07	0	-45385	15246000
1.50E-02	6.36E-03	1.42E+07	0	-47246	14194000
1.50E-02	6.38E-03	1.31E+07	0	-49109	13142000
1.50E-02	6.40E-03	1.21E+07	0	-50974	12090000
1.50E-02	6.42E-03	1.12E+07	0	-53013	11180000
1.50E-02	6.44E-03	1.02E+07	0	-55053	10271000

1.50E-02	6.46E-03	9.33E+06	0	-57096	9362000
1.50E-02	6.48E-03	8.42E+06	0	-59141	8452700
1.50E-02	6.50E-03	7.51E+06	0	-61190	7543500
1.50E-02	6.52E-03	6.77E+06	0	-63212	6805900
1.50E-02	6.54E-03	6.04E+06	0	-65235	6068700
1.50E-02	6.56E-03	5.30E+06	0	-67260	5331500
1.50E-02	6.58E-03	4.56E+06	0	-69286	4594400
1.50E-02	6.60E-03	3.82E+06	0	-71316	3857200
1.50E-02	6.62E-03	3.29E+06	0	-73158	3325900
1.50E-02	6.64E-03	2.76E+06	0	-75001	2795000
1.50E-02	6.66E-03	2.22E+06	0	-76845	2264200
1.50E-02	6.68E-03	1.69E+06	0	-78694	1733600
1.50E-02	6.70E-03	1.16E+06	0	-80550	1203200
1.50E-02	6.72E-03	8.71E+05	0	-79198	913440
1.50E-02	6.74E-03	5.82E+05	0	-78106	625060
1.50E-02	6.76E-03	2.94E+05	0	-77910	340030
1.50E-02	6.78E-03	15409	0	-86840	95481
1.50E-02	6.80E-03	0	-65714	-293550	266830
1.50E-02	6.82E-03	0	-58930	-325280	300180
1.50E-02	6.84E-03	0	-51890	-356740	333830
1.50E-02	6.86E-03	0	-44695	-388360	368050
1.50E-02	6.88E-03	0	-37393	-420080	402690
1.50E-02	6.90E-03	0	-30014	-451880	437650
1.50E-02	6.92E-03	0	-19925	-361500	351960
1.50E-02	6.94E-03	0	-9731.3	-270980	266250
1.50E-02	6.96E-03	695.73	0	-180690	181040
1.50E-02	6.98E-03	11901	0	-91180	97676
1.50E-02	7.00E-03	29589	0	-8151.8	34397



UMP

APPENDIX B-2

An example ANSYS's Mechanical Field Analysis Results

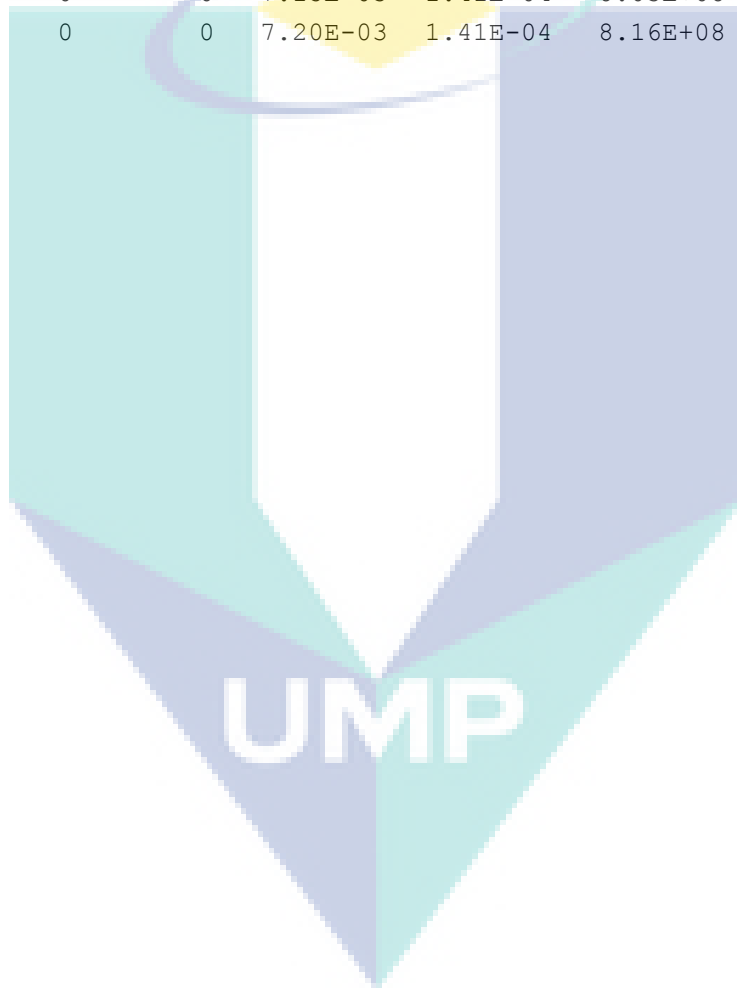
PRINT ALONG PATH DEFINED BY LPATH COMMAND. DSYS= 0
 ***** PATH VARIABLE SUMMARY *****

X	Y	Z	UZ	SX	SXZ	SINT
0	0	0	1.52E-04	-9.16E+08	-4634.3	5.52E+08
0	0	5.00E-05	1.52E-04	-9.03E+08	-4214.8	5.40E+08
0	0	1.00E-04	1.52E-04	-8.90E+08	-3795	5.28E+08
0	0	1.50E-04	1.52E-04	-8.77E+08	-3374.7	5.17E+08
0	0	2.00E-04	1.52E-04	-8.63E+08	-2954	5.05E+08
0	0	2.50E-04	1.52E-04	-8.50E+08	-2532.9	4.93E+08
0	0	3.00E-04	1.52E-04	-8.37E+08	-2111.4	4.82E+08
0	0	3.50E-04	1.52E-04	-8.24E+08	-1689.4	4.70E+08
0	0	4.00E-04	1.52E-04	-8.11E+08	-1267.1	4.58E+08
0	0	4.50E-04	1.52E-04	-7.98E+08	-844.35	4.46E+08
0	0	5.00E-04	1.52E-04	-7.85E+08	-421.19	4.35E+08
0	0	5.50E-04	1.52E-04	-7.72E+08	2.3903	4.23E+08
0	0	6.00E-04	1.52E-04	-7.59E+08	426.38	4.11E+08
0	0	6.50E-04	1.52E-04	-7.45E+08	850.78	4.00E+08
0	0	7.00E-04	1.52E-04	-7.32E+08	1275.6	3.88E+08
0	0	7.50E-04	1.52E-04	-7.19E+08	1700.8	3.76E+08
0	0	8.00E-04	1.52E-04	-7.06E+08	2126.5	3.65E+08
0	0	8.50E-04	1.53E-04	-6.93E+08	2552.5	3.53E+08
0	0	9.00E-04	1.53E-04	-6.80E+08	2979	3.41E+08
0	0	9.50E-04	1.53E-04	-6.67E+08	3405.9	3.30E+08
0	0	1.00E-03	1.53E-04	-6.54E+08	3833.2	3.18E+08
0	0	1.05E-03	1.53E-04	-6.40E+08	4260.9	3.06E+08
0	0	1.10E-03	1.53E-04	-6.27E+08	4689	2.94E+08
0	0	1.15E-03	1.53E-04	-6.14E+08	5117.5	2.83E+08
0	0	1.20E-03	1.53E-04	-6.01E+08	5546.4	2.71E+08
0	0	1.25E-03	1.53E-04	-5.88E+08	5975.8	2.59E+08
0	0	1.30E-03	1.53E-04	-5.75E+08	6405.5	2.48E+08
0	0	1.35E-03	1.53E-04	-5.62E+08	6835.7	2.36E+08
0	0	1.40E-03	1.53E-04	-5.49E+08	7266.3	2.24E+08
0	0	1.45E-03	1.53E-04	-5.36E+08	7697.3	2.13E+08
0	0	1.50E-03	1.53E-04	-5.22E+08	8128.7	2.01E+08
0	0	1.55E-03	1.53E-04	-5.11E+08	8138.9	1.93E+08
0	0	1.60E-03	1.53E-04	-5.01E+08	8149.1	1.85E+08
0	0	1.65E-03	1.53E-04	-4.90E+08	8159.3	1.77E+08
0	0	1.70E-03	1.52E-04	-4.79E+08	8169.5	1.69E+08
0	0	1.75E-03	1.52E-04	-4.68E+08	8179.6	1.61E+08
0	0	1.80E-03	1.52E-04	-4.57E+08	8189.8	1.53E+08
0	0	1.85E-03	1.52E-04	-4.46E+08	8200	1.45E+08

0	0	1.90E-03	1.52E-04	-4.35E+08	8210.2	1.37E+08
0	0	1.95E-03	1.52E-04	-4.24E+08	8220.4	1.30E+08
0	0	2.00E-03	1.52E-04	-4.13E+08	8230.6	1.22E+08
0	0	2.05E-03	1.52E-04	-4.02E+08	8240.8	1.14E+08
0	0	2.10E-03	1.52E-04	-3.91E+08	8250.9	1.06E+08
0	0	2.15E-03	1.52E-04	-3.80E+08	8261.1	9.79E+07
0	0	2.20E-03	1.52E-04	-3.69E+08	8271.3	8.99E+07
0	0	2.25E-03	1.52E-04	-3.59E+08	8289.2	8.28E+07
0	0	2.30E-03	1.52E-04	-3.48E+08	8308.2	7.56E+07
0	0	2.35E-03	1.52E-04	-3.37E+08	8328.5	6.85E+07
0	0	2.40E-03	1.52E-04	-3.27E+08	8350	6.13E+07
0	0	2.45E-03	1.52E-04	-3.16E+08	8372.7	5.42E+07
0	0	2.50E-03	1.52E-04	-3.06E+08	8396.6	4.70E+07
0	0	2.55E-03	1.52E-04	-2.95E+08	8421.8	3.99E+07
0	0	2.60E-03	1.52E-04	-2.85E+08	8448.2	3.27E+07
0	0	2.65E-03	1.52E-04	-2.74E+08	8475.7	2.56E+07
0	0	2.70E-03	1.52E-04	-2.63E+08	8504.5	1.84E+07
0	0	2.75E-03	1.52E-04	-2.53E+08	8534.5	1.13E+07
0	0	2.80E-03	1.52E-04	-2.42E+08	8565.8	4.13E+06
0	0	2.85E-03	1.52E-04	-2.32E+08	8598.2	3.06E+06
0	0	2.90E-03	1.52E-04	-2.21E+08	8631.9	1.02E+07
0	0	2.95E-03	1.52E-04	-2.11E+08	8601.5	1.70E+07
0	0	3.00E-03	1.52E-04	-2.00E+08	8571.5	2.37E+07
0	0	3.05E-03	1.52E-04	-1.90E+08	8542	3.05E+07
0	0	3.10E-03	1.52E-04	-1.79E+08	8512.8	3.73E+07
0	0	3.15E-03	1.52E-04	-1.69E+08	8484.1	4.41E+07
0	0	3.20E-03	1.51E-04	-1.58E+08	8455.8	5.08E+07
0	0	3.25E-03	1.51E-04	-1.48E+08	8427.9	5.76E+07
0	0	3.30E-03	1.51E-04	-1.37E+08	8400.4	6.44E+07
0	0	3.35E-03	1.51E-04	-1.27E+08	8373.4	7.11E+07
0	0	3.40E-03	1.51E-04	-1.16E+08	8346.7	7.79E+07
0	0	3.45E-03	1.51E-04	-1.06E+08	8320.5	8.47E+07
0	0	3.50E-03	1.51E-04	-9.55E+07	8294.7	9.15E+07
0	0	3.55E-03	1.51E-04	-8.50E+07	8269.3	9.82E+07
0	0	3.60E-03	1.51E-04	-7.45E+07	8244.4	1.05E+08
0	0	3.65E-03	1.51E-04	-6.38E+07	8210.4	1.12E+08
0	0	3.70E-03	1.51E-04	-5.31E+07	8176.1	1.19E+08
0	0	3.75E-03	1.51E-04	-4.23E+07	8141.4	1.26E+08
0	0	3.80E-03	1.51E-04	-3.16E+07	8106.3	1.33E+08
0	0	3.85E-03	1.51E-04	-2.09E+07	8070.8	1.40E+08
0	0	3.90E-03	1.51E-04	-1.02E+07	8034.9	1.47E+08
0	0	3.95E-03	1.51E-04	5.27E+05	7998.7	1.54E+08
0	0	4.00E-03	1.50E-04	1.12E+07	7962	1.61E+08
0	0	4.05E-03	1.50E-04	2.20E+07	7925	1.68E+08
0	0	4.10E-03	1.50E-04	3.27E+07	7887.6	1.75E+08
0	0	4.15E-03	1.50E-04	4.34E+07	7849.8	1.82E+08
0	0	4.20E-03	1.50E-04	5.41E+07	7811.6	1.89E+08

0	0	4.25E-03	1.50E-04	6.48E+07	7773	1.96E+08
0	0	4.30E-03	1.50E-04	7.56E+07	7734.1	2.03E+08
0	0	4.35E-03	1.50E-04	8.69E+07	7663.7	2.11E+08
0	0	4.40E-03	1.50E-04	9.82E+07	7592.2	2.19E+08
0	0	4.45E-03	1.50E-04	1.09E+08	7519.4	2.27E+08
0	0	4.50E-03	1.50E-04	1.21E+08	7445.5	2.35E+08
0	0	4.55E-03	1.50E-04	1.32E+08	7370.3	2.42E+08
0	0	4.60E-03	1.50E-04	1.43E+08	7294	2.50E+08
0	0	4.65E-03	1.49E-04	1.55E+08	7216.5	2.58E+08
0	0	4.70E-03	1.49E-04	1.66E+08	7137.7	2.66E+08
0	0	4.75E-03	1.49E-04	1.77E+08	7057.8	2.74E+08
0	0	4.80E-03	1.49E-04	1.89E+08	6976.7	2.82E+08
0	0	4.85E-03	1.49E-04	2.00E+08	6894.4	2.90E+08
0	0	4.90E-03	1.49E-04	2.11E+08	6810.8	2.98E+08
0	0	4.95E-03	1.49E-04	2.22E+08	6726.1	3.05E+08
0	0	5.00E-03	1.49E-04	2.34E+08	6640.2	3.13E+08
0	0	5.05E-03	1.49E-04	2.46E+08	6640.2	3.22E+08
0	0	5.10E-03	1.48E-04	2.58E+08	6638.2	3.31E+08
0	0	5.15E-03	1.48E-04	2.70E+08	6634.4	3.40E+08
0	0	5.20E-03	1.48E-04	2.82E+08	6628.7	3.49E+08
0	0	5.25E-03	1.48E-04	2.94E+08	6621.1	3.58E+08
0	0	5.30E-03	1.48E-04	3.06E+08	6611.6	3.67E+08
0	0	5.35E-03	1.48E-04	3.18E+08	6600.2	3.76E+08
0	0	5.40E-03	1.48E-04	3.29E+08	6586.9	3.85E+08
0	0	5.45E-03	1.48E-04	3.41E+08	6571.8	3.94E+08
0	0	5.50E-03	1.47E-04	3.53E+08	6554.7	4.02E+08
0	0	5.55E-03	1.47E-04	3.65E+08	6535.8	4.11E+08
0	0	5.60E-03	1.47E-04	3.77E+08	6515	4.20E+08
0	0	5.65E-03	1.47E-04	3.89E+08	6492.2	4.29E+08
0	0	5.70E-03	1.47E-04	4.01E+08	6467.6	4.38E+08
0	0	5.75E-03	1.47E-04	4.15E+08	6064.1	4.50E+08
0	0	5.80E-03	1.47E-04	4.29E+08	5659	4.63E+08
0	0	5.85E-03	1.47E-04	4.43E+08	5252.4	4.75E+08
0	0	5.90E-03	1.46E-04	4.57E+08	4844.3	4.88E+08
0	0	5.95E-03	1.46E-04	4.70E+08	4434.7	5.00E+08
0	0	6.00E-03	1.46E-04	4.84E+08	4023.6	5.13E+08
0	0	6.05E-03	1.46E-04	4.98E+08	3611	5.25E+08
0	0	6.10E-03	1.46E-04	5.12E+08	3196.8	5.37E+08
0	0	6.15E-03	1.46E-04	5.26E+08	2781.2	5.50E+08
0	0	6.20E-03	1.45E-04	5.40E+08	2364	5.62E+08
0	0	6.25E-03	1.45E-04	5.53E+08	1945.4	5.75E+08
0	0	6.30E-03	1.45E-04	5.67E+08	1525.2	5.87E+08
0	0	6.35E-03	1.45E-04	5.81E+08	1103.5	5.99E+08
0	0	6.40E-03	1.45E-04	5.95E+08	680.33	6.12E+08
0	0	6.45E-03	1.44E-04	6.09E+08	255.62	6.24E+08
0	0	6.50E-03	1.44E-04	6.23E+08	-170.59	6.37E+08
0	0	6.55E-03	1.44E-04	6.36E+08	-598.32	6.49E+08

0	0	6.60E-03	1.44E-04	6.50E+08	-1027.6	6.61E+08
0	0	6.65E-03	1.44E-04	6.64E+08	-1458.3	6.74E+08
0	0	6.70E-03	1.43E-04	6.78E+08	-1890.6	6.86E+08
0	0	6.75E-03	1.43E-04	6.92E+08	-2324.3	6.99E+08
0	0	6.80E-03	1.43E-04	7.06E+08	-2759.6	7.11E+08
0	0	6.85E-03	1.43E-04	7.20E+08	-3196.4	7.23E+08
0	0	6.90E-03	1.42E-04	7.33E+08	-3634.7	7.36E+08
0	0	6.95E-03	1.42E-04	7.47E+08	-4074.5	7.48E+08
0	0	7.00E-03	1.42E-04	7.61E+08	-4515.8	7.61E+08
0	0	7.05E-03	1.42E-04	7.75E+08	-4958.6	7.73E+08
0	0	7.10E-03	1.42E-04	7.89E+08	-5403	7.85E+08
0	0	7.15E-03	1.41E-04	8.03E+08	-5848.8	7.98E+08
0	0	7.20E-03	1.41E-04	8.16E+08	-6296.2	8.10E+08



APPENDIX B-3

An example ANSYS's Thermal Field Analysis Results

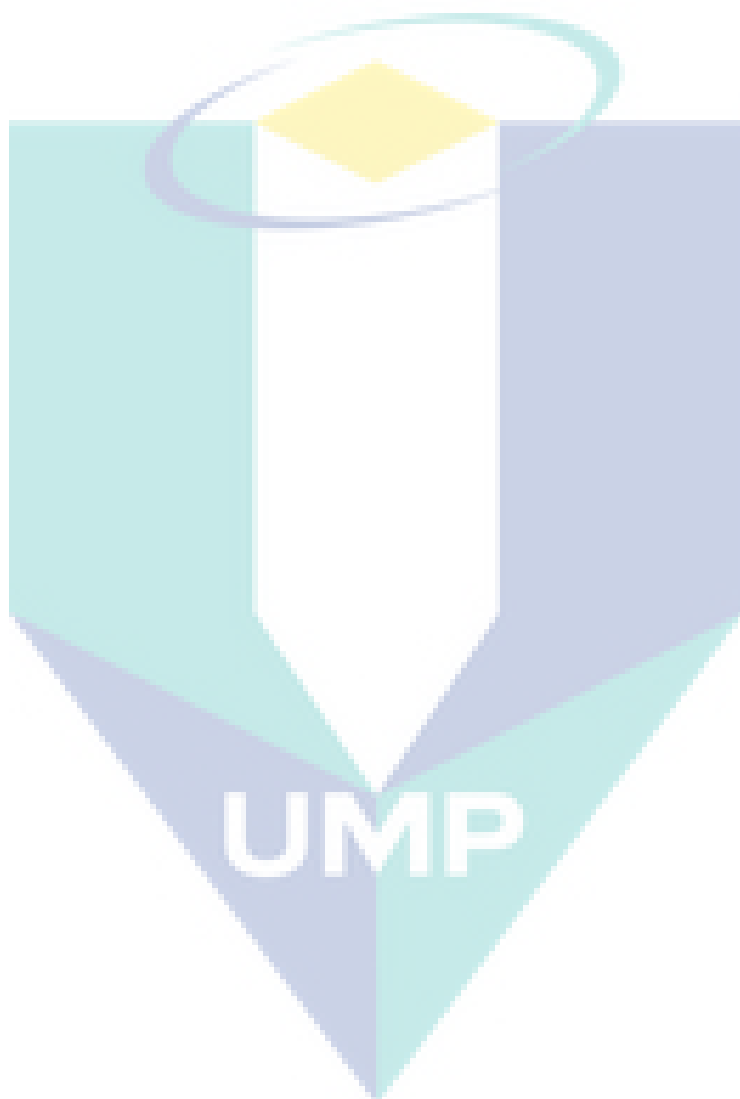
PRINT ALONG PATH DEFINED BY LPATH COMMAND. DSYS= 0
 ***** PATH VARIABLE SUMMARY *****

X	Y	Z	UZ	SX	SXZ	SINT
0	0	0.00E+00	0.00E+00	-7.03E+08	-7.7712	7.03E+08
0	0	5.00E-05	-1.22E-05	-6.91E+08	-52.799	6.91E+08
0	0	1.00E-04	-1.18E-05	-6.80E+08	-97.827	6.80E+08
0	0	1.50E-04	-1.14E-05	-6.69E+08	-142.85	6.69E+08
0	0	2.00E-04	-1.10E-05	-6.58E+08	-187.88	6.58E+08
0	0	2.50E-04	-1.07E-05	-6.47E+08	-232.91	6.47E+08
0	0	3.00E-04	-1.03E-05	-6.35E+08	-277.94	6.35E+08
0	0	3.50E-04	-9.93E-06	-6.24E+08	-322.96	6.24E+08
0	0	4.00E-04	-9.58E-06	-6.13E+08	-367.99	6.13E+08
0	0	4.50E-04	-9.23E-06	-6.02E+08	-413.02	6.02E+08
0	0	5.00E-04	-8.89E-06	-5.91E+08	-458.04	5.91E+08
0	0	5.50E-04	-8.56E-06	-5.80E+08	-503.07	5.80E+08
0	0	6.00E-04	-8.23E-06	-5.68E+08	-548.09	5.68E+08
0	0	6.50E-04	-7.91E-06	-5.57E+08	-593.12	5.57E+08
0	0	7.00E-04	-7.60E-06	-5.46E+08	-638.15	5.46E+08
0	0	7.50E-04	-7.29E-06	-5.35E+08	-683.17	5.35E+08
0	0	8.00E-04	-6.99E-06	-5.24E+08	-728.2	5.24E+08
0	0	8.50E-04	-6.69E-06	-5.12E+08	-773.22	5.12E+08
0	0	9.00E-04	-6.40E-06	-5.01E+08	-818.24	5.01E+08
0	0	9.50E-04	-6.12E-06	-4.90E+08	-863.27	4.90E+08
0	0	1.00E-03	-5.84E-06	-4.79E+08	-908.29	4.79E+08
0	0	1.05E-03	-5.57E-06	-4.68E+08	-953.32	4.68E+08
0	0	1.10E-03	-5.31E-06	-4.56E+08	-998.34	4.56E+08
0	0	1.15E-03	-5.05E-06	-4.45E+08	-1043.4	4.45E+08
0	0	1.20E-03	-4.80E-06	-4.34E+08	-1088.4	4.34E+08
0	0	1.25E-03	-4.56E-06	-4.23E+08	-1133.4	4.23E+08
0	0	1.30E-03	-4.32E-06	-4.12E+08	-1178.4	4.12E+08
0	0	1.35E-03	-4.09E-06	-4.00E+08	-1223.5	4.00E+08
0	0	1.40E-03	-3.86E-06	-3.89E+08	-1268.5	3.89E+08
0	0	1.45E-03	-3.64E-06	-3.78E+08	-1313.5	3.78E+08
0	0	1.50E-03	-3.43E-06	-3.67E+08	-1358.5	3.67E+08
0	0	1.55E-03	-3.23E-06	-3.59E+08	-1367.9	3.59E+08
0	0	1.60E-03	-3.03E-06	-3.52E+08	-1377.3	3.52E+08
0	0	1.65E-03	-2.83E-06	-3.45E+08	-1386.7	3.45E+08
0	0	1.70E-03	-2.64E-06	-3.37E+08	-1396.1	3.37E+08
0	0	1.75E-03	-2.45E-06	-3.30E+08	-1405.5	3.30E+08
0	0	1.80E-03	-2.26E-06	-3.22E+08	-1414.9	3.22E+08
0	0	1.85E-03	-2.08E-06	-3.15E+08	-1424.3	3.15E+08
0	0	1.90E-03	-1.90E-06	-3.08E+08	-1433.7	3.08E+08
0	0	1.95E-03	-1.73E-06	-3.00E+08	-1443.1	3.00E+08
0	0	2.00E-03	-1.56E-06	-2.93E+08	-1452.5	2.93E+08
0	0	2.05E-03	-1.39E-06	-2.85E+08	-1461.9	2.85E+08

0	0	2.10E-03	-1.23E-06	-2.78E+08	-1471.3	2.78E+08
0	0	2.15E-03	-1.08E-06	-2.70E+08	-1480.7	2.70E+08
0	0	2.20E-03	-9.22E-07	-2.63E+08	-1490.1	2.63E+08
0	0	2.25E-03	-7.75E-07	-2.59E+08	-1505.2	2.59E+08
0	0	2.30E-03	-6.31E-07	-2.54E+08	-1520.4	2.54E+08
0	0	2.35E-03	-4.88E-07	-2.50E+08	-1535.5	2.50E+08
0	0	2.40E-03	-3.48E-07	-2.45E+08	-1550.7	2.45E+08
0	0	2.45E-03	-2.10E-07	-2.41E+08	-1565.8	2.41E+08
0	0	2.50E-03	-7.39E-08	-2.37E+08	-1581	2.37E+08
0	0	2.55E-03	0.00E+00	-2.32E+08	-1596.1	2.32E+08
0	0	2.60E-03	0.00E+00	-2.28E+08	-1611.3	2.28E+08
0	0	2.65E-03	0.00E+00	-2.23E+08	-1626.4	2.23E+08
0	0	2.70E-03	0.00E+00	-2.19E+08	-1641.6	2.19E+08
0	0	2.75E-03	0.00E+00	-2.14E+08	-1656.7	2.15E+08
0	0	2.80E-03	0.00E+00	-2.10E+08	-1671.9	2.10E+08
0	0	2.85E-03	0.00E+00	-2.06E+08	-1687	2.06E+08
0	0	2.90E-03	0.00E+00	-2.01E+08	-1702.2	2.01E+08
0	0	2.95E-03	0.00E+00	-1.98E+08	-1696.1	1.98E+08
0	0	3.00E-03	0.00E+00	-1.95E+08	-1690.1	1.95E+08
0	0	3.05E-03	0.00E+00	-1.92E+08	-1684	1.92E+08
0	0	3.10E-03	0.00E+00	-1.89E+08	-1678	1.89E+08
0	0	3.15E-03	0.00E+00	-1.86E+08	-1671.9	1.86E+08
0	0	3.20E-03	0.00E+00	-1.83E+08	-1665.9	1.83E+08
0	0	3.25E-03	0.00E+00	-1.80E+08	-1659.8	1.80E+08
0	0	3.30E-03	0.00E+00	-1.77E+08	-1653.8	1.77E+08
0	0	3.35E-03	0.00E+00	-1.74E+08	-1647.8	1.74E+08
0	0	3.40E-03	0.00E+00	-1.70E+08	-1641.7	1.71E+08
0	0	3.45E-03	0.00E+00	-1.67E+08	-1635.7	1.67E+08
0	0	3.50E-03	0.00E+00	-1.64E+08	-1629.7	1.64E+08
0	0	3.55E-03	0.00E+00	-1.61E+08	-1623.6	1.61E+08
0	0	3.60E-03	0.00E+00	-1.58E+08	-1617.6	1.58E+08
0	0	3.65E-03	0.00E+00	-1.56E+08	-1602.1	1.56E+08
0	0	3.70E-03	0.00E+00	-1.53E+08	-1586.5	1.54E+08
0	0	3.75E-03	0.00E+00	-1.51E+08	-1570.9	1.51E+08
0	0	3.80E-03	0.00E+00	-1.49E+08	-1555.4	1.49E+08
0	0	3.85E-03	0.00E+00	-1.46E+08	-1539.8	1.47E+08
0	0	3.90E-03	0.00E+00	-1.44E+08	-1524.2	1.44E+08
0	0	3.95E-03	0.00E+00	-1.42E+08	-1508.7	1.42E+08
0	0	4.00E-03	0.00E+00	-1.39E+08	-1493.1	1.40E+08
0	0	4.05E-03	0.00E+00	-1.37E+08	-1477.6	1.37E+08
0	0	4.10E-03	0.00E+00	-1.35E+08	-1462.1	1.35E+08
0	0	4.15E-03	0.00E+00	-1.32E+08	-1446.5	1.33E+08
0	0	4.20E-03	0.00E+00	-1.30E+08	-1431	1.30E+08
0	0	4.25E-03	0.00E+00	-1.28E+08	-1415.5	1.28E+08
0	0	4.30E-03	0.00E+00	-1.25E+08	-1399.9	1.26E+08
0	0	4.35E-03	0.00E+00	-1.24E+08	-1390.5	1.24E+08
0	0	4.40E-03	0.00E+00	-1.22E+08	-1381.1	1.22E+08
0	0	4.45E-03	0.00E+00	-1.20E+08	-1371.6	1.20E+08
0	0	4.50E-03	0.00E+00	-1.18E+08	-1362.2	1.18E+08

0	0	4.55E-03	0.00E+00	-1.16E+08	-1352.8	1.16E+08
0	0	4.60E-03	0.00E+00	-1.14E+08	-1343.3	1.14E+08
0	0	4.65E-03	0.00E+00	-1.13E+08	-1333.9	1.13E+08
0	0	4.70E-03	0.00E+00	-1.11E+08	-1324.5	1.11E+08
0	0	4.75E-03	0.00E+00	-1.09E+08	-1315	1.09E+08
0	0	4.80E-03	0.00E+00	-1.07E+08	-1305.6	1.07E+08
0	0	4.85E-03	0.00E+00	-1.05E+08	-1296.2	1.05E+08
0	0	4.90E-03	0.00E+00	-1.03E+08	-1286.7	1.03E+08
0	0	4.95E-03	0.00E+00	-1.01E+08	-1277.3	1.01E+08
0	0	5.00E-03	0.00E+00	-9.95E+07	-1267.9	9.96E+07
0	0	5.05E-03	0.00E+00	-9.81E+07	-1232.6	9.81E+07
0	0	5.10E-03	0.00E+00	-9.66E+07	-1197.4	9.67E+07
0	0	5.15E-03	0.00E+00	-9.52E+07	-1162.1	9.52E+07
0	0	5.20E-03	0.00E+00	-9.37E+07	-1126.9	9.38E+07
0	0	5.25E-03	0.00E+00	-9.23E+07	-1091.6	9.23E+07
0	0	5.30E-03	0.00E+00	-9.08E+07	-1056.4	9.09E+07
0	0	5.35E-03	0.00E+00	-8.94E+07	-1021.1	8.94E+07
0	0	5.40E-03	0.00E+00	-8.80E+07	-985.85	8.80E+07
0	0	5.45E-03	0.00E+00	-8.65E+07	-950.58	8.65E+07
0	0	5.50E-03	0.00E+00	-8.51E+07	-915.31	8.51E+07
0	0	5.55E-03	0.00E+00	-8.36E+07	-880.04	8.36E+07
0	0	5.60E-03	0.00E+00	-8.22E+07	-844.76	8.22E+07
0	0	5.65E-03	0.00E+00	-8.07E+07	-809.48	8.07E+07
0	0	5.70E-03	0.00E+00	-7.93E+07	-774.2	7.93E+07
0	0	5.75E-03	0.00E+00	-7.81E+07	-751.7	7.81E+07
0	0	5.80E-03	0.00E+00	-7.70E+07	-729.19	7.70E+07
0	0	5.85E-03	0.00E+00	-7.58E+07	-706.69	7.58E+07
0	0	5.90E-03	0.00E+00	-7.47E+07	-684.18	7.47E+07
0	0	5.95E-03	0.00E+00	-7.35E+07	-661.67	7.35E+07
0	0	6.00E-03	0.00E+00	-7.24E+07	-639.17	7.24E+07
0	0	6.05E-03	0.00E+00	-7.12E+07	-616.66	7.12E+07
0	0	6.10E-03	0.00E+00	-7.01E+07	-594.15	7.01E+07
0	0	6.15E-03	0.00E+00	-6.89E+07	-571.64	6.89E+07
0	0	6.20E-03	0.00E+00	-6.78E+07	-549.13	6.78E+07
0	0	6.25E-03	0.00E+00	-6.66E+07	-526.62	6.66E+07
0	0	6.30E-03	0.00E+00	-6.55E+07	-504.11	6.55E+07
0	0	6.35E-03	0.00E+00	-6.43E+07	-481.59	6.43E+07
0	0	6.40E-03	0.00E+00	-6.32E+07	-459.08	6.32E+07
0	0	6.45E-03	0.00E+00	-6.20E+07	-436.57	6.20E+07
0	0	6.50E-03	0.00E+00	-6.09E+07	-414.05	6.09E+07
0	0	6.55E-03	0.00E+00	-5.97E+07	-391.54	5.97E+07
0	0	6.60E-03	0.00E+00	-5.86E+07	-369.02	5.86E+07
0	0	6.65E-03	0.00E+00	-5.74E+07	-346.51	5.74E+07
0	0	6.70E-03	0.00E+00	-5.63E+07	-323.99	5.63E+07
0	0	6.75E-03	0.00E+00	-5.51E+07	-301.47	5.51E+07
0	0	6.80E-03	0.00E+00	-5.39E+07	-278.95	5.40E+07
0	0	6.85E-03	0.00E+00	-5.28E+07	-256.43	5.28E+07
0	0	6.90E-03	0.00E+00	-5.16E+07	-233.91	5.17E+07
0	0	6.95E-03	0.00E+00	-5.05E+07	-211.39	5.05E+07

0	0	7.00E-03	0.00E+00	-4.93E+07	-188.87	4.94E+07
0	0	7.05E-03	0.00E+00	-4.82E+07	-166.35	4.82E+07
0	0	7.10E-03	0.00E+00	-4.70E+07	-143.82	4.71E+07
0	0	7.15E-03	0.00E+00	-4.59E+07	-121.3	4.59E+07
0	0	7.20E-03	0.00E+00	-4.47E+07	-98.777	4.48E+07



APPENDIX B-4

An example ANSYS's Thermo-mechanical Field Analysis Results

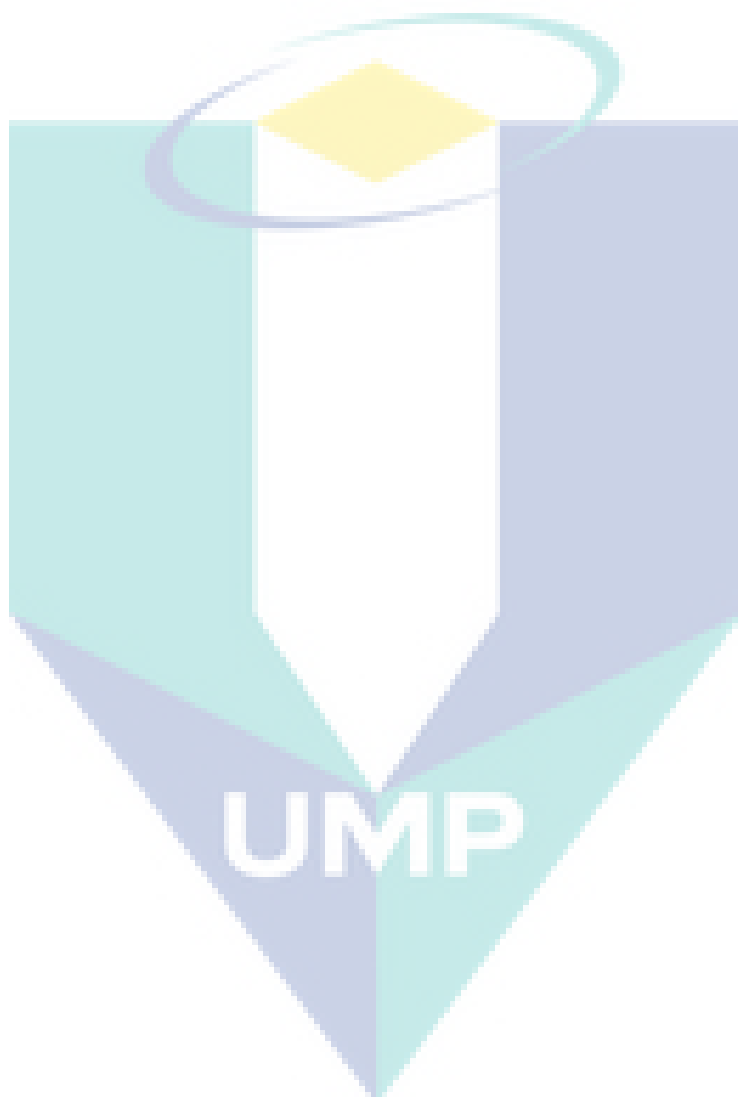
PRINT ALONG PATH DEFINED BY LPATH COMMAND. DSYS= 0
 ***** PATH VARIABLE SUMMARY *****

X	Y	Z	UZ	SX	SXZ	SINT
0	0	0	1.39E-04	-1.62E+09	-4642.1	1.25E+09
0	0	5.00E-05	1.40E-04	-1.59E+09	-4267.6	1.23E+09
0	0	1.00E-04	1.40E-04	-1.57E+09	-3892.8	1.21E+09
0	0	1.50E-04	1.41E-04	-1.55E+09	-3517.5	1.19E+09
0	0	2.00E-04	1.41E-04	-1.52E+09	-3141.9	1.16E+09
0	0	2.50E-04	1.41E-04	-1.50E+09	-2765.8	1.14E+09
0	0	3.00E-04	1.42E-04	-1.47E+09	-2389.3	1.12E+09
0	0	3.50E-04	1.42E-04	-1.45E+09	-2012.4	1.09E+09
0	0	4.00E-04	1.43E-04	-1.42E+09	-1635.1	1.07E+09
0	0	4.50E-04	1.43E-04	-1.40E+09	-1257.4	1.05E+09
0	0	5.00E-04	1.43E-04	-1.38E+09	-879.23	1.03E+09
0	0	5.50E-04	1.44E-04	-1.35E+09	-500.68	1.00E+09
0	0	6.00E-04	1.44E-04	-1.33E+09	-121.71	9.80E+08
0	0	6.50E-04	1.44E-04	-1.30E+09	257.66	9.57E+08
0	0	7.00E-04	1.45E-04	-1.28E+09	637.45	9.34E+08
0	0	7.50E-04	1.45E-04	-1.25E+09	1017.7	9.11E+08
0	0	8.00E-04	1.45E-04	-1.23E+09	1398.3	8.88E+08
0	0	8.50E-04	1.46E-04	-1.21E+09	1779.3	8.65E+08
0	0	9.00E-04	1.46E-04	-1.18E+09	2160.7	8.42E+08
0	0	9.50E-04	1.46E-04	-1.16E+09	2542.6	8.19E+08
0	0	1.00E-03	1.47E-04	-1.13E+09	2924.9	7.97E+08
0	0	1.05E-03	1.47E-04	-1.11E+09	3307.5	7.74E+08
0	0	1.10E-03	1.47E-04	-1.08E+09	3690.6	7.51E+08
0	0	1.15E-03	1.48E-04	-1.06E+09	4074.1	7.28E+08
0	0	1.20E-03	1.48E-04	-1.04E+09	4458	7.05E+08
0	0	1.25E-03	1.48E-04	-1.01E+09	4842.4	6.82E+08
0	0	1.30E-03	1.48E-04	-9.87E+08	5227.1	6.59E+08
0	0	1.35E-03	1.48E-04	-9.62E+08	5612.3	6.36E+08
0	0	1.40E-03	1.49E-04	-9.38E+08	5997.8	6.14E+08
0	0	1.45E-03	1.49E-04	-9.14E+08	6383.8	5.91E+08
0	0	1.50E-03	1.49E-04	-8.89E+08	6770.2	5.68E+08
0	0	1.55E-03	1.49E-04	-8.71E+08	6771	5.52E+08
0	0	1.60E-03	1.49E-04	-8.53E+08	6771.8	5.37E+08
0	0	1.65E-03	1.50E-04	-8.34E+08	6772.6	5.22E+08
0	0	1.70E-03	1.50E-04	-8.16E+08	6773.4	5.06E+08
0	0	1.75E-03	1.50E-04	-7.97E+08	6774.1	4.91E+08
0	0	1.80E-03	1.50E-04	-7.79E+08	6774.9	4.76E+08
0	0	1.85E-03	1.50E-04	-7.61E+08	6775.7	4.60E+08
0	0	1.90E-03	1.51E-04	-7.42E+08	6776.5	4.45E+08
0	0	1.95E-03	1.51E-04	-7.24E+08	6777.3	4.30E+08
0	0	2.00E-03	1.51E-04	-7.06E+08	6778.1	4.14E+08
0	0	2.05E-03	1.51E-04	-6.87E+08	6778.9	3.99E+08

0	0	2.10E-03	1.51E-04	-6.69E+08	6779.7	3.84E+08
0	0	2.15E-03	1.51E-04	-6.51E+08	6780.5	3.68E+08
0	0	2.20E-03	1.51E-04	-6.32E+08	6781.2	3.53E+08
0	0	2.25E-03	1.51E-04	-6.17E+08	6783.9	3.41E+08
0	0	2.30E-03	1.52E-04	-6.02E+08	6787.9	3.30E+08
0	0	2.35E-03	1.52E-04	-5.87E+08	6793	3.18E+08
0	0	2.40E-03	1.52E-04	-5.72E+08	6799.3	3.07E+08
0	0	2.45E-03	1.52E-04	-5.57E+08	6806.9	2.95E+08
0	0	2.50E-03	1.52E-04	-5.42E+08	6815.7	2.84E+08
0	0	2.55E-03	1.52E-04	-5.27E+08	6825.7	2.72E+08
0	0	2.60E-03	1.52E-04	-5.12E+08	6836.9	2.60E+08
0	0	2.65E-03	1.52E-04	-4.97E+08	6849.3	2.49E+08
0	0	2.70E-03	1.52E-04	-4.82E+08	6863	2.37E+08
0	0	2.75E-03	1.52E-04	-4.67E+08	6877.8	2.26E+08
0	0	2.80E-03	1.53E-04	-4.52E+08	6893.9	2.14E+08
0	0	2.85E-03	1.53E-04	-4.37E+08	6911.2	2.03E+08
0	0	2.90E-03	1.53E-04	-4.22E+08	6929.7	1.91E+08
0	0	2.95E-03	1.53E-04	-4.09E+08	6905.4	1.81E+08
0	0	3.00E-03	1.53E-04	-3.95E+08	6881.4	1.71E+08
0	0	3.05E-03	1.53E-04	-3.82E+08	6857.9	1.62E+08
0	0	3.10E-03	1.53E-04	-3.68E+08	6834.8	1.52E+08
0	0	3.15E-03	1.53E-04	-3.55E+08	6812.2	1.42E+08
0	0	3.20E-03	1.53E-04	-3.41E+08	6789.9	1.32E+08
0	0	3.25E-03	1.53E-04	-3.28E+08	6768.1	1.22E+08
0	0	3.30E-03	1.53E-04	-3.14E+08	6746.6	1.12E+08
0	0	3.35E-03	1.53E-04	-3.00E+08	6725.6	1.02E+08
0	0	3.40E-03	1.53E-04	-2.87E+08	6705	9.26E+07
0	0	3.45E-03	1.53E-04	-2.73E+08	6684.8	8.28E+07
0	0	3.50E-03	1.53E-04	-2.60E+08	6665	7.29E+07
0	0	3.55E-03	1.53E-04	-2.46E+08	6645.7	6.30E+07
0	0	3.60E-03	1.53E-04	-2.33E+08	6626.7	5.32E+07
0	0	3.65E-03	1.53E-04	-2.20E+08	6608.4	4.39E+07
0	0	3.70E-03	1.53E-04	-2.07E+08	6589.6	3.45E+07
0	0	3.75E-03	1.53E-04	-1.93E+08	6570.5	2.52E+07
0	0	3.80E-03	1.53E-04	-1.80E+08	6550.9	1.58E+07
0	0	3.85E-03	1.54E-04	-1.67E+08	6531	6.48E+06
0	0	3.90E-03	1.54E-04	-1.54E+08	6510.7	2.87E+06
0	0	3.95E-03	1.54E-04	-1.41E+08	6490	1.22E+07
0	0	4.00E-03	1.54E-04	-1.28E+08	6468.9	2.16E+07
0	0	4.05E-03	1.54E-04	-1.15E+08	6447.4	3.09E+07
0	0	4.10E-03	1.54E-04	-1.02E+08	6425.5	4.03E+07
0	0	4.15E-03	1.54E-04	-8.91E+07	6403.3	4.96E+07
0	0	4.20E-03	1.54E-04	-7.60E+07	6380.6	5.89E+07
0	0	4.25E-03	1.54E-04	-6.30E+07	6357.6	6.83E+07
0	0	4.30E-03	1.54E-04	-4.99E+07	6334.1	7.76E+07
0	0	4.35E-03	1.54E-04	-3.68E+07	6273.2	8.74E+07
0	0	4.40E-03	1.54E-04	-2.36E+07	6211.1	9.71E+07
0	0	4.45E-03	1.54E-04	-1.04E+07	6147.8	1.07E+08
0	0	4.50E-03	1.53E-04	2.71E+06	6083.3	1.17E+08

0	0	4.55E-03	1.53E-04	1.59E+07	6017.6	1.26E+08
0	0	4.60E-03	1.53E-04	2.90E+07	5950.7	1.36E+08
0	0	4.65E-03	1.53E-04	4.22E+07	5882.6	1.46E+08
0	0	4.70E-03	1.53E-04	5.53E+07	5813.3	1.55E+08
0	0	4.75E-03	1.53E-04	6.85E+07	5742.8	1.65E+08
0	0	4.80E-03	1.53E-04	8.16E+07	5671.1	1.75E+08
0	0	4.85E-03	1.53E-04	9.48E+07	5598.2	1.85E+08
0	0	4.90E-03	1.53E-04	1.08E+08	5524.1	1.94E+08
0	0	4.95E-03	1.53E-04	1.21E+08	5448.8	2.04E+08
0	0	5.00E-03	1.53E-04	1.34E+08	5372.3	2.14E+08
0	0	5.05E-03	1.53E-04	1.48E+08	5407.5	2.24E+08
0	0	5.10E-03	1.53E-04	1.61E+08	5440.8	2.34E+08
0	0	5.15E-03	1.53E-04	1.74E+08	5472.3	2.45E+08
0	0	5.20E-03	1.53E-04	1.88E+08	5501.8	2.55E+08
0	0	5.25E-03	1.53E-04	2.01E+08	5529.5	2.66E+08
0	0	5.30E-03	1.53E-04	2.15E+08	5555.2	2.76E+08
0	0	5.35E-03	1.53E-04	2.28E+08	5579.1	2.86E+08
0	0	5.40E-03	1.53E-04	2.42E+08	5601.1	2.97E+08
0	0	5.45E-03	1.53E-04	2.55E+08	5621.2	3.07E+08
0	0	5.50E-03	1.52E-04	2.68E+08	5639.4	3.17E+08
0	0	5.55E-03	1.52E-04	2.82E+08	5655.7	3.28E+08
0	0	5.60E-03	1.52E-04	2.95E+08	5670.2	3.38E+08
0	0	5.65E-03	1.52E-04	3.09E+08	5682.7	3.48E+08
0	0	5.70E-03	1.52E-04	3.22E+08	5693.4	3.59E+08
0	0	5.75E-03	1.52E-04	3.37E+08	5312.4	3.72E+08
0	0	5.80E-03	1.52E-04	3.52E+08	4929.8	3.86E+08
0	0	5.85E-03	1.52E-04	3.67E+08	4545.7	3.99E+08
0	0	5.90E-03	1.52E-04	3.82E+08	4160.1	4.13E+08
0	0	5.95E-03	1.52E-04	3.97E+08	3773	4.27E+08
0	0	6.00E-03	1.51E-04	4.12E+08	3384.4	4.40E+08
0	0	6.05E-03	1.51E-04	4.27E+08	2994.3	4.54E+08
0	0	6.10E-03	1.51E-04	4.42E+08	2602.7	4.67E+08
0	0	6.15E-03	1.51E-04	4.57E+08	2209.6	4.81E+08
0	0	6.20E-03	1.51E-04	4.72E+08	1814.9	4.94E+08
0	0	6.25E-03	1.51E-04	4.87E+08	1418.8	5.08E+08
0	0	6.30E-03	1.51E-04	5.02E+08	1021.1	5.22E+08
0	0	6.35E-03	1.51E-04	5.17E+08	621.93	5.35E+08
0	0	6.40E-03	1.50E-04	5.32E+08	221.25	5.49E+08
0	0	6.45E-03	1.50E-04	5.47E+08	-180.94	5.62E+08
0	0	6.50E-03	1.50E-04	5.62E+08	-584.64	5.76E+08
0	0	6.55E-03	1.50E-04	5.77E+08	-989.85	5.89E+08
0	0	6.60E-03	1.50E-04	5.92E+08	-1396.6	6.03E+08
0	0	6.65E-03	1.50E-04	6.07E+08	-1804.8	6.16E+08
0	0	6.70E-03	1.49E-04	6.22E+08	-2214.5	6.30E+08
0	0	6.75E-03	1.49E-04	6.37E+08	-2625.8	6.44E+08
0	0	6.80E-03	1.49E-04	6.52E+08	-3038.6	6.57E+08
0	0	6.85E-03	1.49E-04	6.67E+08	-3452.8	6.71E+08
0	0	6.90E-03	1.49E-04	6.82E+08	-3868.6	6.84E+08
0	0	6.95E-03	1.48E-04	6.97E+08	-4285.9	6.98E+08

0	0	7.00E-03	1.48E-04	7.12E+08	-4704.7	7.11E+08
0	0	7.05E-03	1.48E-04	7.27E+08	-5125	7.25E+08
0	0	7.10E-03	1.48E-04	7.42E+08	-5546.8	7.38E+08
0	0	7.15E-03	1.48E-04	7.57E+08	-5970.1	7.52E+08
0	0	7.20E-03	1.47E-04	7.72E+08	-6395	7.66E+08



APPENDIX C

Pressure values for different load intensities and thicknesses

P	E_L(Titanium)	h	d	p
1	1.0795E+11	0.0072	0.03	358152192
2	1.0795E+11	0.0072	0.03	716304384
3	1.0795E+11	0.0072	0.03	1074456576
4	1.0795E+11	0.0072	0.03	1432608768
5	1.0795E+11	0.0072	0.03	1790760960
6	1.0795E+11	0.0072	0.03	2148913152
7	1.0795E+11	0.0072	0.03	2507065344
8	1.0795E+11	0.0072	0.03	2865217536
9	1.0795E+11	0.0072	0.03	3223369728
10	1.0795E+11	0.0072	0.03	3581521920
11	1.0795E+11	0.0072	0.03	3939674112
12	1.0795E+11	0.0072	0.03	4297826304

P	E_L(Titanium)	h	d	p
1	1.0795E+11	0.006	0.03	172720000
2	1.0795E+11	0.006	0.03	345440000
3	1.0795E+11	0.006	0.03	518160000
4	1.0795E+11	0.006	0.03	690880000
5	1.0795E+11	0.006	0.03	863600000
6	1.0795E+11	0.006	0.03	1036320000
7	1.0795E+11	0.006	0.03	1209040000
8	1.0795E+11	0.006	0.03	1381760000
9	1.0795E+11	0.006	0.03	1554480000
10	1.0795E+11	0.006	0.03	1727200000
11	1.0795E+11	0.006	0.03	1899920000
12	1.0795E+11	0.006	0.03	2072640000

P	E_L(Titanium)	h	d	p
1	1.0795E+11	0.0084	0.03	663521152
2	1.0795E+11	0.0084	0.03	1327042304
3	1.0795E+11	0.0084	0.03	1990563456
4	1.0795E+11	0.0084	0.03	2654084608
5	1.0795E+11	0.0084	0.03	3317605760
6	1.0795E+11	0.0084	0.03	3981126912
7	1.0795E+11	0.0084	0.03	4644648064
8	1.0795E+11	0.0084	0.03	5308169216
9	1.0795E+11	0.0084	0.03	5971690368
10	1.0795E+11	0.0084	0.03	6635211520
11	1.0795E+11	0.0084	0.03	7298732672
12	1.0795E+11	0.0084	0.03	7962253824

LIST OF PUBLICATIONS

Jamaludin, S.N.S., Mustapha, F., Nuruzzaman, D.M. and Basri, S. 2013. A review on the fabrication techniques of functionally graded ceramic-metallic materials in advanced composites. *Scientific Research and Essays*. **8**(21): 828-840.

Jamaludin, S.N.S., Mustapha, F., Nuruzzaman, D.M., Tuan Ya, T.M.Y. and Basri, S. 2013. Finite element calculation of residual thermal stresses for functionally graded Hydroxyapatite-Titanium plate design. *Academic Platform Journal of Engineering and Science*. **1**(2): 1-10.

Jamaludin, S.N.S., Basri, S., Hussain, A., Al-Othmany, D.S., Mustapha, F. and Nuruzzaman, D.M. 2014. Three-dimensional finite element modeling of thermomechanical problems in functionally graded Hydroxyapatite/Titanium plate. *Mathematical Problems in Engineering*. **2014**(Article ID 371462): 1-20. **(IF:1.38)**

Abdul Latiff, M.I., Jamaludin, S.N.S., Basri, S., Hussain, A., Al-Othmany, D.S., Mustapha, F., Nuruzzaman, D.M., Ismail, N.M. and Ismail, I. 2014. Effect of sintering temperature on functionally graded Nickel/alumina plate. *Applied Mechanics and Materials*. **629**: 437-443. **(SCOPUS)**

Jamaludin, S.N.S., Basri, S., Mustapha, F., Nuruzzaman, D.M., Abdul Latiff, M.I. and Ismail, N.M. Phase contamination characterization of a stepwise built functionally graded Hydroxyapatite/Titanium sintered under various atmospheres. Submitted to *Materials Letter* on March 2015. **(IF:2.269)**

VITA

Siti Nur Sakinah Binti Jamaludin was born in Bukit Mertajam, Pulau Pinang. She finished secondary school in Sekolah Agama Menengah Bestari, USJ Subang Jaya in 2002. She graduated from Universiti Malaysia Pahang (UMP) in 2008 with BEng. Honours in Mechanical Engineering with Manufacturing Engineering. She has furthered her MsC. study in Automotive Engineering from 2009 until 2011. Since then, she has been working as a Research Assistant in Faculty of Mechanical, UMP and enrolled in the PhD programs in March 2012. She was married to Muhd Zahiruddin Bin Shukor in 2009 and has two sons, Zaidul Iman and Zaheen Hanif, aged 4 and 3 years.

